Nanotechnology-based Drug Repurposing for Potential Theranostic Applications

A Thesis

Submitted in Partial Fulfilment of the Requirements for the award of the degree of

DOCTOR OF PHILOSOPHY

by

Konika Choudhury

(Roll no. - 186153103)

Centre for Nanotechnology

Indian Institute of Technology Guwahati

Guwahati, 781039, Assam, India

For my family

And for those who dare to dream

Declaration

I, hereby, declare that the research embodied in this thesis entitled "**Nanotechnology-based Drug Repurposing for Potential Theranostic Applications**" is the result of investigations carried out by me under the supervision of Prof. Siddhartha Sankar Ghosh, Department of Biosciences and Bioengineering and Prof. Arun Chattopadhyay, Department of Chemistry, Indian Institute of Technology Guwahati, India for the award of Degree of **Doctor of Philosophy** in **Nanotechnology**. This work has not been submitted elsewhere for any degree, diploma etc. of any other institute or University to the best of my knowledge and belief.

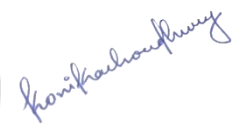

Date: 14.03.2024 Konika Choudhury

Place: Guwahati Roll no. 186153103

Certificate

This is to certify that the thesis titled "**Nanotechnology-based Drug Repurposing for Potential Theranostic Applications**", being submitted to the **Indian Institute of Technology, Guwahati** by ***Konika Choudhury*** (Roll no. **186153103**) for the award of the degree of **Doctor of Philosophy** in **Nanotechnology** is a bonafide record of research work carried out by her. The information and the data reported by her are solely the results of her original findings. She has meticulously carried out the investigations and followed the guidelines of the laboratory. The contents of this thesis have not been submitted to any other university or institute for the award of any degree or diploma.

Date: 14.03.2024

Place: Guwahati

Prof. Siddhartha Sankar Ghosh

Thesis Supervisor

Department of Biosciences and Bioengineering

Indian Institute of Technology Guwahati

Guwahati-781039, Assam, India

Prof. Arun Chattopadhyay

Thesis Supervisor

Department of Chemistry

Indian Institute of Technology Guwahati

Guwahati-781039, Assam, India

Acknowledgement

They say that some journeys are better than the destination itself. While the ending itself is bitter sweet, these five years have been most enjoyable and insightful for me. It would be remiss of me therefore, if I don't extend my gratitude to those responsible. First and foremost, I would like to thank my supervisors Prof. Siddhartha Sankar Ghosh and Prof. Arun Chattopadhyay for giving me the opportunity to work in their lab. I am thankful to them for taking care of all the facilities to carry out my research. Their constant guidance and at times, constructive criticism has helped me hone my skills as a researcher and also, a human in general.

I would also like to thank my doctoral committee members: Dr. Sunanda Chatterjee (Chairman), Prof. Tapas Kumar Mandal and Prof. Lal Mohan Kundu for evaluating my work and providing vital suggestions from time to time. I acknowledge all the faculty members and staff of Centre for Nanotechnology. I also thank the Centre for Nanotechnology, Central Instrumentation Facility, Department of Biosciences and Bioengineering and Department of Chemistry, IIT Guwahati for providing the state-of-art facilities to conduct my research.

In addition, I sincerely thank Dr. Kalyansis Sahu and Dr. Tamanna Bhuyan for providing me the opportunity to work in collaboration and extrapolate the possibilities of my work in multiple disciplines.

I whole-heartedly thank my science teacher from higher secondary school, Mr. Karuppiah Jaisankar, who instilled in me that we don't merely study biology. Instead, we breathe, eat, drink, walk, run and live with biology. I thank Eeshwar Sir and Sreenivasan Sir from Vivekananda Kendra Vidyalaya Itanagar, Arunachal Pradesh for indulging the learner in me. I also thank the entire faculty and staff members of KIIT School of Biotechnology (KSBT) Bhubaneswar, Odisha for teaching me the basics of biotechnology, both theoretically and experimentally. Finally, I am also thankful to Dr. Krishnamohan Atmakuri at the Translational Health Science and Technology Institute (THSTI), Faridabad to have inculcated in me the passion for research.

I am indebted to my lab mates: seniors (Dr. Upashi Goswami, Dr. Srirupa Bhattacharyya, Dr. Anitha T. Simon, Dr. Rajib Shome, Dr. Kasturi Gogoi, Dr. Debashree Debasmita, Dr. Muktashree Saha and Dr. Plaboni Sen), Arupam Patra and juniors (Hirakjyoti Roy, Sayantani

Mukhopadhyay, Sawna Roy, Sayantani Biswas, Sujisha Nambiar, Shilpi Sarkar, Thirukumaran Kandaswamy, Arisha Arora, Basab Ghosh, Pijush, Ujjala Dey and Haseena). We have been (are) a family, for better and for worse, always melting each other into laughter at the end of an exhausting day.

Friends are siblings in disguise and I will always be grateful to have found Sucheta, Souvik and Tarosi who always bring light into my life. It would be remiss of me if I don't mention Plaboni and Narayani, my partners in crime at IIT Guwahati.

Books have been my solace for as long as I can remember. There were days when no pages were turned, but in the end, I always found them waiting. Special thanks to my bookstagram (@of_papercuts) community for a parallel refugee when days were especially trying.

I thank my extended family for their love and support. My grandparents, Late Sri Satish Chandra Chowdhury, Late Smt. Harilata Debi, Late Sri Gopal Chandra Choudhury and Smt. Rani Debi who would have been proud to see me today, for showering their blessings and love. My aunt, Mrs. Sabita Dey for her words of concern and encouragement. Special thanks to my sister from another mother, Paromita for being the company, the rock one always needs.

I am fortunate to have found the kindest parents-in law. I thank my father-in law, Mr. Dinesh Chandra Sur for his love and encouragement; and my mother-in law, Mrs. Dali Sur for her love, support and the delicious most *Dalia* dish in the world.

I can never express in words the deep gratitude and overwhelming sense of abundance that I have for my parents. Yet I dare thank my first teachers, for motivating me and for being the strongest pillars of my life. I am because they are. My *Baba*, Mr. Aloke Choudhury for leaving no stone unturned to fulfil my lamest of wishes, for being my first critic when needed and for believing in me always. My *Ma*, Mrs. Namita Choudhury for instilling in me a life of honest work and kindness; and for teaching me the importance of putting "myself" first at times.

I consider myself blessed and the luckiest to have found my best friend and husband, all in one person, Dr. Dipesh Sur. My heartfelt gratitude to him for being the confidante everybody needs, for encouraging me to get up after every fall and for NOT agreeing with me when needed. He continues to have faith in me, even at times when I am doubtful.

I am grateful for my furry little son, Byomkesh for lighting up my world every moment of the day. I am thankful for my four-legged friends at IIT Guwahati who make me smile with their innocence and playfulness. They will always stay in my heart.

Finally, I am thankful to the almighty God for showing me light even during the darkest hour.

Konika Choudhury

Table of Contents

Abstract

Cancer in any form, results from altered signalling and metabolism culminating into uncontrolled division and survival of transformed cells. Each year millions of cancer related deaths are reported globally and the numbers are still on the rise. Conventionally, cancer has been treated by chemotherapy, radiotherapy or surgery. Some of the more advanced and comprehensive approaches also include immunotherapy, targeted therapy, radiofrequency ablation and stereotactic radiosurgery. However, even with a host of literature and ever evolving medical approaches, a successful cure seems obscure. Developing a drug too is both time-taking and expensive. Moreover, since normal and cancer cells are genetically so similar, unbraiding the two is herculean and often the reason behind failure of most therapies. Not ever cancer cell within a tumor has the same genetic mutations as its neighbour. Therefore, even after prolonged and expensive treatments, when a patient is declared cancer-free, the chance of relapse remains on the horizon. Hence, there is an urgent need to look for alternative therapeutic strategies. In this scenario, repurposing a licensed drug along with means to take care of the limitations can become a very sustainable approach in cancer therapy. To further intensify these responses, nanotechnology would be useful to enhance the drug's delivery, retention while reducing toxicity. This thesis explores the complicated association of cancer and drug repurposing and tries to simplify the same with aid from nanotherapeutics.

Chapter 1 titled as **Introduction and Review of Literature** describes the cancer global burden and the current scenario of therapeutic approaches**.** It also details the progressive stages of cancer while panning out its developmental hallmarks. Furthermore, this chapter compares *de novo* drug development to drug repurposing in terms of advantages and limitations. It discusses the current repositioning scenario with detailed tabulations. It also highlights the dire need to come up with a bypass therapy to target lung adenocarcinoma and triple-negative breast cancer (TNBC). In addition, it mentions the role of non-antibiotics in targeting Gram-stain bacteria and their biofilms. Under potential drugs for repurposing, this chapter elucidates the significance of antihistamines and hints at a trajectory into cancer's relationship with inflammation. While laying out certain limitations associated with free drugs, this section highlights the role nanotherapeutics can play in drug stability, release and delivery. The

remaining part of this chapter discusses in detail previous attempts at refining the benefits of repurposing with nanotechnology and their insights in the biomedical field. Lastly, Chapter 1 lists out the scopes and salient features followed by objectives that target different aspects of the current thesis.

Chapter 2 includes a systematic explanation of **Materials and Methods** used for the experiments. This section also details all the experimental methodologies followed, along with EMT induction, multicellular spheroid formation and biofilm formation. Additionally, methods for all statistical analyses have also been mentioned.

Chapter 3 describes the **Results and Discussions** of the objectives in the thesis. In the first objective, following an exhaustive preliminary screening of six over-the-counter drugs, promethazine hydrochloride was selected for its superior antibacterial property. It was loaded onto mannosylated gold nanoclusters. Mannose functionalization as targeted therapy was aimed at Gram-stained bacteria and their respective biofilms, especially the pili of Gram-negative bacteria. The nanoformulation was fluorescent, water-soluble and exhibited pH-dependent drug release. MIC and MBC determined through established spread-plate method was linked with altered morphology and membrane permeability. The lipid content was reduced while there was suggestive increase in ROS, following treatment. Finally, live-dead staining of treated biofilms revealed successful eradication of biofilm chunks. These findings potentiated the anti-bacterial abilities of the mannosylated gold nanocluster loaded with promethazine hydrochloride.

For the subsequent objective, lung adenocarcinoma cells were directed with a nanotherapeutic module engineered to deliver a repurposed antihistamine. Given the over-expression of mannose receptors on their surface, the nano system was mannosylated to facilitate targeting of the adenocarcinoma cells. Upon uptake, the inherently fluorescent nano system could also be monitored in real time. Anti-proliferative potential of the nanotherapeutic module was determined through cell and spheroid viability assays. Its inhibitory potential was further linked with its ability to generate ROS, depolarize mitochondrial membrane potential and facilitate programmed cell death. Furthermore, the nano system's repercussion on lipid content, colony

forming and migration ability was also scrutinized. Finally, the module's spheroid inhibition capacity was functionally explored through spheroid formation and live-dead staining assays. In the final objective, several over-the-counter antihistamines were tested for anti-proliferative activity on TNBC and breast cancer cell lines. Promethazine hydrochloride, an H1 receptor antagonist was ultimately selected because of the comparatively lower half maximal inhibitory concentrations (IC_{50}). Following this, an attempt was made to alter EMT dynamics of TNBC cell lines through dual therapy using promethazine loaded PLGA nanoparticles and HDACi, SAHA. Interestingly, SAHA treatment prior to exposure to the PLGA-PH nanoparticles sensitized the cells even more. To facilitate bioimaging properties, drug loaded nanoparticles were conjugated with FITC. Following exposure to this module, there was increase in ROS production, mitochondrial membrane depolarization and apoptotic population. Consequentially, the proliferative potential of cells too was greatly affected. In addition, EMT to MET transition was also found to be facilitated due to the pre-treatment therapy.

Chapter 4 titled as **Conclusion and Future Prospects** elucidates the key findings of this thesis and their implications in the biomedical field. Towards developing a sustainable cancer therapy, antihistamine drugs were repositioned and their anti-proliferative activities assessed in lung adenocarcinoma cells and TNBC cells. One of the antihistamine drugs was also utilised to explore antibacterial activity followed by biofilm eradication. It also details the promising possibilities of repositioning when combined with nanotherapeutics.

List of Abbreviations and Acronyms

APS	Ammonium Persulfate
BL1	Basal-like 1
BL2	Basal-like 2
Da	Dalton
DAPI	4′,6-diamidino-2-phenylindole
DCFDA	Dichlorodihydrofluorescein Diacetate
DLS	Dynamic Light Scattering
DMEM	Dulbecco's Modified Eagle Medium
DMSO	Dimethyl Sulfoxide
ECM	Extracellular Matrix
EMT	Epithelial to Mesenchymal Transition
ER	Estrogen Receptor
FBS	Fetal Bovine Serum
FDA	Food and Drug Administration
FESEM	Field Emission Scanning Electron Microscope
FITC	Fluorescein Isothiocyanate
FTIR	Fourier Transform Infrared
GAPDH	Glyceraldehyde 3-phosphate Dehydrogenase
h	Hour
HER-2	Human Epidermal Growth Factor Receptor 2
IC	Inhibitory Concentration
LSM	Laser Scanning Microscopy
min	Minute
MCF	Michigan Cancer Foundation
MET	Mesenchymal to Epithelial Transition
MRI	Magnetic resonance imaging

NCCS	National Centre for Cell Science
PBS	Phosphate Buffer Saline
PBST	Phosphate Buffer Saline with 0.1% Tween
PDT	Photodynamic therapy
PTT	Photothermal therapy
PI	Propidium Iodide
PLGA	poly(lactic-co-glycolic acid)
PR	Progesterone Receptor
PVA	Poly(vinyl alcohol)
RIPA	Radioimmunoprecipitation Assay Buffer
ROS	Reactive Oxygen Species
rpm	Revolutions Per Minute
SAED	Selected Area Electron Diffraction
SAHA	Suberoylanilide Hydroxamic Acid
SDS PAGE	Sodium Dodecyl Sulfate Poly Acrylamide Gel Electrophoresis
siRNA	short interfering ribonucleic acid
TEM	Transmission Electron Microscope
TEMED	Tetramethylethylenediamine
TNBC	Triple-Negative Breast Cancer
Tris	Trizma Base

List of Schemes

3.3. Schematic illustrating the difference between individual components of the therapeutic regime and its application on triple-negative breast cancer cell.

List of Figures

3.1.8. Determination of radii of zones of inhibition of (Man-BSA)-PH-AuNC treated (A) *P. aeruginosa*, (B) *E. coli*, (C) *S. aureus* and (D) *B. subtilis*.

3.1.9. Growth kinetics curve showing the effect of free promethazine (MIC) and (Man-BSA)-PH-AuNCs (MIC) treated (A) *P. aeruginosa*, (B) *E. coli*, (C) *S. aureus* and (D) *B. subtilis* compared to untreated bacteria by measuring absorbance at 595 nm every two hours for 12 hours. Lipid content detection in (E) *P. aeruginosa* and (F) *E. coli* control and treated planktonic bacteria with free promethazine and (Man-BSA)-PH-AuNCs through fluorescence intensity measurement at 570-700 nm.

3.1.10. Confocal microscopy images of Nile red-stained planktonic bacteria for lipid content detection. [A (I-II)] control *P. aeruginosa*: [A(I) Nile red stained, A(II) merged image] and [B(I-II)] Man (BSA-PH-AuNC) treated *P. aeruginosa*: [B(I) Nile red stained, B(II) merged image]. [C (I-II)] control *E. coli*: [C(I) Nile red stained, C(II) merged image] and [D(I-II)] Man (BSA-PH-AuNC) treated *E, coli*: [D(I) Nile red stained, D(II) merged image]. The images were taken at a scale bar of 5µm.

3.1.11. Leakage of UV absorbing materials (at 260 nm and 280 nm) from untreated vs. promethazine-treated and (Man-BSA)-PH-AuNCs-treated bacterial cells. (A) *P. aeruginosa*, (B) *E. coli*, (C) *S. aureus* and (D) *B. subtilis*.

3.1.12. Field emission scanning electron microscopy images of untreated and treated bacteria. A-B: Untreated and treated *P. aeruginosa* (Scale -1 µm). C-D: Untreated and treated *E. coli* (Scale -1 µm). E-F: Untreated and treated *S. aureus* (Scale -100 nm). G-H: Untreated and treated *B. subtilis* (Scale -200 nm).

3.1.13. Formation of ROS in (Man-BSA)-PH-AuNC-treated, promethazine-treated and untreated (control) bacterial cells: (A) *P. aeruginosa*, (B) *E. coli*, (C) *S. aureus* and (D) *B. subtilis*. The intensity of fluorescence is directly proportional to the amount of oxidised DCFH-DA to DCF by intracellular esterases. Fluorescence was detected at an excitation filter of 485 nm and emission filter of 523 nm.

3.1.14. Antibiofilm activity of free promethazine and (Man-BSA)-PH-AuNCs in A- *P. aeruginosa* and B- *S. aureus*. A(I)- free promethazine treated and A(II)- Man (BSA_PH-AuNC) treated *P. aeruginosa* biofilm. B(I)- free promethazine treated and B(II)- Man (BSA_PH-AuNC) treated *E. coli* biofilm. C(I)- free promethazine treated and C(II)- Man (BSA_PH-

AuNC) treated *S. aureus* biofilm. The ANOVA test revealed statistical significance of free promethazine and Man (BSA-PH-AuNC) treated biofilms with respect to control ones. Statistical significance is denoted by * ($p < 0.05$), ** ($p < 0.005$), *** ($p < 0.001$), and **** ($p < 0.0001$). The data are represented as mean ± SD of three individual experiments.

3.1.15. Live/dead confocal microscopy images of AO/PI-stained bacterial biofilm: A- *P. aeruginosa*; B- *E. coli* and C- *S. aureus*. [A (I-III)], [B(1-III)], [C(I-III)] control: [A/B/C(I) AO stained, A/B/C (II) PI-stained, A/B/C(III) merged image]. [A(IV-VI)], [B(IV-VI)], [C(IV-VI)] sub-$MBIC_{50}$ of Man (BSA-PH-AuNC) treated biofilm: [A/B/C(IV) AO stained, A/B/C(V) PI-stained, A/B/C(VI) merged image]. [A(VII-IX), B(VII-IX)], C(VII-IX)] $MBIC_{50}$ of Man (BSA-PH-AuNC) treated biofilm: [A/B/C(VII) AO stained, A/B/C(VIII) PI-stained, A/B/C(IX) merged image]. The images were taken at a scale bar of 100 µm.

3.1.16. Confocal microscopy images of AO/PI-stained and Nile-red stained bacterial biofilm: A, D- *P. aeruginosa*; B, E- *E. coli*; C- *S. aureus*. [A (I-III)] $MBIC_{50}$ of free promethazine treated *P. aeruginosa* biofilm: [A(I) AO stained, A(II) PI-stained, A(III) merged image]. [B(I-III)] $MBIC_{50}$ of free promethazine treated *E. coli* biofilm: [B(I) AO stained, B(II) PI-stained, B(III) merged image]. [C(I-III)] $MBIC_{50}$ of free promethazine treated *S. aureus* biofilm: [B(I) AO stained, B(II) PI-stained, B(III) merged image]. [D (I-II)] $MBIC_{50}$ of free promethazine treated *P. aeruginosa* biofilm: [D(I) Nile red-stained, D(II) merged image]. [E(I-II)] $MBIC_{50}$ of free promethazine treated *E. coli* biofilm: [E(I) Nile red-stained, E(II) merged image]. The images were taken at a scale bar of 100 µm.

3.1.17. Confocal microscopy images of Nile red-stained bacterial biofilm for lipid content detection. A- *P. aeruginosa*, B- *E. coli*. [A (I-II)] control *P. aeruginosa*: [A(I) Nile red-stained; A(II) merged image]. [A(III-IV)] sub-$MBIC_{50}$ of Man (BSA-PH-AuNC) treated *biofilm*: [A(III) Nile red-stained, A(IV) merged image]. [A(V-VI)] $MBIC_{50}$ of (Man-BSA)-PH-AuNCs treated biofilm: [A(V) Nile red-stained, A(VI) merged image]. [B (I-II)] control *E. coli*: [B(I) Nile red-stained, B(II) merged image]. [A(III-IV)] sub-$MBIC_{50}$ of Man (BSA-PH-AuNC) treated *biofilm*: [B(III) Nile red-stained, B(IV) merged image]. [B(V-VI)] $MBIC_{50}$ of (Man-BSA)-PH-AuNCs treated biofilm: [B(V) Nile red-stained, B(VI) merged image]. The images were taken at a scale bar of 100 µm.

3.2.1. Characterisation of copper nanoclusters (CuNCs). (A) Selected area electron diffraction pattern (SAED). (B) X-ray diffraction plot (XRD). (C) Energy dispersive X-ray spectroscopy (EDX) analysis. (D) Zeta potential.

3.2.2. (A) Individual components of the nanocluster and nanocomposite under UV transilluminator. (B) Concentration of Cu in the CuNCs as obtained from the atomic absorption spectroscopy. (C) UV-Vis spectra of CuNC, LH and CuNC-LH. (D) Fluorescence intensity of CuNC and nanocomposite upon excitation at 365 nm. The peaks are at 648 nm for CuNC and 647 nm for nanocomposite, respectively.

3.2.3. Transmission electron microscopy images of (A) copper nanoclusters (CuNC at 20 nm scale); (B) levocetirizine loaded copper nanoclusters (CuNC-LH at 20 nm scale); (C) chitosan nanoparticles (Cnp at 200 nm scale); (D) mannosylated chitosan nanoparticles with thin halos (man-Cnp at 200 nm); (E) nanocomposite (0.5 μm scale) and (F) nanocomposite showing loaded CuNC-LH as tiny dots (100 nm scale).

3.2.4. Characterisation of nanocomposite. (A) Size distribution curve of the nanocomposites. (B) EDX analysis plot of the nanocomposites. (C) DLS size distribution curve of nanocomposites.

3.2.5. Determination of percentage yield. (A) Formula used for calculation. (B) Parameters for percentage yield calculation of man-chitosan. (C) Parameters for percentage yield calculation of nanocomposite. *(D)* Determination of mannose concentration in man-chitosan. (E) Release profile of levocetirizine dihydrochloride from the nanocomposite in acidic and neutral medium. In pH 4.0, a burst release of 76.9% was observed at 36^{th} h. By the 72^{nd} h, it had come down to 61.7%. In pH 7.4, the release pattern was slow and sustained reaching up to 55.5% at 72^{nd} h.

3.2.6. FTIR spectroscopy plots of (A) Mannose; (B) Chitosan and (C) Mannose conjugated chitosan (man-chitosan). Samples were scanned between wavenumber 4000–600 cm^{-1}.

3.2.7. Graphical representation of decrease in cell viability following treatment in monolayer cells. Viability % is quantified as IC_{50} value. Cells were treated with the following: CuNC (A, B, C); levocetirizine dihydrochloride (D, E, F); chitosan nanoparticles (G, H, I) and nanocomposite (J, K, L). The ANOVA test revealed statistical significance of treated cells with respect to control. Statistical significance is denoted by * ($p < 0.05$), ** ($p < 0.005$), *** ($p <$

0.001), and **** ($p < 0.0001$). The data are represented as mean ± SD of three individual experiments.

3.2.8. Live-dead cell visualization of (A, B) A549 and (C, D) HeLa monolayer culture using calcein AM/PI dual staining. Live cells fluoresce in the green region while dead cells in the red region. Cells were treated with the nanocomposite for 48 h before imaging. Scale bar: 100 µm. FESEM-based morphological study of monolayer culture treated with nanocomposites for 48 h before imaging. (E) A549 and (F) HeLa cells. Scale bar- 10 µm. Time-dependent nanocomposite uptake into (G) A549 cells and (H) HeLa cells imaged through confocal microscopy. Flowcytometric analysis of nanocomposite internalisation into (I) A549 and (J) HeLa monolayer cells. Time-dependent uptake of nanocomposites into (K) HEK-293 cells.

3.2.9. Time-dependent nanocomposite uptake into (A) A549 cells and (B) HeLa cells imaged through confocal microscopy. Flowcytometric detection of cellular ROS in (C) A549 and (D) HeLa cells. Fold change observed in CuNC and nanocomposite treated (E) A549 and (F) HeLa cells.

3.2.10. Structure of levocetirizine dihydrochloride. Source: National Centre for Biotechnology Information (2023). PubChem Compound Summary for CID 67336450, Levocetirizine hydrochloride.

3.2.11. Detection of mitochondrial membrane potential depolarization by JC-1 staining flowcytometric assay in (A) A549 and (B) HeLa cells. Detection of apoptotic population by Annexin V-FITC/PI flowcytometric assay in (C) A549 and (D) HeLa cells.

3.2.12. Lipid droplet staining assay performed on A549 monolayer culture. (A) Untreated and (B) treated cells. DAPI was used for counterstaining nuclei. Scale bar – 60 µm. Colony formation assay performed on (C) A549 and (D) HeLa monolayer culture.

3.2.13. Migration assay performed in monolayer cells. (A) A549 cells and (B) HeLa cells. The length of the gap closure was measured using ImageJ software. Scale bar – 100 µm.

3.2.14. Graphical representation of dose dependent decrease in viability of A549 spheroids (A, C, E, G) and HeLa spheroids (B, D, F, H). They were treated with CuNC (A, B); levocetirizine dihydrochloride (C, D); chitosan nanoparticles (E, F) and nanocomposite (G, H). The ANOVA test revealed statistical significance of treated spheroids with respect to control. Statistical

significance is denoted by * ($p < 0.05$), ** ($p < 0.005$), *** ($p < 0.001$), and **** ($p < 0.0001$). The data are represented as mean ± SD of three individual experiments.

3.2.15. Live/dead staining assay using calcein AM and PI dyes in A549 and HeLa multicellular spheroids. (A, E) Control spheroids; (B, F) CuNC treated spheroids; (C, G) nanocomposite (IC_{25}) treated spheroids; (D, H) nanocomposite (IC_{50}) treated spheroids. Scale bar – 200 µm.

3.2.16. Sphere formation assay assessed on (A) A549 and (B) HeLa multicellular spheroids. Scale bar – 200 µm.

3.3.1. Cell viability assay performed on MDA-MB-231 cells for screening (A) Ranitidine, (B) pheniramine maleate and (C) promethazine and (D) cetirizine over the counter drugs. The ANOVA test revealed statistical significance of treated cells with respect to control. Statistical significance is denoted by * ($p < 0.05$), ** ($p < 0.005$), *** ($p < 0.001$), and **** ($p < 0.0001$). The data are represented as mean ± SD of three individual experiments.

3.3.2. Hydrodynamic size of PLGA nanoparticles as measured by Malvern Zetasizer. The graphs reveal an average hydrodynamic size of 224.6 nm.

3.3.3. (A) FESEM image of PLGA nanoparticles at 100 nm scale. (B) TEM image of PLGA nanoparticles at 200 nm scale (C) FESEM image of PLGA-PH nanoparticles at 100 nm scale. (D) TEM image of PLGA-PH nanoparticles at 0.5 µm scale. (E) UV-Vis spectra of PH and PLGA-PH nanoparticles. (F) Release profile of promethazine from PLGA nanoparticles in acidic and neutral medium.

3.3.4. Hydrodynamic size of PLGA-PH_FITC nanoparticles as measured by Malvern Zetasizer. The graphs reveal an average hydrodynamic size of 270 nm.

3.3.5. Comparison of zeta potential values of (A) PLGA nanoparticles, (B) promethazine hydrochloride and (C) PLGA-PH nanoparticles. as measured by Malvern Zetasizer.

3.3.6. Graphical representation of anti-proliferative activity on monolayer cells. Cells were treated with PLGA nanoparticles (A, G); PH (B, H); SAHA (C, I); PLGA-PH nanoparticles (D, J); co-treatment with SAHA and PLGA-PH nanoparticles (E, K) and pre-treatment with SAHA and PLGA-PH nanoparticles (F, L). The ANOVA test revealed statistical significance of treated cells with respect to control. Statistical significance is denoted by * ($p < 0.05$), ** ($p < 0.005$),

*** ($p < 0.001$), and **** ($p < 0.0001$). The data are represented as mean ± SD of three individual experiments.

3.3.7. Graphical representation of the results of cell viability assay performed on MCF-7 monolayer cells. The ANOVA test revealed statistical significance of treated cells with respect to control. Statistical significance is denoted by * ($p < 0.05$), ** ($p < 0.005$), *** ($p < 0.001$), and **** ($p < 0.0001$). The data are represented as mean ± SD of three individual experiments.

3.3.8. Graphical representation of the results of cell viability assay performed on HEK-293 monolayer cells. The ANOVA test revealed statistical significance of treated cells with respect to control. Statistical significance is denoted by * ($p < 0.05$), ** ($p < 0.005$), *** ($p < 0.001$), and **** ($p < 0.0001$). The data are represented as mean ± SD of three individual experiments.

3.3.9. Induction of cell death in monolayer cells using the pre-treatment method. Live-dead cell imaging of MDA-MB-231 and EMT MDA-MB-231 cells using Calcein AM/PI dual stains (scale-100 μm). Live cells stained by Calcein AM fluoresce green and dead cells stained by PI, fluoresce red. Decreased green fluorescence and increased red fluorescence expounds the efficient cell death induction following pre-treatment.

3.3.10. Cellular localisation of PLGA-PH_FITC nanoparticle imaged in (A) MDA-MB-231 (scale – 10 μm) and (B) EMT MDA-MB-231 (scale – 50 μm) monolayer cells. DAPI was used as a nuclear counterstain. Time-dependent uptake of PLGA-PH_FITC nanoparticles in (D) MDA-MB-231, (E) EMT MDA-MB-231 and (F) MCF-7 cells.

3.3.11. DCFDA- based ROS detection in (A) MDA-MB-231 cells and (B) EMT MDA-MB-231 cells. Detection of apoptotic population in (c) MDA-MB-231 and (D) EMT MDA-MB-231 cells using Annexin V-FITC apoptosis detection kit. Green fluorescence indicates Annexin FITC binding to the phosphatidyl serine of the exposed lower leaflet. The red fluorescence indicates PI binding to the permeable cells. Mitochondrial membrane potential depolarization detection by JC-1 dye-based flowcytometric assay in (E) MDA-MB-231 and (F) EMT MDA-MB-231 cells. Green fluorescence depicts the potential-dependent accumulation of JC-1 dye in mitochondria. The decrease in red/green intensity ratio indicates mitochondrial depolarization.

3.3.12. Alteration in cell morphology in treated cells via FESEM imaging in (A) MDA-MB-231 and (B) MCF-7 cells, (C) EMT MDA-MB-231 cells.

3.3.13. Representative immunoblots showing the expression of EMT protein markers (A) and EMT-TFs (B, C) in MDA-MB-231 cells. Graphical representation of the fold change in protein expression in (D) Vimentin, (E) E-Cadherin, (F) Zeb-1 and (G) SNAI1 in MDA-MB-231 cells. B-actin serves as a loading control.

3.3.14. Sphere formation ability assessed on spheroids created from (A) MDA-MB-231 and (B) EMT MDA-MB-231 cells (Scale- 200 μm).

3.3.15. Anti-proliferative effect of combination therapy on 3D multicellular spheroids. They were treated with PLGA nanoparticles (A, G); PH (B, H); SAHA (C, I); PLGA-PH nanoparticles (D, J); co-treatment with SAHA and PLGA-PH nanoparticles and pre-treatment with SAHA and PLGA-PH nanoparticles. The ANOVA test revealed statistical significance of treated spheroids with respect to control. Statistical significance is denoted by * ($p < 0.05$), ** ($p < 0.005$), *** ($p < 0.001$), and **** ($p < 0.0001$). The data are represented as mean ± SD of three individual experiments.

3.3.16. Live-dead spheroids imaged through confocal microscopy using Calcein AM/PI dual stains in (A) MDA-MB-231 and (B) EMT MDA-MB-231 spheroids. Green fluorescence due to Calcein AM indicates live cells while red fluorescence due to PI depicts dead cells (Scale - 200 μm).

List of Tables

3.3.3. Tabulation of % mitochondrial membrane depolarization and % apoptotic population in MDA-MB-231 and EMT MDA-MB-231 cells.

3.3.4. Fold change in protein expression in EMT MDA-MB-231 cells.

Chapter 1

Introduction and Review of Literature

Ameliorating Old Drugs with New Tricks in the Nano Realms

- ***ACS Applied Nano Materials***, *2024*, **7** (4), 3564-3579
DOI: 10.1021/acsanm.3c06195
[ACS publishing group]

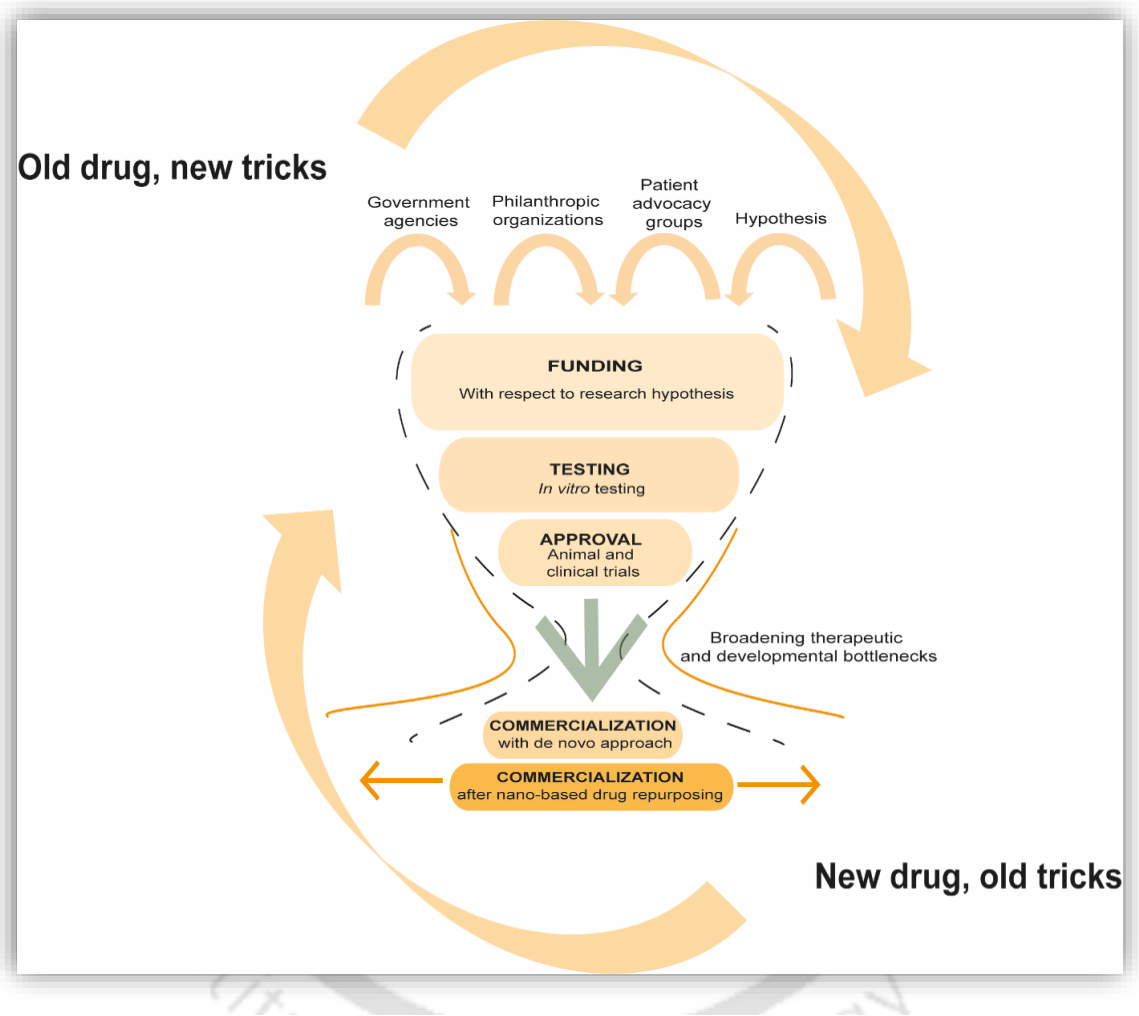

Scheme 4.1. Schematic comparing *de novo* drug development with drug repurposing in combination with nanotherapeutics that can help bypass therapeutic and developmental bottlenecks.

Introduction and Review of Literature

1.1. The enigma of cancer

"And if we, as physicians, found ourselves immersed in cancer, then our patients found their lives virtually obliterated by the disease.", confessed Dr. Siddhartha Mukherjee in his book of biography of cancer, The Emperor of All Maladies. The diagnosis of cancer- not the disease, but the mere stigma of its presence becomes equivalent to a death sentence. It becomes an omnipresent entity in a patient's life, a devouring presence. Although cancer's prevalence has markedly increased in the recent decades, it has been afflicting living organisms since the pre-historic times.[1] Since then we have come a long way in terms of understanding the origins of cancer. The successful eradication of any malady requires an early diagnosis followed by a profound understanding of its biology. It is now widely accepted that cancer results from the accumulation of genetic alterations in cells. These alterations called mutations may occur at the genetic or somatic level. Molecular analyses of cancer cells over the years have revealed abnormalities in tumor suppressor genes and oncogenes that drive tumor progression and correlate with its clinical aggressiveness. Ideally, tumor progression is divided into initiation, promotion and progression. In the first phase, cells undergo uncontrolled cell division followed by tumor growth in the promotion stage. Thereafter, tumor cells from one location travel to others, also known as metastasis, forming secondary tumor growths.[2] Metastatic tumors are known to cause more than 90% of cancer deaths.[3]

As and when the tumors progress, they take over the body, thwart the immune system and adapt with even an increasingly hostile microenvironment. Evidently, they are Darwin's fittest cells. These hallmarks of cancer cells have been well abridged by Hanahan and Weinberg [4] – 1) sustaining proliferative signalling, 2) evading growth suppressors, 3) avoiding immune destruction, 4) deregulating cellular energetics, 5) enabling replicative mortality, 6) inducing angiogenesis, 7) resisting cell death, and 8) activating metastasis. These newly acquired abilities resulting from mutations allow a survival advantage over normal cells, allowing them to expand and replace neighbouring cells. In due time, they travel to establish secondary tumors at other locations. Such cells undergo epithelial to mesenchymal transition (EMT) to attain migratory properties. Originally described with regards to normal cell differentiation

during early development, cancer cells often recapitulate and manipulate this programme to their advantage. The complexity of EMT and metastasis is decided by the heterogeneity of the population. Before the cancer cells can metastasize however, they need to overcome anoikis, a type of programmed cell death activated when anchorage-dependent cells detach from the surrounding ECM.[5,6] One of the ways to achieve that is loss of E-cadherin expression and increase in N-cadherin expression.[5] Disregulation of growth factor receptors is also correlated with anoikis resistance. The gradual progress from epithelial to mesenchymal like features is currently backed by two hypotheses.[5] One that claims that the cancer progenitor cells in a tumor do not undergo differentiation simultaneously. At a given point of time however, a tumor may have cells in various stages of differentiation. Another hypothesis suggests that cancer progenitor cells first undergo EMT and then metastasize following clonal expansion. Thus, every cancer grade should have come from a different progenitor cell. Following this, cancer cells travel to secondary sites and to establish clinically significant growth they regain their epithelial characteristics. Recent studies have demonstrated that induction of mesenchymal to epithelial transition (MET) also suppresses EMT mediators. This elegant modulation of EMT to MET is what drives cancer metastasis.[7]

Despite all advances, cancer remains the leading cause of death with 10 million deaths every year. With 19 million new diagnoses every year, the global cancer burden is expected to shoot to 28.4 million cases by 2040.[8] Owing to the dismal statistics, public healthcare sector has decided to reduce cancer mortality by one third within the next decade. While traditional treatments like surgery, chemotherapy, hormone and target therapy have helped, cases of mortality and relapse are too many to ignore. Perhaps the major issue with chemotherapy resides in resistance. Reduced drug uptake but increased drug outflow is a primary reason for cells acquiring chemoresistance. Approximately, 80-90% of mortality in cancer patients is directly or indirectly associated with drug resistance. Besides this, the side effects associated with chemotherapy like non-specificity, cytotoxicity, and stem-like cell formation has also birthed the need for an intervention.

1.2. Drug repurposing

Repurposing off-patent, licensed and marketed drugs for novel therapeutic indication is although not a new practice, but has definitely been gaining attention in the past few years. With an initial definition provided by Ashburn and Thor, this concept is now being quite

thoroughly explored.[9] The idea behind old drugs with new tricks can be explained by polypharmacology which essentially highlights that every drug has multiple targets in the body.[10,11] This has revealed a new paradigm of therapeutic approaches. Repositioning a drug for a new indication may nevertheless be accompanied with side effects and require validation in the new clinical trial. However, as the pharmacodynamic, pharmacokinetic and toxicity profiles of such drugs is already established, it can allow us to skip over phase 1 and swiftly progress to phases 2 and 3. This not only reduces 30 % of the cost and time involved, but also caters to a less risky business plan (**Scheme 1.2.**).[12]

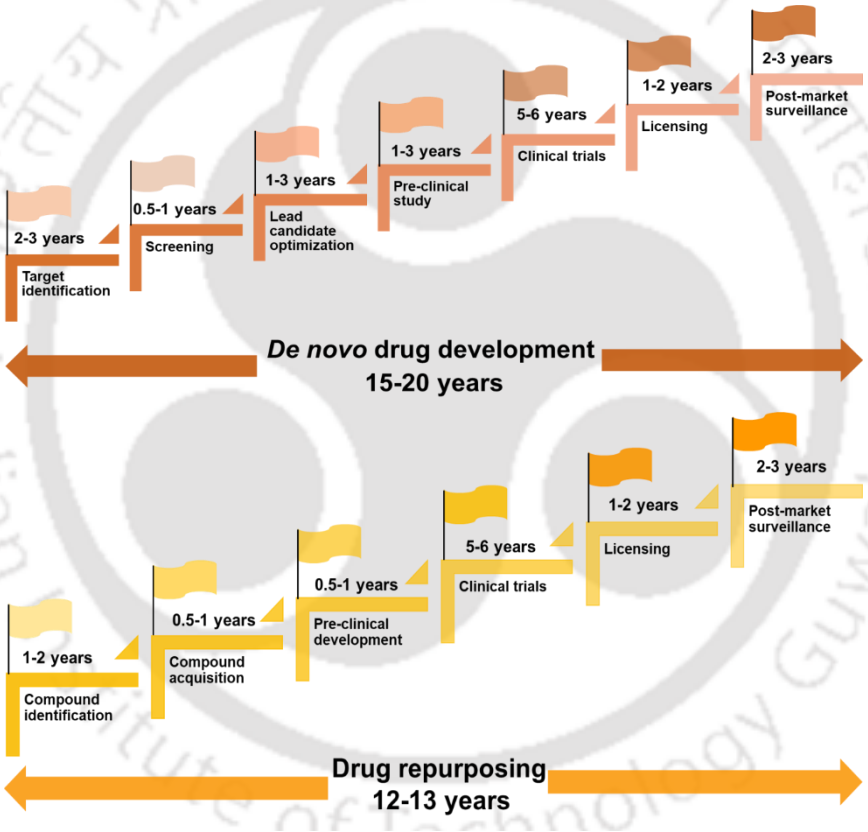

Scheme 1.5. Comparison of timelines in *de novo* drug development and drug repurposing. Repurposing a licensed drug may achieve the same goals as *de novo* approach, but in less time and is financially less burdensome.

1.2.1. Drug repurposing avenues. Repurposing is not a straightforward approach. The anticancer potential of a drug needs to be established prior to establishing its candidature for further screening. Repurposing avenues can be categorized into computational (*in silico*) and experimental approaches. Successful instances have seen the effective exploration of both. Computational analyses, which is a hypothesis driven avenue helps sieve out the broader hits.[13] It can help utilise larger data sets and bring about a more directional approach.[14] *In silico*

repurposing is further classified into discovering new indications for a new drug (drug-centric) and finding effective drugs for an existing condition (disease-centric). While the complete in silico methodology is beyond the scope of this review, we highlight the two technological trends that have made it possible for it to be as influential as it is today. First, high-throughput data from genomics, proteomics, chemo-proteomics and phenomics are generated and accumulated. This highlights the entire pathway map, drug profiles and disease phenotypes. Second, owing to the advances in computational and data sciences, algorithms have developed a database for experimental data. Computational repositioning can be further addressed by machine learning, networks models, text mining and semantic interference too. Alternatively. experimental screening can further help assess their anti-tumor potential, which can be followed by subsequent functional and mechanistic assays. The same can be performed on monolayer cultures and 3D-tumor spheroid models that closely mimic solid tumors.

1.2.2. Repurposing non-antibiotics for antibacterial therapy.

The need for developing potential antimicrobial agents to combat multidrug resistance is universally recognized. Majority of the antibiotics that were discovered decades ago[15] have already become resistant to a variety of pathogens. Apart from plazomicin in 2018[16] and lefamulin in 2019[17], the discovery of new antibiotics has been slow.[18] Therefore, the unavoidable Darwinian consequence of rampant antibiotic usage has led scientists to explore multiple strategies that are becoming increasingly expensive and untenable using conventional routes of developing antibiotics.[19] The medical and research establishments are thus, constantly on the lookout for a creative and sustainable approach towards the identification of new antimicrobials. Drug repurposing or repositioning is one such strategy that focuses on the identification of newer targets for existing drugs.[20] The idea behind such an approach is backed by two concepts. One, that a single drug interacts with multiple targets.[21,22] Another, that a target associated with a particular disease is generally relevant to a number of other pathogenesis.[23] Researchers have been studying this for years against a variety of infectious and non-infectious diseases. Studies have revealed the antimicrobial efficiency of prochlorperazine, an anti-psychotic drug against 103 strains of both Gram-positive and Gram-negative bacteria.[24] Antineoplastics like raloxifene[25] and zoledronic acid[26] have also been studied against *P. aeruginosa* and *C. peumoniae*. Repurposed drugs pose as attractive choices with lower developmental risk that translate to lesser time and cost. They are also particularly suitable for combination doses that lower the risk of monotherapy resistance and side-effects

associated with higher dosage. It has been found that non-antibiotic drug classes such as, neuroleptics, antihistamines, antidepressants, and non-steroidal anti-inflammatory drugs (NSAIDS) act in multiple ways on microbial growth and hence may have a greater degree of broad-spectrum antibacterial activity.[27] One such class is the antihistaminic, which has been explored primarily against infectious diseases.

1.2.3. Repurposing drugs for cancer therapy.

Cancer is a complex disease. Its hallmarks are just as challenging as the disease itself. Despite advancements in research and technology, we are nowhere near understanding each of its idiosyncrasies. Even though genetically connected, cancer cells adapt, thwart and thrive much better than normal cells. Therefore, developing its cure while simultaneously trying to understand the disease itself, is an immense challenge. At this juncture therefore, it is paramount to expand our approaches in combating cancer. Repurposing can be very helpful in tackling many inter-related symptoms of different forms of cancer. Since the discovery of nitrogen mustard (a chemical weaponry used predominantly in the 20th century wars) as an anti-cancer agent[28], doctors and chemists have worked hand in hand to extrude potential therapeutic properties of many such compounds. Currently, drugs like disulfiram and doxycycline are undergoing trial as cancer therapeutics.[29] **Table 1.1.** tabulates a list of few drugs among many who have completed or are undergoing clinical trial. Outside the field of oncology, we have already witnessed successful instances of drug repurposing which include acetylsalicylic acid (Aspirin®), sildenafil (Viagra®), minoxidil and dimethyl fumarate (Fumaderm®).[30] The theoretical ease of repurposing a certain drug is often not translated in reality. A variety of factors are behind this. Foremost, is the economic aspect. Due to intellectual property rights, private sectors are often uninterested in repositioning licensed drugs. Hence, out of the 190 registered clinical trials investigating 72 drugs listed in the ReDo project, about 67% are sponsored by a University or Hospital; 28% by research institutes or non-profit organizations; 3% by small to medium-sized pharmaceutical companies; 2% by government and only 1% by large pharmaceutical companies.[31] Non-scientific factors may also play a huge role where in prescription bias by doctors is prevalent. This influences drug publicity over hard clinical data and impedes the repositioning process.

Drug name	Trade name	Original indication	Cancer type	Status
Acetylsalicylic acid	Aspirin	Pain, fever, inflammation	Gastric cancer Prostate cancer Ovarian cancer	Recruiting Completed Completed
Artesunate	Artesunate	Malaria	Cervical neoplasia	Completed
Digoxin	Lanoxin	Heart condition	Solid malignant tumors Prostate cancer	Completed Completed
Disulfiram	Antabuse	Alcoholism	Metastatic breast cancer Stage IV metastatic melanoma	Recruiting (Phase II) Completed
Doxycycline	Doxycylin, doxylin, doxyhexal	Bacterial infections	Resectable pancreatic cancer Cutaneous schwannoma	Completed Recruiting
Itraconazole	Sporanox	Fungal infections	Advanced solid tumors	Completed
Leflunomide	Arava, arabloc, lunava, repso, elafra	Rheumatism	Metastatic TNBC Stage IV prostate cancer	Recruiting Completed
Mebendazole	Vermox	Parasitic infections	Progressive paediatric brain tumors	Completed
Metformin	Glucophage	Diabetes II	Hormone refractory prostate cancer Relapsed solid tumors	Completed Completed
Naproxen	Aleve, Naprosyn	Anti-inflammatory	Colorectal cancer	Completed
Ritonavir	Norvir	HIV infection	High-grade anal intraepithelial neoplasia Breast cancer	Recruiting Completed
Statins		High cholesterol	Prostate cancer Estrogen receptor positive breast cancer	Completed Recruiting
Thalidomide	Immunoprin	Sedative, Anti-nausea	Melanoma Neuroblastoma	Completed Completed

Table 1.1. List of repurposed drugs which have completed or are under trial for cancer therapy.[7] Current status as of 2023 at the National Library of Medicine (National Center for Biotechnology Information, NCBI). Trials identified by disease/condition name "cancer" and the name of the drug.

1.2.3.1. Lung cancer

According to the latest WHO updates, lung cancer is perceived as the primary cause of cancer-related deaths. It is commonly divided into the small-cell (SCLC) and non-small-cell lung carcinomas (NSCLC) based on distinctive diagnosis and treatment.[32] SCLC is the aggressive most of the two with higher reports of metastasis and accounts for 13% of all lung cancer cases. NSCLC however, includes 85% of all lung cancer cases and is sub-classified into adenocarcinoma, squamous cell carcinoma, and large cell carcinoma. Among its subtypes, lung adenocarcinoma is the most diagnosed subtype followed by squamous cell carcinoma.[32,33] Conventional treatment strategies like surgery, chemotherapy, radiotherapy, targeted therapy, radiofrequency ablation, stereotactic radiosurgery and palliative surgery vary according to the specific stage of lung cancer. Despite such multimodal therapies, patient survival rates have remained abysmally below 20%. Additionally, developing targeted therapeutics for lung cancer is a time and capital consuming process. Even then, only 1 in every 1000 potential anticancer agents and 5% of drugs entering phase 1 trials ever receive U.S. Food and Drug Administration (FDA) approval.[34] Given the challenges, alternate means of therapeutic interventions for NSCLC need to be explored.

1.2.3.2. Breast cancer

Breast cancer is one of the most common afflictions for women across the world. A heterogenous disease, it has been immunohistochemically classified based on the presence of three receptors: estrogen receptor (ER), progesterone receptor (PR) and overexpression of human epidermal growth factor (HER2).[35] Triple negative breast cancer (TNBC) is characterised by the lack of expression of any of these receptors and the lack of approved targeted therapies. It also has the poorest overall survival (OS) and the highest rates of metastases, most commonly in lungs and brain. The gene expression profile subdivides TNBC into, basal-like 1(BL1), basal-like 2 (BL2), luminal androgen receptor (LAR), and mesenchymal (M). Surgery aside, chemotherapy is the only FDA approved treatment approach for non-metastatic TNBC. This includes anthracyclines, alkylating agents, antimetabolites and platinum. The reduction in mortality over the years is a result of improved diagnostic and management abilities.[36] Even though TNBC is comparatively more sensitive to chemotherapeutics, it has a higher rate of metastasis and remission. The reason behind this

chemoresistance being cancer stem cells (CSCs). Additionally, *de novo* drug development and the challenges associated with it further reduce survival chances of a patient.

1.3. Antihistamines as potential anticancer agents

So far, various classes of drugs have been repurposed, antihistamines being one of them. The relation between cancer and inflammation has been explored extensively. In cases of chronic inflammation, repeated tissue damage in presence of reactive nitrogen and oxygen secreted by the inflammatory cells interact with the epithelial DNA causing permanent genomic alteration.[37] Therefore, antihistamines targeting H_1 receptors can be excellent candidates for therapy. Antihistamines are known to be inverse agonists of histamine (H1, H2, H3 and H4) receptors.[38] Depending on their chemical structure, H1 antihistamines are segregated into six classes: alkylamines, ethanolamines, ethylenediamines, phenothiazines, piperazines and piperidines.[38]

Drugs like chlorpromazine have been tested against six glioblastoma cell lines.[39] The results showed an apoptotic-independent pathway, reduced cloning efficiency, and downregulated expression of stemness genes. Levocetirizine dihydrochloride is one such orally active antihistamine that has more affinity for H1 receptor compared to cetirizine hydrochloride.[40] It is one of the second generation antihistamines of piperazine class. It is rapidly absorbed after oral administration with the peak plasma concentration attained in 0.9-1 h.[41] Piperazine, a typical heterocyclic compound is considered as a critical building frame of many anticancer compounds.[42,43] Similarly, promethazine hydrochloride is a tertiary amine where the ring nitrogen at position 10 is attached to C-3 of an N,N-dimethylpropan-2-amine moiety. The FDA approval of anticancer agents carrying a piperazine moiety like 2-oxopyrazine (Olaparib) and 2-aminopyrimidine (Imatinib, Abemaciclib, Palbociclib and Rociletinib) further cements their potential.[43]

There have been studies where antihistamines belonging to different classes showed both bacteriostatic and bactericidal activity against a broad range of bacteria.[44] For example chlorpromazine, thioridazine and trifluprom azine have been tested against *S. aureus*, *E. coli* and MRSA.[45] Additionally, another antihistamine Terfenadine was repurposed against *S. aureus*[46]*;* while Diphenhydramine was found to potentiate levofloxacin activity against

methicillin-resistant *S. aureus* and *P. aeruginosa*.[47] Moreover, since phenothiazines have similarity to acridine's chemical structure, they may also intercalate into bacterial plasmids.[48]

1.4. Nanotherapeutic approach in drug repurposing

Even with all its advantages, repurposing a drug still needs further advances in the field of drug specificity and toxicity, as it is not enough to know its pharmacodynamic and pharmacokinetic properties. Additionally, many free drugs suffer from bioavailability, permeability at tumor site, unwanted localised deposition and other immunological complications. So, to address

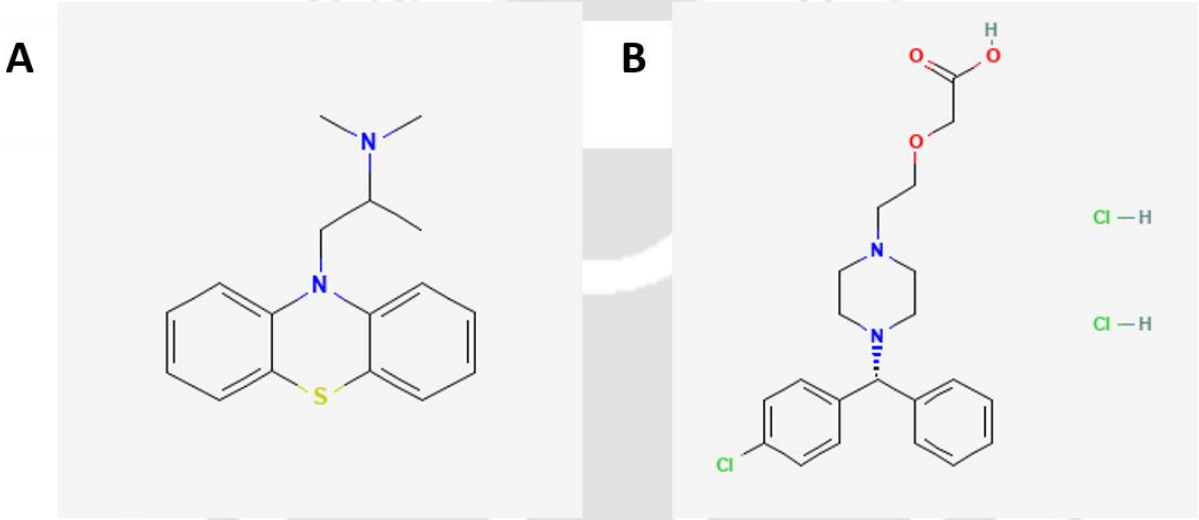

Scheme 1.3. Structure of (A) promethazine chloride and (B) levocetirizine dihydrochloride. Source: National Centre for Biotechnology Information (2023).

numerous such issues, an efficient system needs to be introduced, perfected and utilized to harness the benefits of repurposing in the best possible ways. Interestingly, the growing devotion of scientists towards repurposing coincides with the blooming of nanotechnology as an inter-disciplinary field. Recent findings have proved that it has the potential to revolutionize the face of theranostics by increasing localisation and selectivity; and decreasing side-effects.

Nanotechnology, a nano-scale based technique used in research and technology, at the atomic, molecular and macro-molecular levels, is within the 1-100 nm scale in range. A number of nano-particle systems spanning this range, when used in solving clinical issues, are called 'nanoplatforms'.[49] Nanoplatforms have been used time and again in preclinical and clinical studies as an improved way to administer small molecules, genes and peptides.[50–52] Their "smallness" makes them highly preferable over free drugs as it offers higher surface to volume

ratio for a constant mass of materials. Also, the size-dependent properties of materials like boiling point, electrical conductivity and chemical reactivity are helpful in customising nanomaterials according to the physicochemical properties of a particular drug. Advances have also been made for the co-delivery of hydrophilic and hydrophobic drugs, thus resolving the issue of drug solubility in body fluids.[53] Likewise, relatively large nanoparticles (size >100 nm) can also be fashioned to load therapeutically sufficient amount of drug. Most importantly, to avoid off-target hits, drug delivery can be tuned to respond to certain intracellular and extracellular stimuli like pH, temperature and magnetic field. Apart from that, there are several characteristics of nano-based systems that have rendered them indispensable for translational research (**Scheme 1.4.**), like; 1) biocompatibility, biodegradability and bioavailability of nanoplatforms, 2) drug retention at target site, 3) increased drug solubility, 4) minimal drug leakage during transit, 4) preferential drug localization at the tumor site through active or passive targeting, 5) reduced cytotoxicity, 6) avoidance of premature clearance from the system due to reduced immune response and tissue oxidative stress, 7) improved binding ability to biomolecules, 8) facilitated cellular uptake of the small molecule/peptide/gene being carried.[54] The therapeutic efficacy of such nano-based systems is also based on their specificity, tumor-responsive drug release and drug stability, the lack of which can trigger serious side-effects. This is determined by their interaction with blood proteins, the immune system and the tumor tissue. Hence, surface modification strategies have been opted to increase the selectivity of nanomaterials. It has been used to conjugate drug molecules, natural polymers (polyethylene glycol (PEG), dextran, chitosan and hyaluronic acid), synthetic polymers (polyvinyl pyrrolidone (PVP), polyvinyl alcohol (PVA), polyaminoacids and poloxamers), organic groups and receptor-specific ligands (transferrin, folic acid and mannose) to nanoparticles.[55,56] Alternatively, biomimetic materials like porphylipoprotein (PLP) and cell membranes are also a preferred form of surface functionalization, which help in immune masking.[57,58] Owing to a number of such features, drug repurposing can be combined with nanotechnology to increase its clinical success, and thus giving birth to a new paradigm in therapy.

1.5. Available nanoplatforms for repurposed drug delivery

A variety of materials including polymers such as polyethylene glycol, poly(lactide-o-glycolic) acid (PLGA) chitosan, inorganic metals such as gold, carbon nanotubes, magnetic nanoparticles and lipid-based nanoparticles have been approved by the FDA because they

possess most of the above features plus low-toxicity.[59] The available nanoplatforms have been categorized into multiple classes.[60] **Scheme 1.5.** illustrates the different types of nanoplatforms that have been utilised for drug repurposing in cancer therapy till date – lipid, polymeric, polymer-lipid hybrid and inorganic nanoplatforms (silver nanoparticles (silver NPs), gold nanoparticles and nanoclusters (gold NPs and NCs), mesoporous silica nanoparticles, iron oxide nanoparticles and quantum dots). The physical properties of these particles are often

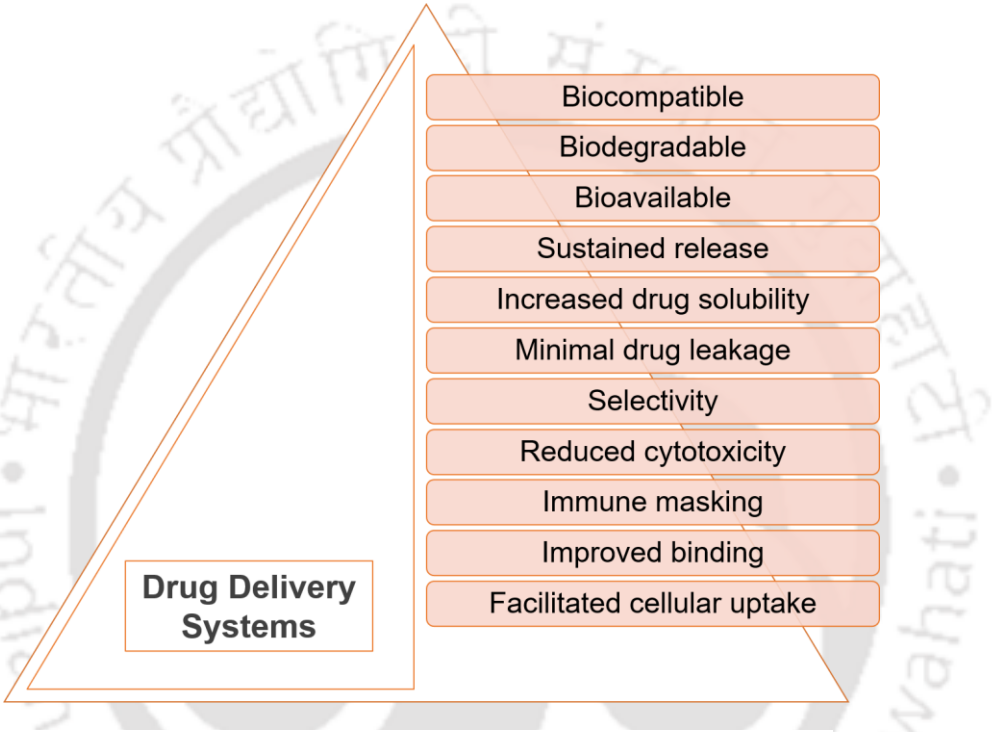

Scheme 1.4. Advantages of drug delivery systems.

tailored according to shape, size, optical, magnetic and electronic properties; since they are the true operators of their functional aspects.[61]

1.5.1. Lipid based nanoplatforms. One of the most studied class of nanoparticles include liposomes, nanostructured lipid carriers (NLCs), and solid lipid NPs. Perhaps their most unique feature is the representation as a bio-inspired platform, which defines the phospholipid bilayer, enacting the cell membrane properties. Also, they serve the dual purpose of carrying both hydrophobic as well as hydrophilic drugs, the former in the hydrophobic membrane and the latter in the aqueous core. Being within 100-200 nm in size, they can easily enter the tumor tissues too. Liposomes have been used as both passive targeting and active targeting agents in

cancer therapy.[62] Additionally, they help improve permeability, cargo loading efficiency, circulation half-life, stability and drug release kinetics.[63] Liposomes have been widely used as nano-carriers to transfer anti-cancer drugs (derivatives of Doxorubicin (DOX), Paclitaxel (PTX) and Platinum based anti-cancer drugs) into tumor tissues. [64]

These favourable features have rendered the use of cationic liposomes as successful carriers for metformin in low-doses (anti-diabetic drug) against breast cancer.[65] The resultant IC_{50} values were as low as 1.2 mM in MDAMB-231 and 1.3 mM in MCF-7 cells, a 5-fold reduction in dosage than free metformin (MDA-MB-231; IC50: 5.3 mM and MCF-7: 5.1 mM). In another instance, liposomes co-loaded with repurposed resveratrol (anti-inflammatory agent) and paclitaxel (anti-cancer agent) to amplify cytotoxicity against MCF-7 and drug resistant MCF-7/Adr BC cells.[66] There was a significant ($p < 0.01$) inhibition of drug resistant tumors in treated mice treated with liposome. Drug loaded liposomes revealed 1.6 to 5 times higher resveratrol dispersal to breast tumors. Additional examples include celecoxib formulated in a liposomal carrier for sustained release as an anti-tumor agent[67] and artemisinin (anti-malaria agent) loaded into nanoliposomes for investigation against hepatocarcinoma xenograft model.[68]

1.5.2. Polymeric nanoplatforms.

Nanoparticles: Polymeric nanoparticles are one of a kind in the sense that they can be engineered to deliver drugs, genes and peptides.[69,70] Also, polymers can be co-loaded with numerous cargoes for cancer targeting and diagnostic purposes.[71] They can be easily synthesized into nanostructures with preferred designs, that are nanoscale in size, compared to lipid-based formulations. They are known for their morphology and polymer composition in the core and corona. Apart from the types illustrated in the figure, Carbon nanotubes and filamentous phage are also commonly used. The therapeutic cargo (drug) is characteristically surface conjugated to the nanoparticles or encapsulated inside the core; while the delivery systems can be premeditated to achieve controlled release or triggered release.[72,73]

Polyethylene glycol (PEG) and poly(lactic-glycolic) acid (PLGA) are expansively used as biocompatible polymers for translational medicine.[74,75]

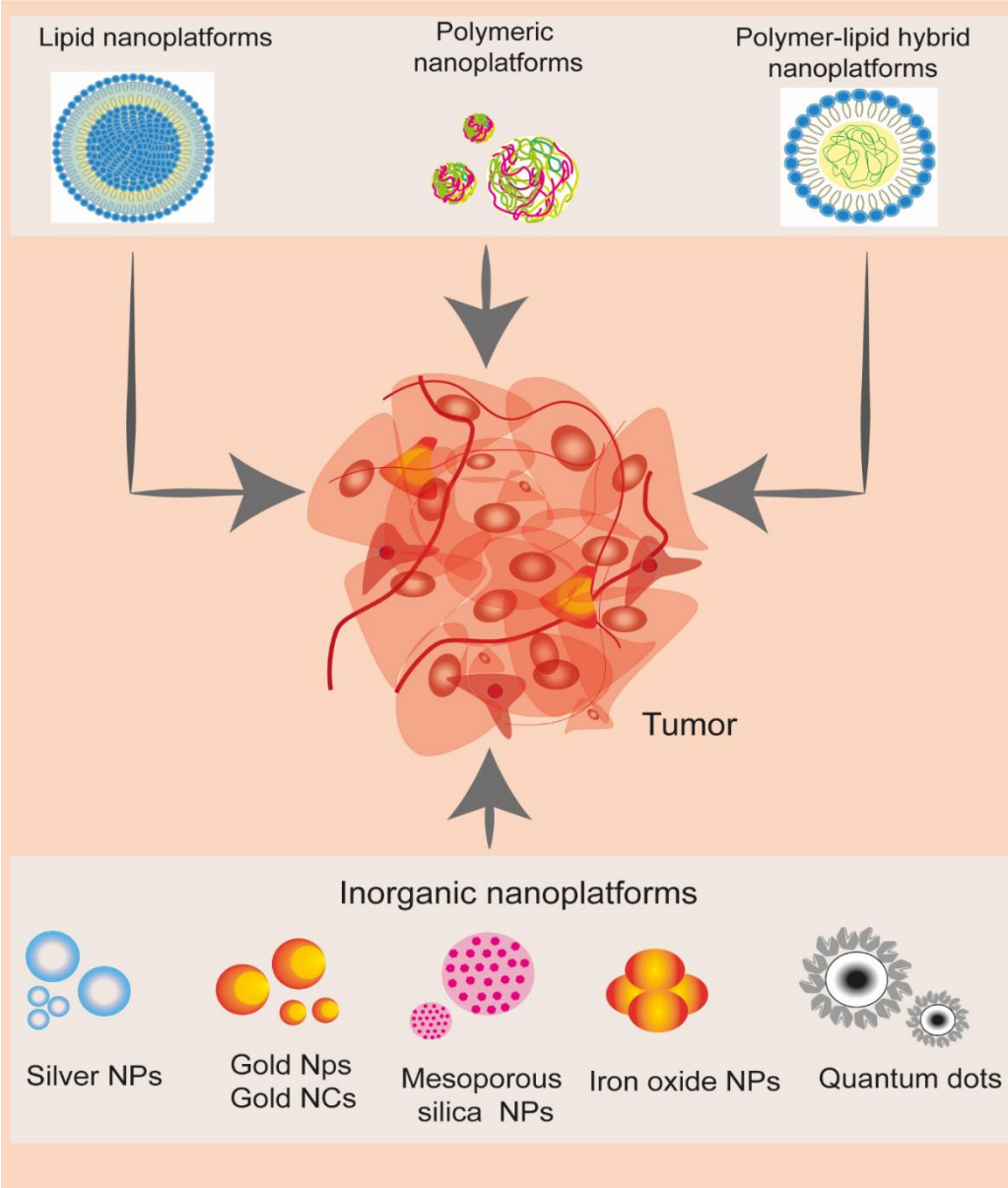

Scheme 1.5. Nanoplatforms that have been used for drug repurposing against cancer. These include lipid nanoplatforms, polymeric nanoplatforms, polymer-lipid nanoplatforms, silver nanoparticles, gold nanoparticles, gold nanoclusters, mesoporous silica nanoparticles, iron oxide nanoparticles and quantum dots.

Poly (ethylene glycol) (PEG) is known as a non-ionic hydrophilic polyether synthesized by polymerization of the monomer ethylene glycol, which can currently be synthesized within a wide range of molecular weight, from 300 to 100,000 Da. For medicinal purposes, PEG serves numerous roles as laxative, as excipient in drug formulations and as coating agent in capsule preparation.[76] Although non-biodegradable, PEG is biocompatible and there's no accumulation especially for low molecular weight chains. Its hydrophilicity allows stabilization of

nanoparticles in aqueous media, whilst increasing solubility and avoiding aggregation. Moreover, since PEG doesn't have any ionic moiety, there aren't any issues when it contacts charged biomolecules.[77] Perhaps the most important advantage of PEG is its stealth effect, the ability to suppress opsonization i.e., rapid recognition of foreign agents by the immune system. Coating drugs or nanocarriers with PEG thus, enhances circulation time *in vivo*. Often, PEG has also been used conjugated with targeting ligands to ornament nanoparticles. This step called, 'PEGylation' essentially helps with camouflaging, avoiding premature flushing out of the system.[78] For example, recently chlorpromazine (anti-psychotic drug) was loaded onto PEGylated PLGA nanoparticles for acute myeloid leukaemia (AML) therapy.[79] The nano formulation had retained the anti-AML activity of the drug without causing toxicity to the central nervous system. Poly (lactic-co-glycolic acid) (PLGA) is a synthetic copolymer obtained by random ring-opening copolymerization of two cyclic dimers of glycolic and lactic acid. These are linked together through ester linkage in a casual order during copolymerization bringing an aliphatic linear polyester.[80] Important properties like degree of crystallinity, mechanical strength, swelling behaviour and capability to hydrolyse are influenced by the molar ratio of the individual monomer components of lactide and glycolide.[81] The first biodegradation products of PLGA are its original monomers, lactic and glycolic acids. They can be metabolized and eliminated as carbon dioxide and water from the body or excreted via the kidney.[82] The biodegradation itself occurs in aqueous media via the hydrolytic degradation of ester linkages present in the polymer chain. It also possesses good mechanical strength making it suitable for a large number of medical artifices like sutures or fibres.[83] Since its approval by the US FDA and European Medicine Agency (EMA), PLGA has been successfully applied for delivery in translational medicine.[84] One investigation boasts of successful dual targeting delivery of artesunate and chloroquine (anti-malaria drugs) by biomimetic PLGA nanoparticles for colorectal cancer treatment.[85] Tumor cell proliferation was inhibited following treatment while there was reversion of immunosuppressive tumor microenvironment (TME). Another group attempted the delivery of Fenbendazole (anti-helminthic drug) to epithelial ovarian cancer via PLGA nanoparticles (FZ-PLGA-NPs).[86] The FZ-PLGA-NPs significantly decreased cell proliferation and reduced tumor weight compared to the control groups. Furthermore, as-synthesized PLGA nanoparticles have been co-loaded with macrolide compound rapamycin and piperine (alkaloid) to treat multi drug resistant (MDR) breast cancer.[87] Suggestive *in vitro* toxicity was observed against MDAMB-231 cells. It also

displayed prominent oral bioavailability (AUC: 95 µg/mL min) which was more than their free drug suspension (AUC: 35 µg/mL min). Finally, the therapeutic efficacy of disulfiram (anti-alcoholism drug)-laden PLGA NPs was evaluated against breast cancer.[88] Disulfiram resulted in tumor cell death owing to considerable cytotoxicity and reactive oxygen species generation.

Another widely used polymer for designing nano carriers is chitosan with exceptional control over drug release. Chitosan, a polysaccharide is derived from chitin via deacetylation.[89,90] In addition to delivery, chitosan has been reported for use in biomaterials and tissue engineering, antibacterial, antifungal and antioxidant agents. Chitosan nanoparticles help increase drug solubility and stability and reduce toxicity. Also, due to their size they have strong mobility and can enter cells easily.[89] Owing to the positive charge, chitosan's affinity for cell membranes can decrease the trans-epithelial electrical resistance (TEER) of cell monolayers. Low-molecular weight chitosan possesses the ability to penetrate cells where it may bind to DNA, prohibit mRNA synthesis, subsequently termination cell proliferation.[90] Towards that, chitosan is known to take numerous routes for drug delivery, like ocular, pulmonary, mucosal, nasal, transdermal and dermal routes.[91] Chitosan nanoparticles can be prepared by a variety of methods ranging from ionic crosslinking, covalent cross linking, precipitation, polymerization, self-assembly and spray-drying.[89] By far, ionic crosslinking is the most preferred approach for nanoparticle synthesis wherein the electrostatic interactions between the amine group of chitosan and a negatively charged group of polyanions such as tripolyphosphate is utilised.[92]

Folic acid targeted chitosan nanoparticles loaded with pH-sensitive mebendazole (anti-helminthic drug) were used to treat murine triple negative breast cancer (TNBC).[93] In another instance, quercetin loaded chitosan nanoparticles were found to be significantly accumulated in breast tumors via the enhanced permeability and retention (EPR) effect.[94] An astounding reduction in tumor volume was also observed in a mice tumor xenograft model with MDA-MB -468 cells. Another study was aimed to prove the anti-tumor potential of ormeloxifene (oral contraceptive) via loading them onto PEGylated chitosan nanoparticles. The resultant IC_{50} values were as low as 5.18 and 6.7 µM in MDA-MB 231 and MCF-7 cells, respectively. The respective IC_{50} values for free drugs were 11.9 and 12.2 µM.[63]

Micelles: Amphiphilic polymers self-assembled into nanosized particles are called Micelles, upon reaching critical micelle concentration.[95] Their ability to load multiple drugs was utilised as a micellar formulation of metformin (anti-diabetic agent) and paclitaxel which was utilised against breast cancer metastases.[96] Additionally, folate receptor targeted micellar nanoparticles carrying orlistat (anti-obesity drug) were used against triple-negative breast cancer (TNBC) cells.[97] The targeted nanoparticles not only improved the solubility of the largely water-insoluble drug, but also increased its bioavailability and stability. There was also a significant reduction in tumor volume in control group. Repurposed atorvastatin loaded into pH-responsive micelles for the therapeutic management of metastases also show the adaptability of micellar nano systems in achieving higher therapeutic efficiency.[98] Finally, ibuprofen was delivered via biocompatible micellar nanocarriers composed of chitosan to breast cancer cells. The ibuprofen loaded micelles were internalized in the intracellular compartment followed by a significant reduction in cell viability (13%).[99]

Hydrogels: By definition, a hydrophilic network of polymer chains is called a hydrogel. The structural integrity of the hydrogel network does not dissolve from the high concentration of water due to the integral crosslinks. Since they are highly absorbent, they are very similar to natural tissue and are often termed 'smart materials' as they respond to external stimulation and release encapsulated material from within. Organogels, Xerogels and nano-composite hydrogels are some of the many variations of this category. Conversely, synthetic hydrogels are modifiable and have limited batch-to-batch variability. Apart from drug delivery, hydrogels have emerged as 3D surrogate platforms in various disease models and applications like scaffolds, cell transplantation. In a pre-clinical evaluation, a synthetic, self-assembling peptide hydrogel (SAPH) of variable stiffness and composition was utilised to screen repurposed and FDA- approved drugs for acute myeloid leukaemia (AML).[100] It had acted as a 3D model of the bone marrow niche. The candidate drugs were salinomycin (antibacterial), vidofludimus (multiple sclerosis drug) and atorvastatin (anti-cholesterol drug).

1.5.3. Polymer-lipid hybrid nanoplatforms. Hybrid nanoparticles are the way when it comes to study the synergistic effect of more than one delivery systems. Other than polymer-lipid nanoplatforms, they can me composed of both organic and inorganic components. This can help vastly in tuning a multitude of physicochemical properties for combination cancer therapy.

There are a plethora of hybrid nanoparticles starting from nanoscale coordination polymers (NCPs) and nanoscale metal-organic frameworks (NMOFs) to polysilsesquioxane (PSQ) and inorganic nanoparticle/organic polymer composite systems.[101] However, to remain consistent with the title, this review discusses the use of hybrid nanoplatforms as a means of drug repurposing.

To achieve the best of both worlds, polymer-lipid nanocarriers have emerged as a new generation of delivery systems. The lipid portion, in some cases serve as the core and the polymers as shell and *vice versa*. They are known to overcome the limitations of their parent platforms like dosage toxicity, short circulation half-life, deprived solubility and non-specific distribution.[102] They have also proven to be structurally robust, more permeable and biostable, thus adaptable to numerous modifications. As they can incorporate both hydrophilic and lipophilic drugs simultaneously, they can aid with multiple drug deliveries.[103] In addition, PEGylation also makes them more biocompatible thus preventing immune detection.[104] In a study, injectable polymer-lipid hybrid nanoparticles were co-loaded with diruthenium-ibuprofen and diruthenium-naproxen (metallodrugs) for use against breast cancer.[105] The nanoparticles revealed significant *in vitro* cytotoxicity against two sets of breast cancer cells, EMT6 and MDA-MB 231. In addition to augmented stability of loaded drugs, there was also reportable accumulation of drugs in the tumors and less dispersal in other organs.

1.5.4. Inorganic platforms. Under this category, several elemental metals, metal oxides and metal salts are included. Inorganic nanocarriers are quite convenient, cost-effective with better surface conjugation properties. They can be made biocompatible through a variety of surface modification strategies like: PEGylation, polysaccharide, polyacrylamide, poly(*N*-vinyl-2-pyrrolidone) (PVP) coating.[106] Alternatively, zwitterionic and bio-inspired coating can also help with *in vivo* imaging and therapy.[106] They also bid biological and chemical inertness, high cargo loading capacity, stability during longer storage periods and sustained release. Many inorganic nanocarriers also possess inherent reactive oxygen species (ROS) generating properties, resulting in cellular death. Among a sea of inorganic platforms, we have narrowed down our review to gold nanoparticles, silver nanoparticles, iron oxide nanoparticles, quantum dots and mesoporous silica nanoparticles.

Gold nanoparticles (AuNPs) and silver nanoparticles (AgNPs): Gold has been used in medicine for a long time**.** The toxicity of gold cyanide for the Tuberculosis bacillus *in vitro* was discovered as early as 1890.[107] Jacques Forestier in 1929 demonstrated that gold derivatives can relieve pain due to rheumatoid arthritis.[108] Eventually however, less toxic albeit more efficient treatments were developed. The beauty of gold as a metal is that it is only active as a catalyst in the form of nanoparticles.[109,110] Hence, the interest for AuNPs in medicine arises essentially from their unique physicochemical properties. Additionally, due to their plasmonic properties, AuNPs have become an attractive choice for biomedicine. Their valence electrons can resonate with an external electromagnetic field thus resulting in a strong absorption in the visible range.[111] This absorption of course is modifiable by the nanoparticles' shape, size and functionalization. Furthermore, their affinity for sulphur-based compounds allows numerous functionalization and can be utilised in favour of drug delivery and specific targeting.[111,112]

One group had developed salinomycin (antibiotic) AuNPs to target breast cancer that exhibited prominent cytotoxicity against MCF-7 stem cells through ferroptosis.[113] Another study was aimed to examine the anti-tumor potential of silver nanoparticles (AgNPs) synthesized using silver-doxycycline complex to target MCF-7 cells.[114] The as-synthesized nano formulation revealed higher cytotoxicity than only silver and free doxycycline. Again, another study interestingly explored the DNA repair inhibitory properties of pyronaridine (anti-malaria drug) in combination with gold nanoparticles and radiation therapy. They showed a significantly high DNA double strand breaks of 42% followed by reduction in cell proliferation in HeLa cells. Here, AuNPs were utilised as radiosensitizers because their highly dense crystalline form allows them to absorb X-ray radiation.[111] Furthermore, curcumin was delivered via folic-acid functionalized Au-PVP NCs to MDA-MB 231 and MCF-7 cell lines.[115] Cytotoxicity assay demonstrated significant anticancer activity at lower doses in estrogen/progesterone receptor (ER/PR)-negative cells. However, it did not show cytotoxicity in mouse fibroblast and human breast epithelial cell lines. Moreover, it also showed an affable inhibitory effect of cell migration and high antitumor efficacy *in vivo*. It is important to tune the size, shape and other mechanical properties of AuNPs as they determine the cytotoxicity, stability and internalisation into cells.[116] Studies with PEGylated AuNPs have shown hepatotoxicity in rodents with malnutrition.[117] Instead of PEGylation, an alternate glutathione coating does not elicit inflammatory response.[118] Therefore, it is of utmost importance that the safety and stability of AuNPs in any form be assessed prior to their administration.

Iron oxide nanoparticles: Ever since their approval for human use as magnetic resonance imaging (MRI) contrast agents, iron oxide NPs have been widely used for cancer immunotherapy and imaging.[119–121] Their degradation products are also absorbed by the body and stored away. They have been modified with cargos such as heat shock protein70 (hsp70)[122], R837 and poly(I:C)[123], CpG-ODN[124], and ICG[125] to improve the anti-tumor response. Interestingly, iron oxide nanoparticles have also been clinically approved agents for magnetic nanoparticle hyperthermia, a notion of heating magnetic iron oxide particles suspended in fluid and exposed to alternating magnetic fields. Hyperthermia essentially raises the local tumor temperature to either kill cancer cells or make them vulnerable to other treatments. PEGylated graphene oxide co-loaded with superparamagnetic iron oxide nanoparticles and artesunate (anti-malaria drug) were explored as cancer therapeutics.[126] Owing to their nano size, the surface area was large enough to load dual cargo with a high loading efficiency. Following the pH-triggered release of iron ions, a seven-fold reduction in IC_{50} values was observed in hepatocellular carcinoma and breast cancer cells. In another study, nanoprecipitation method was utilised to load artemisinin in porous magnetic supraparticles (MSP) against ovarian adenocarcinoma cells.[127] A poly(aspartic acid)-based polymer, consisting of dopamine, indocyanine green, and polyethylene glycol side chain, was coated onto the surface of ART-loaded MSP. Following internalization, significant amount of ROS was generated due to Fe^{2+}-mediated cleavage of the endoperoxide bridge in artemisinin. Furthermore, near-infrared (NIR) increased the tumor local temperature due to the photothermal effects of MSP. Finally, dihydroartemisinin (DHA) was delivered through a magnetically guided mode to cervical cancer and lung adenocarcinoma cells.[128] DHA shows Fe-dependent cytotoxicity which ironically becomes a hurdle due to the insufficiency of iron in cancer cells. Hence, the Fe_3O_4@C@MIL-100(Fe) (FCM) nanoparticles helped in the synchronous delivery of DHA and Fe (III). Additionally, application of an external magnetic field also amplified the antitumor effects.

Biocompatibility is a vital factor that should be addressed before utilising iron oxide nanoparticles *in vivo*. Owing to their broader safety margin, superparamagnetic iron oxide nanoparticles (SPION) are used as MRI contrast agent. A study on human glia, breast cancer and normal cell lines showed that SPIONS demonstrate low toxicity at doses > 100 ug/mL while being non-toxic at lower doses.[129] SPIONs have been found to be biodegraded and

cleared from the body through the endogenous iron metabolic pathway.[130] However, in patients with iron metabolism issues, using SPIONS may not be advisable. In context of biocompatibility, the determining factors are unsurprisingly the magnetic content, size and the nature of coating. In a study, smaller and positively charged nanoparticles demonstrated higher toxicity in normal cells than cancerous cell lines.[131] Hopefully, further studies on SPIONs will indicate towards utilising nanoparticles of various sizes without concerns of cytotoxicity.

Quantum dots: Semiconductor nanocrystals or quantum dots are emerging as an indispensable tool not just as drug delivery systems (DDS), but in biomedical research in general. Their unique optical properties are distinguished from bulk semiconductor solids; hence the size tunable light emission, resistance photobleaching, simultaneous emission of multiple fluorescent signals. Following many successful instances of QDs in biological imaging, sensing and detection, researchers were motivated to utilise them to amplify the efficiency of repurposed drugs as well. As-synthesized chondroitin sulphate and lactoferrin coated quantum dots-based theranostic nano capsules co-loaded with repurposed celecoxib (anti-inflammatory drug) and honokiol (anxiolytic) were actively targeted for malignant breast cancer.[132] Owing to the attachment of the lactoferrin with mercaptopropionic acid-laden cadmium telluride, imaging too was possible. The nano capsules exhibited significant cytotoxicity in MCF-7 cells and MDA-MB 231 cells in comparison to the individual therapeutic components. Confocal microscopy revealed high internalisation of the nano-capsules followed by cell death. Additionally, the efficacy of the formulations was also investigated in female BALB/C mice injected with Ehrlich ascites tumor cells. The % tumor volume observed with combined free celecoxib and honokiol solution was suggestively lower than positive control group. This was attributed to the synergistic effect of the combined therapeutics.

Although there are numerous examples of QDs as valuable drug delivery systems, toxicity remains a hurdle in its clinical translation. QD size, concentration, coating and stability play a combinatorial role in its biocompatibility. Studies with bovine serum albumin (BSA)-QD conjugates suggest towards BSA's protective role against QD induced cytotoxicity.[133] The peptides in albumin were found to reduce toxicity through their extracellular antioxidant defence system. The most common QD cores are composed of cadmium and selenium, both of which are understandably toxic. However, ZnS shell with a robust organic coating can help

avoid the core's exposure to oxidation.[134] Besides toxicity, it is also crucial to study the interaction of QDs with cellular or physiological processes. Such non-specific interactions can be prevented through introducing surface coatings like hydrophilic polymers. Additionally, since most QDs are comparable in size to proteins, smaller QDs can be opted for instances where diffusivity becomes a size-induced hindrance.[135]

Mesoporous silica nanoparticles (MSNs): With their fascinating properties, mesoporous silica nanoparticles have turned the wheel of drug delivery arena into new light. Their sizes and loading capacity can be tuned as preferred, ranging from 2 to 50 nm and with a pore volume greater than 0.6 cm^3 g^{-1}.[136,137] They are not just suitable for drug delivery but also dissolution enhancement. Depending on the synthesis approach, MSNs can be customized to carry hydrophobic and hydrophilic drugs. Besides, owing to large surface area they can be both externally and internally modified for amplified specificity. They are also stable in a wide range of external conditions, including extreme pH, temperatures and humidity.[138] Following functionalization, they are also especially endowed with prolonged circulation time, sustained release and biocompatibility. Moreover, United States Food and Drug Administration (FDA) has also approved silica as "Generally recognized as Safe". Numerous *in vivo* studies have revealed their low toxicity as they are primarily excreted through urine and feces.[139] Following several evidences on their efficiency and safety, they have been explored as drug delivery systems widely.[140,141] MSNs have been used to deliver aspirin in folic acid conjugated polydopamine vehicles to breast cancer (MCF-7) cells.[138] The delivery vehicle supported prolonged release, higher targeting efficiency and compared to free aspirin had superior anti-proliferative effect. Additionally, Artemisinin (ART) again was delivered via a composite with a core of Fe_3O_4 nanocrystals and a shell of mesoporous silica nanoparticles to HeLa cervical cancer cells.[142] MTT-based measurement of antitumor efficacy of ART-loaded FCA@$mSiO_2$ nanoparticles revealed significant enhancement compared to free ART. The nanocomposite was hypothesized to be localized in the acidic compartments of endosomes and lysosomes. This may have helped in releasing the Fe^{2++} ions to non-enzymatically convert ART to cancer cell killing toxic products.

One of the major disadvantages of MSNs is their open porous structure suggesting cargoes could easily diffuse out before reaching the target. To avoid premature drug release, a study was performed with stimuli responsive MSNs.[143] Self-immolative gatekeepers which degrade in a domino like fashion upon receiving a specific stimulus, were utilised to accomplish the same. For clinical translation, it is crucial to properly skim the biocompatibility and biodistribution abilities of MSNs. Many studies have been performed to analyse their biosafety without any common opinion till date.[144] However, their behaviour, biocompatibility and biodistribution can be controlled through simple modifications in particle shape, size, surface properties and dose.

Table 1.2. List of contrast and active agents for biomedical applications.[145]

Contrast agent	Drug	Application
Manganese oxide	siRNA	MRI and RNA delivery
Gold	Doxorubicin	Diagnosis, tumor targeting, PTT
Iron oxide	siRNA, Doxorubicin, Docetaxel	Targeting, MRI, therapy
Silica	Pyropheophorbide, Doxorubicin	PDT, drug carrier, CT imaging
Carbon nanotubes	DNA plasmid, Doxorubicin, Paclitaxel	Diagnosis, DNA, drug delivery
Quantum dots	Doxorubicin, Methotrexate	Imaging, sensing, therapy

1.5.5. Theranostic nanoparticles. The terms therapy and diagnostic gives "theranostic" its origin, meaning a procedure that can diagnose, deliver and monitor a targeted therapy. Today, it has become the fundamental behind imaging-guided nanotherapeutics. Designing a theranostic agent demands understanding of molecular mechanisms, diagnostic strategies, therapeutic efficiency, side-effects of materials and nanoparticle synthesis techniques. The past few years has witnessed an enormous rise in theranostic agents.[145] A list of various contrast and active agents along with their biomedical applications has been tabulated (**Table 1.2.**). Iron oxide nanoparticles owing to their superparamagnetism are preferred as contrast agents.

Using them theranostically, allows the use of various active agents. Methotrexate-(MTX) modified IONPs, DOX and PTX coupled IONPs have already been used for MRI and drug delivery purposes.[145] Similarly, DOX loaded carbon nanotubes (CNTs) were used for detection and delivery both *in vivo* and *in vitro*. PTX delivery was also aided by coupling surface-

modified CNTs for cancer treatment.[146] While drug repurposing with theranostic agents is yet to be explored, in a few cases repurposed theranostic agents have been used for cancer treatment *in vivo*. Ferumoxytol, an intravenous iron oxide nanoparticle formulation has been approved by the U.S. Food and Drug Administration (FDA) as a treatment for anaemic patients with chronic kidney disease.[147] However, ferumoxytol has also demonstrated other potential biomedical applications mostly due to its superparamagnetism, biocatalytic activity and immunomodulatory properties. It had an intrinsic therapeutic effect on the growth of early

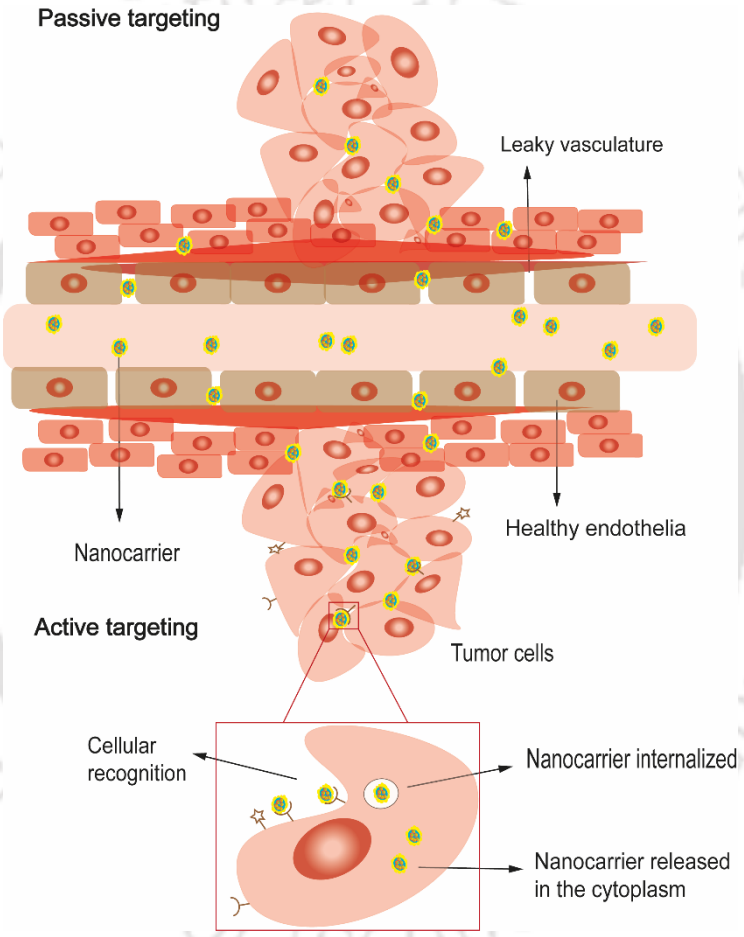

Scheme 1.6. Schematic depiction of passive and active cellular targeting. Passive targeting utilises the fenestrations created to support tumor development as passageways for therapeutic molecules accumulation. In active targeting, a homing moiety is used for target recognition.

mammary cancers, lung cancer metastases in liver and lungs.[148] *In vitro*, adenocarcinoma cells co-incubated with ferumoxytol and macrophages indicated increased caspase-3 activity. *In vivo*, it suggestively inhibited the growth of subcutaneous adenocarcinoma in mice along with the prevention of liver metastasis post intravenous administration. Theranostic nanoparticles therefore, offer interesting applications in oncology. The development of such multifunctional

nanoplatforms has certainly fuelled expectations for cancer therapy. Combining them with repurposed drugs can open several avenues for multifunctional nanoparticles, finally resulting in timely diagnosis and proper disease management.

1.6. Modes of targeting: For a drug, repurposed or otherwise to be effective, it should first reach the target site without hindrance. Again, following arrival, it should be selective towards the tumor cells without affecting the normal cells. For effective drug delivery, the nanocarrier must be retained in the bloodstream without expulsion. Their size should meet the important criteria of being large enough to prevent rapid leakage but small enough to help in immune masking. In addition, nanocarriers with hydrophilic surfaces are preferred to escape macrophages.[149] These strategies although basic, form the foundation of any drug delivery system. Hence, successful DDS are associated with lower side-effects, and in extension, better patient survival. Two modes of targeted delivery are always preferred depending on the type of carrier and drug involved, (i) passive targeting, and (ii) active targeting.

1.6.1. Passive targeting: Years of experimental evidences have reinforced that tumor vasculature is leaky in nature.[150] One of the reasons behind this is the unresponsive nature of malignant cell signalling to support orderly vasculogenesis. In addition, to compensate for the insufficient replenishment by endothelial cells owing to their rapid growth, such vascular endothelial crevices are created. The crevices or fenestrations range from 200 to 2000 nm depending on the cancer type, tumor microenvironment and localization.[151] Certain macromolecules may thus enter the tumor through these crevices and persist due to reduced lymph clearance in tumors.

Described as the enhanced permeability and retention effect (EPR) first coined by Maeda and Matsumura, it has been widely utilised in favour of passively targeted nanomedicine (**Scheme 1.6.**).[152] However, localization of molecules via EPR is critically controlled by their size which should be over 40 kDa-800 kDa in terms of molecular weight. In case of globular proteins this size corresponds to a minimal radii of 2.3 to 6.1 nm.[150] Interestingly, numerous nanoparticles have been localized in tumor tissues like carbon nanotubes, liposomes, gold nanorods and viral

nanoparticles. Hence, passive targeting predominantly relies on tumor biology (degree of angiogenesis, extent of tumor invasion and intratumor pressure) and certain carrier characteristics (size, hydrophobicity and circulation time). Keeping that in mind, numerous carriers have been synthesized to successfully deliver several drugs to tumor site. A list of drugs repurposed for different cancer types and delivered via passive targeting has been tabulated (**Table 1.3.**). Even with all the success stories, it is important to beware of certain limitations that come with passive targeting. The variability of the EPR effect is one of the prime reasons for that.[153] Inconsistent drug accumulation is a common occurrence and can vary in intensity, both between tumors and within a single tumor. Additionally, due to the presence of strong

Table 1.3. List of repurposed drugs delivered via passive targeting to different cancer types.

Nanoplatform	Repurposed drug	Tumor type	References
Liposome	Metformin	Breast cancer	65
	Resveratrol	Breast cancer	66
	Artemisinin	Hepatocellular carcinoma	68
PLGA nanoparticle	Rapamycin and Piperine	Breast cancer	87
Micelle	Ibuprofen	Breast cancer	99
Polymer-lipid hybrid	Ibuprofen	Breast cancer	105
Gold nanoparticle	Salinomycin	Breast cancer	113
Silver nanoparticle	Doxycycline	Breast cancer	114
Iron oxide nanoparticle	Artesunate	Hepatocellular carcinoma	126
	Artemisinin	Ovarian adenocarcinoma	127
	Dihydroartemisinin	Cervical cancer and lung adenocarcinoma	128
Mesoporous silica nanoparticle	Artemisinin	Cervical cancer	142

extracellular matrix, larger particles may face difficulty penetrating deep inside. Tumor heterogeneity can also cause inefficient drug distribution owing to inaccessibility. Most importantly, the lack of selectivity in passive targeting poses danger to healthy tissues. Finally, its efficacy can also come down if the cancer cells upregulate efflux pumps thus, rejecting the particles. The success of passive targeting therefore, depends on overcoming these obstacles.

By combining them with some form of active or stimuli responsive targeting can help bring down a lot of limitations and off-target hits.

Table 1.4. List of repurposed drugs delivered via active targeting to different cancer types.

Nanoplatform	Target	Ligand	Repurposed drug	Tumor type	References
Chitosan	Folate receptor	Folic acid	Mebendazole	TNBC	[93]
Micelle	Folate receptor	Folic acid	Orlistat	TNBC	[97]
Gold nanoparticle	Folate receptor	Folic acid	Curcumin	Breast cancer	[115]
Quantum dots	Transferrin receptor	Lactoferrin	Celecoxib and Honokiol	Breast cancer	[132]
Mesoporous silica nanoparticle	Folate receptor	Folic acid	Aspirin	Breast cancer	[138]
Nanoexosomes	EpCAM protein	Aptamer	Aspirin	Breast and colorectal cancer	[154]
PEGylated PLGA nanoparticle	Folate receptor	Folic acid	Saquinavir	Breast cancer	[155]

1.6.2. Active targeting: Another form of targeting often includes the tuning of surface functionalities aimed towards site specific delivery and selectivity. A homing moiety is often associated with active targeting wherein a ligand or antibody is used for target recognition **(Scheme 1.6.)**. Contextually, growth factor receptors like epidermal growth factor receptor (EGFR)[156], transferrin receptor[157], death receptor (DR) complexes[158] and folate ligand and tumor-specific antigens[159] have been explored for the active targeting of malignant cells. Ligands in the form of chemical and biological molecules like peptides, sugars, vitamins, antibodies and nucleic acid aptamers[160,161] have also been used to direct nanocarriers to their malignant targets. Active targeting is a preferred choice to deliver variable therapeutic molecules like protein, DNA/RNA etc, thus opening the arena for a more advanced form of cancer therapy.[162]

The initial indication of same was observed from liposomes when grafted with antibodies in 1980s followed by various other ligands like peptides, nucleic acids and aptamers.[163] The aim of active targeting therefore, is to increase the specific interactions between nanocarrier and the target. The multivalent of nanocarriers often improves this interaction and this is why nanocarrier design is complex. Apart from that, administration route, ligand density and size of the nanocarrier also contribute to its delivery success. Although theoretically active targeting may seem forthright but it also suffers from non-homogenous localization. While targeted nanocarriers may be internalized preferentially by a cell within a tumor, they don't always reach the tumors that way. Instance includes the failure of monoclonal antibodies at enhancing uniform tumor localization.[164] Also, to prevent protein corona formation, surface characteristics must be carefully avoided.[165] Protein corona may hinder intracellular uptake and also, result in particle instability. Hence, utilizing active targeted nanocarriers require caution before establishing them as delivery systems. **Table 1.4.** includes a list of repurposed drugs that have been actively targeted for different cancer types.

Table 1.5. List of metabolism inhibiting drugs under clinical trial; with EMT inhibiting features.

1.7. Stimuli responsive nanoplatforms. To circumvent delivery barriers and abnormal tumor environments, stimuli responsive nanocarriers have been explored. They can effectively deliver drugs at the tumor site while improving their pharmaceutical properties and release kinetics. They can yield significant benefits mediated by adaptive transition application during drug delivery.[166] Such nanocarriers also trigger themselves in response to tumor microenvironment like acidic pH[167], hypoxia[168] and enzyme induction.[169] Categorically, stimuli responsive nanocarriers can respond to exogenous stimuli (temperature, magnetic field and light) and endogenous stimuli (pH, adenosine triphosphate (ATP), H_2O_2, enzyme, redox-potential and hypoxia). Today, multi-stimuli-responsive nanocarriers are emerging as the preferred delivery systems.[170] Several repurposed drugs have also been delivered to tumor sites using such delivery systems. Thermosensitive betulinic acid-loaded magnetoliposomes were used against breast adenocarcinoma cells in a promising study.[171] Under hyperthermal conditions, this platform demonstrated significant therapeutic effects. In another study, a pH sensitive nanotherapeutic system was designed to target breast cancer.[172] Here, chemotherapy was combined with COX-2 inhibition using Celecoxib. While stimuli responsive nanocarriers are promising, there is still scope for more study with respect to their behaviour in solid tumors and altering tumor microenvironment.

Drug	Target	Original indication	Tumor type	References
Ascorbate	Vitamin C		Metastatic pancreatic cancer Malignant tumor	173
Disulfiram	ALDH1	Alcoholism	Metastatic breast cancer	174
Etodolac	COX-2	Pain and inflammation	Colorectal metastasis Colorectal metastasis	175
L-NAME	iNOS		Cardiovascular	176
L-NMMA			Multiple cancers Metastatic TNBC	177
Olaparib	PARP	Cancer	Metastatic renal cell carcinoma	178
Rolipram	PDE4	depression	Multiple sclerosis	179
Simvastatin	MG-CoA	Hypolipidemia	Advanced rectal cancer	180,181
Suramin	Heparanase	Trypanosomiasis A	Prostate cancer Advanced solid tumors	182
2-Deoxyglucose	Glycolysis		Advanced tumors	183

1.8. Repurposing drugs to target epithelial-to-mesenchymal transition (EMT) in cancer

Epithelial-to-mesenchymal transition (EMT) has become the defining factor for most aggressive forms of cancer like metastasis, cancer stemness and multidrug resistance. Herein, epithelial cells undergo reprogramming to acquire mesenchymal phenotype. Originally described with regards to normal cell differentiation during early development, tumor cells often recapitulate and manipulate this programme to their advantage. Upon activation, tumor cells undergo physical alterations in succession, like tight junction dissolution, disruption of apical-basal polarity and the overall reorganisation of cytoskeletal backbone. These changes facilitate the migration of cells from one site to another, invading surrounding tissues and dodging circulatory ejection on the way. Several studies back the central role of EMT in chemoresistance[184,185] and resistance to immune checkpoint blockade[186] leading to poor clinical outcomes.[187] EMT therefore, has become an attractive therapeutic target in oncology.

While traditional chemotherapy continues its combat, the time had long since arisen for an adjunct, if not a more powerful approach. Emerging research has demonstrated the pivotal role

of metabolism in meeting the bioenergetic demands of a tumor cell, especially during EMT.[188,189] Concurrently, recent studies have demonstrated metabolic reprogramming during EMT. For instance, ZEB1 and SNAl1 both transcriptional EMT regulators are involved in metabolic rewiring. While ZEB1 aids the cells' mesenchymal condition by promoting glycosphingolipid metabolism[190], SNAl1 brings about fructose-1,6-bisphosphatase 1 (FBP1) clampdown to activate glycolysis in breast cancer.[191] Furthermore, it was found that mesenchymal cell specific compounds essentially targeted glutathione peroxidase 4 (GPX4), involved in the lipid peroxidase pathway to elude ferroptosis, a nonapoptotic form of cell death.[192] Understanding these switches from normal metabolic pathways therefore, can be the key to unravelling newer therapeutic options. The tabulated list of metabolism inhibiting drugs under clinical trial demonstrated anti-EMT abilities (**Table 1.5.**). They can pose as a valuable repository for emerging clinical research on anti-EMT strategies.

1.9. Clinical translation of nanoplatforms

The most commonly translated nanoplatforms are liposome-based because of their higher feasibility, biocompatibility and biodegradability.[193] It is also helpful that liposomes can trap both hydrophilic and hydrophobic drugs along with the ability to be functionalised. Additionally, the liposomal bilayer chaperones the drugs from proteasomal degradation.[194] This also aids in protecting the healthy tissue surrounding the cancer cells. Following liposomes, all others based on polymeric micelles, metal and metal oxides, polymer/lipids, and other conjugates, are in various stages of approvals or trials. In that context, platinum has been widely explored to develop anti-cancer drugs. In fact, cisplatin is clinically approved as the first choice for malignant tumor treatment.[195] However, owing to its rampant cytotoxicity, second generation platinum drugs were developed closely followed by several other nanocomplexes.[196] Today, multiple studies are ongoing to test the efficacy of metal-based nanodrugs. Another new nanodrug system was developed based on polymer/lipids that combine the benefits of both systems.[197] A versatile delivery platform, it has adjustable drug release kinetics and also reduced degradation prior to reaching the target. Furthermore, nanoconjugate drug systems have been tested on animal models. Biocompatible copper sulfide nanodot were designed anchored to folic-acid modified black phosphorous nanosheets. It was aimed at enhancing the efficacy of photodynamic therapy and photothermal therapy.[198]

Even though the applications of nanotechnology are well past the stage of academic interests, their translation from bench to bedside faces a multitude of challenges. The stringent waters of regulatory approval are difficult to navigate for most nanoplatforms, owing to their unique yet dynamic properties. This includes their size, shape, surface charge and stability. A quick search reveals that only 16 nano-based cancer drugs are FDA approved and about 75 nano formulations are under clinical trials.[196] There are several reasons behind such low numbers. To start with, understanding the interaction of nanoparticles with the biological system in a clinical environment is complex; and requires an interdisciplinary approach involving both nanotechnological and biological backgrounds. The uniqueness of nano formulations raises concerns about potential safety issues that must be thoroughly investigated before approval. Additionally, biocompatibility and biodistribution studies delay the progress even further. Also, due to the lack of standard synthesis and characterisation protocols, it is difficult to compare data across studies. On top of it, lack of financial investments and resources also cause a lag in the developmental pipeline. Since, several studies exploring the nano-based repurposing avenue are still at infancy; evidently, a nano-repurposed drug is yet to become translationally viable. Since the future of nano-based drug repurposing looks promising, researchers and industries must strive together to overcome the challenges. Towards that, collaborations are an excellent way to pave the road for promising innovations and translational validations. Additionally, streamlining regulatory pathways and standardized guidelines for their approval may become useful in their incorporation into mainstream cancer treatment protocols.[199,200]

In this respect, artificial intelligence-based tumor targeting can also be a helpful strategy in drug discovery and delivery.[201] Nanoinformatics has led to the prediction of structural and functional properties of nanoparticles via non-invasive methods. Principally speaking, machine learning technology can aid in assessing tumor vessel permeability, thereby helping in the selection of appropriate nanocarriers. It also includes the effect of particle's physicochemical characteristics on internalisation, cytotoxicity and molecular release. Also, predictive algorithms can help calculated factors like encapsulation efficiency beforehand. Furthermore, controlled release is one of the important properties for any drug delivery systems to avoid surrounding tissue damage. However, owing to the sophistication of many nanoformulations, most controlled release drug delivery systems (CRDDS) face hurdles at the translational level. A novel statistical approach called artificial neural network (ANN) has been used for CRDDS development.[202] It is quite beneficial for the modelling of sophisticated biological data and non-

linear systems; and when the functional dependence between inputs and outputs is negligible. AI, therefore would play an important role in optimizing the administration of nanotherapeutics. It can help in overcoming the number of clinical trial failures, thereby increasing the number of approved nanodrugs.

1.10. Summary

Cancer remains a persistent health issue and one of the leading causes for deaths worldwide. While *de novo* approach continues to occupy most of the developmental pipeline, there is also the need and opportunity to follow repositioning of old drugs. The major aim of repurposing is to shorten developmental time and costs involved, without compromising with the efficacy of the treatment. Hence, it would overcome both therapeutic and developmental bottlenecks. Computational and experimental screening of potential candidates followed by an in-depth analysis of cancer molecular pathways can be instrumental in cementing the benefits of drug repurposing. Although, it also comes with certain challenges with respect to patents and market selectness; this can be overcome by new dosage formulations. Even then, the benefits of repurposing are limited due to the poor solubility, retarded bioavailability and biocompatibility of most free drugs. Besides, their non-specificity often leads to general toxicity, ultimately nullifying the advantages. Complexity of tumours, heterogeneity within a single tumor, low immunogenicity, metastasis and side effects also present a sizable number of hurdles. Thus, delivering such drugs via nanomaterials makes an attractive platform to tackle the limitations.

These upcoming studies illustrate the role of drug repurposing in cancer and bacterial infections along with several nanotechnology-based solutions that can shape the landscape of therapeutics. Under that umbrella, they also highlight different nanoplatforms, which are the carriers or conjugates of repurposed drugs. However, there have always been some underlying reality checks with regards to the safety, dosage and size-efficacy of the nanoparticles that retard their clinical translation. The approaches known till date aren't straightforward and need further understanding of their mechanistic pathways. Emphasis on EMT also needs to be cemented so that repurposing as a both chemopreventative and chemotherapeutic option can be explored. In the days to come, newer nanoplatforms will be further developed, while the existing ones will be better accentuated for therapeutic and theranostic purposes.

1.11. Key Features and Scope of Research

The development of alternate therapeutic approach that is sustainable, inexpensive and targeted is highly preferred for any disease. Any forms of cancer and bacterial infections are no different, since the number of people afflicted by both is quite high globally. This research investigates potential alternatives to conventional cancer and bacterial therapy. Towards that this thesis elucidates the following scopes as potential research areas:

- Experimental screening and identification of licensed drugs originally indicated for different disease, for potential anti-cancer and antibacterial activity.
- Designing a targeted nano vehicle to deliver repurposed drug to Gram-stained bacteria and their respective biofilms.
- Understanding the effect of a common histone deacetylase inhibitors (HDACi) on TNBC cells.
- Understanding the functional impact of the repurposed drugs on lung adenocarcinoma cells, TNBC cells, Gram-stained bacteria and their respective biofilms.
- Engineering an actively targeted nano system for the delivery of a second repurposed to lung adenocarcinoma cells and 3D spheroids.
- Exploring the combined implications of the nanoformulated repurposed drug and HDACi on the EMT dynamics of TNBC.

1.12. Objectives of the Thesis

- *Screening licensed drugs for potential antibacterial and anti-biofilm activity and developing a suitable nanocarrier for their delivery.*
- *Understanding the effect of antihistamines in lung adenocarcinoma.*
- *Exploring the combinatorial role of HDACi and antihistamines in TNBC.*

1.13. Salient Outcomes

- This thesis attempted to engineer a nanoformulation of mannosylated gold nanoclusters loaded with repurposed drug promethazine. D-mannose functionalisation was aimed at the selective disarming of the adhesive appendage of Gram-negative pili.
- Application of the nanoformulation successfully inhibited bacteria with a zone of inhibition of 5 mm. It also inhibited their biofilms by inducing ROS production and altering membrane permeability.

- The current study is the first of its kind in repurposing levocetirizine dihydrochloride, an antihistamine to retard lung adenocarcinoma cells.
- Fluorescent copper nanocluster loaded levocetirizine was delivered to lung adenocarcinoma cells and spheroids through a biocompatible chitosan nano vehicle.
- The nanocomposite demonstrated better anti-proliferative capacity with an IC_{50} value of 31.05 μM, compared to the drug alone and the same was established through its ability to induce apoptosis while reducing migration and colony forming potential.
- Exposure to the nanocomposite also inhibited lung adenocarcinoma multicellular spheroids, as evidenced by the numerous dead cells in staining assays.
- Following screening studies, an antihistamine of the phenothiazine class, promethazine hydrochloride was selected to investigate its effects on the EMT dynamics of TNBC. Promethazine was delivered through biocompatible PLGA nanoparticles in combination with SAHA, a HDACi.
- Cell exposure to the combination decreased viability even with lower drug and HDACi concentrations of 26.53 μM and 21.72 μM in MDA-MB 231 and EMT MDA-MB 231 cells. It also increased ROS generation by 1-fold and 1.5-fold, respectively.
- The combination treatment also abrogated SAHA's ability to facilitate EMT in the TNBC cells.
- TNBC cells exposed to promethazine loaded nanoparticles and SAHA also demonstrated poor spheroid forming potential.

Chapter 2

Materials and Methods

Materials and Methods

2.1. Materials

2.1.1. Chemicals. For the experiments, following chemicals were purchased:

Acetic acid – **Merck Specialities Pvt. Ltd., India**

Acetone – **Merck Specialities Pvt. Ltd., India**

Agar powder (bacteriological grade) - **HiMedia**

Bovine serum albumin (BSA) - **Sisco Research Laboratories Pvt. Ltd., India**

Brain heart infusion (BHI) broth - **Sigma-Aldrich Company Ltd.**

Chitosan - **Sigma-Aldrich Company Ltd.**

Copper sulphate pentahydrate ($CuSO_4.\ H_2O$) – **HiMedia Laboratories Pvt. Ltd., India**

2′,7′-Dichlorofluorescin Diacetate (DCFDA) - **Sigma-Aldrich Company Ltd.**

Ethanol – **Merck Specialities Pvt. Ltd., India**

Fetal bovine serum (FBS) - **Sigma-Aldrich Company Ltd.**

Fluorescein isothiocyanate (FITC) - **Sigma-Aldrich Company Ltd.**

Hydrazine hydrate (N_2H_2) – **Merck Specialities Pvt. Ltd., India**

Hydrogen tetrachloroaurate trihydrate ($HAuCl_4.3H_2O$) - **Sigma-Aldrich Company Ltd.**

JC-1 - **Sigma-Aldrich Company Ltd.**

Levocetirizine dihydrochloride - **Sigma-Aldrich Company Ltd.**

Luria-Bertani (LB) broth – **HiMedia Laboratories Pvt. Ltd., India**

Mannose – **HiMedia Laboratories Pvt. Ltd., India**

MTT (3-(4,5-Dimethyl-2-thiazolyl)-2,5-diphenyl-2H-tetrazolium bromide) – **HiMedia Laboratories Pvt. Ltd., India**

Nutrient broth (NB) - **Sigma-Aldrich Company Ltd.**

Penicillin-Streptomycin (Penstrep) - **Thermo Fisher Scientific India Pvt. Ltd.**

Phosphate buffer saline (PBS) - **Sigma-Aldrich Company Ltd.**

Poly (lactic-co-glycolic acid) (PLGA) - **Sigma-Aldrich Company Ltd.**

Poly (vinyl alcohol) (PVA) - **Sigma-Aldrich Company Ltd.**

Sodium hydroxide (NaOH) – **Merck Specialities Pvt. Ltd., India**

Sodium triacetoxyborohydride ($Na[(CH_3COO)_3BH]$) - **Sigma-Aldrich Company Ltd.**

Sodium tripolyphosphate (STPP) - **Sigma-Aldrich Company Ltd.**

Suberoylanilide hydroxamic acid (SAHA) - **Sigma-Aldrich Company Ltd.**

Trypsin-EDTA (0.25%) – **Gibco Pvt. Ltd., India.**

2.1.2. Milli-Q grade water (>18 MΩ cm−1, **Millipore**) was used in all the experiments.

2.1.3. Dead cell Apoptosis Kit (V13245) with Annexin V Alexa Fluor was procured from **Invitrogen, Thermo Fisher Scientific India Pvt. Ltd**.

2.1.4. All glassware were procured from **Borosil Pvt. Ltd., India**

2.1.5. All plasticware were procured from **Tarsons Product Pvt. Ltd.**

2.2. Cell lines and culture conditions

2.2.1. Monolayer cells. For performing cell culture studies, A549 (lung adenocarcinoma), HeLa (cervical cancer cells), MCF-7 (breast cancer cells), MDA-MB-231 (triple-negative breast cancer) and HEK-293 (human embryonic kidney-293 cells) were procured from National Centre for Cell Sciences (NCCS), Pune, India. Dulbecco's modified Eagle's medium (DMEM) supplemented with L-glutamine (4 mM), penicillin (50 units per mL), streptomycin (10 mg/mL, Sigma-Aldrich), and fetal bovine serum (10% v/v, Gibco) was used to maintain them. The cells were incubated in a 5% CO2 humidified incubator at 37 °C.

2.2.2. Multicellular spheroids. Initially, A549, HeLa, MCF-7 and MDA-MB-231 cells were grown as monolayer cells till 80-85% confluency. Cells were then harvested in fresh 10% DMEM media and seeded on wells pre-coated with 1.5% agarose containing serum-free media. Cell density per well was kept at 20000. They were centrifuged at 700 rcf for 10 min. Following

this, the 96-well plates were incubated in a 5% CO_2 humidified incubator at 37 °C for 96 h. Once generated, these spheroids were used for further experiments.

2.3. Methods

2.3.1. Synthesis of BSA-AuNCs. BSA stabilized gold nanoclusters were synthesized by modifying a reported protocol.[203] Briefly, 30 mg/mL BSA was dissolved in 5 mL deionised water. Next, 5 mL aqueous $HAuCl_4$ solution (20 mM) was added and the reaction heated at 50 ℃ for one minute. Following this, as the reaction cooled to room temperature, 1 M NaOH solution was used to adjust the pH to 12.0. The above reaction was then allowed to stir vigorously for 15 min at 60 ℃, resulting in the formation of a deep brown solution.

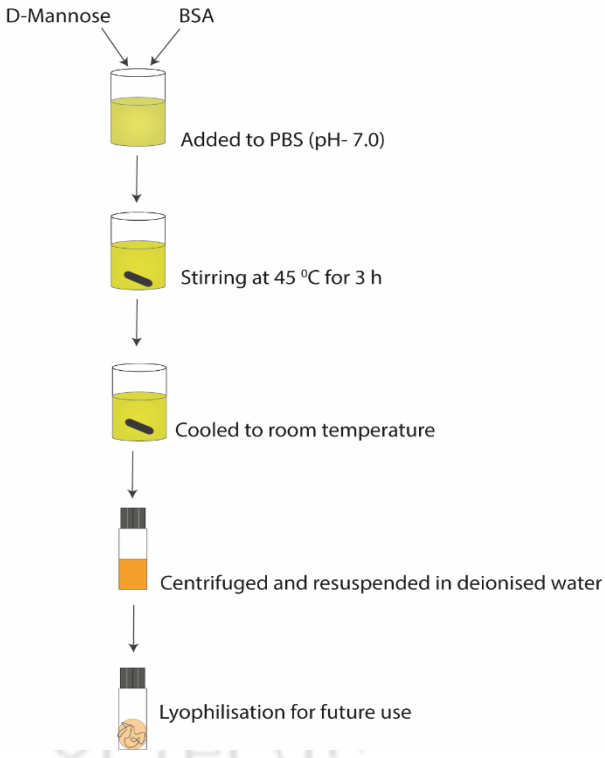

Schematic 2.3.1. Schematic for the conjugation of D-Mannose and BSA.

2.3.2. Conjugation of D-Mannose to BSA. D-Mannose and BSA were conjugated through Maillard reaction by modifying a known protocol (**Schematic 2.3.1.**).[204] 0.5 g of D-Mannose and BSA each was dissolved together in 50 mL phosphate buffer saline (pH-7.0) and stirred at room temperature until a homogenous solution was formed. It was then stirred at 45 ℃ for 3

h. The solution was cooled to room temperature and then centrifuged at 10,000 rpm for 30 min at 4 ℃ to remove unreacted products. The final solution was lyophilized for future use.

2.3.3. Synthesis of (Man-BSA)-PH-AuNCs. Herein, we used the previously conjugated Man-BSA instead of BSA. Briefly, 30 mg/mL of lyophilised Man-BSA was dissolved in deionised

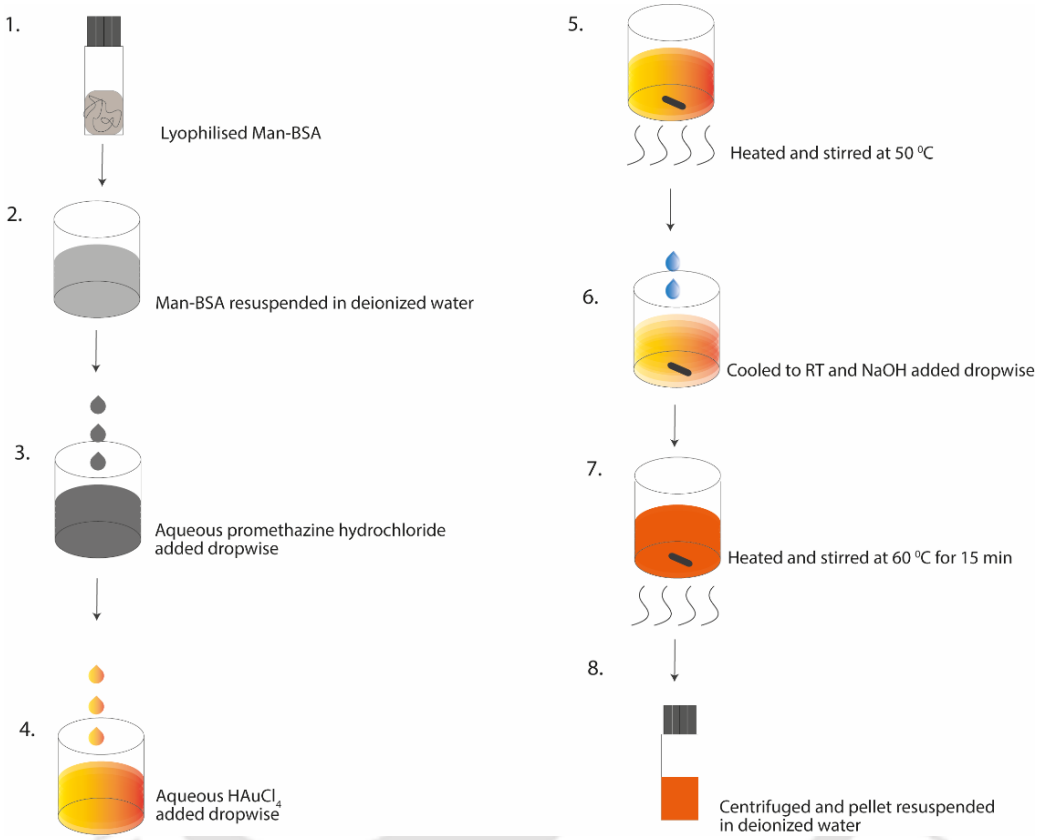

Schematic 2.3.2. Schematic for the synthesis of (Man-BSA)-PH-AuNCs.

5 mL water. 1 mL of aqueous promethazine hydrochloride (20 mM) solution was added to it and stirred at room temperature. Next, 5 mL aqueous $HAuCl_4$ solution (20 mM) was added and the reaction was heated at 50 ℃ for one minute. Following this, as the reaction cooled to room temperature, 1 M NaOH solution was used to adjust the pH to 12.0. The above reaction was then allowed to stir vigorously for 15 min at 60 ℃, resulting in formation of a deep orange solution. The resultant solution was centrifuged at 15000 rpm for 40 min at 4 ℃ to remove the unreacted drug. The final pellet was re-dispersed in water (**Schematic 2.3.2.**). The reaction was performed at three different pH (10.0, 12.0 and14.0) to check the difference in the fluorescence intensity of the formed clusters.

2.3.4. Synthesis of CuNC. To synthesize BSA-stabilized copper nanoclusters, a previously reported protocol was further optimised (**Schematic 2.3.3.**). In brief 300 mg BSA was added to 30 mL water. 30 mg $CuSO_4.5H_2O$ was then added to the BSA solution. The bluish turbid suspension was stirred at room temperature followed by addition of 1 M NaOH until the colour turns purple. 250 µL N_2H_2 was added. The pale brown suspension was then stirred at 80 ^{0}C and transferred to 4 ^{0}C.

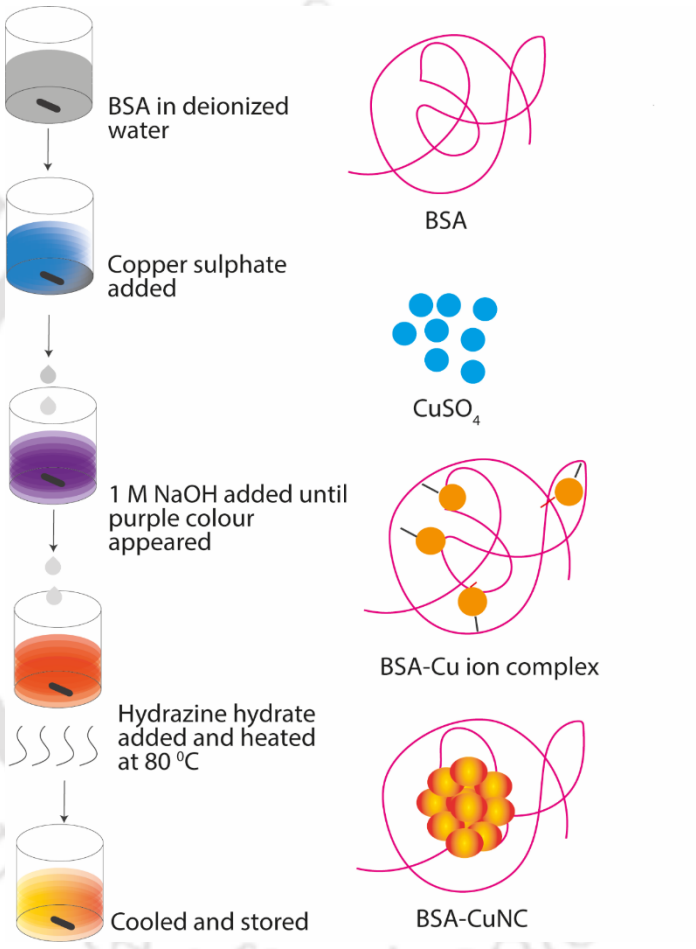

Schematic 2.3.3. Schematic depicting the synthesis of copper nanoclusters (CuNC).

2.3.5. Mannose conjugation to chitosan. Chitosan was dissolved in 1% aqueous acetic acid. The pH of the solution was maintained at 5.0 using 1 M NaOH. An aqueous solution of D-Mannose and ($Na[(CH_3COO)_3BH]$) was prepared. Chitosan solution was slowly added to it dropwise. The resultant solution was stirred at room temperature at 300 rpm for 48 h. After that, it was centrifuged at 4000 rpm for 10-15 min and resuspended in 0.5% acetic acid. This was filtered through 0.4-micron pore size filter and lyophilised (**Schematic 2.3.4.**).

2.3.6. Synthesis of chitosan nanoparticles. Nanoparticles were synthesized through ionic gelation technique. STPP solution (0.2 mg/mL) was added dropwise into the chitosan solution at room temperature. The resultant solution was stirred for 4 h followed by centrifugation at 6000 rpm for 10 min. The final pellet was redispersed in PBS.

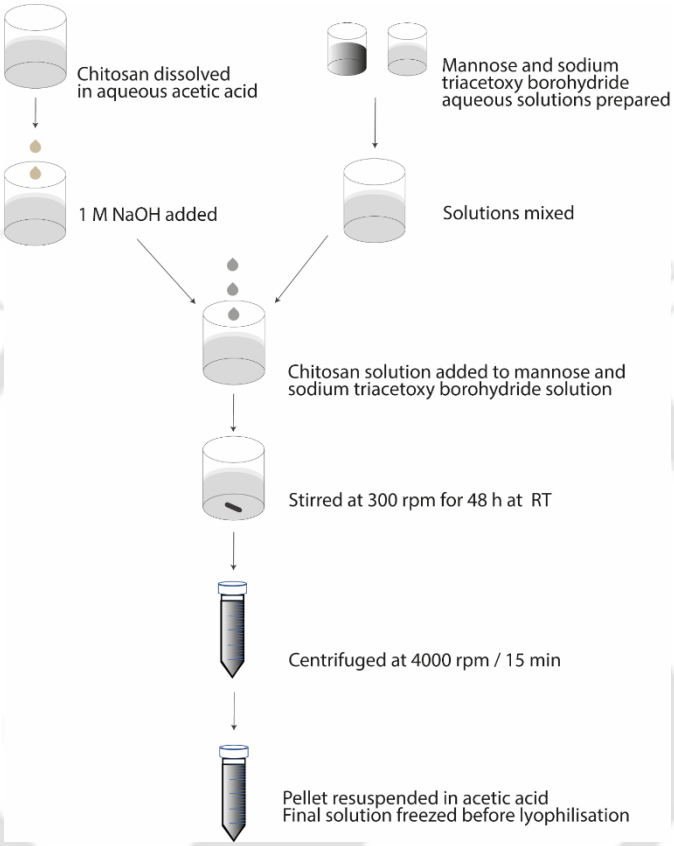

Schematic 2.3.4. Schematic depicting mannose conjugation to chitosan via reductive amination.

2.3.7. Synthesis of man-chitosan_CuNC-LH. This was achieved by dissolving the previously prepared man-chitosan in 1% aqueous acetic acid solution. The pH was adjusted by 10 M NaOH. This solution was further added to deionized water and stirred. BSA followed by $CuSO_4$ was added and stirred again as the pH was brought to 14.0 using 10 M NaOH. 300 µL N_2H_2 was added followed by heating at 80 ^{0}C. Levocetirizine was added to BSA for loading. The resultant transparent and light reddish solution was then washed with deionized water and stored at 4 ^{0}C for further use (**Schematic 2.3.5. A**).

2.3.8. Synthesis of nanocomposite. Man-chitosan_CuNC-LH was dissolved in water for half an hour.

STPP solution (0.4 mg/mL) was prepared and added dropwise into the former solution. The resultant solution was stirred at room temperature for 4 h. The solid nanocomposite was collected by collected by centrifugation at 6000 rpm for 10 min and redispersed in sterile PBS (**Schematic 2.3.5. B**)

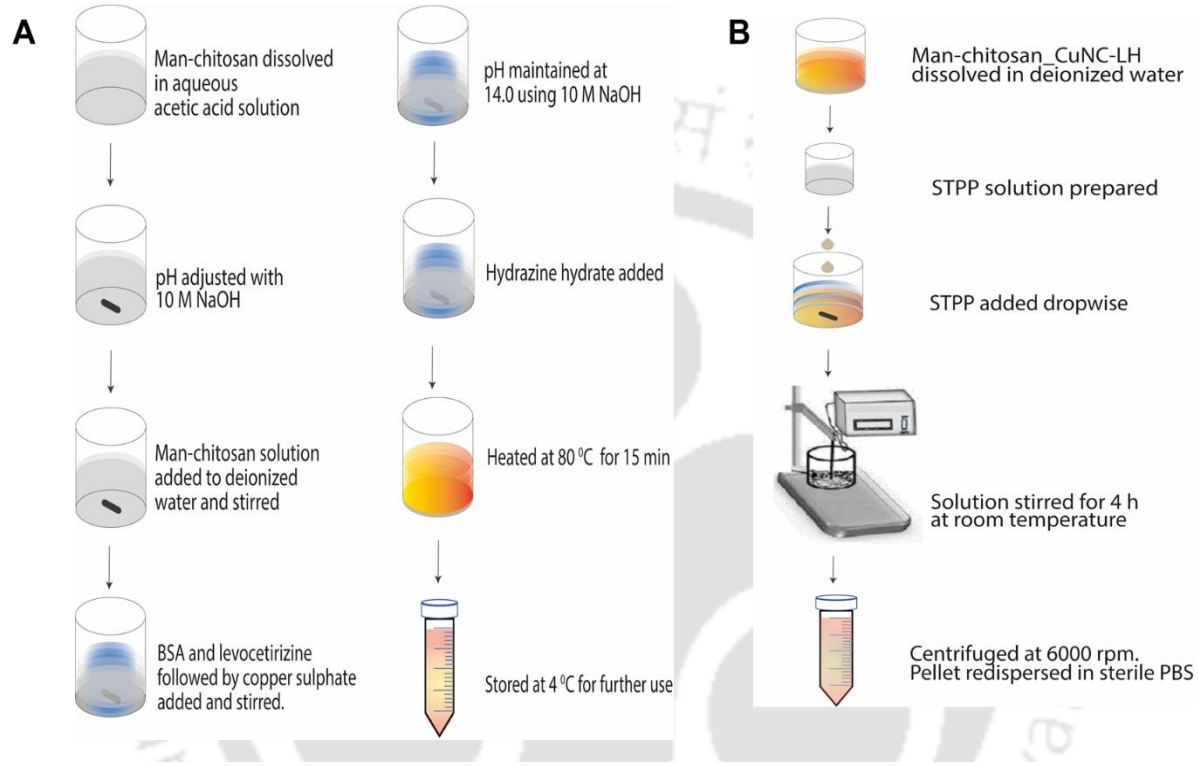

Schematic 2.3.5. (A) Schematic showing man-chitosan_CuNC-LH synthesis. (B) Schematic showing the synthesis of nanocomposite.

2.3.9. Synthesis of PLGA nanoparticles. PLGA pellets were dissolved in acetone and ethanol and mixed till a homogenous solution was obtained. This organic solution was added to 1% PVA solution and stirred at room temperature for 5 minutes. The resultant milky suspension was centrifuged at 6000 rpm at room temperature. The pellet was washed thrice or more with deionized water until devoid of all organic solvent trace.

2.3.10. Synthesis of PLGA-PH_FITC nanoparticles. Promethazine loaded PLGA nanoparticles were prepared by adding an aqueous solution of promethazine hydrochloride to the polymer solution prior to the addition in PVA solution. To allow real time tracking, fluorescein isothiocyanate (FITC) dye was added to the suspension, and the reaction performed in dark for 6 hours, followed by centrifugation. Rest of the steps remained identical, albeit in dark. Finally, the pellet was dispersed in deionized water and stored at 4 ℃ for further use.

2.3.11. Transmission electron microscopy. The samples were analysed under a transmission electron microscope, having a maximum accelerating voltage of 200 keV (JEM 2100; JEOL, Peabody, MA). The imaging was carried out by drop-casting 7 µL of the desired sample onto a carbon-coated copper grid. The sample was air-dried overnight.

2.3.12. Field emission scanning electron microscopy. To study the morphology of the as-synthesized samples, FESEM (JEOL JSM-7610F) imaging was conducted. About 20 µL of the sample was drop-cast to an aluminium foil-covered glass slide and air-dried overnight.

To analyse the cell surface morphology, the treated and untreated cells were imaged using FESEM. Both treated and untreated cells were incubated at 37 ^{0}C for 24 h. Following that, cells were washed using PBS and trypsinized. The cells were fixed with 4% formaldehyde followed by washing with PBS. The final cell pellet was dispersed in deionized water. To an aluminium foil-covered glass slide, 20 µL of the diluted culture was drop-cast and air-dried overnight.

2.3.13. Zeta potential measurements. The zeta potential of as-synthesized samples was recorded using a Malvern Zetasizer Nano ZS.

2.3.14. Measurement of browning. Browning and intermediate products of BSA glycation products were determined by measuring the peak absorbance at 420 nm and 294 nm, respectively with UV− visible spectroscopy (Jasco V-630 spectrophotometer).

2.3.15. Atomic absorption spectroscopy (AAS). The amount of gold present in the as-synthesized (Man-BSA)-PH-AuNCs; and copper in copper nanoclusters was measured using as atomic absorption spectrophotometer: AA220 FS; make: M/s Varian, Netherland**.**

2.3.16. UV−Vis Spectroscopy. The absorbance characteristics of the as-synthesized drug, nanoparticles and drug loaded nanoparticles in the UV-vis range were recorded using UV-visible spectroscopy (Jasco V-630 spectrophotometer).

2.3.17. ***Cell viability assay.*** The cell viability assay using MTT [3-(4,5-dimethylthiazol-2-yl)-2,5-diphenyltetrazolium bromide] was carried out on monolayer cells. For the assay, 5000 cells/well were seeded into a 96-well plate and cultured in DMEM media inside a 5% CO_2-humidified incubator overnight at 37 °C for 24 h. The cells were treated for 48 hours. Following treatment, MTT assay was performed where the respiratory mitochondrial enzyme in the live cell reduces MTT to an insoluble formazan product which when dissolved in DMSO,

can be detected spectrophotometrically at 570 nm with the reference filter at 655 nm. The amount of formazan formed is directly proportional to the number of live cells. The percentage (%) of cell viability was calculated as follows:

$$\% \text{ of viable cells} = \frac{(A570-A655)\ of\ treated\ cells}{(A570-A655)\ of\ untreated\ cells} \times 100$$

2.3.18. ***Cellular uptake study.*** Cells were counted and seeded at a density of 1.5×10^5 cells per well. After 24 h, cells were treated with respective drug/nanocomposite for 1 and 2 h. Following this, they were washed with PBS, trypsinized, centrifuged and finally re-dispersed in PBS for analysis in CytoFLEX flowcytometer (Beckman Coulter).

2.3.19. ***Reactive oxygen species detection.*** Cells were counted and seeded at a density of 1.5×10^5 cells per well. After 24 h, cells were treated with respective drug/nanocomposite for 3 h. At 2 h 30 min, cells were incubated with 5 µM DCFDA (2,7-dichlorofluoresceindiacetate) for 30 min. Thereafter, the cells were washed with PBS, harvested with Trypsin, followed by washing and final resuspension in PBS. The resultant cells were further analysed in CytoFLEX flowcytometer (Beckman Coulter).

2.3.20. ***Mitochondrial membrane potential detection.*** Following treatment for 48 h, 8 µM JC-1 dye was added to the wells and further incubated for 30 min. For positive controls, cells were treated with carbonylcyanide m-chlorophenylhydrazone (CCCP) for 30 min at a concentration of 50 µM. Next, cells were subjected to trypsinization, washing and examined using CytoFLEX flowcytometer (Beckman Coulter).

2.3.21. ***Apoptosis assay.*** Apoptotic cell population following treatment was determined by using Dead cell Apoptosis Kit with Annexin V Alexa Fluor. Briefly, cells were treated with respective drug/nanocomposite for 48 h. Samples were trypsinized, washed and resuspended in PBS. Following this, samples were incubated with respective dyes at room temperature for 15 min. They were analysed in CytoFLEX flow cytometer (Beckman Coulter). This software was further used for fluorescence compensation and data analysis.

2.3.22. Colony formation assay. Cells were counted and seeded at a density of 2×10^5 cells per well. After 24 h, cells were treated with respective drug/nanocomposite for 48 h. Following this, both untreated and treated cells were washed with PBS, trypsinized and resuspended in 10% FBS-DMEM media. The resuspended cells were counted and re-plated at a density of 5

$\times 10^2$ cells per well. After this, cells were maintained for 15 days in the incubator and tracked for colony formation. Cells need to be maintained anywhere between 7-21 days depending on the colony population in the plate for negative control. Once they appeared, they were washed with PBS, fixed with 100% methanol for 30 min and stained with 0.5% crystal violet for 1 h. The stained colonies were washed with excess water, dried overnight and visualized under the microscope.

2.3.23. Lipid droplet staining with Nile red. Cells were counted and seeded at a density of 1.5×10^5 cells per well. After 24 h, cells were treated with drug/nanocomposite for 12 h. After that, they were washed with PBS and fixed with 4% formaldehyde. After 15 min, cells were stained with 0.01 mg/mL Nile red for 10 min in dark. Then, cells were again washed with PBS and counterstained with 1µg/mL DAPI for 5 min in dark. Following PBS wash thrice again, cells were imaged in Zeiss LSM 880 confocal microscope.

2.3.24. Spheroid viability assay. This assay was carried out by treating 3D spheroids with nanocomposites having varying concentration of the drug for 72 h at 37 ℃. At the end of treatment, viability was assessed using alamarBlue assay by recording the absorbance at 570 nm, fixing the reference filter at 655 nm. The viability percentage (%) was determined using the following formula:

$$\% \text{ of viable cells} = \frac{(A570-A655)\ of\ treated\ cells}{(A570-A655)\ of\ untreated\ cells} \times 100$$

2.3.25. Sphere formation assay. For this assay, following treatment with respective drug/nanocomposite, the spheroids were generated using the force floatation method. Briefly, cells were seeded at a density of 2×10^6 cells per well in a 6-well plate. After 24 h, they were treated for a period of 48 h, following which cells were trypsinized, counted and re-seeded at a density of 2×10^4 cells per well in a 96 well plate. It was pre-coated with 1.5% agarose in serum-free DMEM media. The cells were then centrifuged at 700 rcf for 15 min and incubated at 37 ℃ in a humidified environment containing 5% CO_2 for a period of 96 h. After that, cells were imaged using a microscope.

2.3.26. Live/dead staining assay. To begin with, monolayer cells were seeded on 35 mm tissue culture plate at a density of 1.5×10^6 cells per well and on 96 well plate at a density of 2×10^4 cells per well (for 3D spheroids). After 24 h and 96 h of incubation respectively, they were treated with respective drug/nanocomposite for 48 h and 72 h. Following this, cells and

spheroids were washed with PBS and Calcein AM and propidium iodide (PI) dye was added at a concentration of 2 µM and 4 µM. They were incubated for 0.5 h and 2 h respectively and imaged using Zeiss confocal LSM 880 microscope.

2.3.27. Immunoblotting. In order to extract total protein, RIPA lysis buffer was used. Samples were quantified to begin with and equivalent amount was run on SDS-PAGE. Protein from the gel was transferred to the PVDF membrane, blocked using blocking buffer (4% BSA in TBST), and incubated with primary antibody for 12 h at 4 ℃. Membranes were then washed thoroughly with TBST, incubated with secondary antibody, and re-washed. Eventually, signals were developed using chemiluminescent reagent, and to acquire image ChemiDoc (Bio-Rad) was used. ImageJ software was used for blot quantification and GraphPad Prism software for graphical representation.

2.3.28. Studies on planktonic bacteria. The following strains were used for the antibacterial studies: Gram-positive bacteria (*Staphylococcus aureus* MTCC 96 and *Bacillus subtilis* MTCC 1305) and Gram-negative bacteria (*Pseudomonas aeruginosa* MTCC 2488 and *Escherichia coli* DH5*α*). *S. aureus* MTCC 96 was grown in BHI at 37 °C (180 rpm) for 12 h. *B. subtilis* MTCC 1305 and *P. aeruginosa* MTCC 2488 were grown in NB at 37 °C (180 rpm) for 12 h. *E. coli* DH5*α* was grown in LB at 37 °C (180 rpm) for 12 h. The bacterial strains were treated with varying concentrations of free promethazine hydrochloride and (Man-BSA)-PH-AuNCs. The bacterial growth was monitored by recording the optical density (OD) at 595 nm using the UV−visible spectrophotometer (Jasco V-630). The measurements were recorded in triplicates. Further, the minimum inhibitory concentration (MIC) and the minimum bactericidal concentration (MBC) were established by plating the bacteria on nutrient agar media. Here, 100 µL of bacteria treated with the MIC and MBC of free promethazine hydrochloride and (Man-BSA)-PH-AuNCs was spread-plated on the media using L-rod and incubated at 37 °C for 12 h.

2.3.29. Growth Kinetics Study. The growth curve was analysed for *S. aureus* MTCC 96 and *P. aeruginosa* MTCC 2488 after treating the bacteria with the MIC and MBC of (Man-BSA)-PH-AuNCs and free promethazine hydrochloride. Their growth was monitored for 12 h at 37 °C (180 rpm) with an interval of 2 h.

2.3.30. Leakage Study. Overnight grown bacterial cultures were used to re-inoculate into respective medium and incubated for 12 h. Aliquots of bacterial suspensions were treated with

sub-MIC concentrations of free promethazine and (Man-BSA)-PH-AuNCs were incubated at 37 ℃ for 12 h. A control was included in each case containing untreated bacteria. The suspensions were centrifuged at 5000 rpm for 2 min. and the supernatant was passed through 0.45 µ filters. The absorbance of the clear supernatant was estimated at 260 and 280 nm using UV-Vis spectrophotometer.

2.3.31. DCFDA Assay. The ROS generated after treating the bacterial cells was measured through 2',7'-dichlorofluorescein diacetate (DCFDA) based assay. Overnight grown cultures were adjusted to 10^5 cfu/mL. Sub-MIC concentration of free promethazine and (Man-BSA)-PH-AuNCs was used to treat them for 6 h at 37°C and 180 rpm. Following incubation, the cells were centrifuged at 12,000 rpm/ 10 °C for 30 min for disruption. The supernatant was collected and treated with 100 µM DCFDA for 1 h in dark. Fluorescence was detected at an excitation filter of 485 nm and emission filter of 523 nm using a Perkin Elmer fluorescence spectrophotometer.

2.3.32. Lipid Content Detection. Lipid content was determined for planktonic bacteria. The overnight grown culture was diluted to 1 ×10^6 cfu/mL and incubated for 12 h. Following this, they were treated with (Man-BSA)-PH-AuNCs at its ½ MIC for 12 h. Spectrophotometric data were collected from a Perkin Elmer fluorescence spectrophotometer at excitation and emission filter of 549 nm and 570-700 nm, respectively.

2.3.33. Studies on bacterial biofilm. Bacterial Biofilm Assay. The bacteria were diluted to 1 × 10^6 cfu /mL using the NB (for *P. aeruginosa*) and BHI (for S. aureus MTCC 96) media from which 100 µL of bacteria was added to a 96-well plate and incubated at 37 °C in static condition. After 24 h, the medium was removed, and fresh medium was added. To this, different concentrations of free promethazine hydrochloride and (Man-BSA)-PH-AuNCs were added and incubated for 12 h. After incubation, the medium was removed, and biofilm was stained with 0.01% crystal violet. The stained biofilm was incubated for 15 min at 37 °C. The crystal violet was dissolved using 95% ethanol, and absorbance (in triplicate) was measured at 595 nm using the microplate reader.

2.3.34. Acridine Orange/Propidium Iodide Dual Staining Assay. The bacteria were grown overnight and the culture, diluted to 1 × 10^6 cfu/mL. A 100 µL of the diluted culture was added to the 96-well plate and incubated for 24 h. After incubation, the grown biofilm was treated with (Man-BSA)-PH-AuNCs at its sub-$MBIC_{50}$ and $MBIC_{50}$ and incubated for 12 h. The

biofilm was then gently washed and stained with 0.01 mg/mL of propidium iodide (PI) and 0.01 mg/mL of acridine orange (AO), followed by incubation in dark. The excess dye was removed, and imaging was done at an excitation filter of 465−495 nm for AO and 540/25 nm for PI.

2.3.35. Lipid Content Detection. For biofilm formation, bacteria grown overnight were diluted to 1×10^6 cfu/mL. 100 µL of the culture was then added to a 96-well plate and incubated for 24 h. Following incubation, the biofilm was treated with (Man-BSA)-PH-AuNCs at its sub-$MBIC_{50}$ and $MBIC_{50,}$ and incubated for 12 h. The cells were washed and stained with 0.01 mg/mL of Nile red and incubated in dark. The excess dye was removed, and imaging was carried out with a Zeiss Laser scanning confocal microscope (LSM 880) at an excitation filter of 561 nm and emission filter of 628 nm.

2.3.36. Statistical analysis. All the statistical analysis were carried out using the GraphPad Prism software. The experimental data are expressed as mean ± SEM. Additionally, the one-way and two-way ANOVA test was used to access the correlations among the groups. A p-value < 0.05 (*) is considered to be statistically significant, where (*) $p<0.05$, (**) $p<0.01$, (***) $p<0.001$ and (****) $p<0.0001$ are considered to be highly significant.

2.3.37. Illustrations and schematics. All illustrations and schematics were drawn using Adobe Illustrator 2021 software.

Chapter 3

Results and Discussions

3.1. Mannosylated gold nanoclusters incorporated with repurposed antihistamine drug promethazine for antibacterial and anti-biofilm applications.

-***ACS Applied Bio Materials***, *2022*, **5 (**12), 5911-5923
DOI: 10.1021/acsabm.2c00867
[**ACS publishing group]**

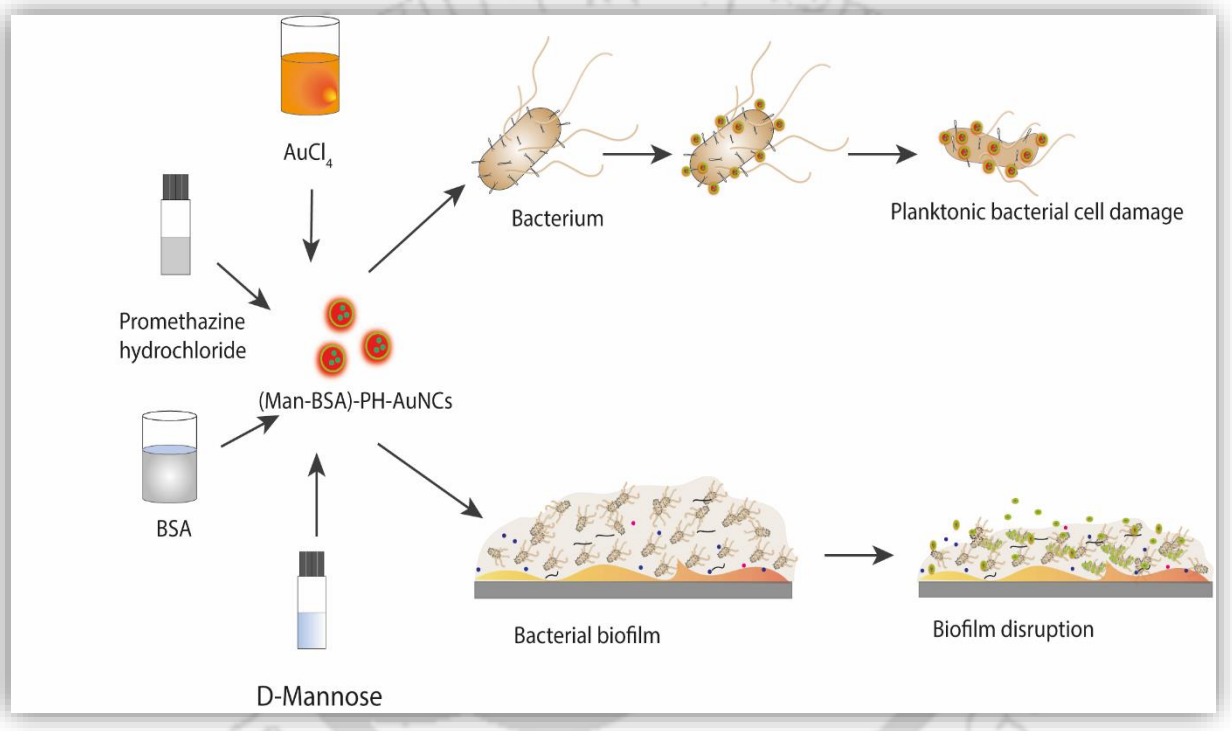

Scheme 3.1. Schematic depicting the synthesis of gold nanoclusters incorporated with promethazine for antibacterial and antibiofilm applications.

Results and Discussions

Abstract

Drug repurposing presents a workable strategy in tackling antibiotic resistance. Many known drugs have been repurposed for their applications against different targets. Antihistamines that are usually used to treat allergy symptoms can be combined with nanoscale materials to enhance their efficiency. Herein, the anti-microbial properties of a common antihistamine drug, promethazine was explored in Gram-positive and Gram-negative bacteria. Being positively charged, promethazine was easily incorporated into the mannose conjugated BSA-stabilized promethazine hydrochloride gold nanoclusters. Capping with D-Mannose helped in targeting the bacteria by inhibiting their adhesive appendage called pili. Following their uptake, drug released inside the bacteria caused reactive oxygen species production and membrane permeability alteration, ultimately resulting in bacterial inhibition. Additionally, they were also explored for biofilm eradication. As observed through staining assays, the number of dead cells increased with increasing concentration of drug loaded gold nanoclusters in the biofilm mass. Therefore, the as-synthesized mannosylated gold nanoclusters incorporated with promethazine were analysed for potential anti-bacterial and anti-biofilm applications.

3.1.1. Preliminary screening of antihistamine drugs for potential antibacterial activity.

Table 3.1.1. Over the counter drugs used for preliminary screening and their classes.

Drug	Class	Sub-class
Promethazine	H1 – 1st generation	Phenothiazine
Ranitidine	H2	-
Ebastine	H1 – 2nd generation	Piperidine
Levocetirizine	H1 – 2nd generation	Piperazine
Cetirizine	H1 – 2nd generation	Piperazine
Pheniramine	H1 – 1st generation	Alkylamine

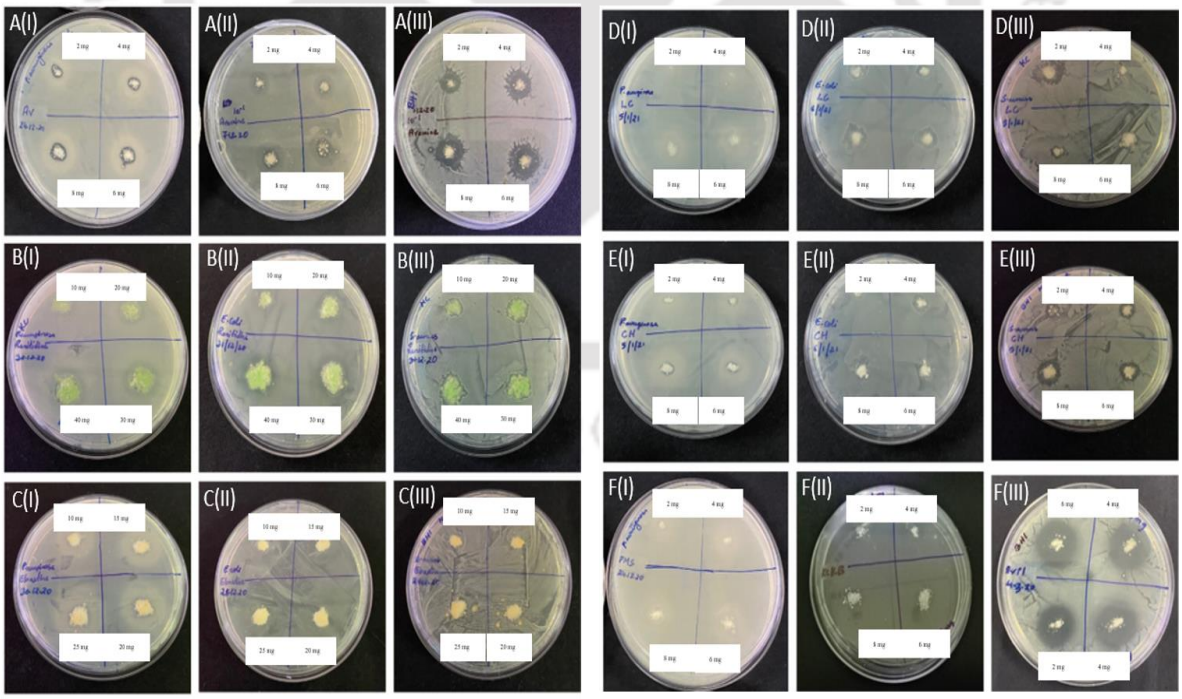

Figure 3.1.1. Experimental screening of over-the-counter drugs through spread plate technique. A- promethazine, B- ranitidine, C- ebastine, D- levocetirizine, E- cetirizine and F- pheniramine maleate. Numbers (I) denote *P. aeruginosa*, (II) denote *E. coli* and (III) denote *S. aureus*.

Six different types of antihistamine drugs that are available over-the-counter (OTC) were used for the initial screening in *P. aeruginosa*, *E. coli* and *S. aureus* strains. Their chemical classes have been listed in **Table 3.1.1**. The details of the procedure have been described in the supplementary information. Among all the drugs, promethazine displayed activity against all three strains with zones of radii as high as 6 mm for Gram-positive and 4 mm for Gram-negative bacteria (**Figure 3.1.1**). Hence, based on the spread plate method, promethazine was selected for its best inhibitory activity against all the three strains, at the given concentrations (**Table 3.1.2**).

Table 3.1.2 Radii of zones of inhibition of over-the-counter drugs against *P. aeruginosa*, *E. coli* and *S. aureus*. The radii are expressed in mm.

Drugs	*P. aeruginosa*	*E. coli*	*S. aureus*
Promethazine	8 mg - <1 mm	2 mg - 1 mm 4 mg - <2 mm 6 mg - 3 mm 8 mg - 4 mm	2 mg - <3 mm 4 mg – 4 mm 6 mg - <5 mm 8 mg – 6 mm
Ranitidine	-	-	-
Ebastine	-	-	-
Levocetirizine	-	-	4 mg - <2 mm
Cetirizine	-	-	4 mg - <1 mm 6 mg - <1 mm 8 mg - 1 mm
Pheniramine	-	-	2 mg - 7 mm 4 mg - 8 mm 6 mg - 9 mm 8 mg – 9mm

3.1.2. Development and characterisation of Mannose coated BSA-stabilized gold nanoclusters encapsulating promethazine hydrochloride ((Man-BSA)-PH-AuNCs). Nanotechnology based antimicrobial targeting has become an important strategy in tackling off-target hits, biocompatibility, stability and solubility issues. To reap even better benefits of nanocarriers, functionalisation is a well-known approach. While the gold nanoclusters aided

with tracking, the D-Mannose coating helped increase the carriers' overall specificity towards the target. They can also help reduce toxicity and prolong circulation time. Following the conjugation of BSA and D-Mannose, following experiments were performed to confirm the same.

In a Maillard reaction, a reducing sugar like Mannose reacts with the free amino groups in proteins to form brown complex polymers that contain nitrogen.[205,206] These brown products are often used to validate the reaction. Therefore, to confirm the conjugation of D-Mannose to BSA, absorbances at 420 nm and 294 nm for free BSA and Man-BSA were compared. Increase in A_{420} value after glycation indicated that browning had occurred. Similarly, increase in A_{294} of Man-BSA compared to BSA is an indication of intermediate reaction products (**Figure 3.1.2. A**). Such significant changes in the absorbance values indicated the successful conjugation of D-Mannose to BSA. Additionally, the fluorescence spectra of BSA and Man-BSA was compared. The fluorescence spectrum of BSA showed λ_{max} at 356 nm, but after glycation with D-Mannose, it had moved to 352 nm (**Figure 3.1.2. B**). This blue-shit can be attributed to the

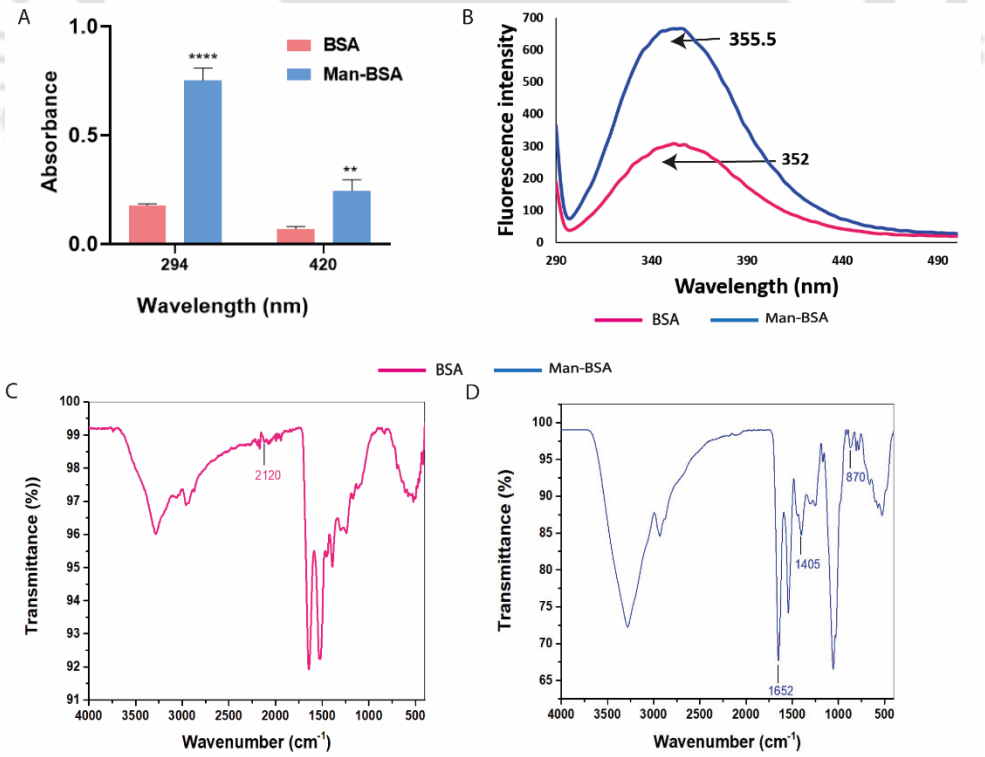

Figure 3.1.2. (A) Absorbance of BSA and Man-BSA measured at 294 nm and 420 nm. (B) Fluorescence spectra of BSA and Man-BSA in PBS (pH-7.0). FTIR spectra of (C) BSA and (D) Man-BSA.

attachment of the monosaccharide to the protein interior thus, masking the tryptophan residues. Besides, there was also a significant decrease in Man-BSA fluorescence intensity. The interaction of tryptophan residues with the newly formed quenching products of glycation may have resulted in the decreased fluorescence intensity. For further confirmation of conjugation, the infrared spectra of BSA and Man-BSA were obtained and analysed through FTIR. The peak at 2120 cm $^{-1}$ (**Figure 3.1.2. C**) that is usually assigned to C≡C and C≡N disappeared after glycation to D-Mannose. The vibrations at 1652-1405 cm^{-1} (**Figure 3.1.2. D**) indicated the attachment of carbonyl (C=O) from mannose, while the peak at 870 cm^{-1} was resultant of the carbon-nitrogen (C-N) bond, a characteristic of any glycoprotein conjugate. Based on the above results, it may be concluded that D-Mannose was successfully conjugated to BSA, thus forming the glycation products. Finally, the concentration of mannose was measured through anthrone based estimation of carbohydrates and found to have a mannose concentration of 383 µM (**Figure 3.1.5. C**).

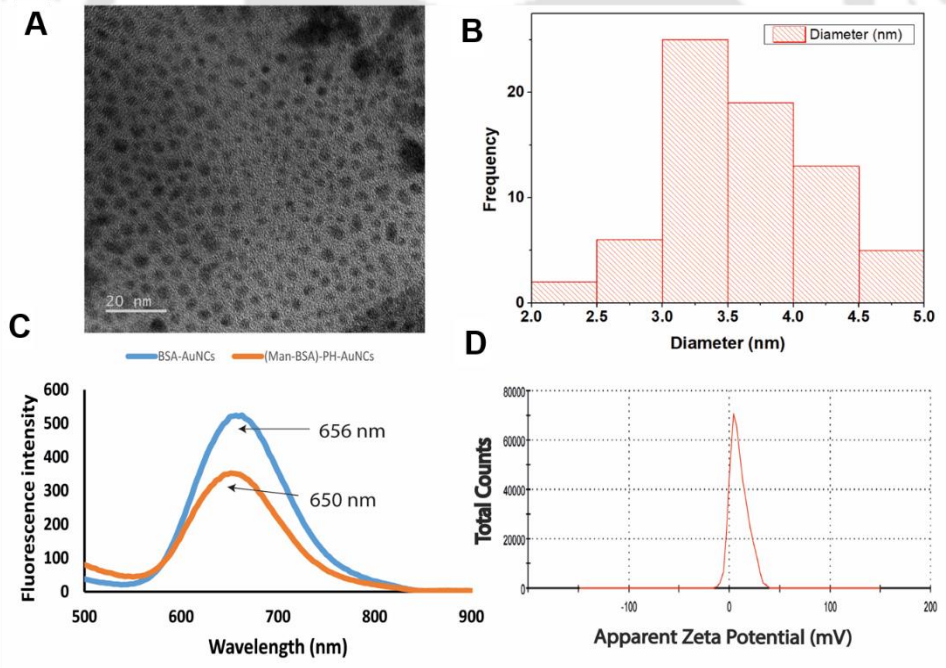

Figure 3.1.3. (A) TEM image of (Man-BSA)-PH-AuNCs. (B) Size distribution graph of (Man-BSA)-PH-AuNCs. (C) Fluorescence intensity measurement of BSA-AuNCs at λ_{em} = 656 nm and (Man-BSA)-PH-AuNCs at λ_{em}= 650 nm when excited at 365 nm. (D) Zeta potential measurement of (Man-BSA)-PH-AuNCs (-17.5 mV).

BSA was selected as both the stabilizing and protective agent. It is widely known as a model protein because the disulphide bond and the free SH groups of BSA provide steric protection,

thus stabilizing the cluster.[207] The as-synthesized (Man-BSA)-PH-AuNCs appeared transparent and deep orange in colour. Under UV light, they exhibited a strong red emission. When excited at 365 nm, they had a λ_{em} of 650 nm, while BSA-AuNCs had a λ_{em} of 656 nm (**Figure 3.1.3. C**). TEM images revealed (Man-BSA)-PH-AuNCs with an average size of 3.57 $\pm$ 0.5 nm (**Figure 3.1.3. A, B**). Similarly, the average size of BSA-AuNCs was found to be 2.5 $\pm$ 0.9 nm (**Figure 3.1.4 A**). The size calculations were carried out using the ImageJ software. Thus, from the TEM images, the successful synthesis of the (Man-BSA)-PH-AuNCs was confirmed. The selected area electron diffraction pattern for BSA-AuNCs did not show any significant pattern (**Figure 3.1.4. C**), which is in corelation with the XRD data obtained (**Figure 3.1.4. F**). Additionally, the UV-vis graph of the (Man-BSA)-PH-AuNCs revealed a feeble peak at 248 nm for promethazine and 280 nm for BSA. This is in concurrence with promethazine's UV-Vis spectral peak at 248 nm and a weak shoulder at 297 nm (**Figure 3.1.4. D**). However, there was

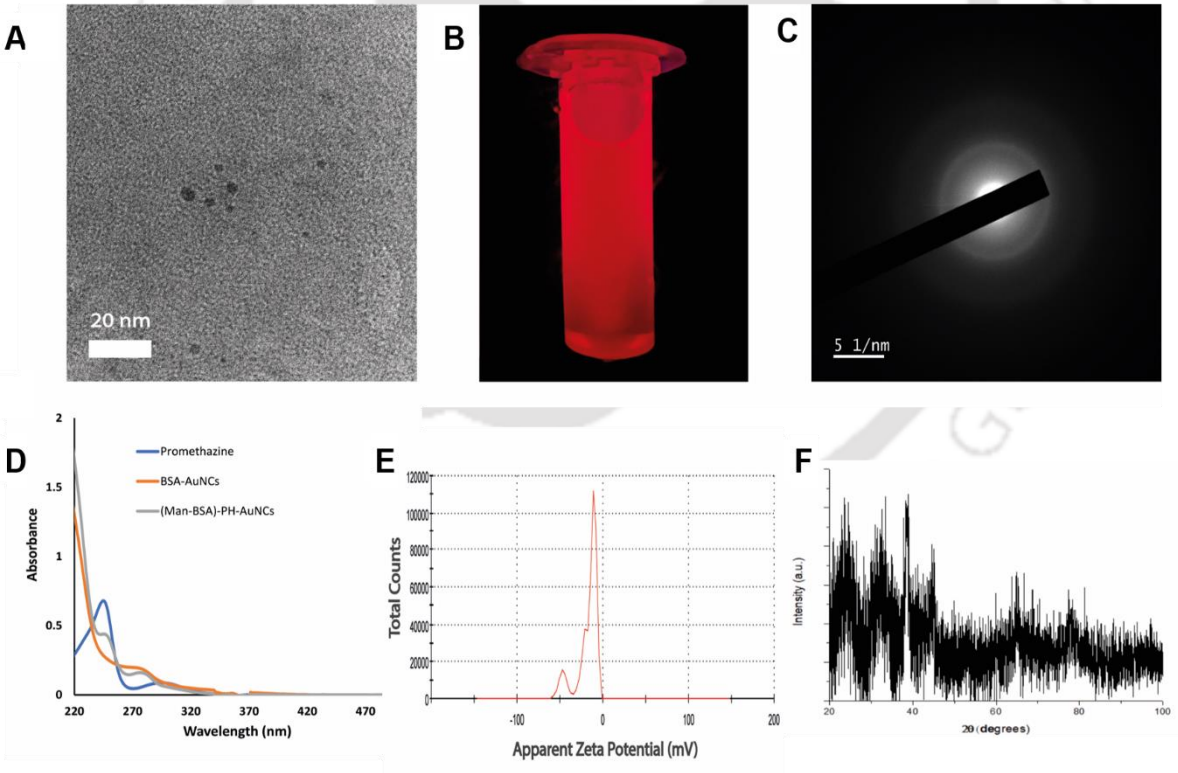

Figure 3.1.4. Characterisation of BSA-stabilized gold nanoclusters (BSA-AuNCs). (A)TEM image of BSA-AuNCs (scale-20 nm). (B) As-synthesized BSA-AuNCs under UV transilluminator. (C) SAED pattern of BSA-AuNCs. (D) UV-vis spectra of free promethazine, BSA-AuNCs and (Man-BSA)-PH-AuNCs. (E) Zeta potential measurement of BSA-AuNCs. (F) XRD plot of BSA-AuNCs.

no peak in the visible region for gold thus, discounting the possibility of formation of surface plasmon resonance active gold nanoparticles in the reaction medium.

The zeta potential analysis confirmed that the (Man-BSA)-PH-AuNCs have a surface charge of −17.5 mV (**Figure 3.1.3. D**), while BSA-AuNCs have a surface charge of −22.5 mV (**Figure 3.1.4. E**). Surface functionality is a critical parameter regulating the biodistribution and pharmacokinetics of nanoparticles. The negative charge on the nanocarrier is preferable for drug delivery as positively charged drugs can be loaded into it through electrostatic interaction. Also, negative charge ensures significantly prolonged circulating half-lives while highly cationic nanocarriers are rapidly cleared off from the circulation.[208] Furthermore, they have reduced plasma protein adsorption and lower non-specific uptake.[209] To explore the effect of pH during synthesis, (Man-BSA)-PH-AuNCs were synthesized at three different pH- 10, 12

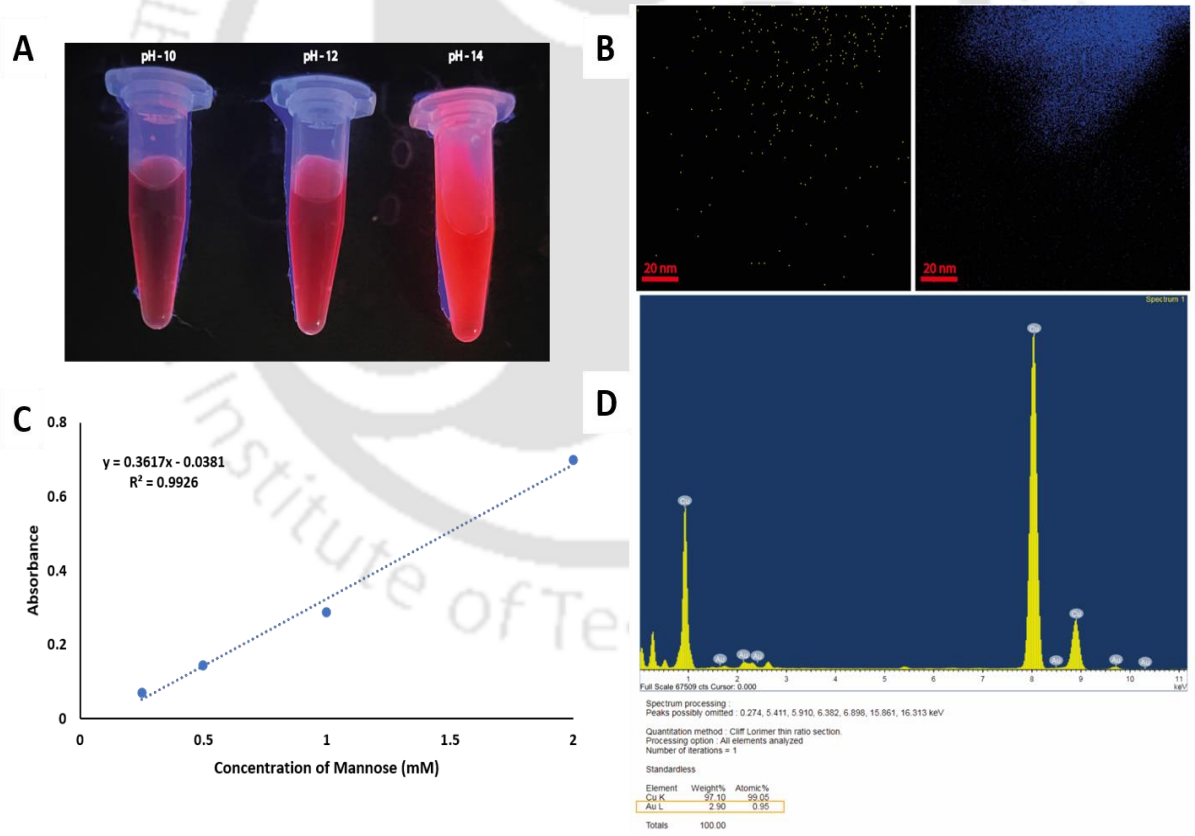

Figure 3.1.5. (A) (Man-BSA)-PH-AuNCs synthesized at three different pH (10, 12 and 14) under the UV transilluminator. (B) Elemental mapping of (Man-BSA)-PH-AuNCs. (C) Concentration of mannose calculated based on standard curve obtained through anthrone-based carbohydrate estimation method. (D) EDX plot of (Man-BSA)-PH-AuNCs.

and 14. It was observed that with increasing pH there was a slight blue shift and reduction in the fluorescence intensity (**Figure 3.1.5. A**).

Following this, atomic absorption spectroscopy (AAS) revealed the concentration of gold in the (Man-BSA)-PH_AuNCs to be 76.4 µg/mL (**Figure 3.1.6. A**). Additionally, the elemental composition was supported by mapping performed using energy dispersive X-ray spectroscopy (**Figure 3.1.5. B, D**). Then, using UV-vis spectroscopy, the loading efficiency of promethazine was found to be 62% and consecutively the concentration of promethazine loaded was calculated to be 12.4 mM. The encapsulation of promethazine into the gold nanoclusters might be a result of the covalent bond between the gold and sulphur interface.[210] The formation of gold-thiolate bond requires the sulfhydryl group to be deprotonated, creating a thiyl radical ($RS^{\cdot}$), whereas the protonated SH group can interact with gold only by weaker coordination bonds through sulphur's lone-pair electrons. Since, the thiolate–gold (RS–Au) bond has a strength close to that of the gold–gold bond, it can modify the gold–gold bonding at the gold–sulphur interface.

Furthermore, to understand the release profile of promethazine (**Figure 3.1.6. B**), (Man-BSA)-PH-AuNCs were suspended in acidic and neutral environment (acetate buffer and PBS buffer) and studied it for a certain interval. In pH 4 (acetate buffer), higher release was observed compared to that of pH 7 (PBS buffer). Thus, a pH responsive release pattern of promethazine was observed, which is significant in the understanding of drug release *in vitro*.

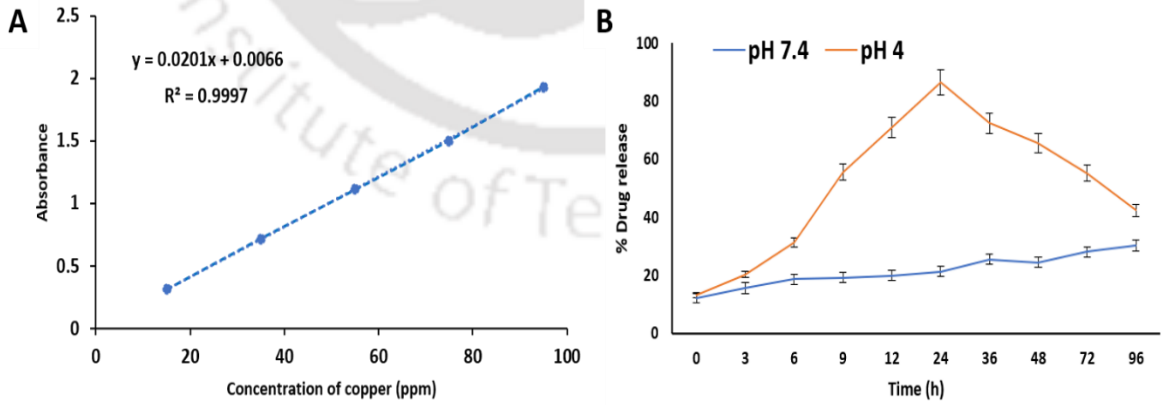

Figure 3.1.6. (A) Concentration of gold calculated based on the standard curve obtained from atomic absorption spectroscopy. (B) Release profile of promethazine from (Man-BSA)-PH-AuNCs in acidic and neutral buffer. At pH 4, a burst release of 86.3% was observed at 24th h. By the 96th h, it had come down to a sustained release of 42.3%. At pH 7.4, the release was slow and sustained reaching up to 30.2% at the 96th h.

3.1.3. Anti-bacterial effect of (Man-BSA)-PH-AuNCs against Gram-negative and Gram-positive bacteria.

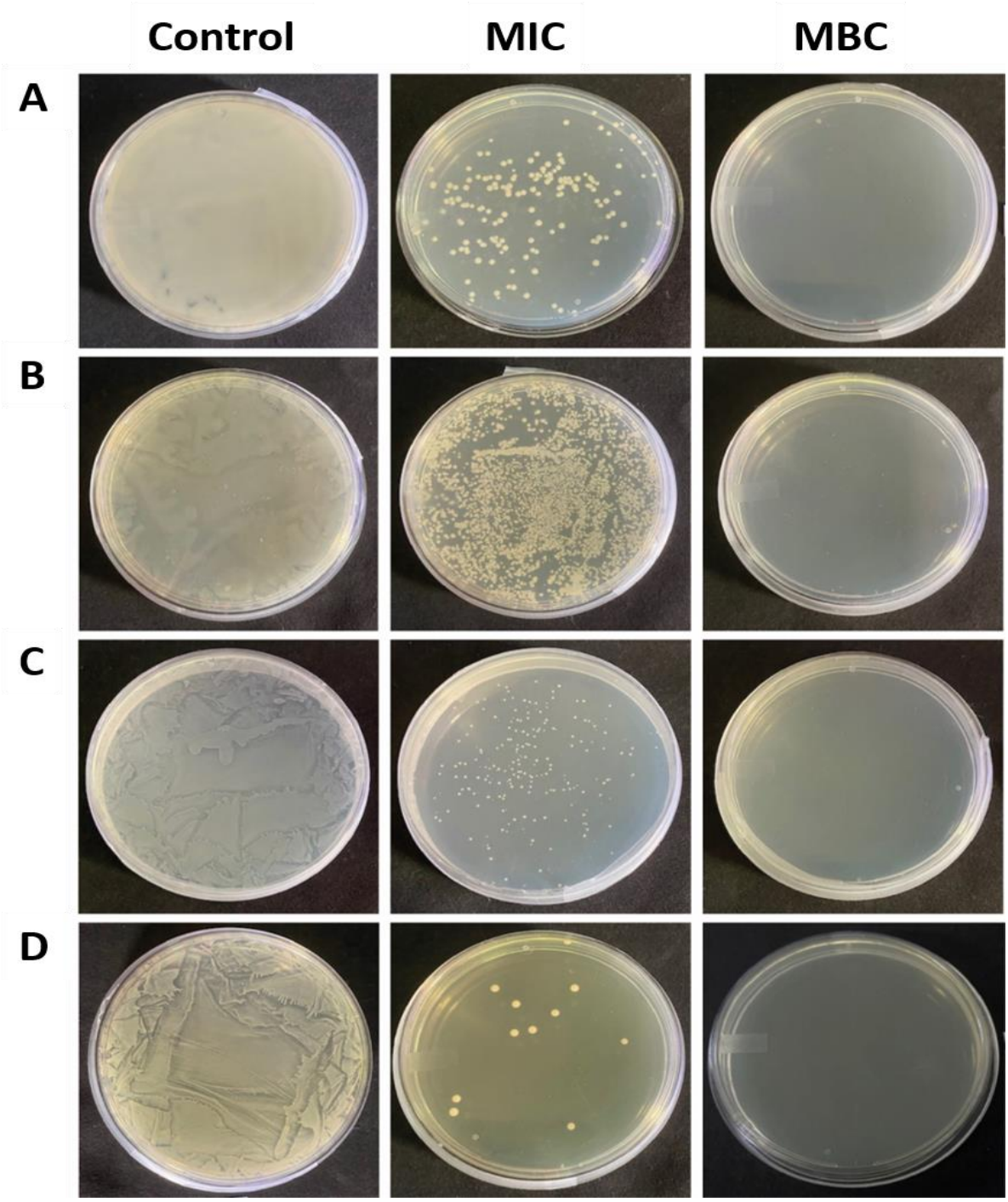

Figure 3.1.7. Bacteria grown on respective nutrient agar. (A) *P. aeruginosa*, (B) *E. coli*, (C) *S. aureus* and (D) *B. subtilis* control and treated bacteria treated with MIC and MBC of (Man-BSA)-PH-AuNCs.

The antibacterial activity of (Man-BSA)-PH-AuNCs was determined on Gram-positive bacteria (*Staphylococcus aureus* MTCC 96 and *Bacillus subtilis* MTCC 1305) and Gram-negative bacteria (*Pseudomonas aeruginosa* MTCC 2488 and *Escherichia coli* DH5α). The MIC and MBC values obtained for promethazine and (Man-BSA)-PH-AuNCs are listed in the table (**Table 3.1.3**). Upon treatment, the MIC value for *B. subtilis* (459 µM) was the lowest, followed by *S. aureus* (678 µM), *P. aeruginosa* (687 µM) and *E. coli* (698 µM). The results were also further substantiated through spread plate method, where bacteria were plated on their respective agar and then treated (**Figure 3.1.7.**). A lesser number of colonies compared to negative control (lawn like appearance) were observed in MIC; while at MBC, no colonies were observed. The zones of radii of inhibition of (Man-BSA)-PH- AuNCs on spread plated bacteria were also determined and compared with respective positive and negative controls

Table 3.1.3. MIC and MBC values tabulated for (a) free promethazine and (b) (Man-BSA)-PH-AuNCs against *P. aeruginosa*, *E. coli*, *S. aureus* and *B. subtilis*.

	Promethazine		(Man-BSA)-PH-AuNCs	
Bacterial strain	**MIC (µM)**	**MBC (µM)**	**MIC (µM)**	**MBC (µM)**
P. aeruginosa	611	803	687	939
E. coli	623	826	698	912
S. aureus	489	611	678	723
B. subtilis	312	546	459	652

Table 3.1.4. List of radii of zones of inhibition of (Man-BSA)-PH-AuNC treated bacteria. The radii are expressed in mm.

Bacterial strain	Positive control (mm)	Negative control (mm)	25 µL (mm)	50 µL (mm)	100 µL (mm)
P. aeruginosa	3	-	-	<4	8
E. coli	6	-	5	7	10
S. aureus	6	-	-	8	10
B. subtilis	4	-	-	5	11

(**Figure 3.1.8.**). The radii values are listed in table (**Table 3.1.4.**). A 5 mm zone of inhibition had formed in the spread plated *E. coli* even when the volume of (Man-BSA)-PH-AuNCs was as low as 25 µL. As is evident from the values, the free drug seems to have higher inhibitory potential compared to the loaded one. This is in coherence with previous reports on nanocarrier based delivery systems that suggest a partial and sustained release of drug from the clusters.[211,212] Loaded therapeutic drugs over free drugs have several merits like reduced toxicity but higher stability. Nanocarrier based transport, therefore, ensures a prolonged circulation time.

The physical attachment of bacteria to host cells is important for bacterial pathogenesis. The loss of these adhesive appendages can result in reduction of virulence too.[213] One of the

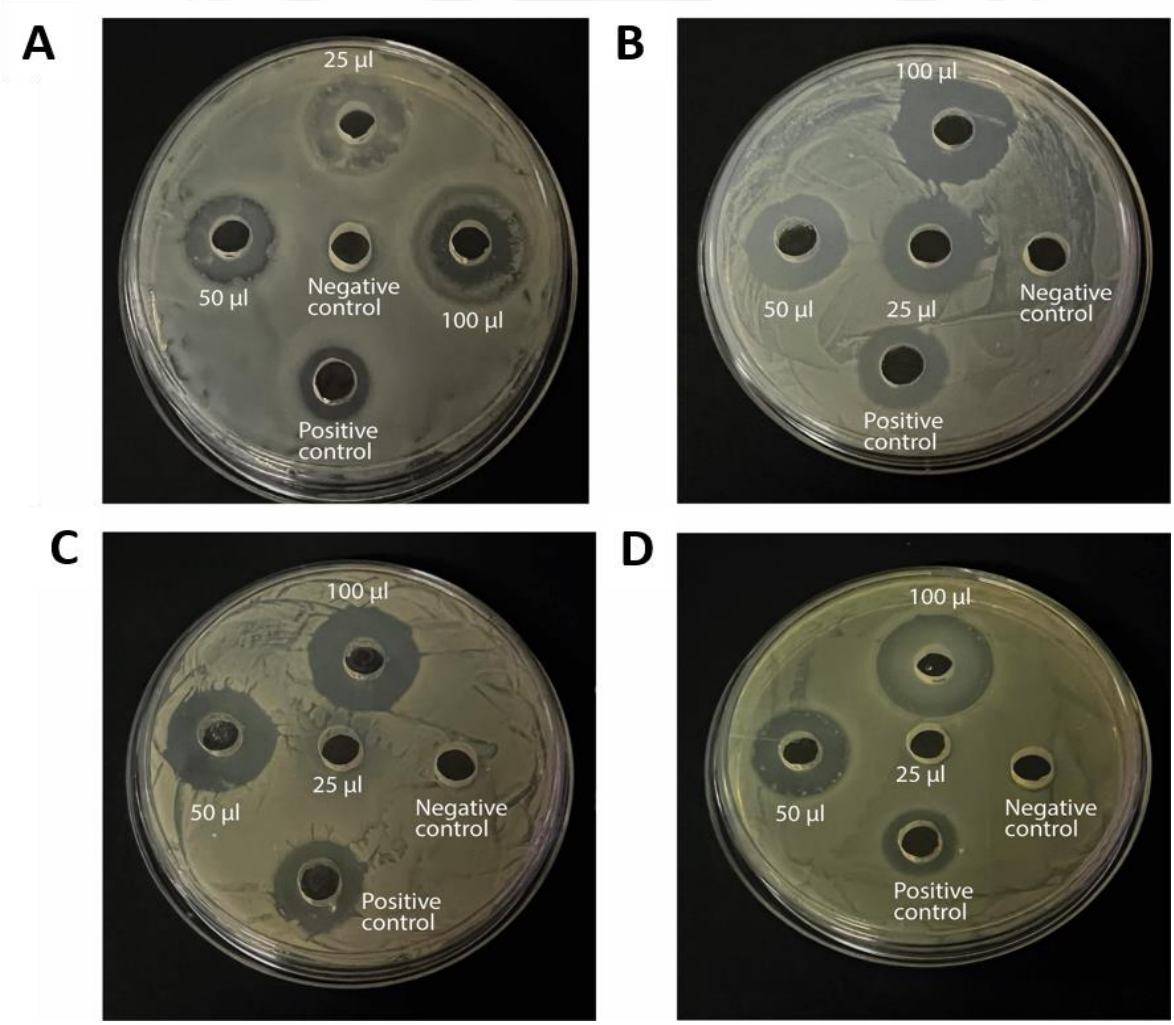

Figure 3.1.8. Determination of zone of inhibition of (Man-BSA)-PH-AuNC treated (A) *P. aeruginosa*, (B) *E. coli*, (C) *S. aureus* and (D) *B. subtilis*.

strategies thus, to inhibit pilus-mediated function involves the prevention of pathogen binding to host cells. Several carbohydrate derivatives have been found to block the efficiency of both Type 1 and P pili in biophysical and hemagglutinin assays.[214] The D-Mannose coating over the drug loaded nanoclusters is an attempt at selectively disarming pathogens by the chemical targeting of pili. The type 1 pili are filamentous proteinaceous appendages that extend out of most Gram-negative microorganisms. They are composed of FimA, FimF, FimG, FimH proteins[215], where FimA accounts for about 98% of the pilus protein while FimH is exclusively responsible for binding to D-Mannose.[216] Phenothiazines too, are known to affect pili-mediated adhesion or multiplication of *E. coli* on epithelial cells.[217] This could possibly explain the lesser difference between MIC values of promethazine and (Man-BSA)-PH-AuNCs in *E. coli* compared to *S. aureus* and *B. subtilis* (**Table 3.1.3.**).

Furthermore, the growth kinetics study of all the four strains of bacteria treated with (Man-BSA)-PH-AuNCs revealed that at MIC there was growth arrest compared to the control bacteria (**Figure 3.1.9. A-D**). In a typical bacterial batch culture, there five different stages. First comes the lag phase, which is a delay just before the multiplication. This is followed by exponential phase when bacterial cells multiply constantly. In the stationary phase, multiplication ceases because of unfavourable conditions. Finally, in the death phase cells lose their viability followed by long term stationary phase that can stretch for years. Bacteria can lie dormant in this stage for years before conditions become favourable again for growth. Understanding the pattern of growth phase arrest is crucial in deciphering the mechanistic path of (Man-BSA)-PH-AuNCs.

To confirm the same, lipid content detection assay was performed. Since Gram-negative bacteria like *P. aeruginosa* and *E. coli* are known to have an outer membrane rich in lipid content, [218] this study was performed only in the above mentioned strains' planktonic and biofilm forms. The Nile red fluorescence intensity was found to be the highest for control bacteria (**Figure 3.1.9. E, F**), followed by promethazine treated and then (Man-BSA)-PH-AuNCs treated bacteria. The confocal microscopy images **(Figure 3.1.10. A (I-II), C(I-II))** of control bacteria in both strains had visibly higher fluorescence than the (Man-BSA)-PH-AuNCs treated bacteria (**Figure 3.1.10. B (I-II), D(I-II**)).

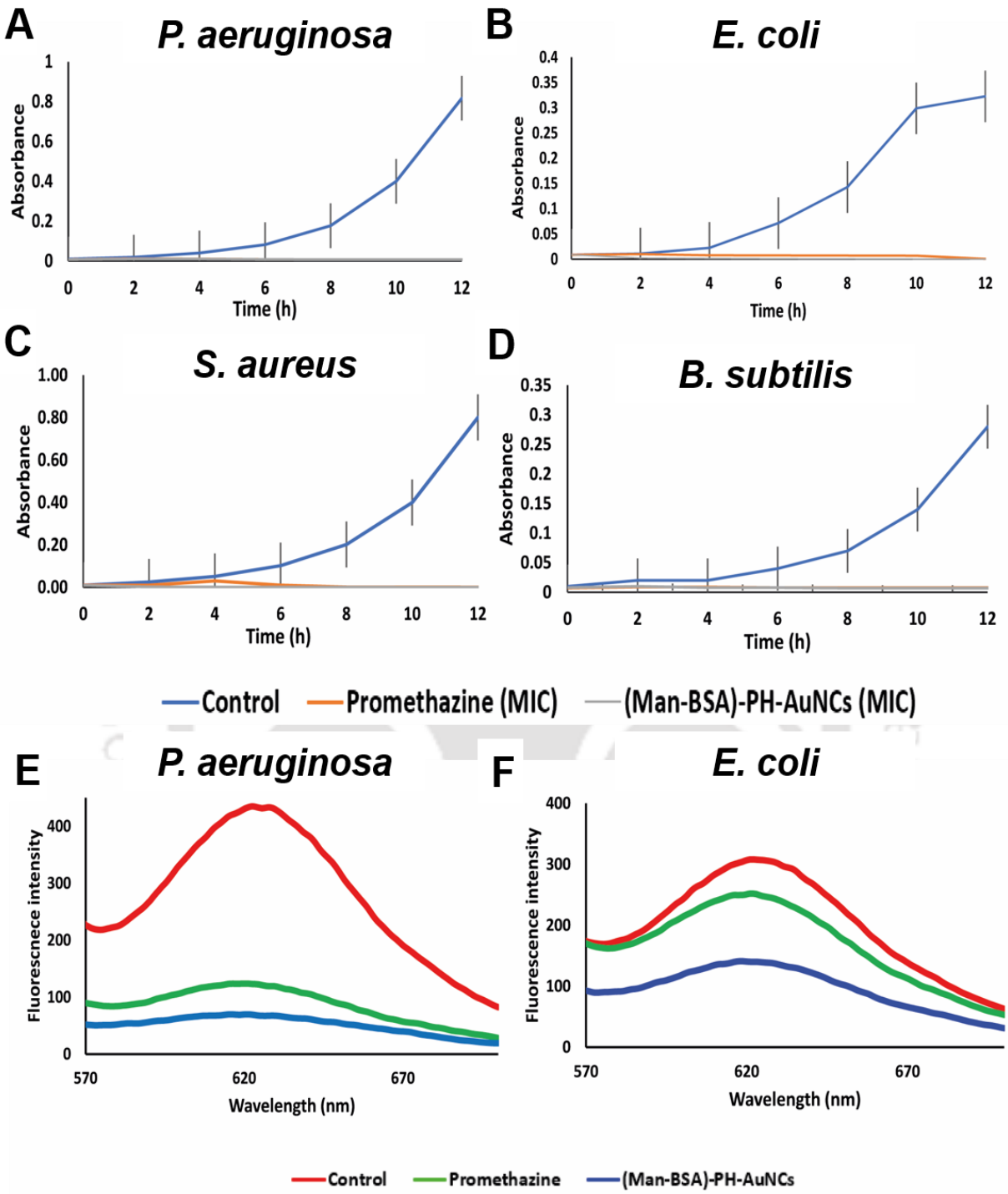

Figure 3.1.9. Growth kinetics curve showing the effect of free promethazine (MIC) and (Man-BSA)-PH-AuNCs (MIC) treated (A) *P. aeruginosa*, (B) *E. coli*, (C) *S. aureus* and (D) *B. subtilis* compared to untreated bacteria by measuring absorbance at 595 nm every two hours for 12 hours. Lipid content detection in (E) *P. aeruginosa* and (F) *E. coli* control and treated planktonic bacteria with free promethazine and (Man-BSA)-PH-AuNCs through fluorescence intensity measurement at 570-700 nm.

3.1.4. Mechanism of anti-bacterial activity. To decipher the effect of (Man-BSA)-PH-AuNCs on bacterial membrane permeability, a leakage study was performed. The increase in the absorbance values **(Figure 3.1.11.)** at 260 and 280 nm of (Man-BSA)-PH-AuNCs and promethazine- treated bacteria compared to untreated bacteria is an indication of membrane damage. Due to this, cellular components like protein and genetic material leaks out of the cells and seeps into the media which gives the higher absorbance.

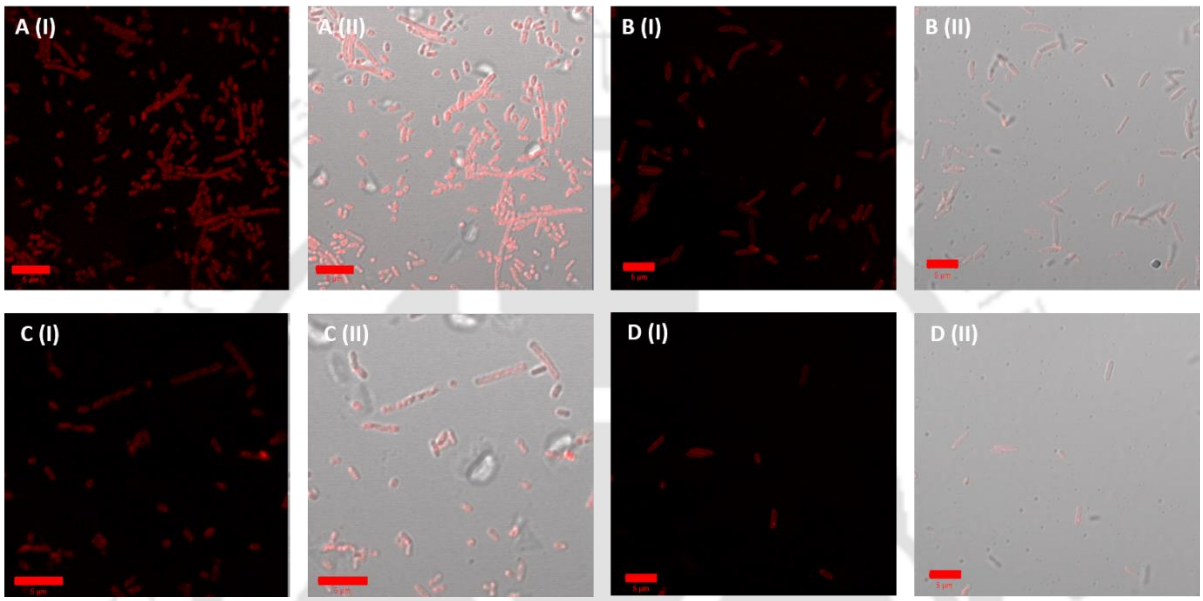

Figure 3.1.10. Confocal microscopy images of Nile red-stained planktonic bacteria for lipid content detection. [A (I-II)] control *P. aeruginosa*: [A(I) Nile red stained, A(II) merged image] and [B(I-II)] (Man-BSA)-PH-AuNCs treated *P. aeruginosa*: [B(I) Nile red stained, B(II) merged image]. [C (I-II)] control *E. coli*: [C(I) Nile red stained, C(II) merged image] and [D(I-II)] (Man-BSA)-PH-AuNCs treated *E, coli*: [D(I) Nile red stained, D(II) merged image]. The images were taken at a scale bar of 5µm.

At sub-MIC concentrations, phenothiazine class of drugs depolarise the membrane and increase its permeability and fluidity.[219] This may lead to changes in the cellular structure and inner and outer membrane-bound protein functionality.[220] The possession of certain surfactant like characters, owing to a tertiary amino group and a bulky aromatic structure could be linked to their membrane altering effects.[221] However, the increase in leakage of (Man-BSA)-PH-AuNCs treated bacteria compared to free promethazine can be attributed to the combinatorial effects of promethazine and gold nanoclusters[222,223] delivered through a nanocarrier.

Furthermore, the results of the leakage study can also be corelated with the morphological study of the treated bacteria through field emission scanning electron microscopy (FESEM). While control bacteria (**A**- *P. aeruginosa*, **C**- *E. coli*, **E**- *S. aureus* and **G**- *B. subtilis*) had smoother and intact morphology, the treated bacteria (**B**- *P. aeruginosa*, **D**- *E. coli*, **F**- *S. aureus* and **H**- *B. subtilis*) appeared smaller and with a disrupted cell membrane (**Figure 3.1.12.**). This further confirmed the anti-bacterial effect of (Man-BSA)-PH-AuNCs via membrane permeability alteration.

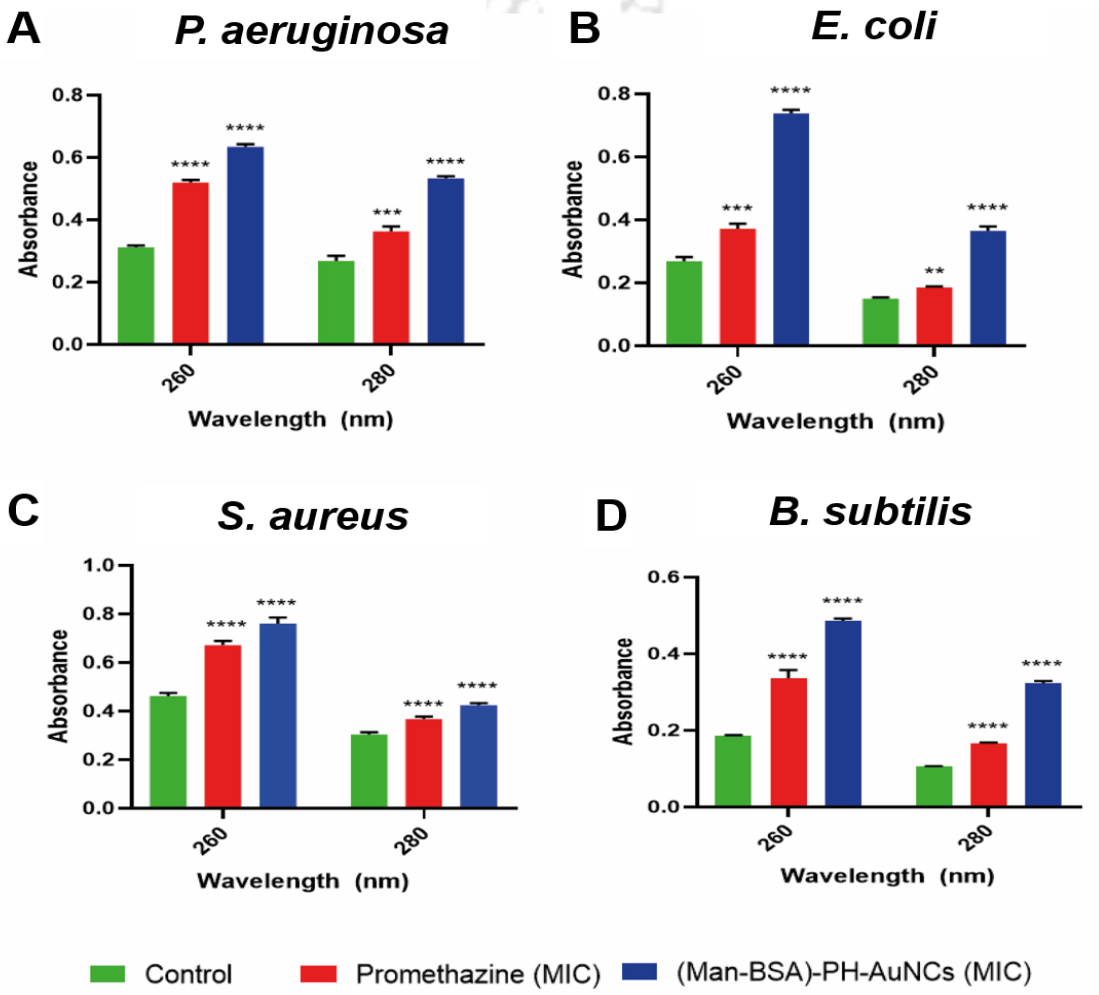

Figure 3.1.11. Leakage of UV absorbing materials (at 260 nm and 280 nm) from untreated vs. promethazine-treated and (Man-BSA)-PH-AuNCs -treated bacterial cells. (A) *P. aeruginosa*, (B) *E. coli*, (C) *S. aureus* and (D) *B. subtilis*.

3.1.5. Generation of reactive oxygen species (ROS). To determine whether treatment with the as-synthesized (Man-BSA)-PH-AuNCs generated reactive oxygen species (ROS) in bacteria, 2′,7′-dichlorofluorescein diacetate (DCFDA) dye, a cell permeable non-fluorescent

precursor of DCF was used for its detection. Endogenously cells produce ROS, which eventually is converted to hydrogen peroxide through superoxide dismutases and catalases.[224]

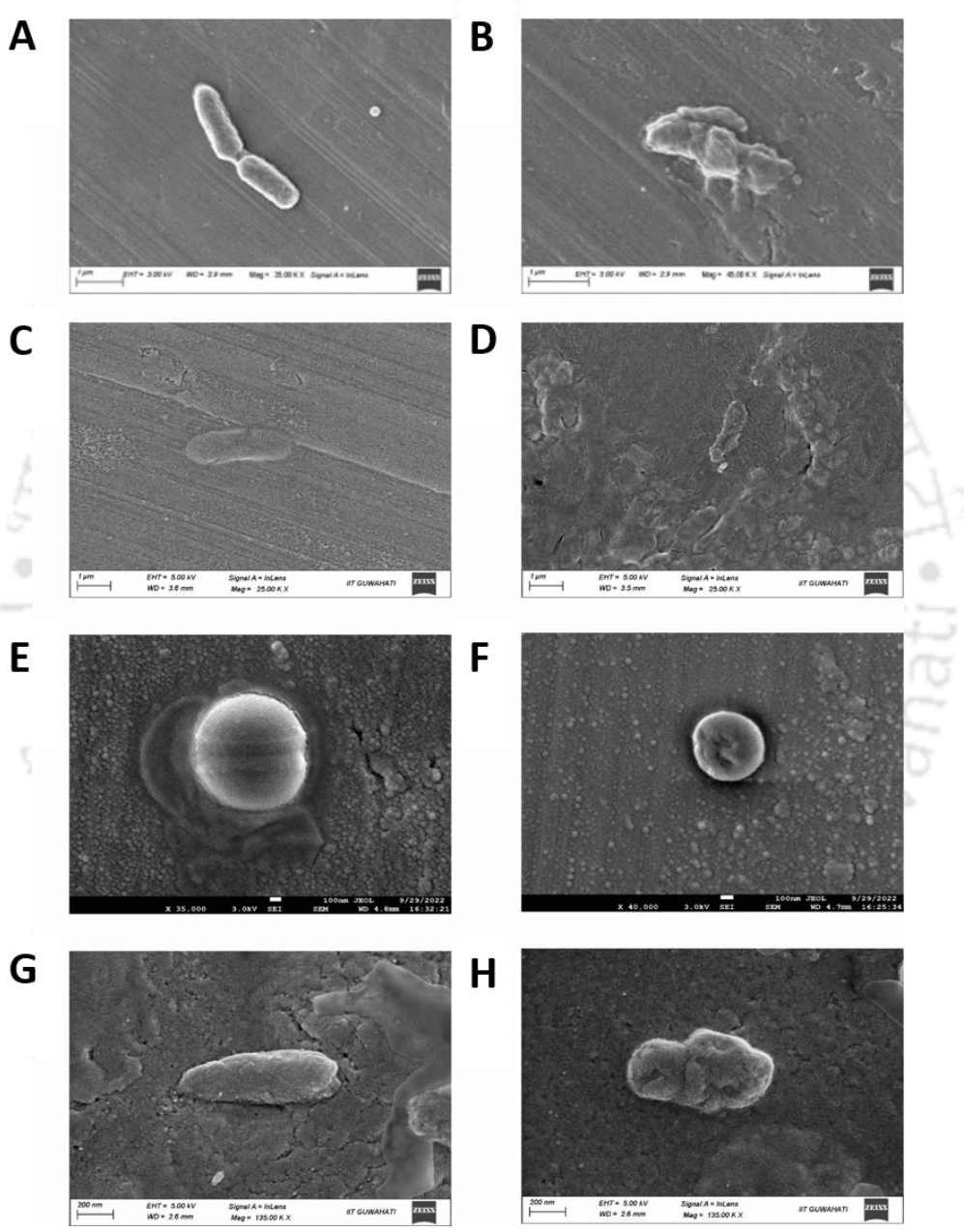

Figure 3.1.12. Field emission scanning electron microscopy images of untreated and treated bacteria. A-B: Untreated and treated *P. aeruginosa* (Scale -1 µm). C-D: Untreated and treated *E. coli* (Scale -1 µm). E-F: Untreated and treated *S. aureus* (Scale -100 nm). G-H: Untreated and treated *B. subtilis* (Scale -200 nm).

However, under stress such as hypoxia, there can be excessive ROS accumulation. This may damage proteins, DNA and intracellular systems such as respiratory systems.

Initially, through spectrophotometry fluorescence was quantified in treated vs. untreated bacteria. The intensity of fluorescence is directly proportional to the amount of oxidised DCFH-DA to DCF. Intracellular esterases can cleave DCFH-DA at its two ester bonds and produce H_2DCF. The subsequent oxidation of this accumulated product yields the highly fluorescent DCF. It was observed that upon treatment, there was a significant increase in fluorescence intensity at 523 nm compared to the untreated bacteria (**Figure 3.1.13.**).

The suggestive production of ROS in treated bacteria may be attributed to a combination of factors. First, AuNCs in the as-synthesized (Man-BSA)-PH-AuNCs are known to cause oxidative stress in bacterial cells.[225] This may be because even though bulk gold is chemically

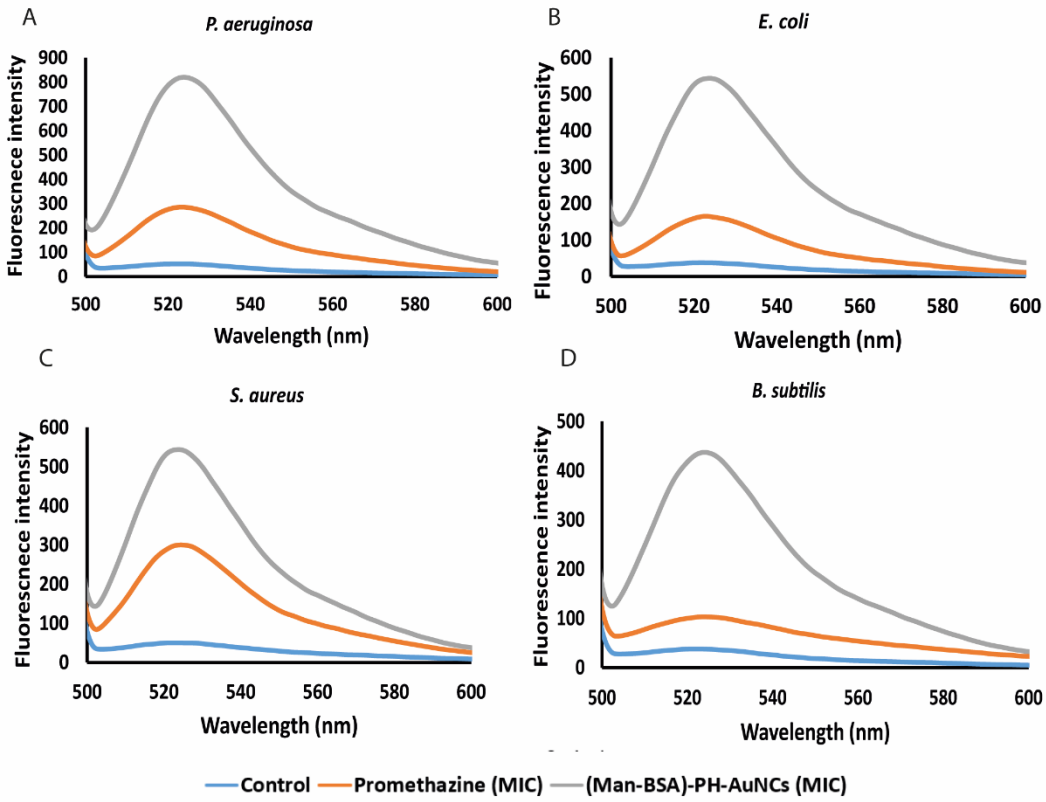

Figure 3.1.13. Formation of ROS in (Man-BSA)-PH-AuNC treated, promethazine-treated and untreated (control) bacterial cells: (A) *P. aeruginosa*, (B) *E. coli*, (C) *S. aureus* and (D) *B. subtilis*. The intensity of fluorescence is directly proportional to the amount of oxidised DCFH-DA to DCF by intracellular esterases. Fluorescence was detected at an excitation filter of 485 nm and emission filter of 523 nm.

inactive, the ultrasmall gold nanoclusters undergo a drastic change in their physical and chemical properties. Secondly, studies show that phenothiazine derivatives like Methylene blue can inhibit bacteria via photodynamic inactivation.[226] Promethazine being a member of the same chemical class may also have functioned in a similar manner once inside the cell. Hence, the treatment may have caused intracellular imbalance, leading to ROS generation and subsequent bacterial inhibition.

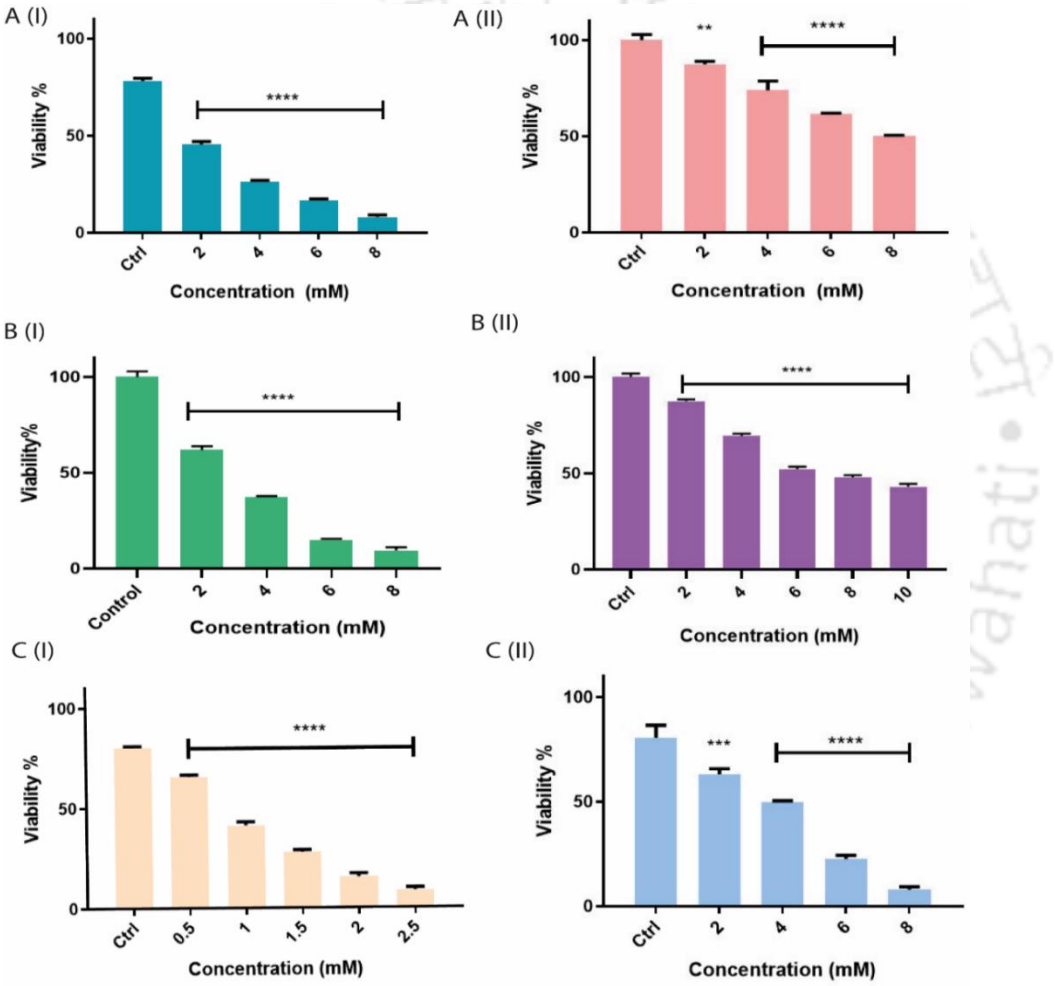

Figure 3.1.14. Antibiofilm activity of free promethazine and (Man-BSA)-PH-AuNCs in A- *P. aeruginosa* and B- *S. aureus*. A(I)- free promethazine treated and A(II)- (Man-BSA)-PH-AuNC treated *P. aeruginosa* biofilm. B(I)- free promethazine treated and B(II)- (Man-BSA)-PH-AuNC treated *E. coli* biofilm. C(I)- free promethazine treated and C(II)- (Man-BSA)-PH-AuNC treated *S. aureus* biofilm. The ANOVA test revealed statistical significance of free promethazine and (Man-BSA)-PH-AuNC treated biofilms with respect to control ones. Statistical significance is denoted by * ($p < 0.05$), ** ($p < 0.005$), *** ($p < 0.001$), and **** ($p < 0.0001$). The data are represented as mean ± SD of three individual experiments.

3.1.6. Inhibition of bacterial biofilm. Following the determination of bactericidal activity of (Man-BSA)-PH-AuNCs, it was utilised against bacterial biofilms. These well-structured communities of adherent bacterial cells are enclosed in a self-produced extracellular polysaccharide matrix (EPS).[227] Biofilms are known to pose a serious threat to life forms through nosocomial infections[228] related to medical implants[228] and chronic infections like cystic fibrosis.[229] Gram-negative bacteria like *P. aeruginosa* can arm themselves with biofilm formation to survive in hostile environments.[230] Similarly, Gram-positive *S. aureus* are also known to form biofilms on animate and inanimate surfaces, thus posing complications which is rapidly becoming a case of concern.[231] The antibiofilm studies carried out on *P. aeruginosa*, *E. coli* and *S. aureus* confirmed 50% inhibition ($MBIC_{50}$) by (Man-BSA)-PH-AuNCs at a concentration of 8 mM, 6.9 mM and 4.2 mM, respectively (**Figure 3.1.14. A-C (II)**). The same study carried out with only free promethazine hydrochloride inhibited 50% of the biofilms at 2.8 mM, 2.9 mM and 1.4 mM, respectively (**Figure 3.1.14. A-C (I)**). Altogether, these results were found to be in coherence with studies on planktonic bacteria.

3.1.7. Staining of biofilms. The AO/PI dual staining study revealed that the (Man-BSA)-PH-AuNCs could successfully reduce the biofilm mass in case of both Gram-negative *P. aeruginosa* and *E. coli*, and Gram-positive *S. aureus*. AO could permeate the control cells and they emitted green fluorescence (**Figure 3.1.15. A-C:(I-III)**).

The emission of red fluorescence due to PI was negligible in control biofilms of both *P. aeruginosa* and *S. aureus*, possibly because of the smaller number of dead cells. In case of biofilm treated with sub-$MBIC_{50}$ (**Figure 3.1.15 A-C:(IV-VI)**) and $MBIC_{50}$ of (Man-BSA)-PH-AuNCs (**Figure 3.1.15 A-C:(VII-IX)**), a prominent red fluorescence was observed that increased with the increase in concentration of composite. The red fluorescence is a result of penetration of PI dye through the damaged bacterial membrane. The green fluorescence emitted from live cells was very limited at the highest treatment concentration. For comparison, *P. aeruginosa* and *S. aureus* biofilms were also treated with $MBIC_{50}$ concentration of free promethazine (**Figure 3.1.16. A-C**). The as synthesised (Man-BSA)-PH-AuNC antibiofilm activity was further characterised through confocal microscopy where Nile red dye was used to study the lipid content in Gram-negative bacterial biofilm. (**Figure 3.1.17.**). In case of the control biofilm, the confocal microscopy images revealed higher lipid content over the entire individual well in a 96-well plate emitting a higher red fluorescence (**Figure 3.1.17.** A-B: (I-

II)). However, upon treatment with sub-$MBIC_{50}$ (**Figure 3.1.17.** A-B: (III-IV)) and $MBIC_{50}$ of (Man-BSA)-PH-AuNCs (**Figure 3.1.17.** A-B: (V-VI)), there was a concomitant reduction in red fluorescence with fragments of degraded biofilm visible in the bright-field and merged images. This suggested the successful inhibition of biofilm mass as indicated by the diminished

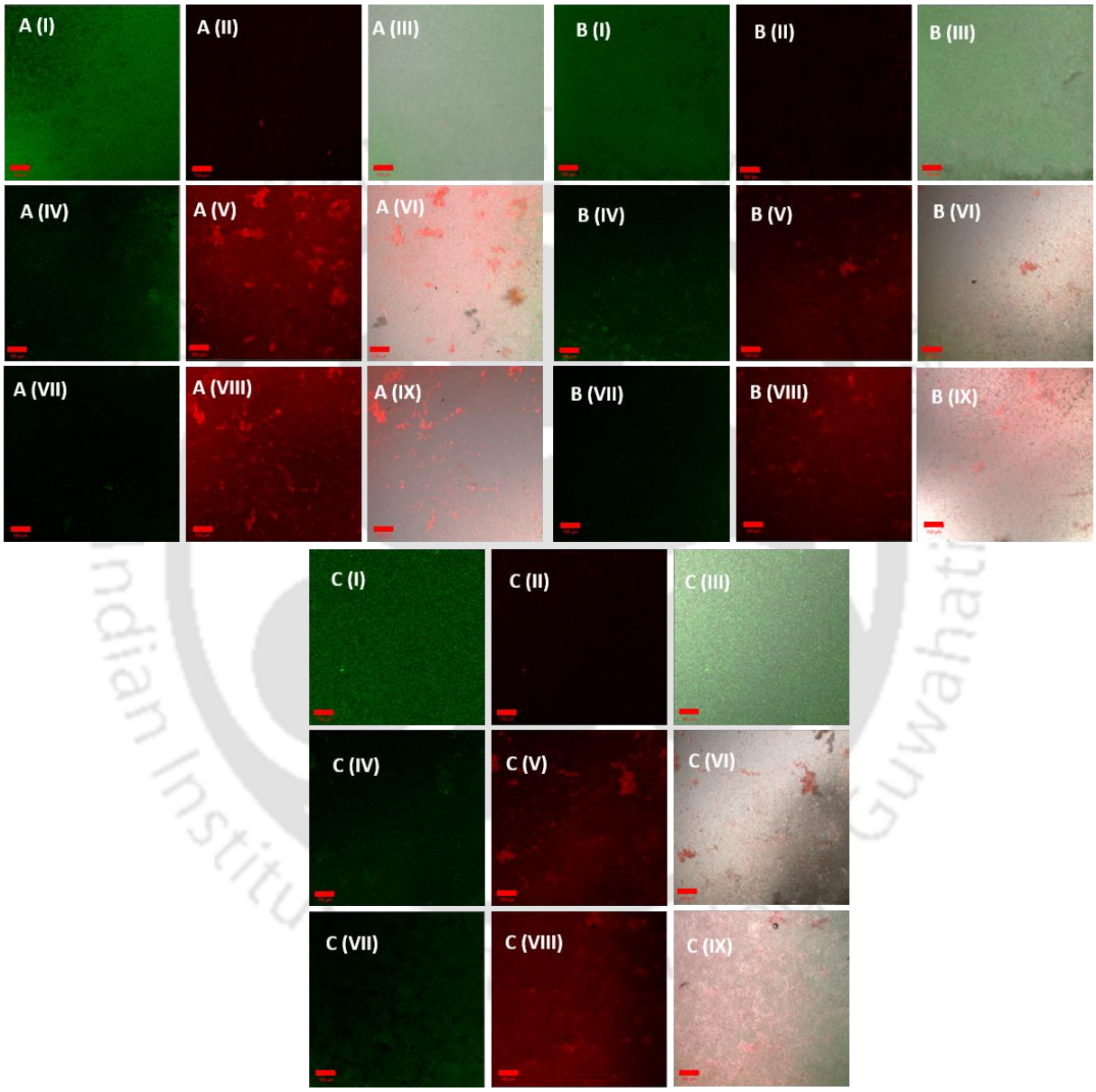

Figure 3.1.15. Live/dead confocal microscopy images of AO/PI-stained bacterial biofilm: A- *P. aeruginosa*; B- *E. coli* and C- *S. aureus*. [A (I-III)], [B(1-III)], [C(I-III)] control: [A/B/C(I) AO stained, A/B/C (II) PI-stained, A/B/C(III) merged image]. [A(IV-VI)], [B(IV-VI)], [C(IV-VI)] sub-$MBIC_{50}$ of (Man-BSA)-PH-AuNC treated biofilm: [A/B/C(IV) AO stained, A/B/C(V) PI-stained, A/B/C(VI) merged image]. [A(VII-IX), B(VII-IX)], C(VII-IX)] $MBIC_{50}$ of (Man-BSA)-PH-AuNCs treated biofilm: [A/B/C(VII) AO stained, A/B/C(VIII) PI-stained, A/B/C(IX) merged image]. The images were taken at a scale bar of 100 µm.

lipid content. The confocal mages of $MBIC_{50}$ of promethazine treated and Nile red-stained biofilms are also added in the supporting information (**Figure 3.1.16. D, E**).

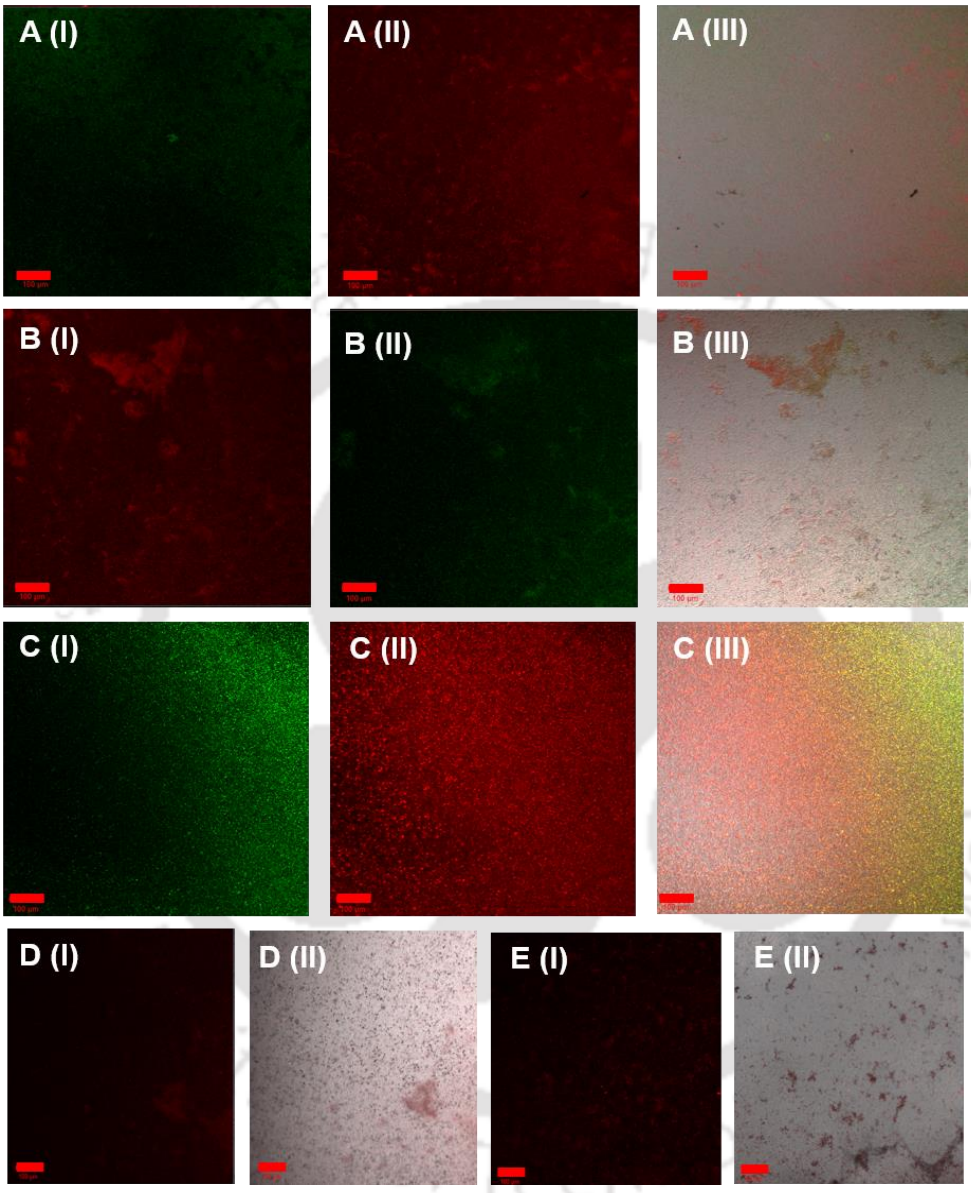

Figure 3.1.16. Confocal microscopy images of AO/PI-stained and Nile-red stained bacterial biofilm: A, D- *P. aeruginosa*; B, E- *E. coli*; C- *S. aureus*. [A (I-III)] $MBIC_{50}$ of free promethazine treated *P. aeruginosa* biofilm: [A(I) AO stained, A(II) PI-stained, A(III) merged image]. [B(I-III)] $MBIC_{50}$ of free promethazine treated *E. coli* biofilm: [B(I) AO stained, B(II) PI-stained, B(III) merged image]. [C(I-III)] $MBIC_{50}$ of free promethazine treated *S. aureus* biofilm: [B(I) AO stained, B(II) PI-stained, B(III) merged image]. [D (I-II)] $MBIC_{50}$ of free promethazine treated *P. aeruginosa* biofilm: [D(I) Nile red-stained, D(II) merged image]. [E(I-II)] $MBIC_{50}$ of free promethazine treated *E. coli* biofilm: [E(I) Nile red-stained, E(II) merged image]. The images were taken at a scale bar of 100 µm.

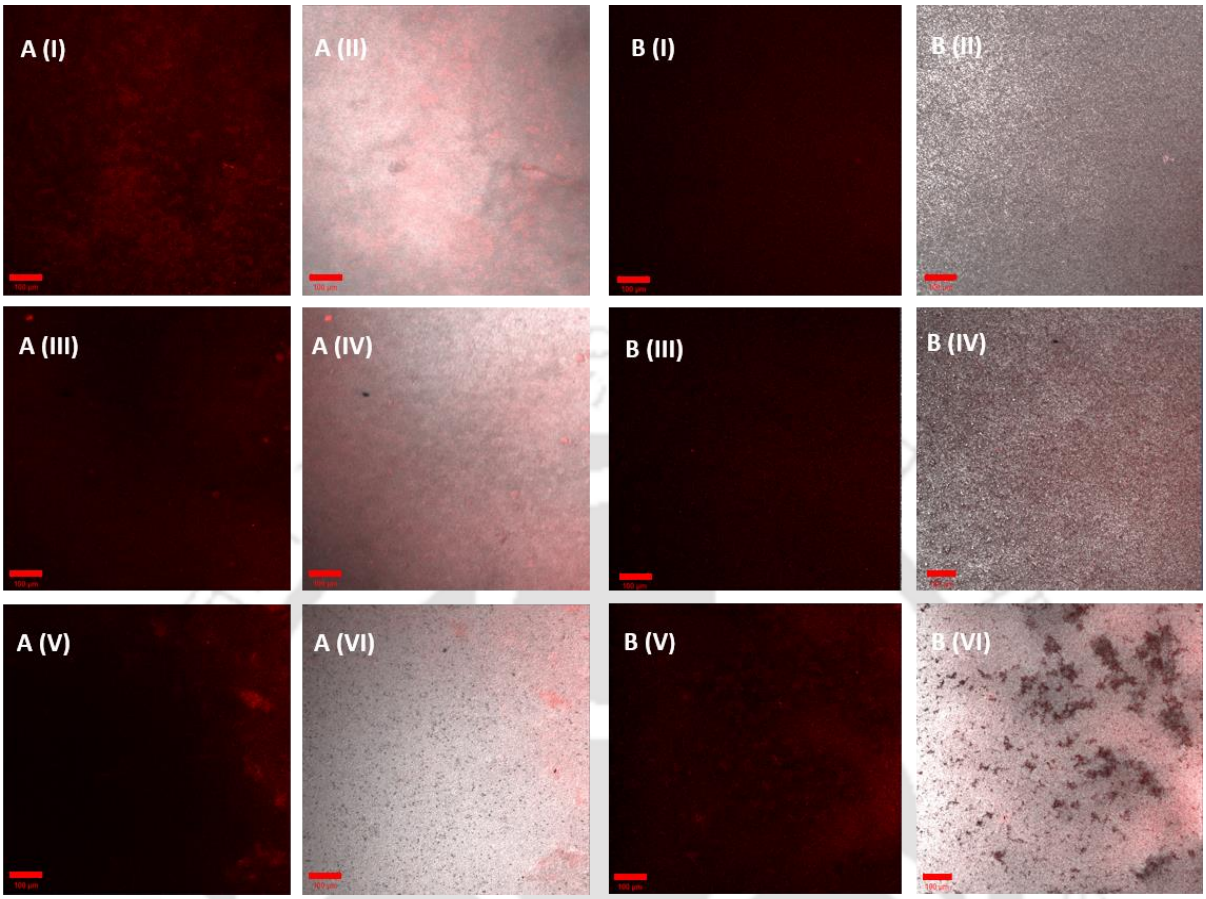

Figure 3.1.17. Confocal microscopy images of Nile red-stained bacterial biofilm for lipid content detection. A- *P. aeruginosa*, B- *E. coli*. [A (I-II)] control *P. aeruginosa*: [A(I) Nile red-stained; A(II) merged image]. [A(III-IV)] sub-$MBIC_{50}$ of (Man-BSA)-PH-AuNCs treated *biofilm*: [A(III) Nile red-stained, A(IV) merged image]. [A(V-VI)] $MBIC_{50}$ of (Man-BSA)-PH-AuNCs treated biofilm: [A(V) Nile red-stained, A(VI) merged image]. [B (I-II)] control *E. coli*: [B(I) Nile red-stained, B(II) merged image]. [A(III-IV)] sub-$MBIC_{50}$ of (Man-BSA)-PH-AuNC treated *biofilm*: [B(III) Nile red-stained, B(IV) merged image]. [B(V-VI)] $MBIC_{50}$ of (Man-BSA)-PH-AuNCs treated biofilm: [B(V) Nile red-stained, B(VI) merged image]. The images were taken at a scale bar of 100 µm.

3.1.8. Summary

With increasing resistance towards common antibiotics, infectious diseases are predominantly becoming an impossible wall to break. Towards exploring alternate options, an antihistamine drug promethazine was repurposed for potential activity against Gram-negative, Gram-positive bacteria and their respective biofilms. A phenothiazine class of drugs, it is known to alter bacterial membrane permeability and intercalate into plasmids. Promethazine was successfully loaded onto mannosylated BSA stabilized gold nanoclusters for better stability, specificity, and

prolonged circulation time. The as-synthesized drug loaded clusters were nano-sized, luminescent, and stable in nature. Although promethazine has been known to affect the pili of Gram-negative *E. coli*, it was found to have superior activity against Gram-positive *S. aureus* and *B. subtilis,* possibly due to their lack of an outer membrane that allowed easy entry into the cells. The mannosylation of the gold nanoclusters helped in better targeting of the Gram-negative bacteria as well, especially *E. coli*. D-Mannose can also bind to the Gram-negative pili and inhibit them. Furthermore, the growth kinetics curve of all four strains of treated bacteria showed arrest. Upon treatment, the consequent drug release may have resulted in cell death following intracellular ROS generation and cell membrane damage. Additionally, the sustained release of promethazine from the nanoclusters also helped to inhibit bacterial biofilms of *P. aeruginosa*, *E. coli* and *S. aureus*. As promethazine is a clinically approved drug, its safety profile has been established. Drug delivery via carriers over free drugs have become the preferred approach lately.[232,233] Utilizing gold nanoclusters for the same is backed by their use in biomedical history. This also marks their biocompatibility and stability. Hence, with shorter timelines and reduced costs, the combination of drug repurposing and nanoscale delivery system indicates towards a translational validation. Overall, the findings reveal that the as-synthesized nanoclusters can act as effective drug delivery cargos that have significant therapeutic potential to battle antibiotic resistance.

3.2. Therapeutic targeting of lung adenocarcinoma with mannose-coated chitosan/Cu nanocluster-levocetirizine nanocomposite.

-***ACS Applied Nano Materials**, 2023*, **6** (22), 21371-21384
DOI: 10.1021/acsanm.3c04868
[ACS publishing group]

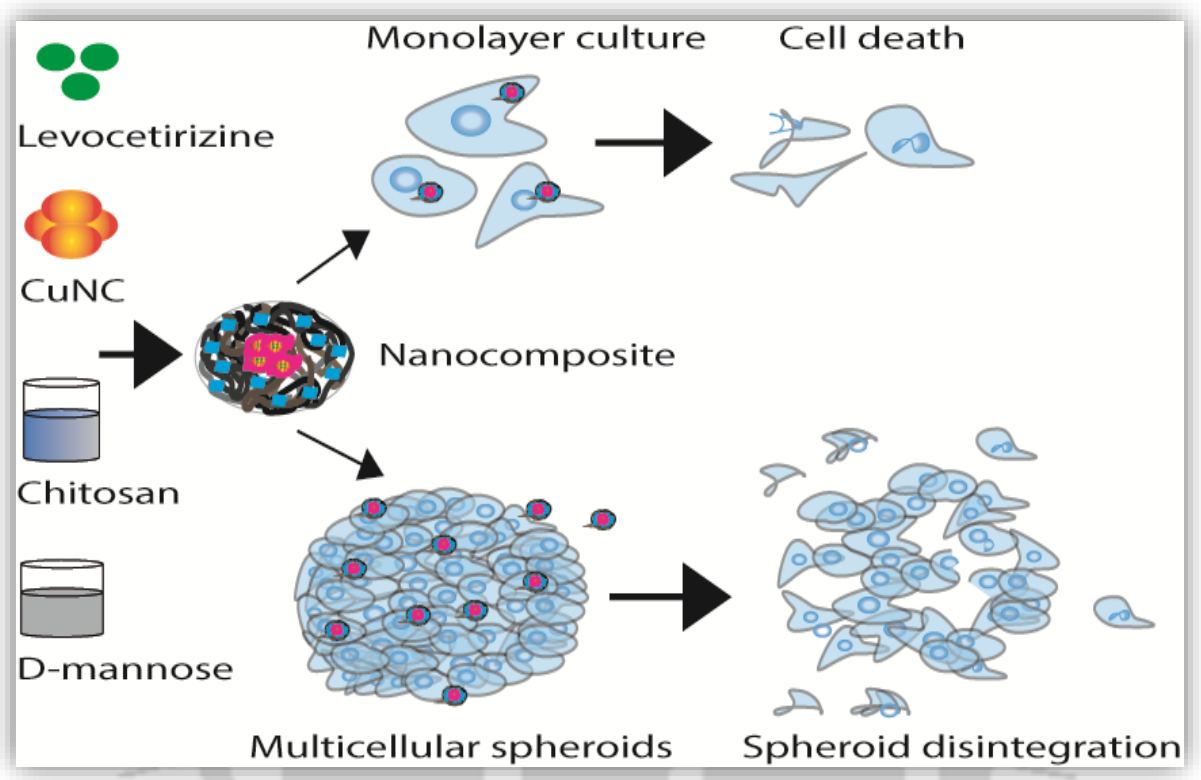

Scheme 3.2. Schematic demonstrating the application of nanocomposite in monolayer cells and spheroids of lung adenocarcinoma.

Results and Discussions

Abstract

Lung adenocarcinoma is regarded as the most common form of lung cancer as per the latest epidemiological data. The combined efforts from chemotherapy and radiotherapy have done little to increase survival rates. Thus, repurposing licensed drugs has become a feasible approach to fill such gaps. Copper nanoclusters were loaded with levocetirizine dihydrochloride, a common antihistamine. The subsequent levocetirizine loaded copper nanoclusters were loaded into mannose functionalised chitosan nanoparticles. This therapeutic module has been established to target lung adenocarcinoma cells in both monolayer and tumor spheroids. The nanocomposite was found to be inherently fluorescent, biocompatible and water-soluble. The drug release profile was found to be pH-dependent with maximum release in the acidic medium. Experimental results concluded efficient cellular localization followed by significant anti-proliferative activity. Subsequent functional assays revealed suggestive ROS generation, membrane potential depolarization, reduced lipid droplets leading up to apoptosis. A remarkable reduction in colony forming and migration capacity was also observed. A549 and HeLa spheroids were also inhibited effectively. Briefly, the as-synthesized nanocomposites showed promising scope as an anti-cancer treatment approach.

3.2.1. Characterisation of copper nanoclusters (CuNC) and levocetirizine loaded copper nanoclusters (CuNC-LH). The synthesis procedure of the nanocomposite and its individual

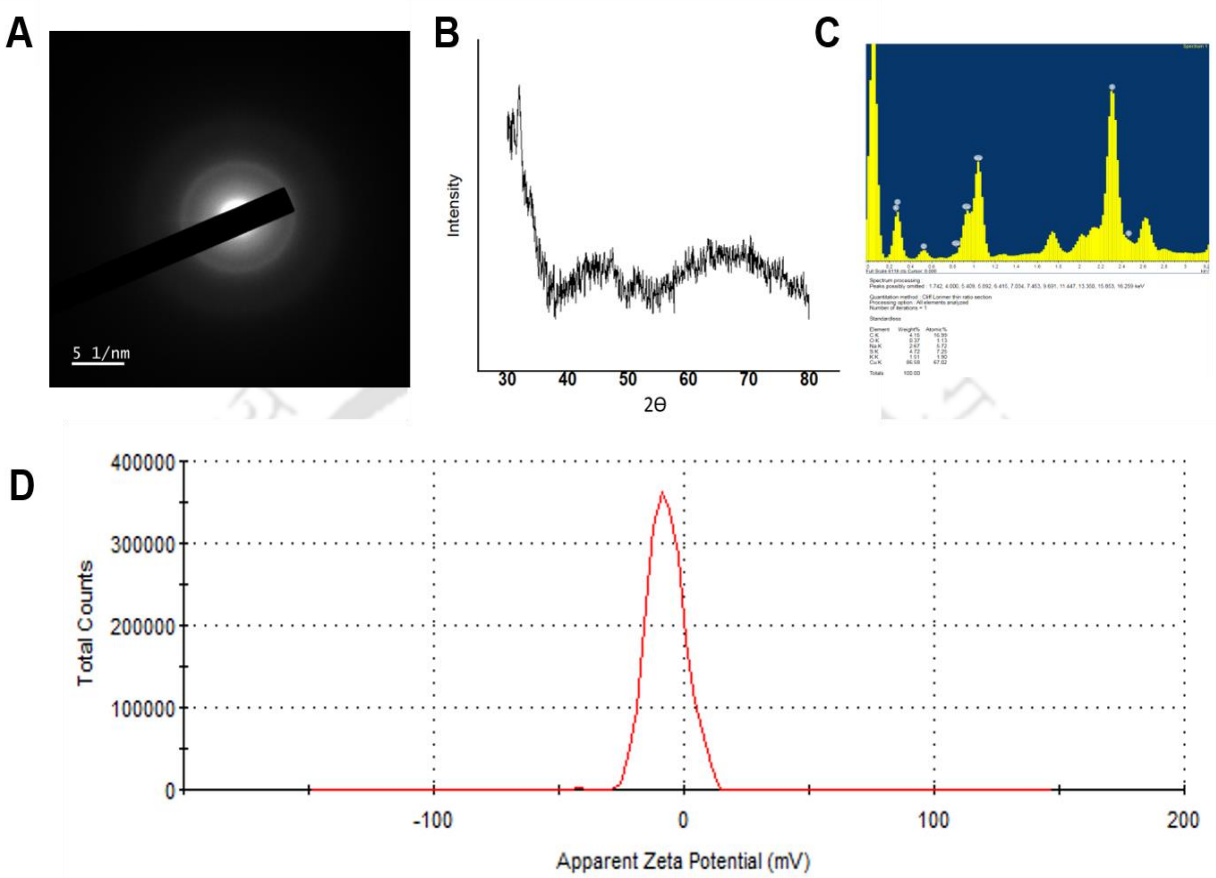

Figure 3.2.1. Characterisation of copper nanoclusters (CuNCs). (A) Selected area electron diffraction pattern (SAED). (B) X-ray diffraction plot (XRD). (C) Energy dispersive X-ray spectroscopy (EDX) analysis. (D) Zeta potential.

components has been illustrated in **Figure 2.1.** The as-synthesized CuNCs were transparent and deep red in colour. They fluoresced in the red region when illuminated under UV light (**Figure 3.2.2. A**). When excited (λ_{ex}) at 365 nm, an emission maximum (λ_{em}) at 648 nm was observed. Furthermore, images from transmission electron microscopy (TEM) revealed that the CuNCs had an average size of 2.5 $\pm$ 0.86 nm (**Figure 3.2.3. A**). Also, no significant selected area electron diffraction (SAED) pattern was observed (**Figure 3.2.1. A**); which further correlated with the XRD plot (**Figure 3.2.1. B**). The energy X-ray dispersive analysis (EDX) revealed the presence of 67.02 % copper in the nanoclusters (**Figure 3.2.1. C**). Finally, the Cu concentration in the CuNCs was found to be 13.8 µg/mL through atomic absorption

spectroscopy (**Figure 3.2.2. B**). For comparison, copper nanoclusters loaded levocetirizine (CuNC-LH) were synthesized and their average size was found to be 3 ± 0.8 nm (**Figure 3.2.3. B**). The comparison of UV-Vis spectra of CuNC, LH and CuNC-LH confirmed the successful incorporation of levocetirizine in the nanoclusters (**Figure 3.2.2. C**). The loading efficiency of levocetirizine was found to be 55.5 % and consecutively the final concentration totalled to 13.8 mM. Following loading, the CuNC-LH, remained transparent but light reddish in colour while also fluorescing in the red region (**Figure 3.2.2. A**).

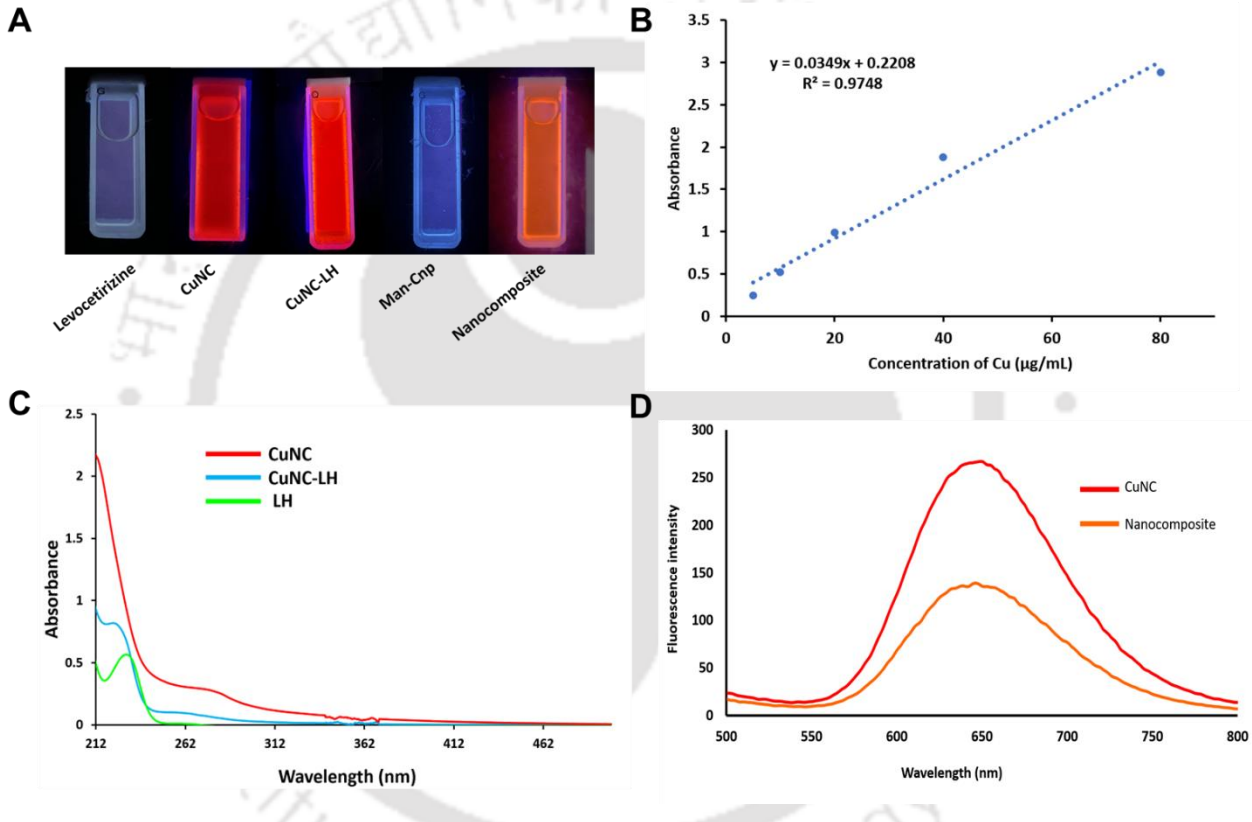

Figure 3.2.2. (A) Individual components of the nanocluster and nanocomposite under UV transilluminator. (B) Concentration of Cu in the CuNCs as obtained from the atomic absorption spectroscopy. (C) UV-Vis spectra of CuNC, LH and CuNC-LH. (D) Fluorescence intensity of CuNC and nanocomposite upon excitation at 365 nm. The peaks are at 648 nm for CuNC and 647 nm for nanocomposite, respectively.

3.2.2. Characterisation of man-chitosan nanoparticles (man-Cnp). The nanoparticles were synthesized via ionic gelation technique wherein the cations of chitosan crosslink with the polyanions of STPP. When STPP is added dropwise to the chitosan solution, the polyanions bind to the amino groups through electrostatic interaction causing the chitosan to undergo a gel ionization process. TEM images revealed that the average size of the chitosan

nanoparticles were 95.8 ± 12.6 nm (**Figure 3.2.3. C**); whereas that of man-chitosan nanoparticles was 102.7 ± 15.4 nm (**Figure 3.2.3. D**). A thin halo was observed along the circumference of the nanoparticles, which could be an indication of the mannosylation of chitosan.

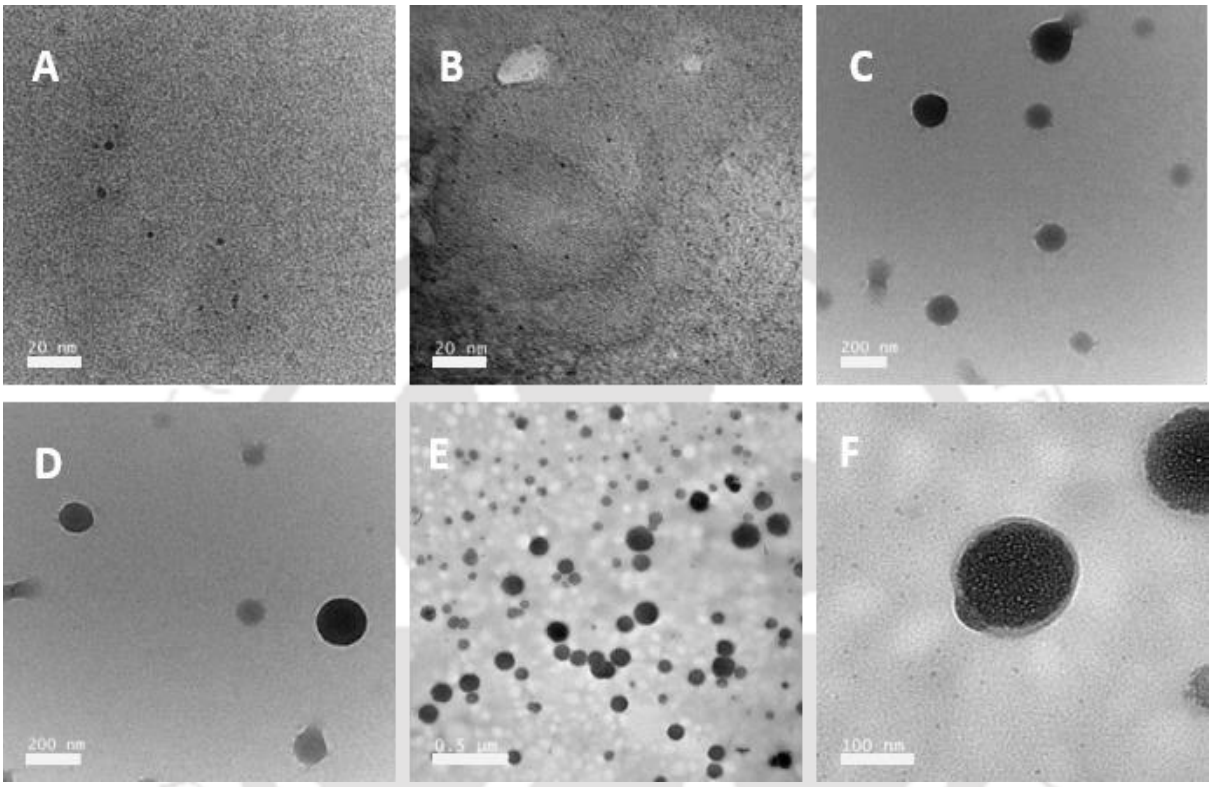

Figure 3.2.3. Transmission electron microscopy images of (A) copper nanoclusters (CuNC at 20 nm scale); (B) levocetirizine loaded copper nanoclusters (CuNC-LH at 20 nm scale); (C) chitosan nanoparticles (Cnp at 200 nm scale); (D) mannosylated chitosan nanoparticles with thin halos (man-Cnp at 200 nm); (E) nanocomposite (0.5 µm scale) and (F) nanocomposite showing loaded CuNC-LH as tiny dots (100 nm scale).

3.2.3. Characterisation of the nanocomposites. The as-synthesized nanocomposite was semi-transparent and orangish in colour (**Figure 3.2.2. A**). A similar luminescence peak was observed around 650 nm, when they were excited at 365 nm confirming the successful incorporation of CuNC-LH (**Figure 3.2.2. D**). TEM images also revealed tiny dotted structures within the nanocomposite as an indication of CuNC-LH loaded core (**Figure 3.2.3. E, F**). Through size distribution curve, the average size of the nanocomposite was found to be 107 ± 1.3 nm (**Figure 3.2.4. A**). DLS analysis revealed the hydrodynamic size of the nanocomposites to be 265.8 nm (**Figure 3.2.4. C**). Furthermore, the presence of copper was also confirmed through energy dispersive X-ray spectroscopy (EDX)

analysis (**Figure 3.2.4. B**). The percentage particle yield for man-chitosan and nanocomposites was found to be 77.9% and 74 % (**Figure 3.2.5. A, B, C**). In addition, the release kinetics of levocetirizine was studied for a period of 72 h (**Figure 3.2.5. E**), that revealed a pH-dependent pattern. It has been demonstrated both *in vivo* and *in vitro* that polymeric nanoparticles undergo degradation by hydrolysis or biodegradation through cleavage of its backbone ester linkages into oligomers and, finally monomers; in this case into lactic acid and glycolic acid.[234,235] The degradation itself is the collective process of bulk diffusion, surface diffusion, bulk erosion and surface erosion.[236] Since there are many variables that influence the degradation process, the release rate pattern can be unpredictable. Moreover, at lower pH medium, there is a faster release of drugs including burst release, as demonstrated by many studies.[237] However, the

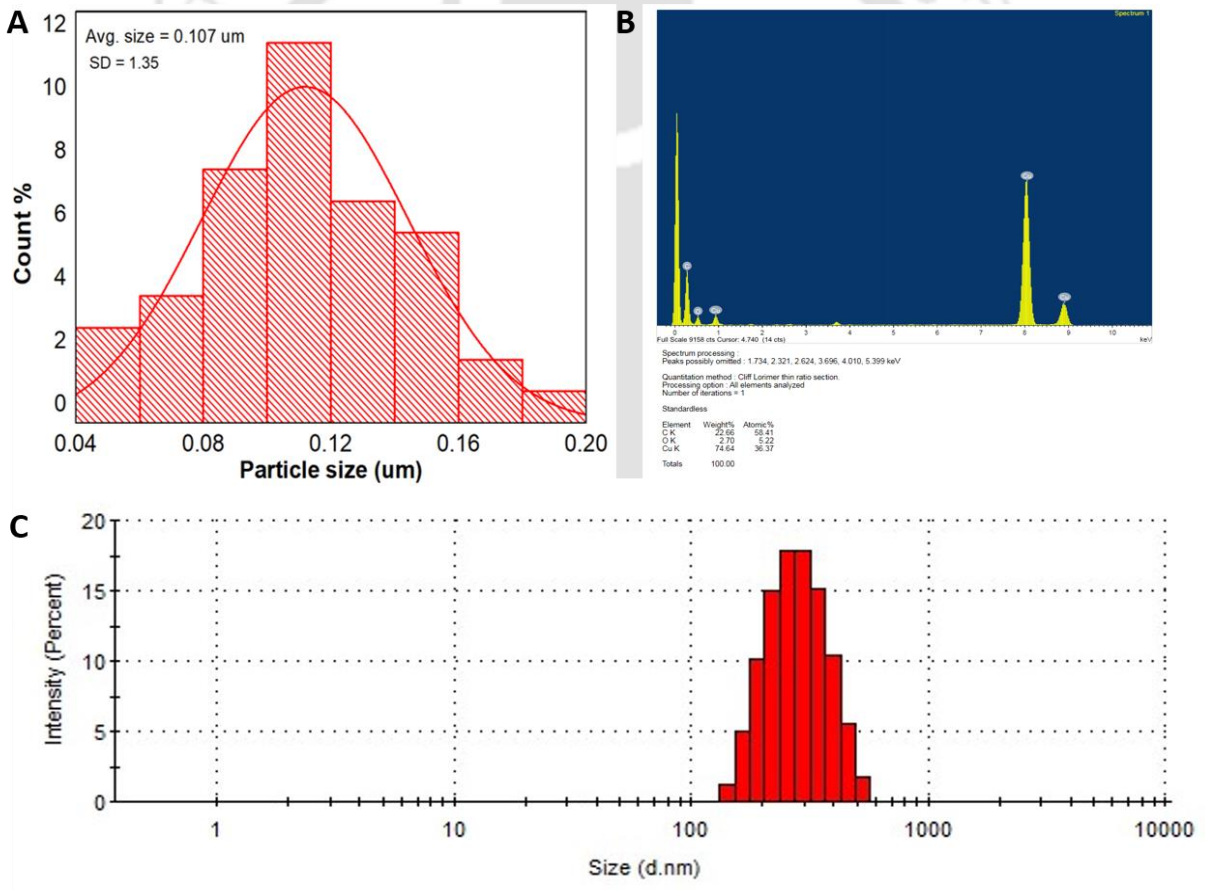

Figure 3.2.4. Characterisation of nanocomposite. (A) Size distribution curve of the nanocomposites. (B) EDX analysis plot of the nanocomposites. (C) DLS size distribution curve of nanocomposites.

overall pattern itself is biphasic in nature indicating that levocetirizine may have initially released via diffusion followed by bulk erosion.

3.2.4. Characterisation of mannose modified chitosan. Mannose modified chitosan was synthesized through reductive amination, following a previously reported protocol.[238] To confirm whether the modification was successful, the FTIR spectra of mannose, chitosan and

A

$$\text{Percentage yield} = \frac{\text{Weight of lyophilized final product (W1)} \times 100}{\text{Sum of initial dry weight of precursor material (W2)}}$$

B

Parameters	Values
W1	60 mg
W2	77 mg

C

Parameters	Values
W1	40 mg
W2	54 mg

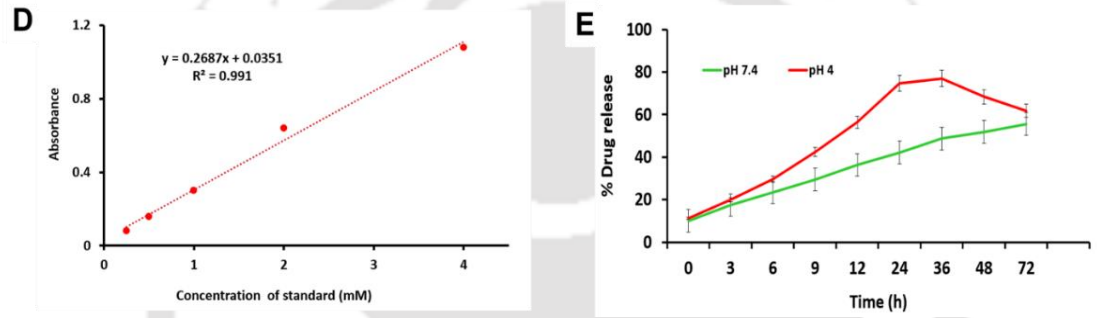

Figure 3.2.5. Determination of percentage yield. (A) Formula used for calculation. (B) Parameters for percentage yield calculation of man-chitosan. (C) Parameters for percentage yield calculation of nanocomposite. *(D)* Determination of mannose concentration in man-chitosan. (E) Release profile of levocetirizine dihydrochloride from the nanocomposite in acidic and neutral medium. In pH 4.0, a burst release of 76.9% was observed at 36th h. By the 72nd h, it had come down to 61.7%. In pH 7.4, the release pattern was slow and sustained reaching up to 55.5% at 72nd h.

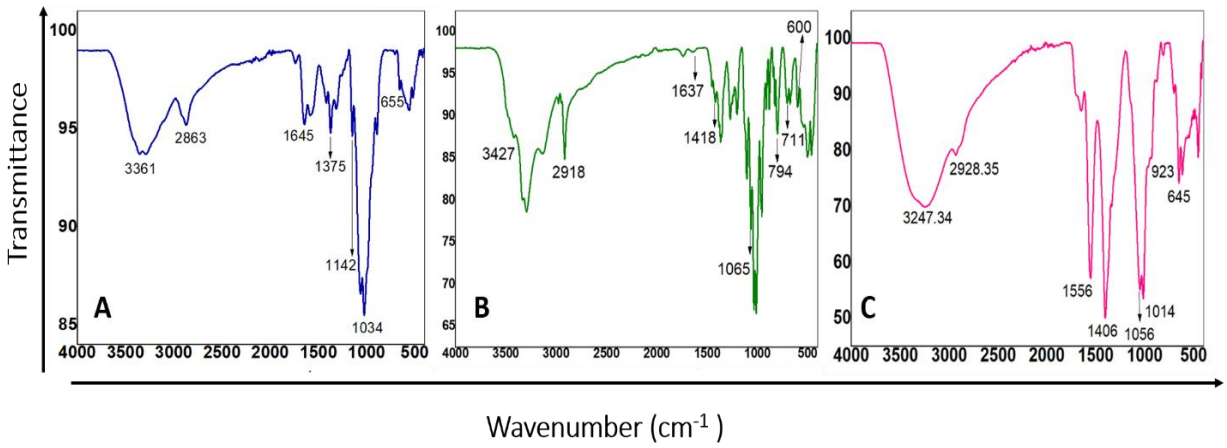

Figure 3.2.6. FTIR spectroscopy plots of (A) Mannose; (B) Chitosan and (C) Mannose conjugated chitosan (man-chitosan). Samples were scanned between wavenumber 4000–600 cm^{-1}.

man-chitosan in the 400-4000 cm^{-1} range were compared (**Figure 3.2.6.**). Man-chitosan contained all the characteristic peaks of chitosan. This included the broad peak between 3200 to 3600 $cm^{-1,}$ corresponding to hydroxyl and amino group stretching vibrations; and the characteristic methyl and methylene stretching vibrations at 2928.35 cm^{-1}. Another peak between 1500 to 1600 cm^{-1} confirmed C=O asymmetric stretching.

In addition, the peaks at 1056 cm^{-1} and 645 cm^{-1} represented characteristic vibrations similar to mannose. Thus, the coherence in the man-chitosan FTIR plot with that of mannose and chitosan was consistent with the successful synthesis of man-chitosan. Additionally, the concentration of mannose in man-chitosan determined by anthrone-based carbohydrate estimation, was found to be 0.57 mM (**Figure 3.2.5. D**).

3.2.5. Nanocomposites show significant anti-proliferative activity. Following the characterisation of nanocomposites and their individual components, cell culture studies were performed to determine their anti-proliferative activity. Cell viability assays on A549, HeLa and HEK-293 cells were performed and the results quantified as half maximal inhibitory concentration (IC_{50}). Monolayer cultures were treated with varying concentrations of the nanocomposite for 48 h. Comparatively, cells were also treated with the individual components of the nanocomposite. Results from this assay exhibited dose dependent decrease in cell viability in A549 (**Figure 3.2.7. J**), HeLa (**Figure 3.2.7. K**) and HEK-293 cells (**Figure 3.2.7. L**) with increase in drug concentration within the nanocomposite. While CuNC showed commendable cytotoxicity (**Figure 3.2.7. A-C**), cells treated with only levocetirizine (**Figure**

Table 6.2.1. Tabulation of IC_{50} values in monolayer cells and multicellular spheroids.

Cell line	CuNC (μM)	LH (μM)	Chitosan nanoparticles (μM)	Nanocomposite (μM)
Monolayer cells				
A549	2.59	-	-	31.05
HeLa	2.63	-	-	49.35
HEK-293	6.48	-	-	45.63
Multicellular spheroids				
A549	62.5	-	-	169.3
HeLa	65.04	-	-	256

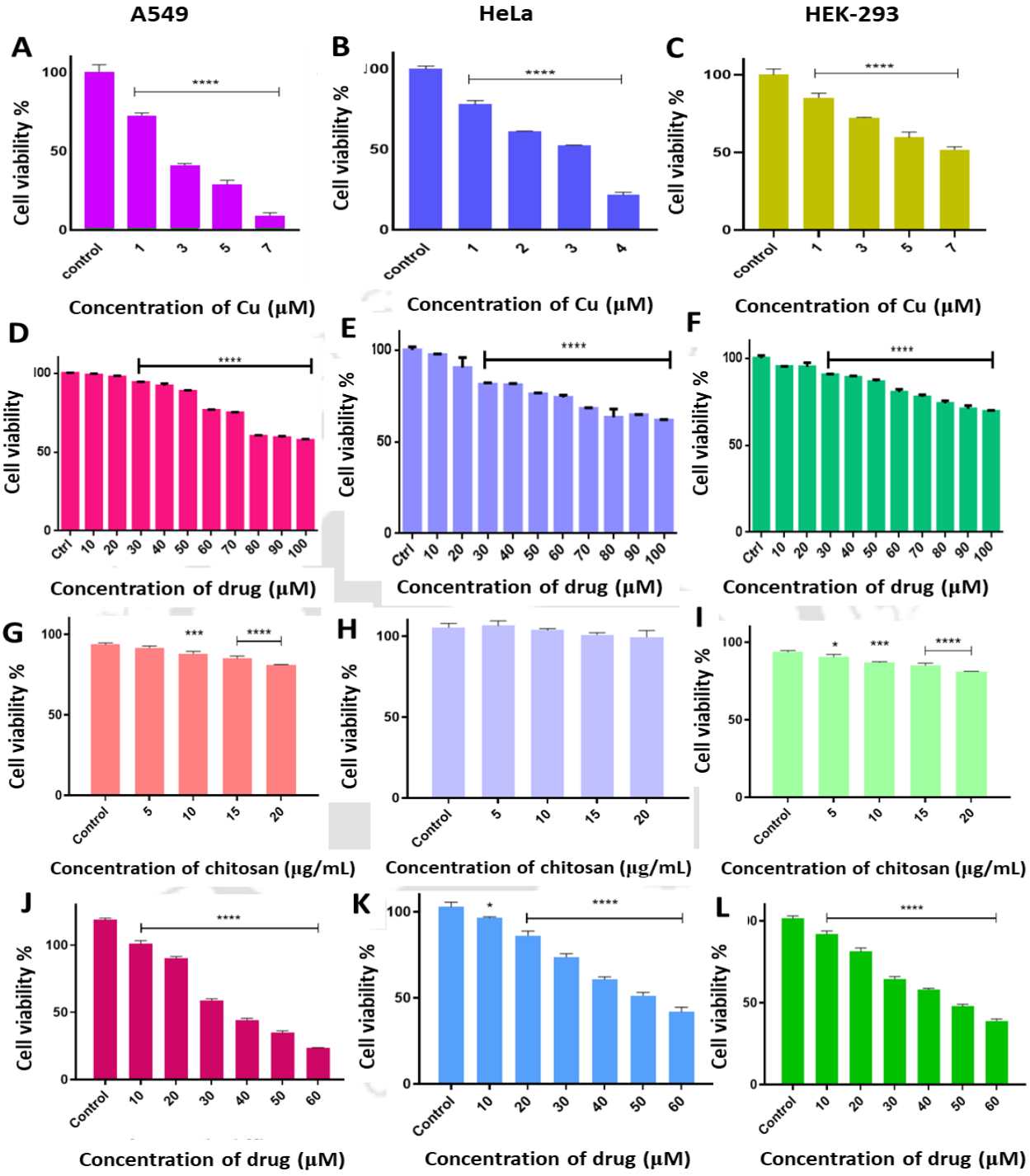

Figure 3.2.7. Graphical representation of decrease in cell viability following treatment in monolayer cells. Viability % is quantified as IC_{50} value. Cells were treated with the following: CuNC (A, B, C); levocetirizine dihydrochloride (D, E, F); chitosan nanoparticles (G, H, I) and nanocomposite (J, K, L). The ANOVA test revealed statistical significance of treated cells with respect to control. Statistical significance is denoted by * ($p < 0.05$), ** ($p < 0.005$), *** ($p < 0.001$), and **** ($p < 0.0001$). The data are represented as mean ± SD of three individual experiments.

3.2.16. D-F) and chitosan nanoparticles (**Figure 3.2.7. G-I**) exhibited much higher viability. At the IC_{50} concentration of the nanocomposite, approximately 64.4% of HEK-293 cells were still viable thus indicating that the as-synthesized nanocomposite is biocompatible in nature. The IC_{50} values determined from the MTT assay have been tabulated in **Table 3.2.1**.

Connectively, live-dead cell imaging of the monolayer culture revealed significant anti-proliferative effect of the nanocomposite (**Figure 3.2.8. A-D**). The intensity of green fluorescence (due to Calcein AM) in untreated cells was considerably higher compared to treated cells. Similarly, the intensity of red fluorescence (due to propidium iodide) was higher

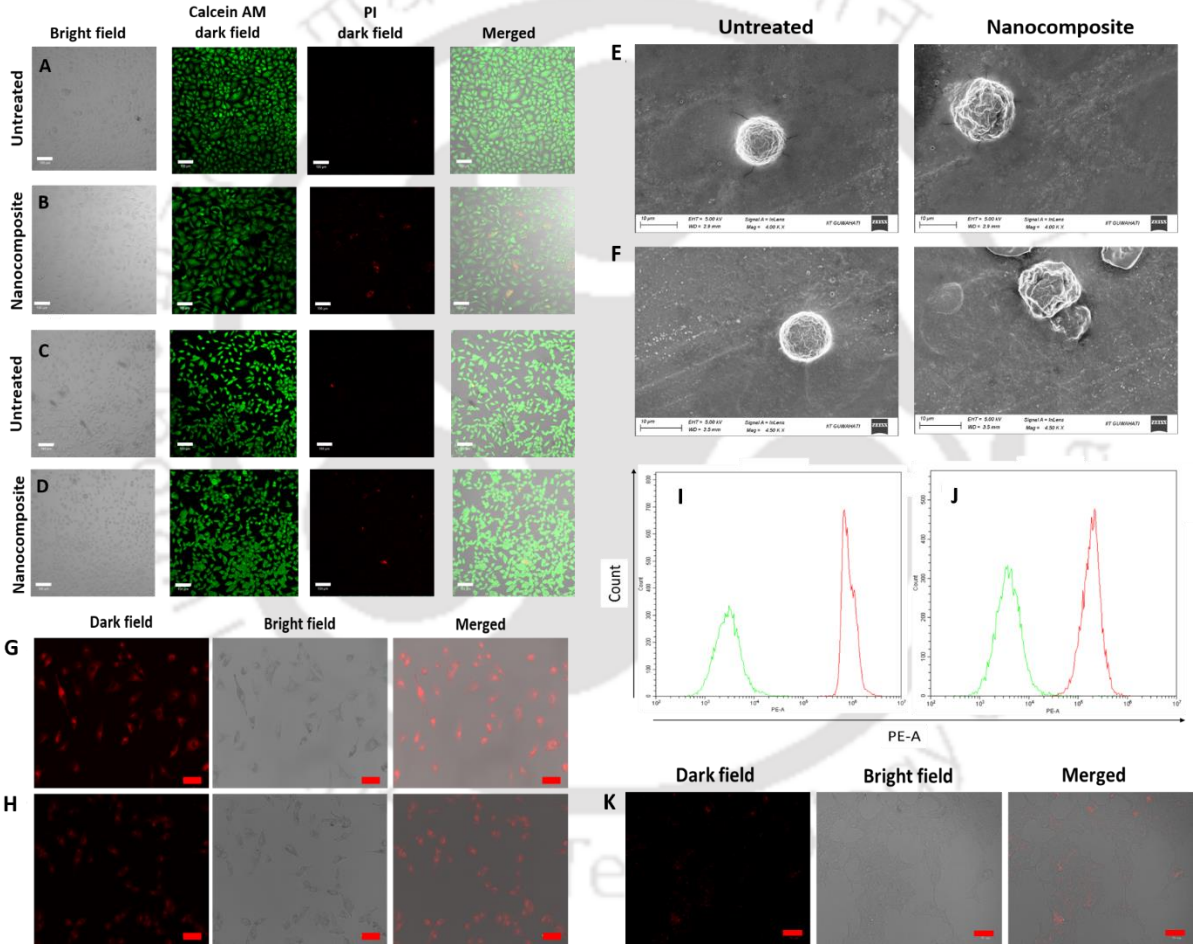

Figure 3.2.8. Live-dead cell visualization of (A, B) A549 and (C, D) HeLa monolayer culture using calcein AM/PI dual staining. Live cells fluoresce in the green region while dead cells in the red region. Cells were treated with the nanocomposite for 48 h before imaging. Scale bar: 100 µm. FESEM-based morphological study of monolayer culture treated with nanocomposites for 48 h before imaging. (E) A549 and (F) HeLa cells. Scale bar- 10 µm. Time-dependent nanocomposite uptake into (G) A549 cells and (H) HeLa cells imaged through confocal microscopy. Flowcytometric analysis of nanocomposite internalisation into (I) A549 and (J) HeLa monolayer cells. Time-dependent uptake of nanocomposites into (K) HEK-293 cells.

in treated cells compared to untreated cells. Additionally, data from FESEM-based morphological study showed rugged cell surface and signs of membrane damage in the treated cells, while the untreated cells appeared healthier (**Figure 3.2.8. E-F**).

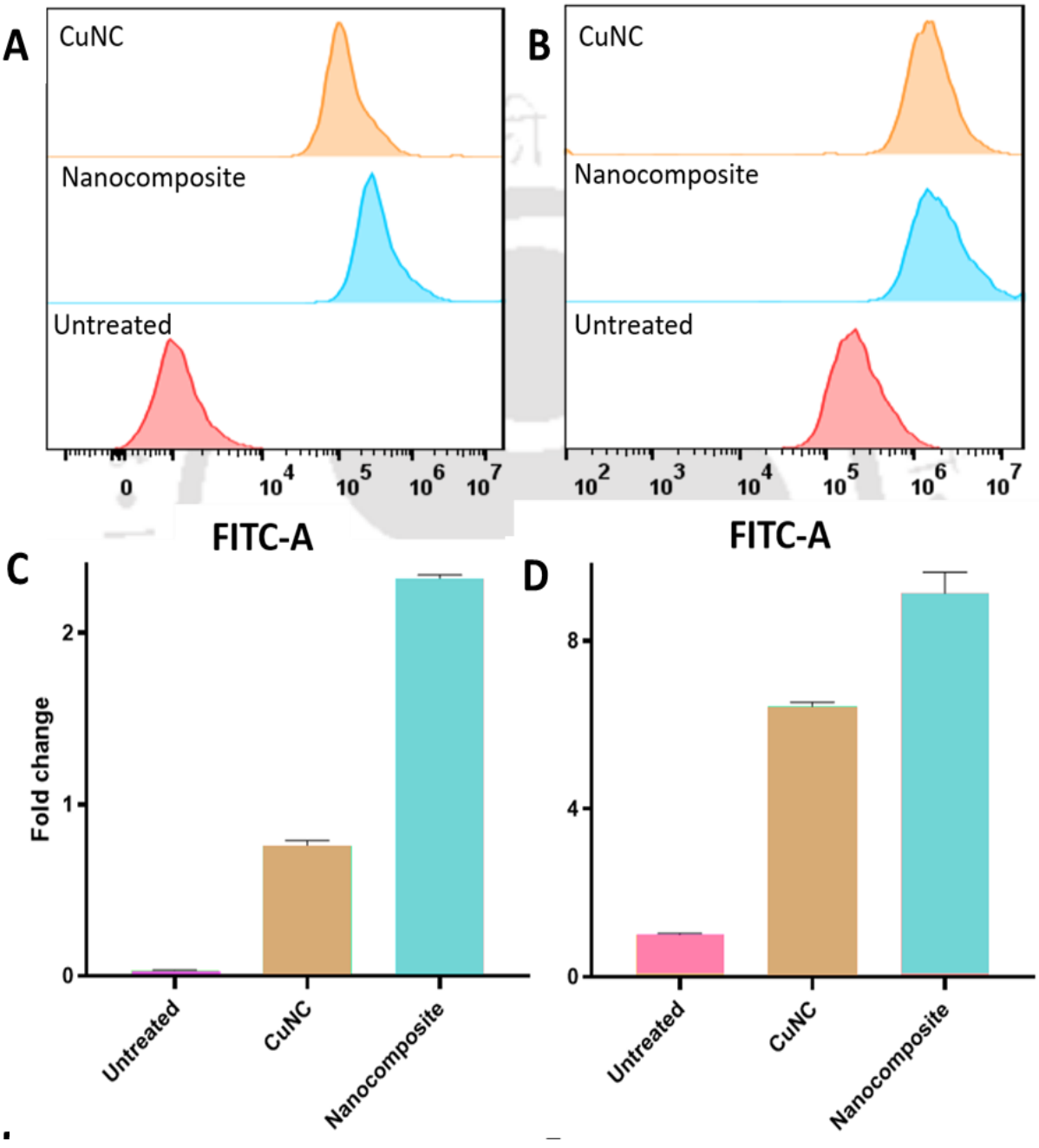

Figure 3.2.9. Time-dependent nanocomposite uptake into (A) A549 cells and (B) HeLa cells imaged through confocal microscopy. Flowcytometric detection of cellular ROS in (C) A549 and (D) HeLa cells. Fold change observed in CuNC and nanocomposite treated (E) A549 and (F) HeLa cells.

3.2.6. Nanocomposites localize in the cellular cytoplasm. In order to understand the anti-proliferative mechanism of the nanocomposite, the need to know its homing tendencies is primal. Therefore, to study its localization, cells were incubated with the nanocomposite for two different time points followed by fluorescent microscopy. The microscopy images revealed exclusive localization in the cellular cytoplasm in A549 and HeLa cells, as indicated by the reddish fluorescence due to the CuNC (**Figure 3.2.8. G, H**). Additionally, a time-dependent uptake assay on HEK-293 cells was also performed using the same nanocomposite concentration as that in A549 cells (**Figure 3.2.8. K**). It was observed that the intensity of red fluorescence was significantly low, thus indicating the lower specificity of the nanocomposite towards them. It has been reported that mannose receptor is overexpressed in A549 cell line compared to HeLa and HEK-293 cell lines.[239,240] Most tumor cells often have high metabolic demand than their normal counterparts. Overexpression of receptors such as that of mannose can increase their sensitivity for monosaccharides.[241,242] Therefore, mannose coating over chitosan was aimed at targeting the overexpressed mannose receptors on the surface of A549 cells. Consecutively, the higher intensity of red fluorescence in A549 cells showed preferential uptake of the nanocomposites after incubation, as compared to HeLa cells. This was further confirmed by flowcytometric assay to study the nanocomposite uptake in cells. The resultant histogram clearly demonstrates the preferential uptake of nanocomposite in A549 cells compared to the HeLa cells after 2 h of treatment (**Figure 3.2.8. I, J**).

3.2.7. Nanocomposites provoke ROS generation, membrane potential depolarization and apoptosis in lung adenocarcinoma cells. Normally, every cell maintains a homeostasis between oxidant and antioxidant species.[243] However, increase in oxidative stress may result

Table 3.2.2. Tabulation of fold change with respect to reactive oxygen species generation in (A) A549 and (B) HeLa monolayer culture.

Cell lines	Sample	Fold change
A549	CuNC	6.42
	Nanocomposite	9.11
HeLa	CuNC	0.75
	Nanocomposite	2.31

from a variety of factors thus, leading to cell damage. To determine the nanocomposites' ability to produce ROS, DCFDA-based detection assay was performed. The cell permeant agent DCFDA after diffusing, is deacetylated by cellular esterase into a non-fluorescent compound. This intermediate compound is oxidized by ROS into DCF, a highly fluorescent product with a maximum emission spectrum at 529 nm. After processing, the cells were analysed by flowcytometry. It was observed that with respect to untreated cells, treatment with nanocomposites resulted in 9.11-fold in A549 (**Figure 3.2.9. A, C**) and 2.31-fold increase in HeLa cells (**Figure 3.2.9. B, D**), respectively. The changes have been tabulated in **Table 3.2.2**. The suggestive ROS generation in the nanocomposite treatment can be attributed to levocetirizine, essentially a phenothiazine (**Figure 3.2.10.**), which is known to trigger oxidative stress in NSCLC, oral cancer and glioblastoma.[39,244,245]

Also, although copper is an essential element in the human body, it has dual activity when it comes to cancer. Several preclinical studies have shown that slightly elevated copper levels promote tumor initiation and progression. However, in established tumors, copper-based compounds have shown commendable inhibitory activity upon increasing copper concentration beyond the threshold.[246] The inhibition in such cases, begin with generation of reactive oxygen species (ROS). Thus, the cumulative fold change in nanocomposite treated cells could be the result of both levocetirizine and CuNC.

Table 3.2.3. Detection of mitochondrial membrane potential depolarization by JC-1 staining flowcytometric assay in (A) A549 and (B) HeLa cells. Detection of apoptotic population by Annexin-FITC/PI flowcytometric assay in (C) A549 and (D) HeLa cells.

% Population of	Cell lines	CuNC (%)	Nanocomposite (%)
Mitochondrial Membrane Potential Depolarization	A549	0.23	29.89
	HeLa	3.59	18.19
Apoptosis	A549	15.73	55.35
	HeLa	8.44	29.39

Connectively, increase in cellular ROS can compromise mitochondrial membrane integrity. In order to determine the effect of oxidative stress on mitochondria, JC-1 staining analysis was

performed. A cyanin dye JC-1, exists as red aggregates in polarized mitochondria, while in depolarized mitochondria it remains as monomer. Red fluorescence was detected from the healthy mitochondria of the untreated cells. However, there was 29.89 % and 18.19 % increase in green fluorescence in nanocomposite treated A549 cells (**Figure 3.2.11. A**) and HeLa cells (**Figure 3.2.11. B**), respectively. The values are tabulated in **Table 3.2.3**. This indicated the depolarization of mitochondrial membrane potential following treatment with the nanocomposites. Furthermore, redox imbalance is one of the early events in programmed cell death i.e., apoptosis.[247] To determine the percentage of apoptotic cells, Annexin V-FITC/PI

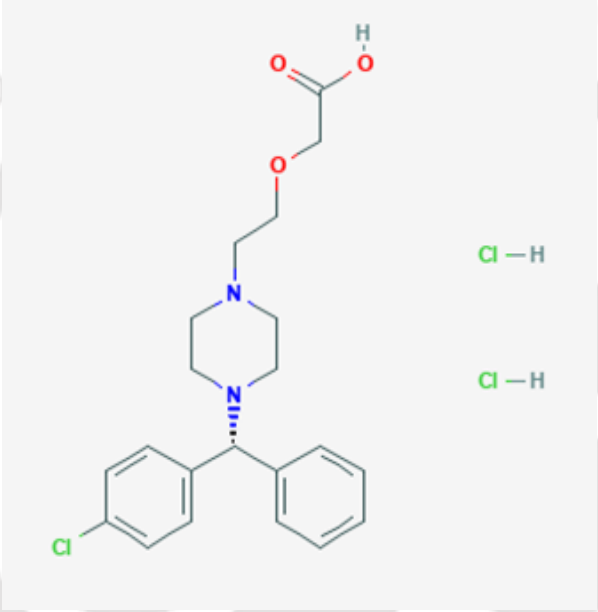

Figure 3.2.10. Structure of levocetirizine dihydrochloride. Source: National Centre for Biotechnology Information (2023). PubChem Compound Summary for CID 67336450, Levocetirizine hydrochloride.

based apoptosis assay was performed. In a healthy cell, phosphatidylserine is located in the inner leaflet of the plasma membrane. However, during early apoptosis, the leaflet flips, exposing the phosphatidylserine. Annexin V, an anticoagulant protein can bind to it with high affinity and upon conjugation with FITC, also fluoresces in the green region. In parallel, cells with membrane damage are stained with propidium iodide and fluoresce in the red region. From the flowcytometric data, an increase of 55.35 % and 29.39 % apoptotic cell population in nanocomposite treated A549 (**Figure 3.2.11. C**) and HeLa cells (**Figure 3.2.11. D**),

respectively was observed. Additionally, in CuNC treated A549 and HeLa cells, considerably lesser apoptotic population was observed than their nanocomposite treated counterparts. The

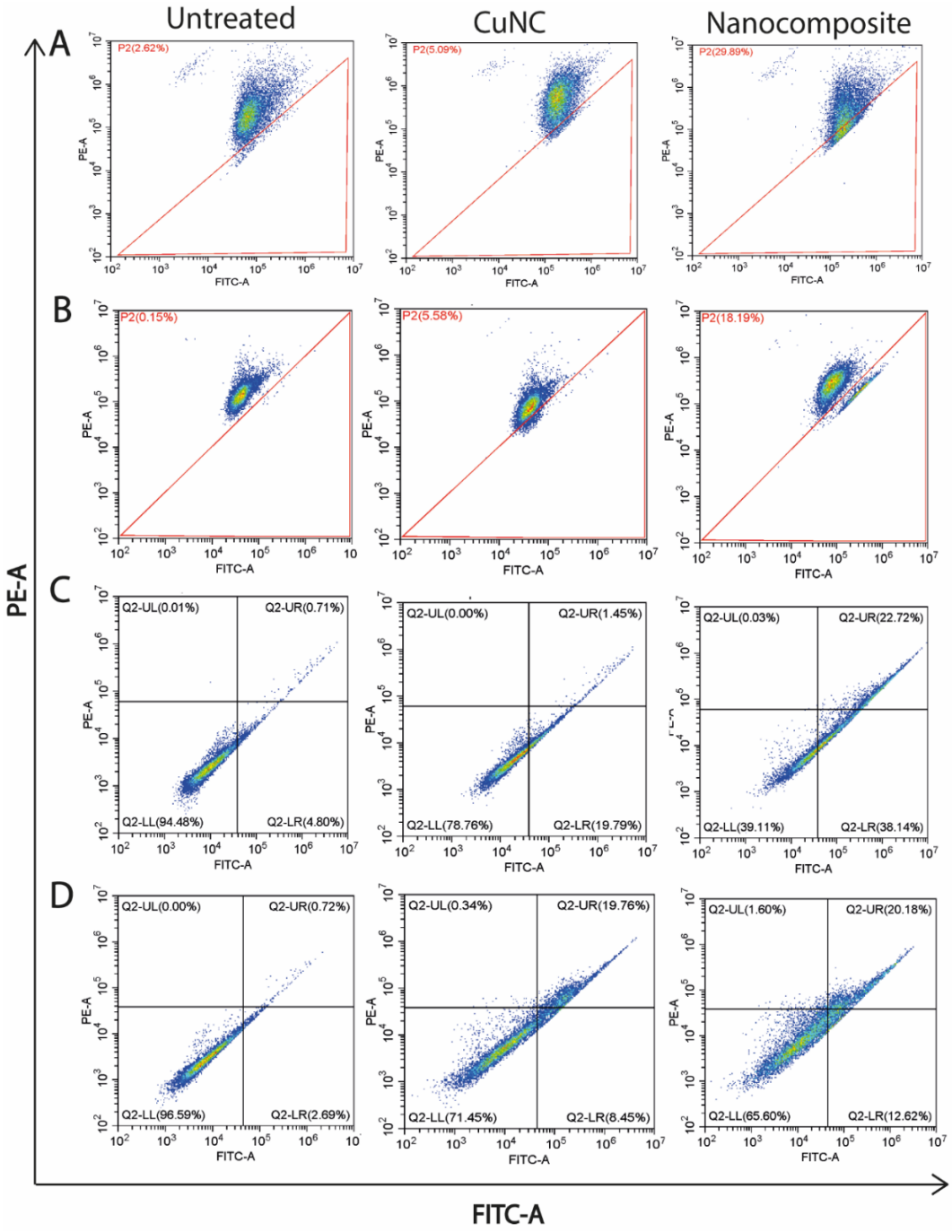

Figure 3.2.11. Detection of mitochondrial membrane potential depolarization by JC-1 staining flowcytometric assay in (A) A549 and (B) HeLa cells. Detection of apoptotic population by Annexin-FITC/PI flowcytometric assay in (C) A549 and (D) HeLa cells. All comparisons are made with respect to control vs. test sample.

respective values have been tabulated in **Table 3.2.3**. Finally, these data indicate the mechanism of nanocomposite action on cells.

3.2.8. Treatment with nanocomposites result in loss of lipid droplets, colony forming ability and migration potential of lung adenocarcinoma cells. Lipid droplets are understood

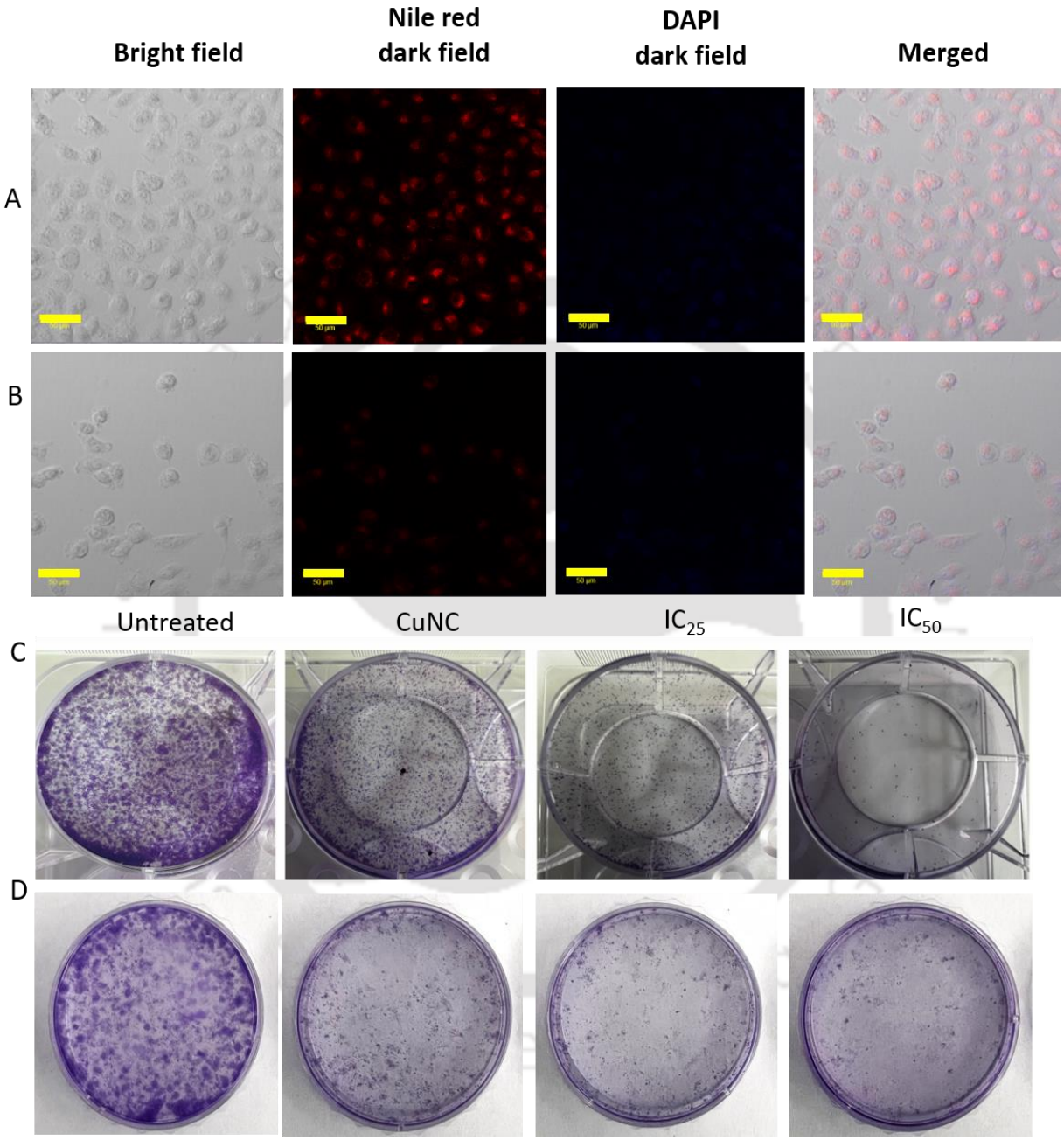

Figure 3.2.12. Lipid droplet staining assay performed on A549 monolayer culture. (A) Untreated and (B) treated cells. DAPI was used for counterstaining nuclei. Scale bar – 60 µm. Colony formation assay performed on (C) A549 and (D) HeLa monolayer culture.

as unique organelles with a neutral lipid core and a monolayer phospholipid membrane embedded with several lipid-associated proteins.[248]

They are associated with a variety of physiological processes like cell proliferation, apoptosis, metabolism, membrane transport, protein degradation and transcriptional regulation.[249] In most cancer cells, lipid metabolism undergoes reprogramming.[250] Their synthesis pathway is constitutively activated while the breakdown process is inhibited, resulting in excessive lipid accumulation.[251] These excess lipids are often stored as lipid droplets, thus making them a prominent feature of cancer cells.[252] Additionally, in lung adeno carcinoma higher expression of a lipid associated protein, adipophilin is also reported. Adipophilin expression is often associated with poor prognosis in such patients.[253] To understand the effect of nanocomposite treatment on lipid droplets, nile red staining assay was performed. DAPI was used as a counterstain for nuclei. After treating A549 cells for 24 h, significant reduction in the intensity of red fluorescence compared to untreated cells was observed (**Figure 3.2.12. A, B**). Additionally, decrease in the number of cells in the treated sample was also evident.

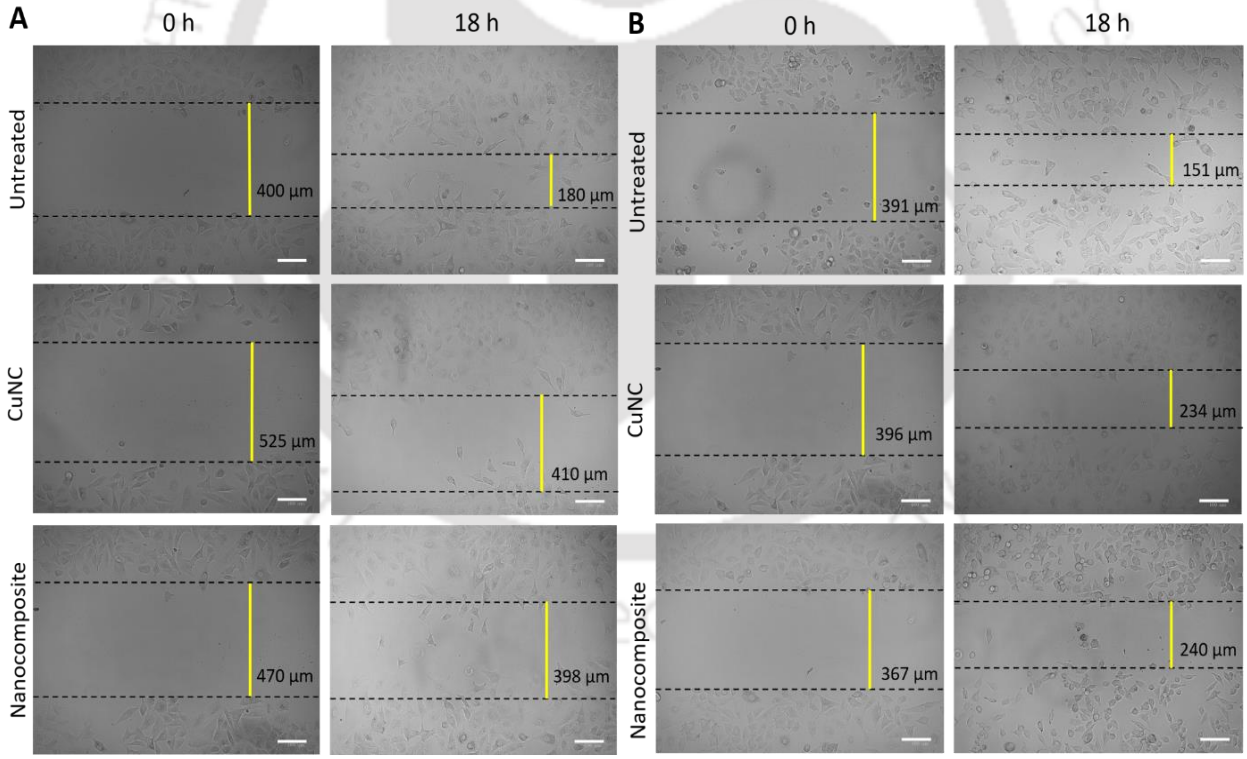

Figure 3.2.13. Migration assay performed in monolayer cells. (A) A549 cells and (B) HeLa cells. The length of the gap closure was measured using ImageJ software. Scale bar – 100 µm.

In parallel, colony formation assay was performed on untreated and nanocomposite treated monolayer culture to assess their ability to proliferate from single to multiple colonies. Nanocomposite treated cells failed to survive and reproduce as multiple colonies in both A549

(**Figure 3.2.12. C**) and HeLa cells (**Figure 3.2.12. D**). Migration assay on monolayer cultures was also performed to test their wound healing ability. An artificial wound was created via exclusion on the plate where the cells are attached. Following treatment, the cells' ability to cover the wound was assessed.[254–256] It was observed that the wound healing capacity was the lowest following 18 h of nanocomposite treatment (**Figure 3.2.13. A, B**). Altogether, the above data highlight the mechanistic path of the nanocomposites' effect on lung adenocarcinoma cells.

3.2.9. Nanocomposites inhibit the viability and sphere forming ability of multicellular spheroids. After successfully evaluating the inhibitory potential of nanocomposites on

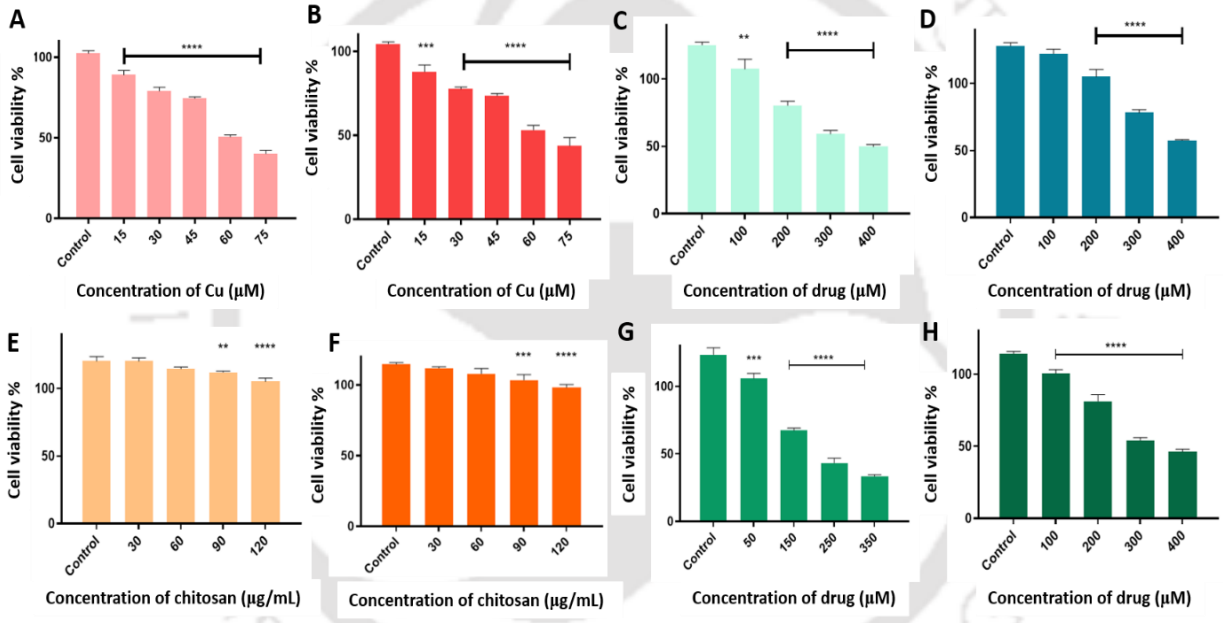

Figure 3.2.14. Graphical representation of dose dependent decrease in viability of A549 spheroids (A, C, E, G) and HeLa spheroids (B, D, F, H). They were treated with CuNC (A, B); levocetirizine dihydrochloride (C, D); chitosan nanoparticles (E, F) and nanocomposite (G, H). The ANOVA test revealed statistical significance of treated spheroids with respect to control. Statistical significance is denoted by * ($p < 0.05$), ** ($p < 0.005$), *** ($p < 0.001$), and **** ($p < 0.0001$). The data are represented as mean ± SD of three individual experiments.

monolayer cells, their effect on 3D-tumor spheroids was verified. Multicellular tumor spheroids (MCTS) are self-organizing, round cultures of tumor cells with principal intercellular and cell extracellular matrix interactions.[257] Research in 3D models are more coherent with in vivo studies because of their similarity to the native tissues. Apart from tackling the limitations of monolayer cells, spheroids also preserve native tissue architecture, genetic heterogeneity, cell polarity, increased drug resistance and nutrient diffusion gradients.[257,258]

Similar to cell viability assay, spheroid viability assay was performed where spheroids were treated with varying concentrations of the nanocomposite and their individual components for 72 h followed by colorimetric detection using alamarBlue. The results exhibited a dose-dependent reduction in viability with nanocomposite treatment (**Figure 3.2.14.**). It is to be

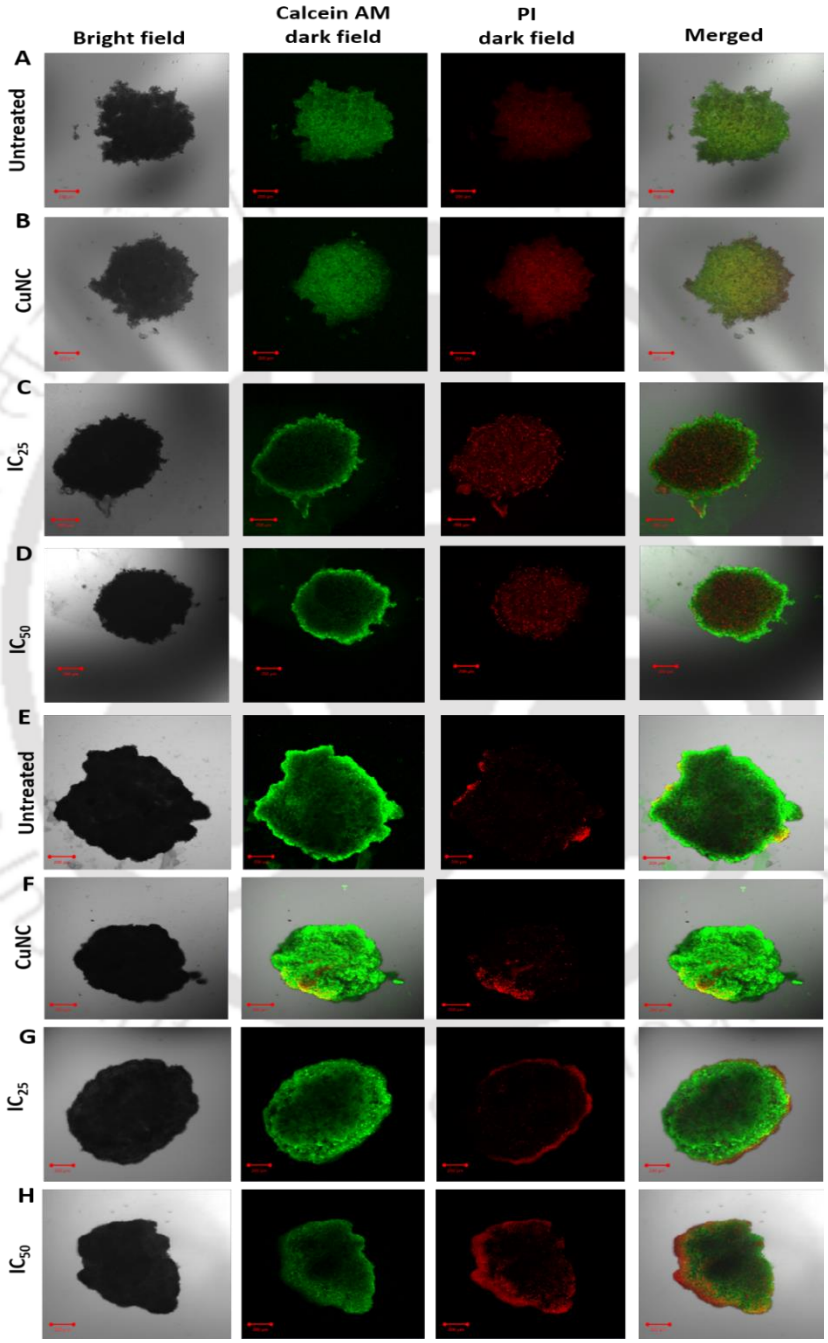

Figure 3.2.15. Live/dead staining assay using calcein AM and PI dyes in A549 and HeLa multicellular spheroids. (A, E) Control spheroids; (B, F) CuNC treated spheroids; (C, G) nanocomposite (IC_{25}) treated spheroids; (D, H) nanocomposite (IC_{50}) treated spheroids. Scale bar – 200 μm.

noted that the concentration of nanocomposite required to achieve IC_{50} in case of spheroids is quite higher compared to monolayer cells. This could be because tumor spheroids larger than 500 µm in diameter often have hypoxic cores that are inaccessible and are the reason behind drug resistance.[257] The IC_{50} values are tabulated in **Table 3.2.1**. Live-dead imaging of untreated vs. treated spheroids also reveal the nanocomposite's inhibitory effect on both A549 (**Figure 3.2.15. A-D**) and HeLa spheroids (**Figure 3.2.15. E-H**). Similar to monolayer cells, increase in treatment concentrations resulted in the decrease of live cells. This is confirmed by the increase in red fluorescence intensity in the treated spheroids.

To discern the full therapeutic potential of the nanocomposites, the sphere forming ability of treated monolayer cells (**Figure 3.2.16.**) was investigated. There was visible reduction in size and cells appeared quite compact and healthy in nature. This depicts the noteworthy efficacy of the nanocomposite over tumor spheroids as well.

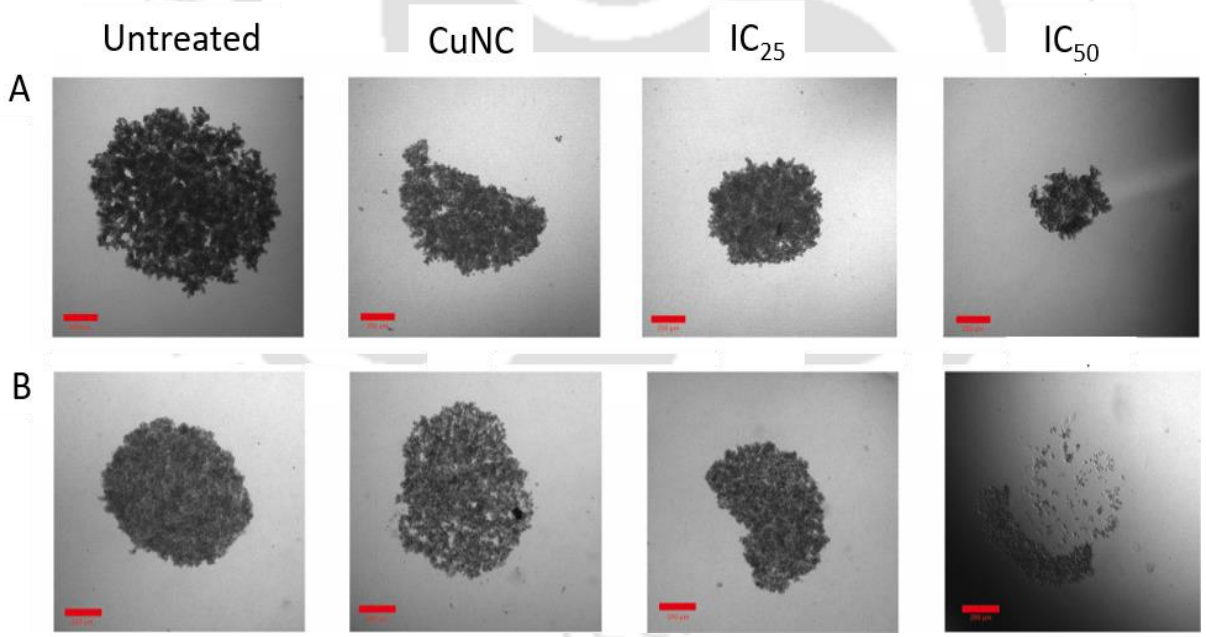

Figure 3.2.16. Sphere formation assay assessed on (A) A549 and (B) HeLa multicellular spheroids. Scale bar – 200 µm.

3.2.10. Summary

Lung adenocarcinoma is one of the frequent and aggressive most forms of lung cancer. While it mostly affects tobacco smokers, its incidence is quite alarming in non-smokers with the adenocarcinoma subtype too. Therefore, despite the availability of conventional treatments, both medical and research fields are on the lookout for alternate approaches. Towards that, an

attempt was made to synthesize a nanotherapeutic module that utilises the combined effect of drug repurposing and nanotechnology. The mannose coated chitosan Cu nanocluster-levocetirizine nanoparticles termed as nanocomposites were synthesized and successfully characterised. Their photoluminescence revealed localisation mostly in the cellular cytoplasm. Owing to the mannosylation that targets the over-expressed mannose receptors, their uptake into A549 cells was slightly preferential. They revealed excellent anti-proliferative activity against monolayer cultures and multicellular spheroids of A549 and HeLa cell lines. Notably, this inhibition was a result of significant ROS generation, mitochondrial membrane imbalance and subsequent cell death. Further investigation revealed their ability to retard wound healing, colony formation and sphere formation capacity of monolayer cells. The ability to accumulate lipid droplets in the cellular cytoplasm as a means of survival was also lowered following nanocomposite treatment. With further standardization, these nanocomposites can be utilised as nanodrug against lung adenocarcinoma. Overall, the evidences from the present work highlight the prominent role of drug repurposing and nanotechnology in cancer therapeutic research.

3.3. SAHA potentiates the activity of repurposed drug promethazine loaded PLGA nanoparticles in triple-negative breast cancer cells.

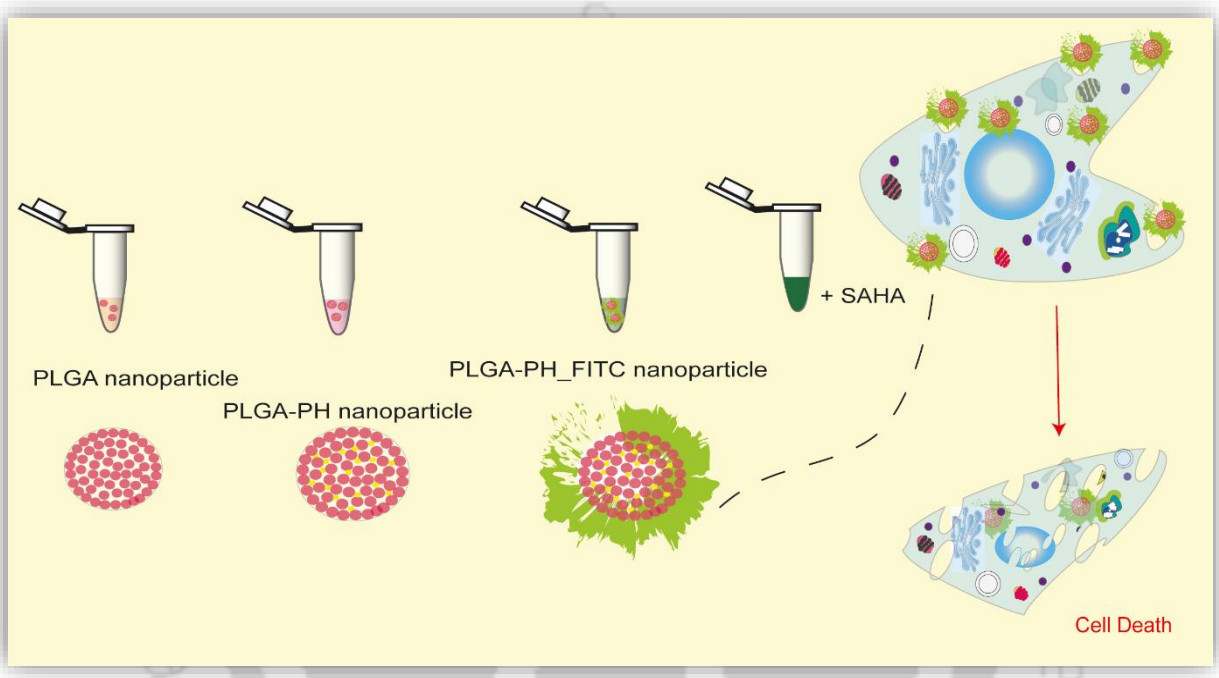

Scheme 3.3. Schematic illustrating the difference between individual components of the therapeutic regime and its application on triple-negative breast cancer cell.

Results and Discussions

Abstract

Epithelial to mesenchymal transition (EMT) associated with metastatic abilities is now crucial for anti-EMT therapeutic target in caner. Alternate approaches like repurposing may lower drug development time and costs without compromising patient safety. Towards that, promethazine hydrochloride, a phenothiazine class of antihistamine topped the preliminary screening process. To aid with its stability, delivery and release however, it was loaded into biocompatible PLGA nanoparticles conjugated to FITC for real-time tracking. Additionally, SAHA, a common histone deacetylase inhibitor was also used as a form of pre-treatment. SAHA was hypothesised to sensitise triple-negative breast cancer (TNBC) cells towards repurposed drug loaded PLGA nanoparticles. Consequently, it was observed that the combination treatment efficiently lowered IC_{50} values across cell lines compared to monotherapy. This was mechanistically mediated by ROS generation, depolarization of mitochondria, programmed cell death and diminished proliferative potential. Investigations into protein expression also revealed reduction of mesenchymal proteins while increase in epithelial marker, thus indicating an altered EMT dynamics. Altogether, our findings provide a better insight into the benefits of SAHA potentiated targeting of tumor spheroids that mimic solid tumors of triple-negative breast cancer. This study paves the avenue to a more rational translational validation of combining nanotherapeutics with drug repurposing.

3.3.1. Preliminary screening of antihistamine drugs for potential anti-proliferative activity. Four over the counter antihistamine drugs were screened initially on MDA-MB-231

Table 3.3.1. Classes of antihistamine drugs used for preliminary screening.

Drug	Antihistamine class	Sub-class
Ranitidine	H2	-
Pheniramine maleate	H1 (1st generation)	Alkylamine
Promethazine hydrochloride	H1 (1st generation)	Phenothiazine
Cetirizine	H1 (2nd generation)	Piperazine

and HEK-293 cell lines. The chemical classes of the drugs are mentioned in **Table 3.3.1**. Cell viability assays revealed the anti-proliferative property of promethazine hydrochloride. The representative viability graphs for MDA-MB-231 cells and HEK-293 cells are depicted in **Figure 3.3.1.**

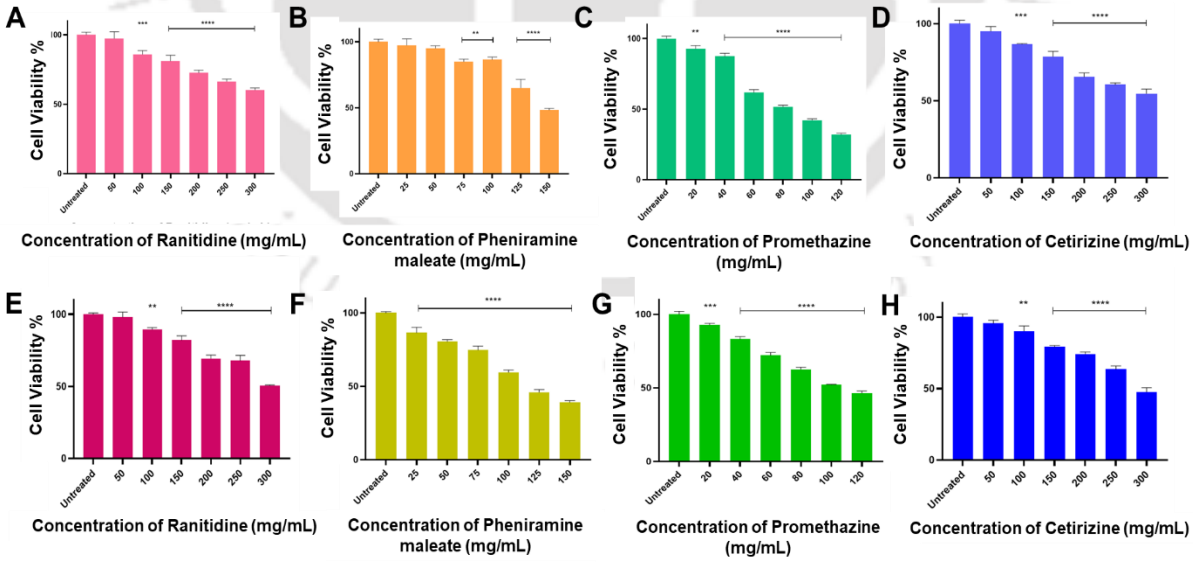

Figure 3.3.1. Cell viability assay performed on MDA-MB-231 cells for screening (A) Ranitidine, (B) pheniramine maleate and (C) promethazine and (D) cetirizine over the counter drugs. The ANOVA test revealed statistical significance of treated cells with respect to control. Statistical significance is denoted by * ($p < 0.05$), ** ($p < 0.005$), *** ($p < 0.001$), and **** ($p < 0.0001$). The data are represented as mean ± SD of three individual experiments.

3.3.2. Characterisation of nanoparticles. PLGA nanoparticles were prepared via a slightly modified spontaneous emulsion solvent diffusion method [259] in water. The use of two freely water miscible organic solvent, acetone and ethanol was aimed at decreasing the overall nanoparticles size and narrowing the distribution. Earlier studies have reported that solvents with a high diffusion coefficient favour the formation of smaller nanoparticles with a narrower distribution.[260–262] Besides acetone and ethanol are comparatively less toxic than other solvents like dichloromethane, that has been extensively used for nanoparticles preparation earlier.[259,263] For stabilization, Polyvinyl alcohol was utilised as its surfactant properties protect the PLGA containing droplets against coalescence.[264] PVA also efficiently subdued nanoparticles aggregation because of its low hydrolyzation and polymerization that prevented the local gelatinization of PVA at the surfaces of emulsion droplets induced by the diffusion of acetone.

The prepared PLGA nanoparticles were characterised for morphology. Hydrodynamic diameter and Zeta potential of the resultant nanoparticles were measured by Malvern Zetasizer nano ZSP**.** The average size of PLGA nanoparticles was found to be 224.6 nm **(Figure 3.3.2.**). They were also found to have a negative charge of -25.1 mV (**Figure 3.3.5.**). FESEM images

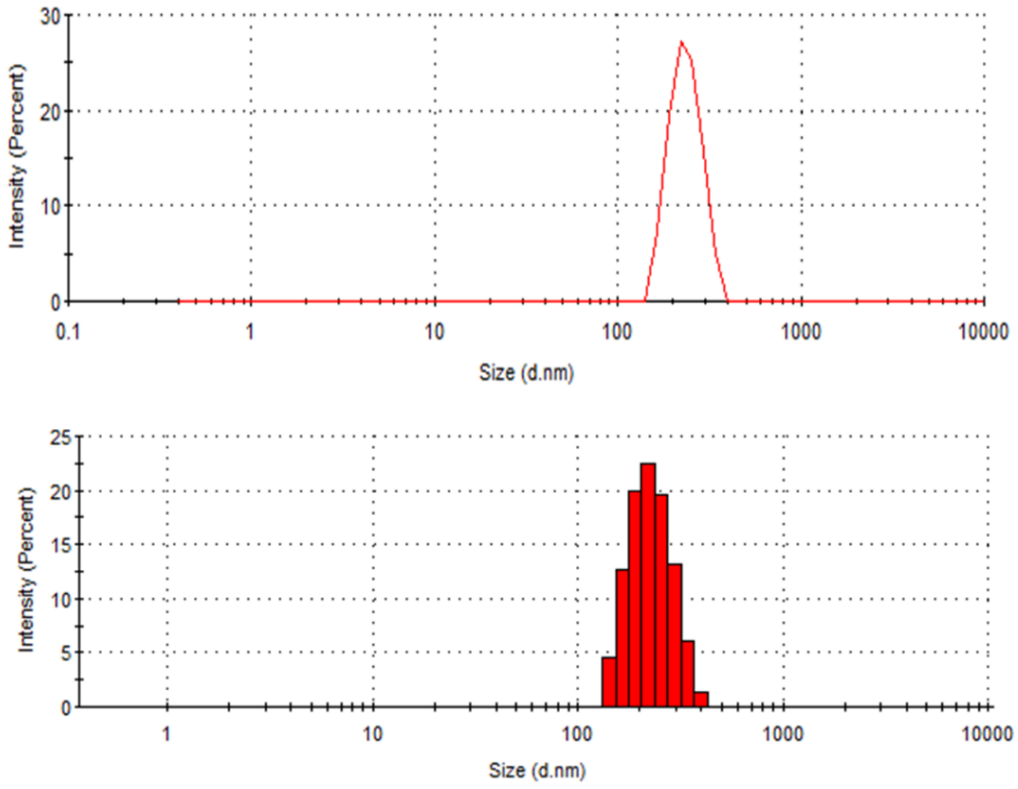

Figure 3.3.2. Hydrodynamic size of PLGA nanoparticles as measured by Malvern Zetasizer. The graphs reveal an average hydrodynamic size of 224.6 nm.

revealed the particle diameter to be 90.35 ± **13.3** nm, while through TEM images, spherical particles of 140.45 ± **26.4** nm were found (**Figure 3.3.3. A, B**). The formation of promethazine loaded PLGA nanoparticles (PLGA-PH_FITC nanoparticles) was validated through FESEM, where there was a slight increase in the size of the nanoparticles, 196.83 ± **16.5 nm** (**Figure 3.2.3. C**). TEM images also correlated with the increase in their size i.e. 215.25 ± **23.4** nm

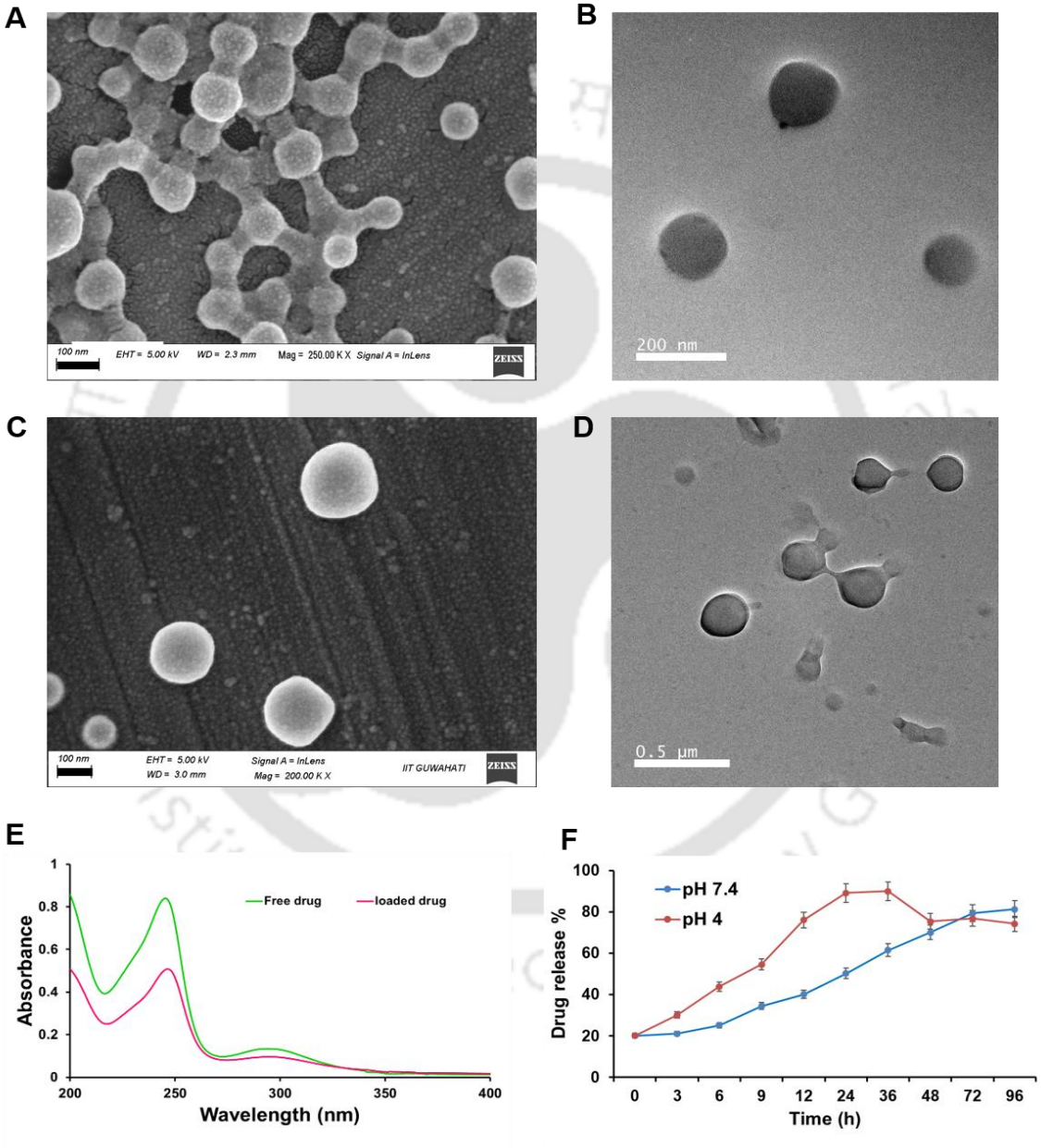

Figure 3.3.3. (A) FESEM image of PLGA nanoparticles at 100 nm scale. (B) TEM image of PLGA nanoparticles at 200 nm scale (C) FESEM image of PLGA-PH nanoparticles at 100 nm scale. (D) TEM image of PLGA-PH nanoparticles at 0.5 µm scale. (E) UV-Vis spectra of PH and PLGA-PH nanoparticles. (F) Release profile of promethazine from PLGA nanoparticles in acidic and neutral medium.

(**Figure 3.3.3. D**). Comparatively, DLS measurements revealed an average hydrodynamic size of 270 nm (**Figure 3.3.4.**). Furthermore, peaks at around 247 nm and 248 nm in the case of both PLGA-PH_FITC nanoparticles and free promethazine respectively, were observed in the UV-Vis graphs. A weaker peak at 297 nm was also observed in the case of free promethazine. A weak shoulder at 297 nm further supported the incorporation of promethazine in PLGA nanoparticles (**Figure 3.3.3. E**). This concurred with the earlier reports, which suggest that promethazine thus loaded on to the PLGA nanoparticles was calculated to be 2 mM, with a loading efficiency of 40 %. PH loading was also further confirmed through shift in the zeta potential peaks (**Figure 3.3.5. A-C**).

From the release profile of promethazine from PLGA nanoparticles, it was observed that in neutral pH about 40% of the drug had released within the first 12 h, followed by a more sustained pattern continuing up to 48 hours (**Figure 3.3.4. F**). The total drug release however required a little more than that as until the 48th h only 81% of drug had released. In acidic pH, about 76% of the drug had released within the first 12 h. It has been demonstrated both *in vivo* and *in vitro* that PLGA copolymer undergoes degradation by hydrolysis or biodegradation

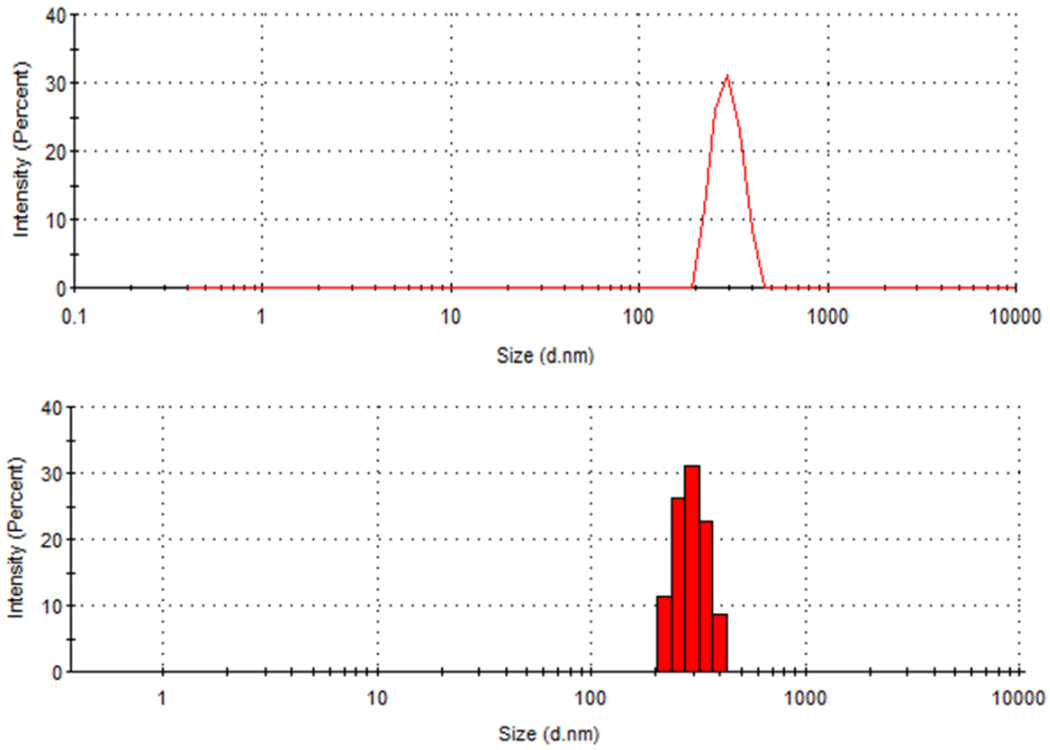

Figure 3.3.4. Hydrodynamic size of PLGA-PH_FITC nanoparticles as measured by Malvern Zetasizer. The graphs reveal an average hydrodynamic size of 270 nm.

through cleavage of its backbone ester linkages into oligomers and, finally monomers.[234,235] PLGA degradation is the collective process of bulk diffusion, surface diffusion, bulk erosion and surface erosion. The release rate pattern of promethazine or any drug for that matter, is often difficult to anticipate. Carriers prepared via polar method, support a more constant release

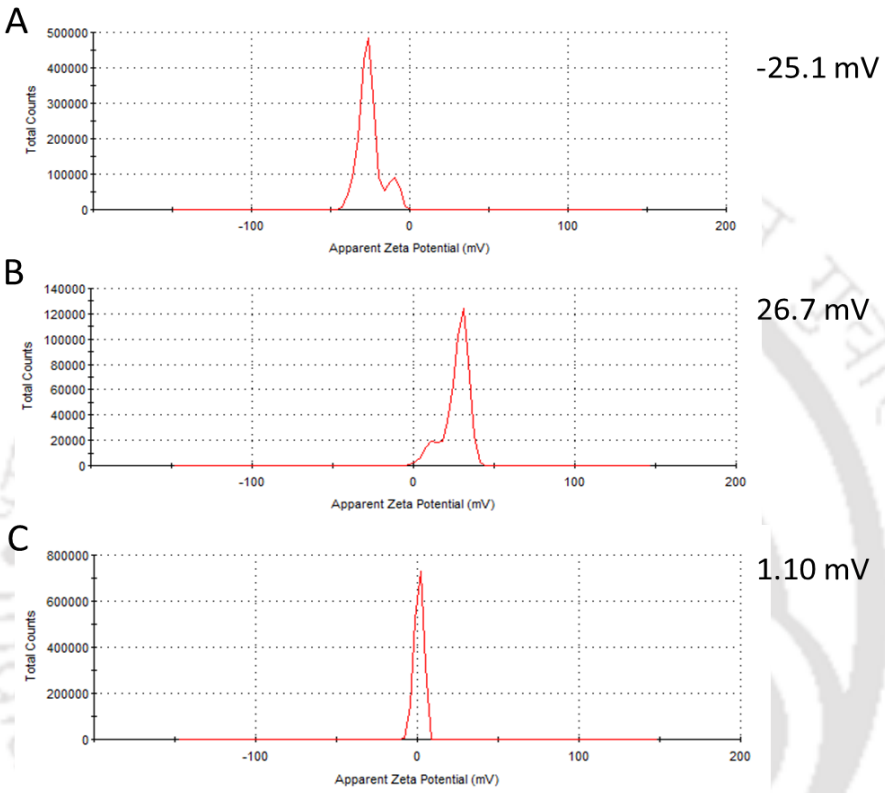

Figure 3.3.5. Comparison of zeta potential values of (A) PLGA nanoparticles, (B) promethazine hydrochloride and (C) PLGA-PH nanoparticles. as measured by Malvern Zetasizer.

compared to carriers prepared via non polar method. They swelled to a lesser extent because of a denser, more closely packed matrix, resulting in a slower uptake of the medium, and hence slower drug release.[265] The pattern of release, however in both polar and nonpolar implants are biphasic, indicating that promethazine may have been first released through diffusion followed by bulk erosion. Thus, a pH dependent promethazine release pattern was observed from the PLGA nanoparticles, with a maximum release in acidic medium. This pattern of release could be an advantage in acidic tumour microenvironment.

3.3.3. Combined effect of SAHA and PLGA-PH nanoparticles is anti-proliferative and dose-dependent. The effect of PLGA-PH nanoparticles and SAHA treated MDA-MB-231, EMT MDA-MB-231, MCF-7 and HEK-293 cells were assessed via an MTT-based cell

viability assay expressed quantitatively in terms of IC_{50} value (**Figure 3.3.6.**). Cells were treated with PLGA-PH nanoparticles, PH, SAHA and a combination of SAHA and PLGA-PH nanoparticles through two strategies. In first instance, cells were co-treated with the combination for 48 h and secondly, they were pre-treated with SAHA for 7 h followed by treatment with PLGA-PH nanoparticles for 48 h. Cell viability following pre-treatment and co-treatment decreased in a concentration dependent manner. IC_{50} values of combination treatment (pre-treatment and co-treatment) were significantly lower than monotherapy, indicating the efficient anti-proliferative

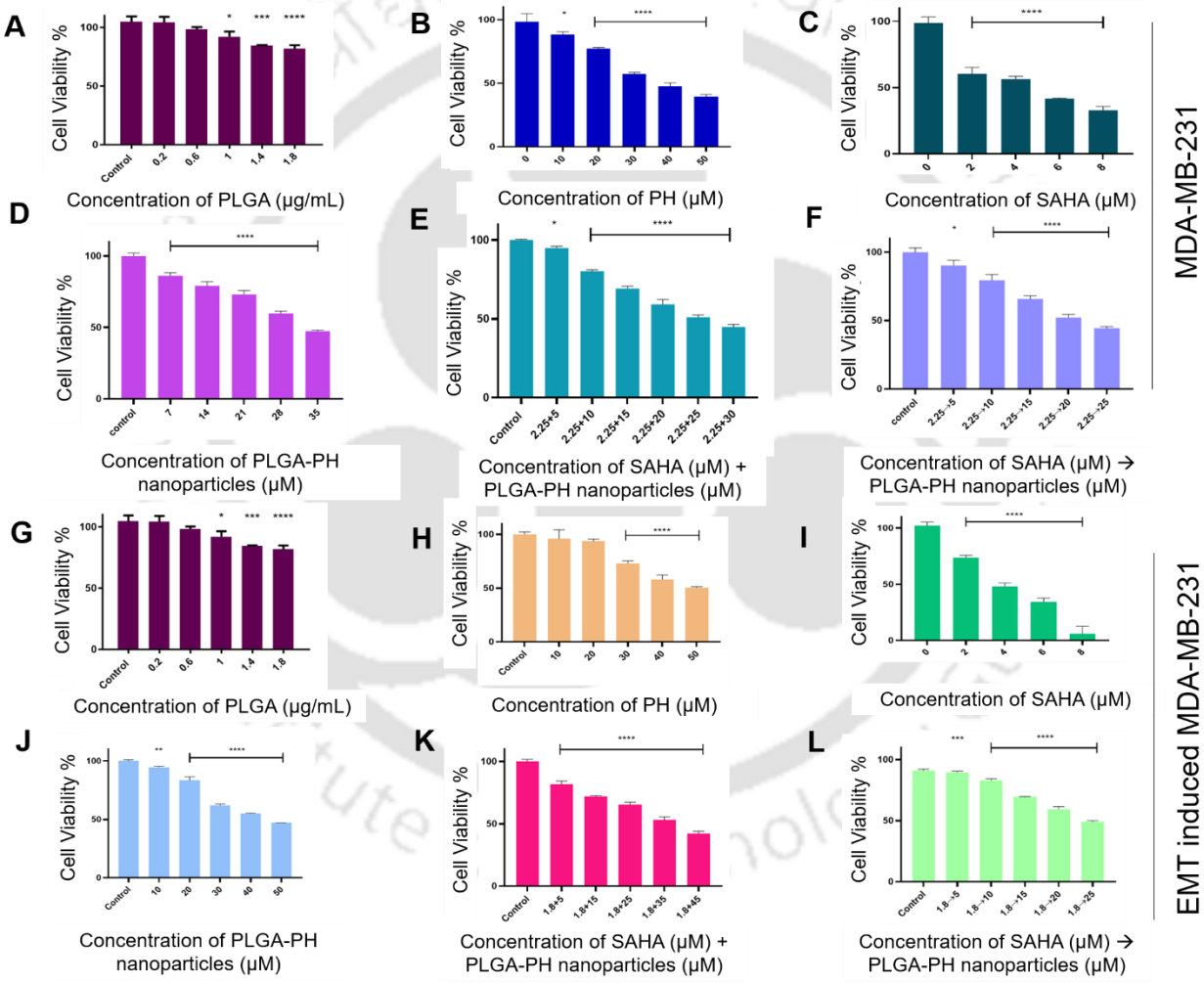

Figure 3.3.6. Graphical representation of anti-proliferative activity on monolayer cells. Cells were treated with PLGA nanoparticles (A, G); PH (B, H); SAHA (C, I); PLGA-PH nanoparticles (D, J); co-treatment with SAHA and PLGA-PH nanoparticles (E, K) and pre-treatment with SAHA and PLGA-PH nanoparticles (F, L). The ANOVA test revealed statistical significance of treated cells with respect to control. Statistical significance is denoted by * ($p < 0.05$), ** ($p < 0.005$), *** ($p < 0.001$), and **** ($p < 0.0001$). The data are represented as mean ± SD of three individual experiments.

activity. Interestingly however, pre-treating the cells prior to treatment with PLGA-PH nanoparticles lowered viability even further. The corresponding IC_{50} values for co-treatment

Table 3.3.2. Tabulation of IC_{50} values of monolayer cells and multicellular spheroids.

Cell lines	PLGA nanoparticles (µg/mL)	PH (µm)	SAHA (µm)	PLGA-PH nanoparticles (µm)	Co-treatment (µm)	Pre-treatment (µm)
EMT induced monolayer cells						
MDA-MB-231	_	48.13	3.64	44.61	27.61	26.53
Monolayer cells						
MDA-MB-231	_	38.7	4.5	36.7	25.63	21.72
MCF-7	_	35.58	3	32.5	19.39	19.99
HEK-293	_	37.08	9	28.5	27.61	24.52
3D multicellular spheroids created from EMT induced cells						
MDA-MB-231	_	140.6	23.57	134.1	130.2	126.5
3D multicellular spheroids						
MDA-MB-231	_	130.3	15.78	126.5	120.5	111.6
MCF-7	_	116	9.91	112.7	112.4	109.6

and pre-treatment have been tabulated in **Table 3.3.2.** Cell viability assays were also performed on MCF-7 (**Figure 3.3.7.**) and HEK-293 (**Figure 3.3.8.**) cells for better understanding of the efficiency of treatment modes. To test our hypothesis however, MDA-MB-231 and EMT

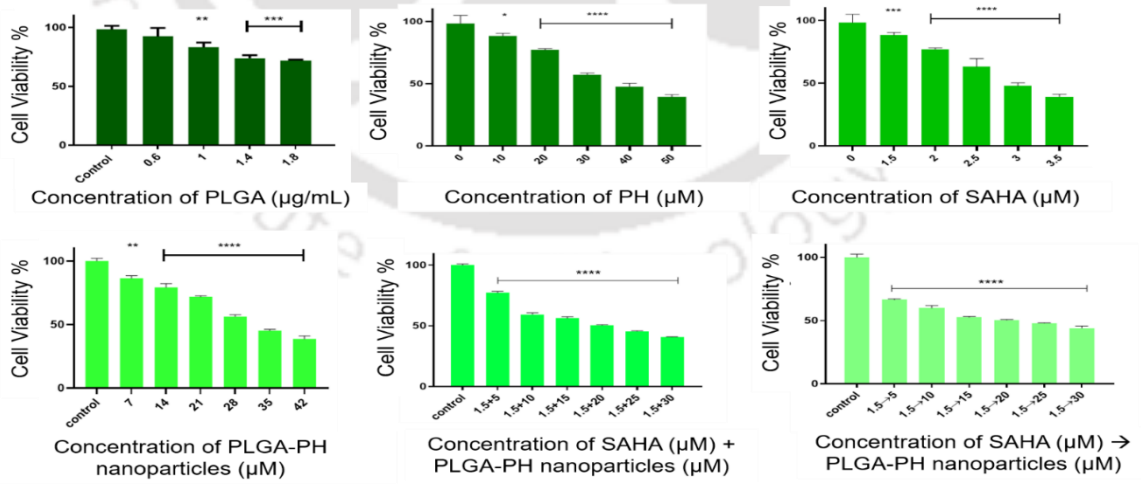

Figure 3.3.7. Graphical representation of the results of cell viability assay performed on MCF-7 monolayer cells. The ANOVA test revealed statistical significance of treated cells with respect to control. Statistical significance is denoted by * ($p < 0.05$), ** ($p < 0.005$), *** ($p < 0.001$), and **** ($p < 0.0001$). The data are represented as mean ± SD of three individual experiments.

MDA-MB-231 cells were explored. To further ascertain the results of cell viability assay, untreated and pre-treated cells were stained with Calcein AM and PI to detect live and dead cell populations. Calcein AM and PI dye were used to stain the live and dead cells, respectively. Calcein AM with acetomethoxy (AM) modified carboxylic acid groups, is a non-fluorescent cell permeable derivate of calcein. AM endows calcein with high hydrophobicity facilitating membrane penetration. Following hydrolysis of AM by intracellular esterases in live cells, the restored calcein molecule fluoresces at 515 nm. PI, on the other hand, can only cross compromised cell membranes, an indicator of cell death. Therefore, increase in the green fluorescence depicted live cells, increase in red fluorescence indicated dead cells. Untreated MDA-MB-231 cells and EMT MDA-MB-231 cells demonstrated higher green fluorescence compared to the pre-treated cells with considerable lesser fluorescence (**Figure 3.3.9.**). However, pre-treated cells showed significant increase in red fluorescence, thus indicating cell death.

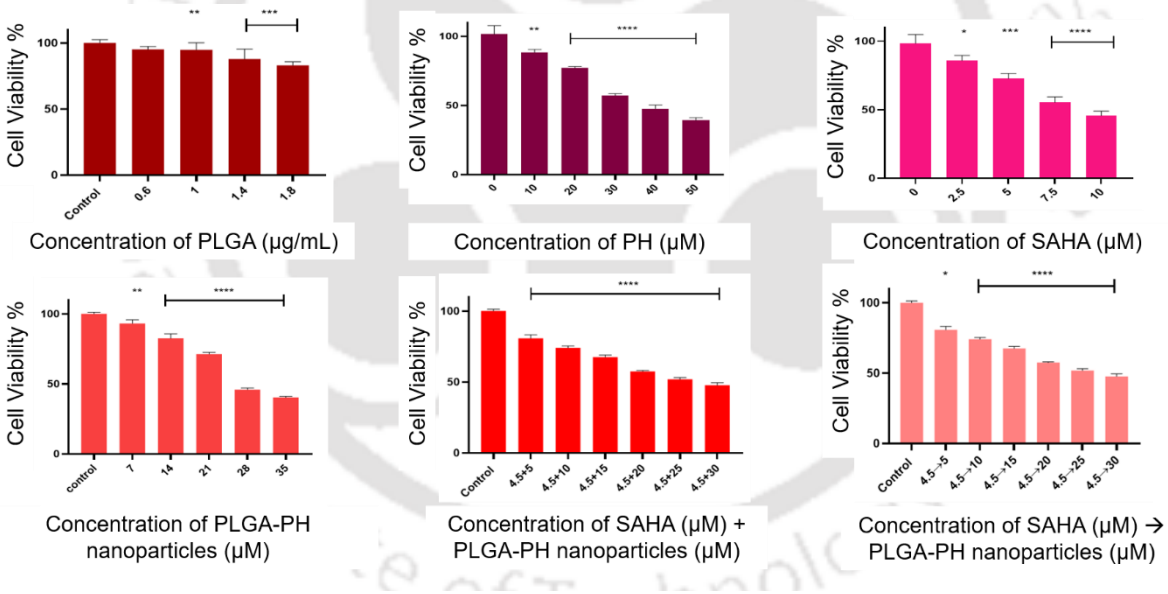

Figure 3.3.8. Graphical representation of the results of cell viability assay performed on HEK-293 monolayer cells. The ANOVA test revealed statistical significance of treated cells with respect to control. Statistical significance is denoted by * ($p < 0.05$), ** ($p < 0.005$), *** ($p < 0.001$), and **** ($p < 0.0001$). The data are represented as mean ± SD of three individual experiments.

3.3.4. PLGA-PH_FITC nanoparticles localise in the cytoplasm. Nanoparticles localisation can provide insights into their anti-proliferative mechanism. Therefore, monolayer cells were incubated with PLGA-PH_FITC nanoparticles for 1 h, following which they were imaged under confocal microscope. It was observed that they had localised exclusively in the cellular cytoplasm in MDA-MB-231 (**Figure 3.3.10. A**) and EMT MDA-MB-231 cells (**Figure 3.3.10. B**).

Additionally, MCF-7 monolayer cells also demonstrated similar homing tendencies (**Figure 3.3.10. C**) whereas untreated cells in all three cases did not exhibit any fluorescence. Time-

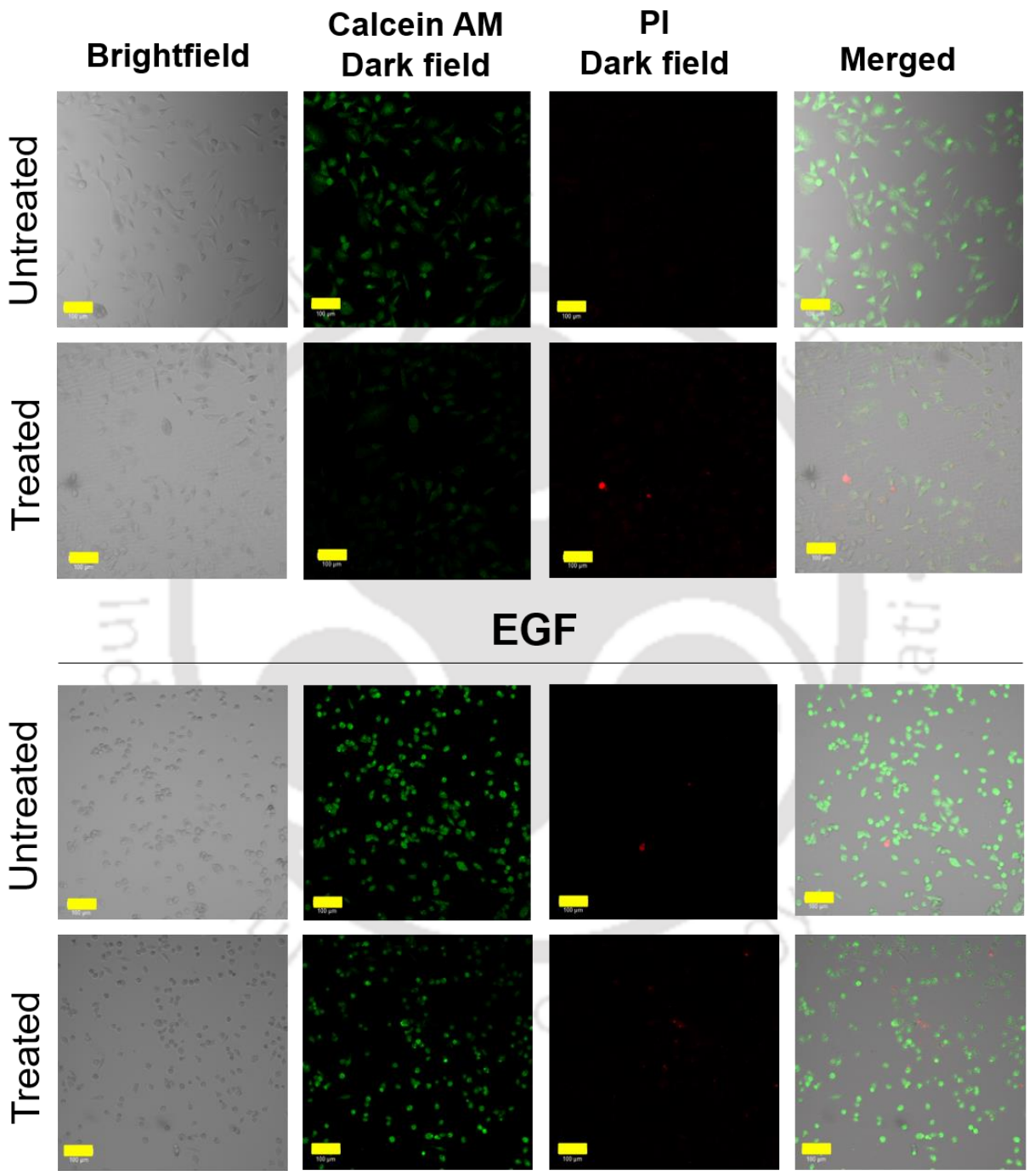

Figure 3.3.9. Induction of cell death in monolayer cells using the pre-treatment method. Live-dead cell imaging of MDA-MB-231 and EMT MDA-MB-231 cells using Calcein AM/PI dual stains (scale-100 µm). Live cells stained by Calcein AM fluoresce green and dead cells stained by PI, fluoresce red. Decreased green fluorescence and increased red fluorescence expounds the efficient cell death induction following pre-treatment.

dependent uptake of the nanoparticles analysed through flowcytometry also corroborated similar results (**Figure 3.3.10. D-F**).

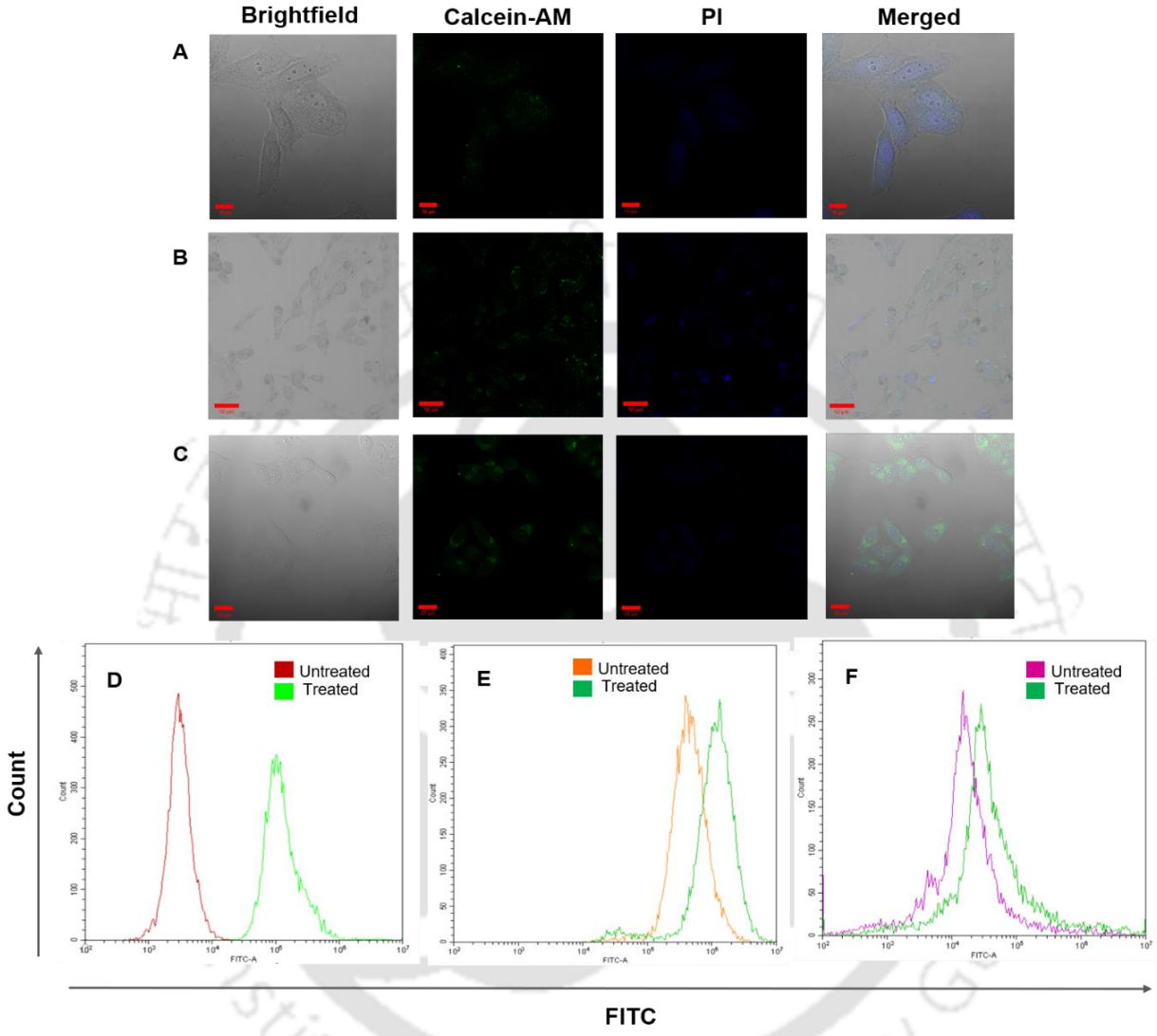

Figure 3.3.10. Cellular localisation of PLGA-PH_FITC nanoparticle imaged in (A) MDA-MB-231 (scale – 10 µm) and (B) EMT MDA-MB-231 (scale – 50 µm) monolayer cells. DAPI was used as a nuclear counterstain. Time-dependent uptake of PLGA-PH_FITC nanoparticles in (D) MDA-MB-231, (E) EMT MDA-MB-231 and (F) MCF-7 cells.

3.3.5. Pre-treatment incites ROS production, depolarizes mitochondrial membrane potential and triggers apoptosis. The cytotoxic effects of pre-treatment could be connected to a variety of mechanistic manifestations; first of these being a significant increase in ROS production. This was confirmed through DCF-DA-based flowcytometry. A noticeable amount of ROS was generated following pre-treatment for 6 h, in contrast to control cells **(Figure 3.3.11. A, B)**. Also, at the same concentrations, treatment with free promethazine and SAHA

alone resulted in less ROS production compared to the pre-treatment regime. SAHA and its

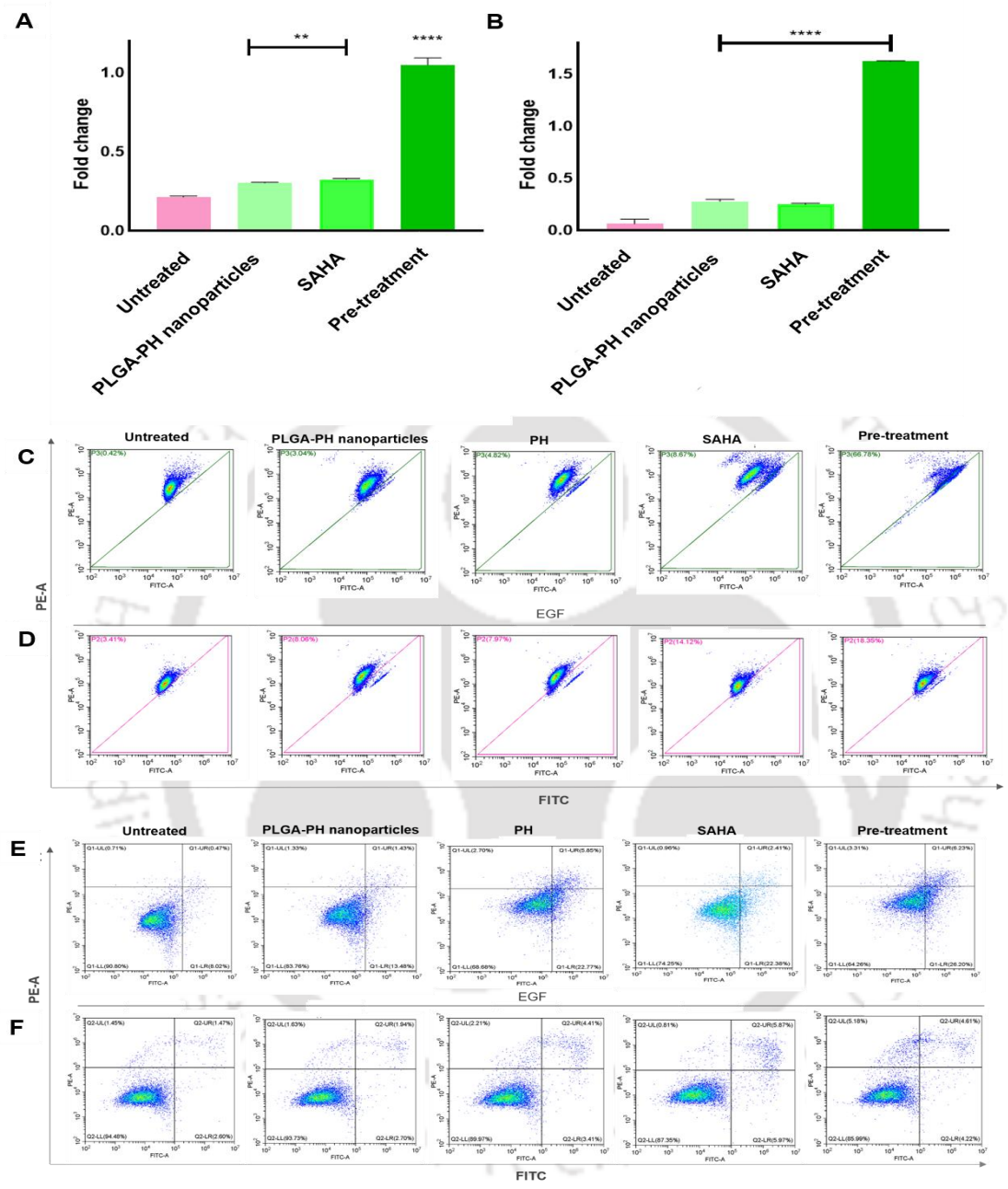

Figure 3.3.11. DCFDA- based ROS detection in (A) MDA-MB-231 cells and (B) EMT MDA-MB-231 cells. Detection of apoptotic population in (c) MDA-MB-231 and (D) EMT MDA-MB-231 cells using Annexin V-FITC apoptosis detection kit. Green fluorescence indicates Annexin FITC binding to the phosphatidyl serine of the exposed lower leaflet. The red fluorescence indicates PI binding to the permeable cells. Mitochondrial membrane potential depolarization detection by JC-1 dye-based flowcytometric assay in (E) MDA-MB-231 and (F) EMT MDA-MB-231 cells. Green fluorescence depicts the potential-dependent accumulation of JC-1 dye in mitochondria. The decrease in red/green intensity ratio indicates mitochondrial depolarization. All comparisons made with respect to control vs. test samples.

anti-proliferative activity owing to ROS generation has been investigated before.[266] It has been known to generate ROS in NB4 and U937 cells[267]. Similarly, the phenothiazine class of compounds too have been studied for their anti-cancer activity, where Trifluoperazine alone generated moderate intracellular ROS in U1810 cells[268], while Bleomycin and Cisplatin synergistically augmented ROS production by several fold. Trifluoperazine was also modified to form A4 [10-(3-(piperazin-1-yl)propyl)-2-(trifluoromethyl)-10H-phenothiazine], which exhibited multi-fold higher apoptosis-inducing activity than the parent compound in Ca922 oral cancer cells.[269] Thus, the equilibrium shifting ROS generation in the treated cells may have been a result from the combined effect of pre-treatment. This concurs with the results of MTT assay too, that suggested that the number of cells were halved at the cell's respective IC_{50} concentration.

Table 3.3.3. Tabulation of % mitochondrial membrane depolarization and % apoptotic population in MDA-MB-231 and EMT MDA-MB-231 cells.

	PH-PLGA nanoparticles	PH	SAHA	Pre-treatment
EMT induced monolayer cells (%)				
% Mitochondrial membrane depolarization	3.41	7.97	14.12	18.35
% Apoptotic population	6.27	10.03	12.65	14.01
Monolayer cells (%)				
% Mitochondrial membrane depolarization	3.04	4.82	8.67	66.78
% Apoptotic population	16.24	31.32	25.75	35.74

Elevated ROS levels often channel their pernicious effects through alteration of mitochondrial membrane. To assess the same, JC-1 based flowcytometry was performed in treated monolayer cells. JC-1, a cyanin dye exists as an aggregate in healthy mitochondria exhibiting red fluorescence, while it fluoresces green and exists as a monomer in unhealthy mitochondria. Treated MDA-MB-231 cells demonstrated 66.78% (**Figure 3.3.11. C**) and EMT MDA-MB-231 cells (**Figure 3.3.11. D**) showed 18.35% increase in green fluorescence (**Table 3.3.3.**). Overall, this suggests the loss of mitochondrial membrane integrity due to excessive ROS production.

ROS imbalance and depolarization of mitochondrial membrane potential often are the precursors of programmed cell death. Hence, the apoptotic population was detected using annexin V-FITC/PI apoptosis assay. It was observed that pre-treated cells resulted in 35.74%

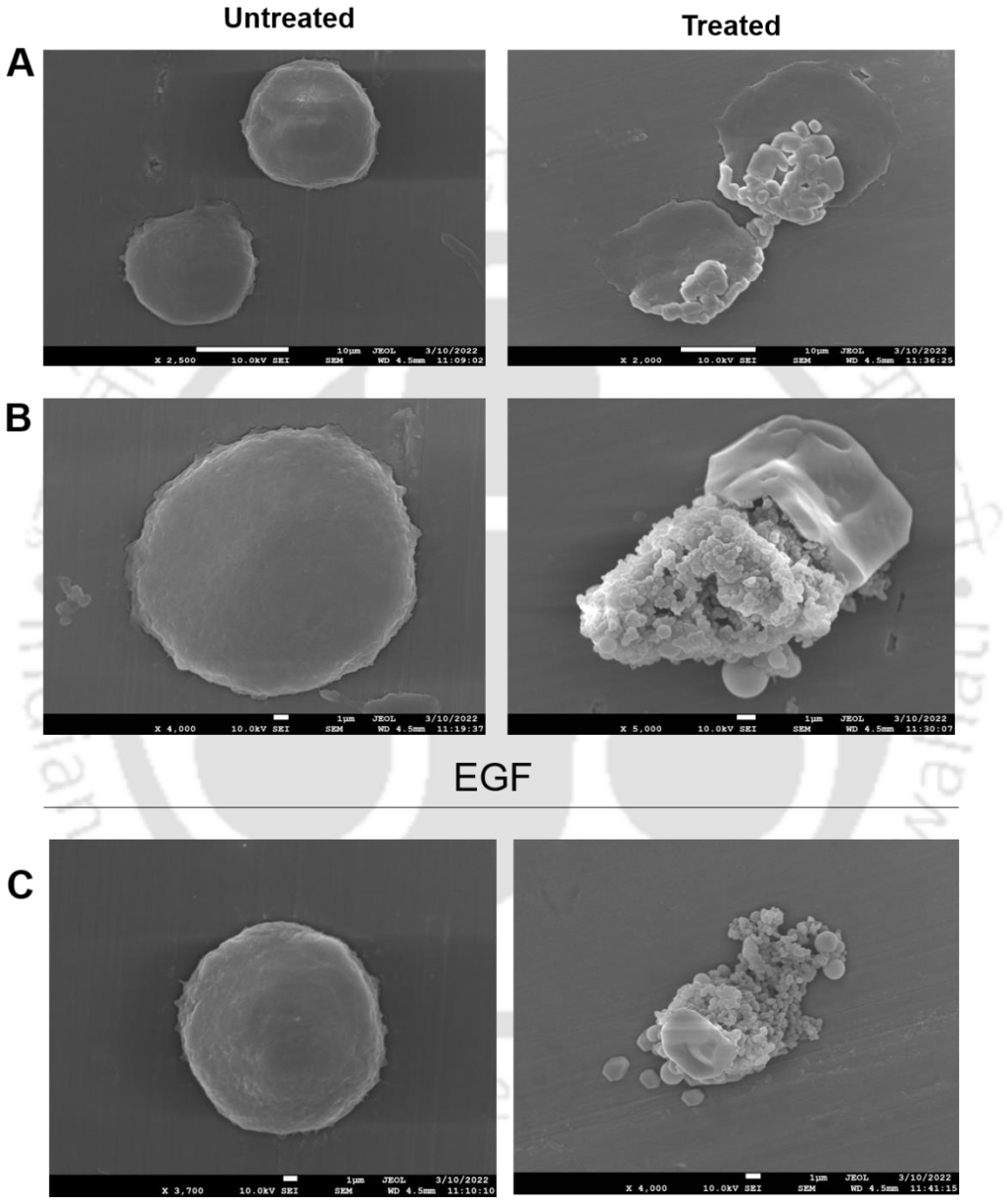

Figure 3.3.12. Alteration in cell morphology in treated cells via FESEM imaging in (A) MDA-MB-231 and (B) MCF-7 cells, (C) EMT MDA-MB-231 cells.

and 14.01% increase in apoptotic population in MDA-MB-231 (**Figure 3.3.11. E**) and EMT MDA-MB-231 cells (**Figure 3.3.11. F**), respectively (**Table 3.3.3.**). Also, the necrotic population remained insignificant in treated cells, an indicator of the therapy's potential of killing cancer cells without the deleterious effects of necrosis. Interestingly, SAHA-treated

cells also exhibited a higher apoptotic population indicating the HDACi's prominent role in inducing apoptosis in TNBC cells.

To study the morphology of pre-treated cells, FESEM microscopy (JEOL JSM-7610F) was conducted. Treated cells at IC_{50} concentration for 12 h show visible blebbing, an indicator of apoptotic pathway (**Figure 3.3.12.**). The mechanism behind such an alteration can be possibly due to the accumulation of ROS, which results in disruption of protein and lipid bilayer, leading to a loss of cell membrane integrity. Besides, ROS can also act as a step towards apoptosis, that is discerned by a plethora of morphological changes such as shrinkage, breakage and membrane blebbing.[270,271] Hence, the findings suggested that the combination of SAHA and PLGA-PH nanoparticles suitably bring about morphological deformation of treated cells that is symbolic of their intracellular changes.

3.3.6. Pre-treatment regime halts EMT progression. EMT in TNBC cells is characterised by increase in mesenchymal features and reduction in epithelial features. Since the basal MDA-MB-231

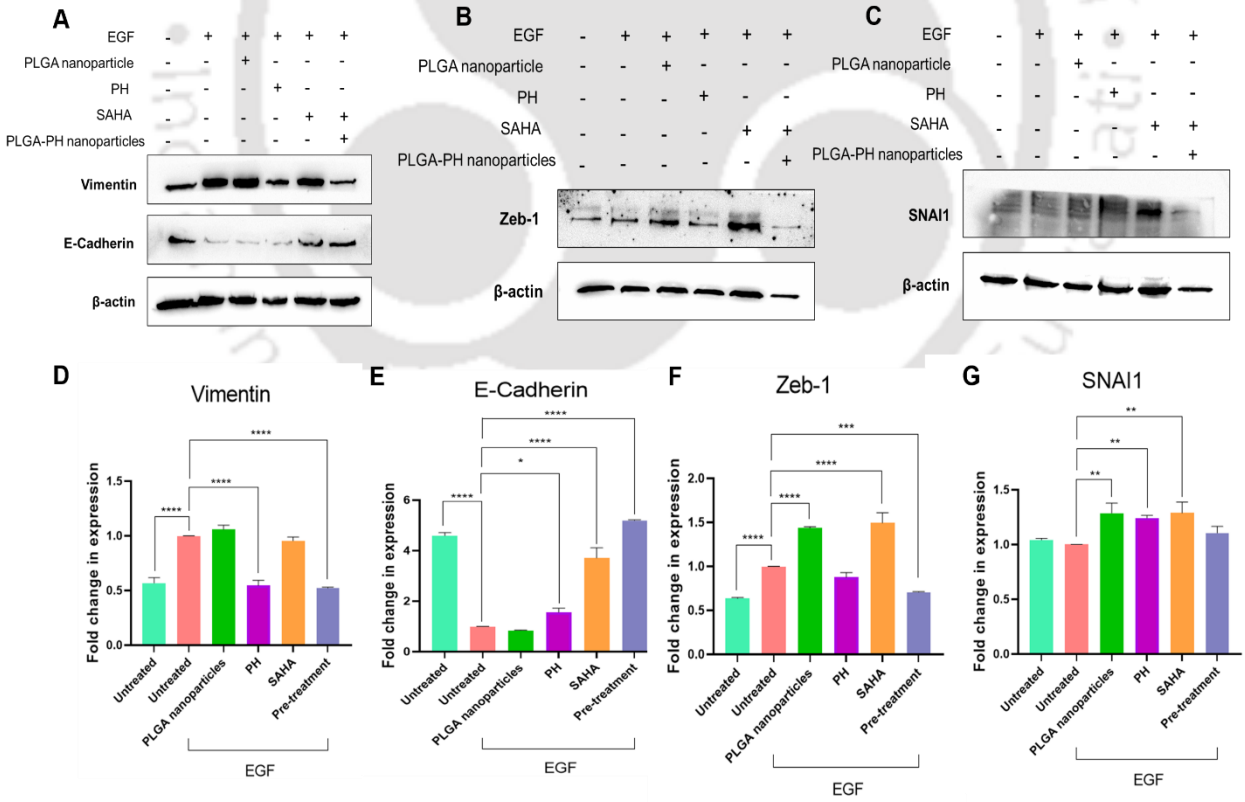

Figure 3.3.13. Representative immunoblots showing the expression of EMT protein markers (A) and EMT-TFs (B, C) in MDA-MB-231 cells. Graphical representation of the fold change in protein expression in (D) Vimentin, (E) E-Cadherin, (F) Zeb-1 and (G) SNAI1 in MDA-MB-231 cells. B-actin serves as a loading control.

cell line is highly responsive to the anti-proliferative effects of SAHA, it has been used as a model to study EMT phenomenon when exposed to the pre-treatment regime. Therefore, to assess the alterations in molecular mechanisms of EMT following pre-treatment, immunoblot analysis was performed (**Figure 3.3.13.**). For comparisons, the cells were also subjected to monotherapy.

As and when EMT progresses, there is loss of E-Cadherin, which is a cell-cell junction protein. They play a predominant role in epithelial cell adhesion and maintenance of tissue architecture. The protein expression profile of E-Cadherin increased by 1.42-fold following pre-treatment in MDA-MB-231 cells. While with PH treatment the increase was 1.16-fold, with SAHA treatment it was 1.26-fold. Similarly, vimentin too is acknowledged as a canonical biomarker of EMT. Vimentin filaments are known to protect cells from mechanical stress during metastasis, thus keeping the integrity of nucleus and other organelles intact. Following pre-

Table 3.3.4. Fold change in protein expression in EMT MDA-MB-231 cells.

Protein	MDA-MB-231				
	Untreated	**PLGA nanoparticles**	**PH**	**SAHA**	**Pre-treatment**
E-Cadherin	1.27	1.01	1.16	1.26	1.42
Vimentin	1.68	1.08	1.67	1.03	1.90
SNAI1	1.05	1.32	1.27	1.39	1.08
Zeb-1	1.58	1.45	1.09	1.56	1.41

treatment, vimentin expression had reduced by 1.90-fold, while upon monotherapy with PH and SAHA it had reduced by 1.67-fold and 1.03-fold. Apart from these two proteins, EMT is also enabled by transcription factors of zinc-finger proteins like SNAI1 and zinc-finger E-box-binding-homeobox protein like Zeb. SAHA upregulated the expression of SNAI1 by 1.39-fold which higher than that of pre-treatment (1.08-fold). While pre-treatment ensured the downregulation of Zeb-1 by 1.41-fold, SAHA interestingly upregulated its expression by 1.56-fold. It could be attributed to the findings that although HDACis show anti-proliferative activity against many cancers, they also promote EMT in some, including TNBC.[272] The fold change table of protein expression profile have been mentioned in **Table 3.3.4**. Hence, the protein expression profile suggested that promethazine hydrochloride abrogates SAHA facilitated

EMT at the molecular level. Altogether, the findings cement the pre-treatment regime's ability to curb the metastatic potential of TNBC.

3.3.7. PLGA-PH nanoparticles exposure following SAHA pre-treatment inhibits the proliferative potential of TNBC. The proliferative potential of TNBC is often correlated to stem-cell-like property among others such as self-renewal and colony forming ability. Therefore, sphere formation assay was performed to determine the proliferative potential of cancer stem cells (CSCs) in forming solid tumors in non-adherent serum-free gel matrix

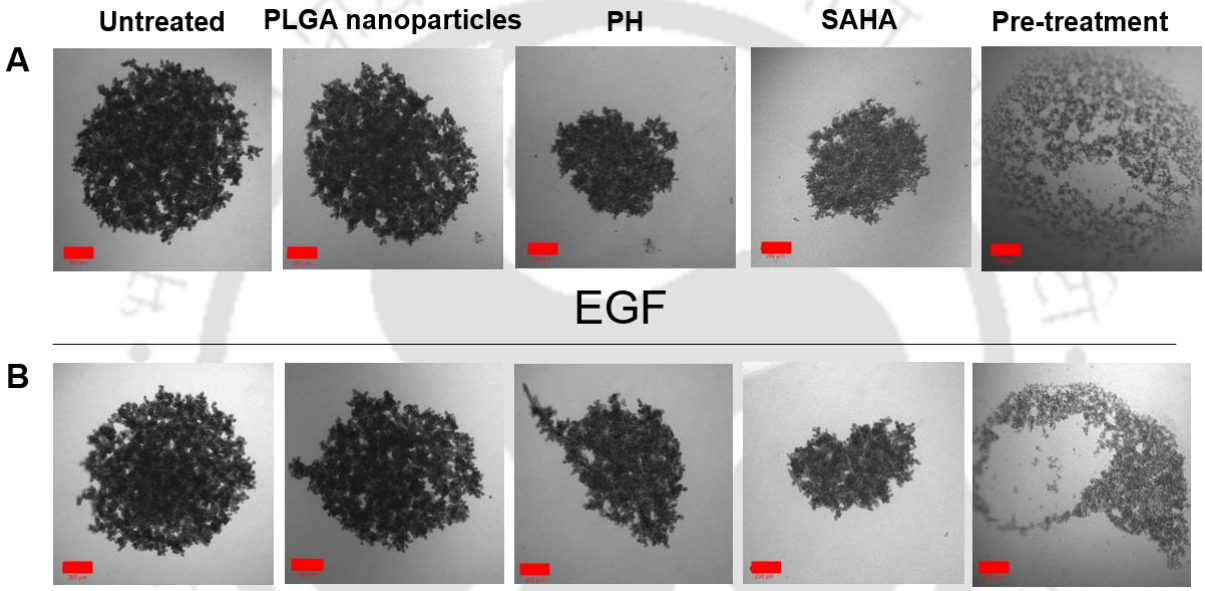

Figure 3.3.14. Sphere formation ability assessed on spheroids created from (A) MDA-MB-231 and (B) EMT MDA-MB-231 cells (Scale- 200 µm).

(**Figure 3.3.14.**). The pre-treatment approach of combination therapy greatly reduced their sphere forming ability. Representative confocal bright-field images reveal unfastened chunks of would-be spheroid. However, monotherapy with PH and SAHA mostly resulted in the formation of smaller spheroids.

3.3.8. Pre-treatment impedes the viability of TNBC spheroids. Multicellular spheroids (MCTs) are now routinely utilised to study cell metabolism, tumor growth and drug delivery systems. They display startling similarities to solid tumors, especially spheroids with diameter >400 µm. Such spheroids usually have an exterior layer of proliferating cells, an intermediate layer of quiescent cells and a necrotic core.[273] Therefore, to explore and extrapolate the potential of SAHA and PLGA-PH nanoparticles in spheroids, viability assay was performed

on them. Spheroids created via force floatation method were treated with PLGA nanoparticles, PH, SAHA and the pre-treatment combination approach. Following 72 h of exposure, the IC_{50} values were lowered in case of pre-treatment exhibiting a dose-dependent reduction in cell viability (**Figure 3.3.15.**). IC_{50} values of all spheroid treatments have been tabulated in **Table 3.3.2**.

To further establish the spheroid inhibiting potential of SAHA and PLGA-PH nanoparticles, treated and untreated spheroids were visualised under confocal microscope. The live/dead

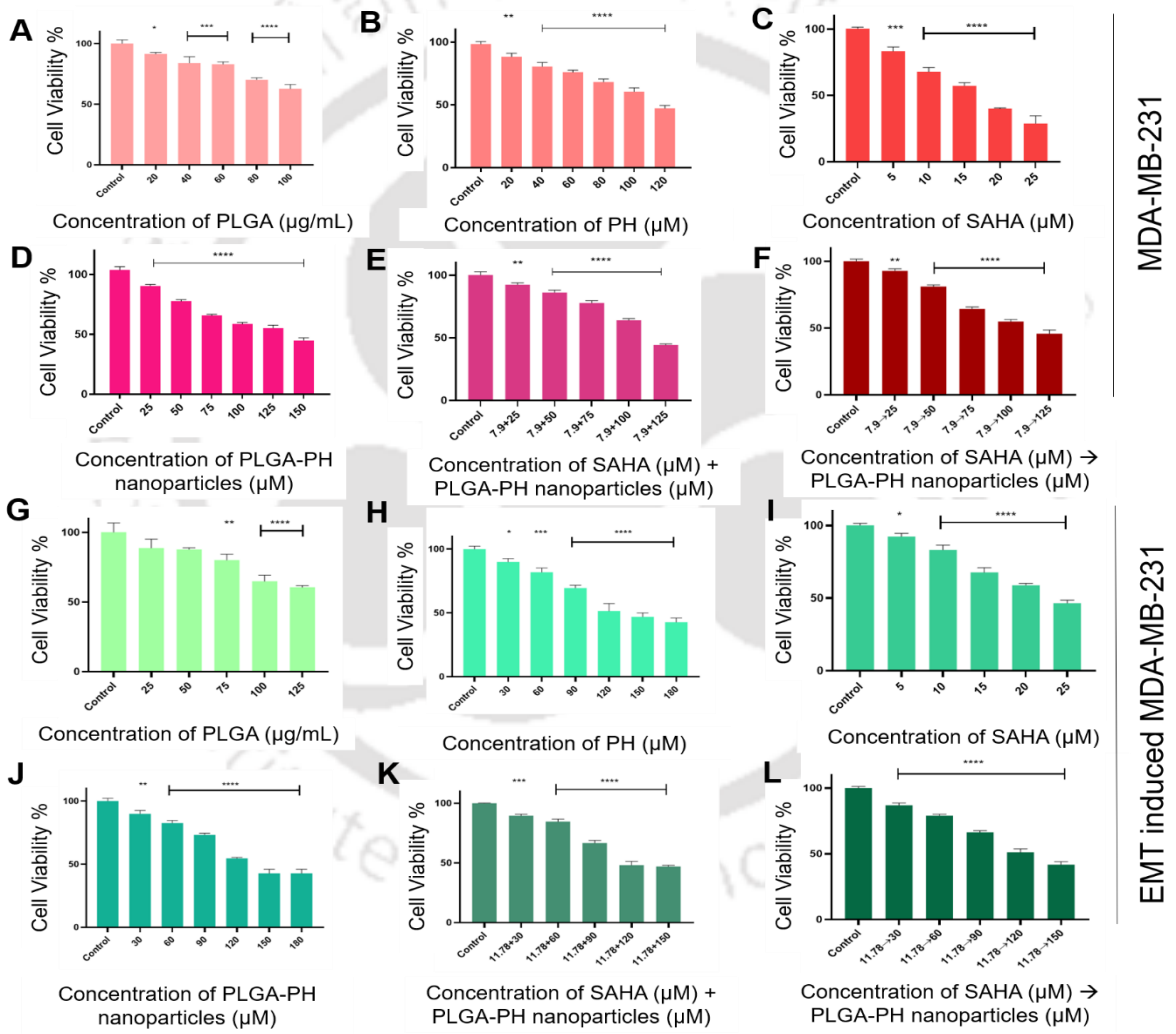

Figure 3.3.15. Anti-proliferative effect of combination therapy on 3D multicellular spheroids. They were treated with PLGA nanoparticles (A, G); PH (B, H); SAHA (C, I); PLGA-PH nanoparticles (D, J); co-treatment with SAHA and PLGA-PH nanoparticles and pre-treatment with SAHA and PLGA-PH nanoparticles. The ANOVA test revealed statistical significance of treated spheroids with respect to control. Statistical significance is denoted by * ($p < 0.05$), ** ($p < 0.005$), *** ($p < 0.001$), and **** ($p < 0.0001$). The data are represented as mean ± SD of three individual experiments.

imaging of spheroids reveal the inhibitory effects on both MDA-MB-231 and EMT MDA-MB-231 spheroids. The treated MDA-MB-231 spheroids revealed a disintegrated periphery with a more or less intact core and high red fluorescence (**Figure 3.3.16. A**). Interestingly, EMT MDA-MB-231 spheroids demonstrated only the increase in dead cell number as compared to its untreated counterpart (**Figure 3.3.16. B**). The spheroid itself, however remained intact but a little shrunk.

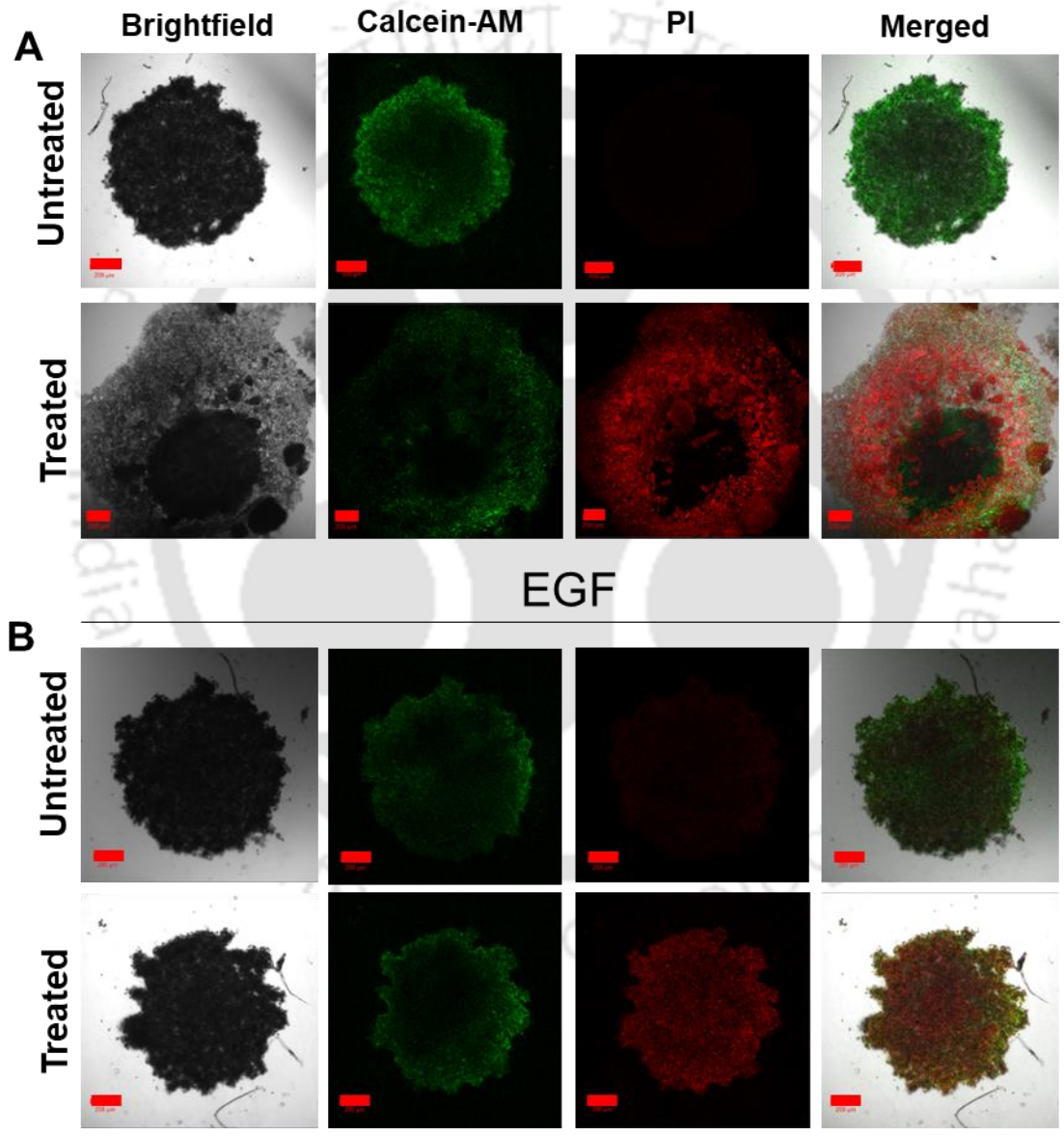

Figure 3.3.16. Live-dead spheroids imaged through confocal microscopy using Calcein AM/PI dual stains in (A) MDA-MB-231 and (B) EMT MDA-MB-231 spheroids. Green fluorescence due to Calcein AM indicates live cells while red fluorescence due to PI depicts dead cells (Scale - 200 μm).

3.2.9. Summary

Owing to its inherent molecular and histopathologic complexity, TNBC poses a major health risk today. Its aggressiveness combined with the lack of targeted therapies and overly stretched *de novo* drug development timeline strongly reduces the chance of patient recovery and survival. Rescuing or repurposing orphan or licensed drugs, respectively can bring about a new paradigm in the healthcare field. While ensuring patient safety, it can also lower time and expenditures involved, because of previously recognised safety and kinetic profiles. The importance of fresh trials however, before establishing any drug's role in a totally different indication, goes without saying. Experimental screening of several over the counter antihistamines helped us narrow down our search to promethazine hydrochloride, a first-generation phenothiazine. Consecutively, a regimen with promethazine loaded PLGA nanoparticles in combination with a well-known HDACi, SAHA was structured. After exploring two different approaches, pre-treatment fared better as treating cells with SAHA for 7 h sensitized them more towards PLGA-PH nanoparticles. Following viability assays, IC_{50} values from pre-treatment were lowered considerably in comparison to monotherapy. Further investigation also proved the biocompatibility of PLGA nanoparticles and their use as theranostics due to conjugation with FITC. Functional assessment revealed mitochondrial membrane depolarisation and apoptosis, initiated because of profound ROS generation. Pre-treatment also suggestively reduced the proliferative potential of cells. Additionally, spheroid viability assays also demonstrated a dose-dependent reduction along with increase in dead cells as indicated by increase in PI induced red fluorescence. Considering the limited insight into TNBC progression, the combined roles of SAHA and PLGA-PH nanoparticles in altering EMT dynamics was also investigated. Individually, SAHA can facilitate EMT progress in TNBC. However, immunoblots revealed significant reduction in mesenchymal protein expression. Inclusively, the present findings indicate a better action plan with the pre-treatment regimen of combination therapy and validate the current need to repurpose, rescue and redirect. This will fast track the drug developmental pipeline, thus helping to combat the dreadful TNBC.

Chapter 4

Conclusion and Future Prospects

Conclusion and Future Prospects

5.1 Conclusion

Recent improvements in our understanding of cancer origins, growth and metastasis have led to ground-breaking treatments and diagnostics. The quest for a gold standard treatment however, still remains elusive. As cancer is a many-headed monster, dual therapies can help target its various aspects and prevent relapse. Hence, the current dissertation aims towards developing multi-faceted regimes involving repurposed drugs and nanoscale materials.

This thesis includes exploratory, experimental and quantitative studies. It aims at extrapolating the benefits of drug repurposing through the nano realms. While nanomaterials help with stability, solubility and selectivity; repurposed drugs are sustainable and safe. Together, they can smoothen the edges of a therapeutic module that would otherwise be unreliable. Since inflammation is often correlated with cancer, the anti-proliferative potential of antihistamines was explored. Following the experimental screening of several over the counter drugs, promethazine hydrochloride and levocetirizine dihydrochloride were sieved in. Further investigations demonstrated promethazine's obvious potential against triple-negative cancer and levocetirizine's against lung adenocarcinoma. Anti-bacterial studies also demonstrated promethazine's remarkable inhibitory abilities.

In the first study, promethazine-gold nanoclusters were mannosylated to neutralize the Gram-negative bacterial appendage, pili. Their superior antimicrobial property was further assessed through their leakage potential and ability to create oxidative stress. Additional investigations also revealed stark reduction in lipid content which is often connected to pathogenicity. Comparable to antibiotics, biofilm eradication was achieved using the nanoclusters. Besides antimicrobial activity, the mannosylated promethazine-gold nanoclusters were also ideal for real-time tracking due to their luminescent property.

In view of a drug's inherent ability to affect normal cells/tissues, a nanocomposite for the delivery of levocetirizine to the lung adenocarcinoma cells was designed. Levocetirizine conjugated copper nanoclusters were loaded onto chitosan nanoparticles, where the chitosan itself was mannose conjugated. Mannosylation was an attempt at the selective reduction of off-target hits, as lung adenocarcinoma cells over-express surface mannose receptors. The resultant

nanocomposite was an ideal 107 nm in size, stable, biocompatible and fluorescent. Subsequent functional assessments demonstrated remarkable reduction in cell viability due to oxidative damage and mitochondrial depolarization. Cells exposed to the nanocomposite also suffered reduced proliferative potential, lipid droplet and wound healing abilities. Treated lung adenocarcinoma spheroids also had a greater number of dead cells.

The final investigation involved a dual regime structured to act on TNBC cells. SAHA, an HDACi was used to pre-sensitize cells to PLGA nanoparticles loaded with promethazine. In comparison to co-treatment, pre-treating the cells invariably lowered IC_{50} across cell lines preceded by disruption of oxidative homeostasis and depolarization of mitochondria. Mesenchymal protein expression was reduced to alter the EMT dynamics. In addition, cytotoxicity was prominent in the TME mimicking spheroids, as established by lower viability and altered integrity.

5.2 Future prospects

Although the advantages of drug repurposing are ostensible, there has always persisted some hesitance among drug developers regarding allocating resources for research on approved drugs. Thus, augmenting the idea of repositioning with nanotechnology can present a sustainable and workable strategy. Channelling the combined benefits of nanomaterials with repurposed drugs attributes a paradigm shift in the medical field. It is unquestionable that nanomaterials present a versatile platform for repurposing drugs by addressing challenges related to drug delivery, efficacy, and targeted release. They offer the potential of maximizing therapeutic effect on new targets and expanding their applications for infectious diseases including, bacterial, parasitic, fungal and viral diseases. The nano-enhanced repurposed therapeutics can be further modified to evade immune system. This will increase their circulation span and efficacy. Since TME mimicking spheroids bridge the gap between *in vitro* and *in vivo* research, they can be deployed extensively for further understanding of solid tumors. The difference in molecular responses following treatment in monolayer and spheroids can be explored in future studies. Further, *in vivo* investigations would be able to solidify the use of regimes from this study as a therapeutic module. Altogether, we are hopeful that the numerous findings from this thesis will pave certain prospects for future investigations that further cement the faith in repurposing.

References

1. Faguet, G. B. A brief history of cancer: Age-old milestones underlying our current knowledge database. *Int. J. Cancer* **136**, 2022–2036 (2015).

2. Rakoff-Nahoum, S. Why cancer and inflammation? *Yale J. Biol. Med.* **79**, 123–130 (2006).

3. Guan, X. Cancer metastases: Challenges and opportunities. *Acta Pharm. Sin. B* **5**, 402–418 (2015).

4. Hanahan, D. & Weinberg, R. A. Hallmarks of cancer: The next generation. *Cell* **144**, 646–674 (2011).

5. Heerboth, S. *et al.* EMT and tumor metastasis. *Clin. Transl. Med.* **4**, (2015).

6. Chunhacha, P., Sriuranpong, V. & Chanvorachote, P. Epithelial-mesenchymal transition mediates anoikis resistance and enhances invasion in pleural effusion-derived human lung cancer cells. *Oncol. Lett.* **5**, 1043–1047 (2013).

7. Huang, Y., Hong, W. & Wei, X. The molecular mechanisms and therapeutic strategies of EMT in tumor progression and metastasis. *J. Hematol. Oncol.* **15**, 1–27 (2022).

8. GLOBOCAN. Global Cancer Statistics 2020: GLOBOCAN Estimates of Incidence and Mortality Worldwide for 36 Cancers in 185 Countries. *Global Cancer Statistics* vol. 163 1–2.

9. Jourdan, J.-P., Bureau, R., Rochais, C. & Dallemagne, P. Drug repositioning: a brief overview. 1145–1151 (2020).

10. Lucio, O. M.- & Navega, J. J. One Drug for Multiple Targets: A Computational Perspective. 168–181 (2016).

11. Anighoro, A., Bajorath, J. & Rastelli, G. Polypharmacology: Challenges and opportunities in drug discovery. *Journal of Medicinal Chemistry* vol. 57 7874–7887 (2014).

12. Zhang, Z. *et al.* Overcoming cancer therapeutic bottleneck by drug repurposing. *Signal Transduction and Targeted Therapy* vol. 5 (2020).

13. Ko, Y. Computational drug repositioning: Current progress and challenges. *Appl. Sci.* **10**, 4–9 (2020).

14. Mottini, C., Napolitano, F. & Li, Z. Computer aided drug repurposing for cancer therapy: Approaches and opportunities to challenge anticancer targets. 59–74 (2021).

15. Silver, L. L. Challenges of antibacterial discovery. *Clin. Microbiol. Rev.* **24**, 71–109 (2011).

16. Clark, J. A. & Burgess, D. S. Plazomicin: a new aminoglycoside in the fight against antimicrobial resistance. *Ther. Adv. Vaccines* **7**, 1–15 (2020).

17. File, T. M. *et al.* Lefamulin efficacy and safety in a pooled phase 3 clinical trial population with community-acquired bacterial pneumonia and common clinical comorbidities. *BMC Pulmonary Medicine* vol. 21 1–10 (2021).

18. Böttcher, L., Gersbach, H. & Wernli, D. Restoring the antibiotic R&D market to combat the resistance crisis. *Sci. Public Policy* **49**, 127–131 (2022).

19. Nikaido, H. Multidrug resistance in bacteria. *Annu. Rev. Biochem.* **78**, 119–146 (2009).

20. Ashburn, T. T. & Thor, K. B. Drug repositioning: Identifying and developing new uses for existing drugs. *Nat. Rev. Drug Discov.* **3**, 673–683 (2004).

21. Paolini, G. V, Shapland, R. H. B., Hoorn, W. P. van, Mason, J. S. & Hopkins, A. I. Global mapping of pharmacological space. 805–815 (2006).

22. Koch, U., Hamacher, M. & Nussbaumer, P. Cheminformatics at the interface of medicinal chemistry and proteomics. *Biochimica et Biophysica Acta - Proteins and Proteomics* vol. 1844 156–161 (2014).

23. Hodos, R. A., Kidd, B. A., Shameer, K., Readhead, B. P. & Dudley, J. T. In silico methods for drug repurposing and pharmacology. *Wiley Interdiscip. Rev. Syst. Biol. Med.* **8**, 186–210 (2016).

24. Mazumder, R., Chaudhuri, S. R. & Mazumder, A. Antimicrobial potentiality of a phenothiazine group of antipsychotic drug-prochlorperazine. *Indian J. Exp. Biol.* **40**, 828–830 (2002).

25. Sui, S. J. H. Raloxifene attenuates PA pyocyanin production and virulence. 246–251 (2012).

26. Rizzo, A. *et al.* Zoledronic acid affects the cytotoxic effects of Chlamydia pneumoniae and the modulation of cytokine production in human osteosarcoma cells. *International Immunopharmacology* vol. 22 66–72 (2014).

27. Lima e Silva, A. A. de & Martins Silva, P. Non-Antibiotic Compounds: The Activity of the NSAID Diclofenac on Bacteria- A Review. *Int. J. Curr. Microbiol. Appl. Sci.* **7**, 340–351 (2018).

28. Schein, C. H. Repurposing approved drugs for cancer therapy. *Br. Med. Bull.* **137**, 13–27 (2021).

29. Sleire, L. & Forde, H. E. Drug repurposing in cancer. (2017).

30. Ahmad, S., Qazi, S. & Raza, K. Translational bioinformatics methods for drug discovery and drug repurposing. *Translational Bioinformatics in Healthcare and Medicine* vol. 13 127–139 (2021).

31. Gonzalez-Fierro, A. & Dueñas-González, A. Drug repurposing for cancer therapy, easier said than done. *Semin. Cancer Biol.* **68**, 123–131 (2021).

32. Devarakonda, S., Morgensztern, D. & Govindan, R. Genomic alterations in lung adenocarcinoma. *Lancet Oncol.* **16**, e342–e351 (2015).

33. Lee, W. H. *et al.* The potential to treat lung cancer via inhalation of repurposed drugs. *Adv. Drug Deliv. Rev.* **133**, 107–130 (2018).

34. Saxena, A. *et al.* Therapeutic Effects of Repurposed Therapies in Non-Small Cell Lung Cancer: What Is Old Is New Again. *Oncologist* **20**, 934–945 (2015).

35. Ávalos-Moreno, M. *et al.* Drug repurposing for triple-negative breast cancer. *J. Pers. Med.* **10**, 1–34 (2020).

36. Correia, A. S., Gärtner, F. & Vale, N. Drug combination and repurposing for cancer therapy: the example of breast cancer. *Heliyon* **7**, (2021).

37. Hussain, S. P. & Harris, C. C. Inflammation and cancer An ancient link with novel

potentials. 2373–2380 (2007).

38. Faustino-Rocha, A. I., Ferreira, R., Gama, A., Oliveira, P. A. & Ginja, M. Antihistamines as promising drugs in cancer therapy. *Life Sci.* **172**, 27–41 (2017).

39. Matteoni, S. & Abbruzzese, C. Chlorpromazine induces cytotoxic autophagy in glioblastoma cells via endoplasmic reticulum stress and unfolded protein response. (2021).

40. Prabhu, P., Malli, R. & Koland, M. Formulation and evaluation of fast dissolving films of levocitirizine di hydrochloride. *International Journal of Pharmaceutical Investigation* vol. 1 99 (2011).

41. Takahashi, H., Ishida-Yanamoto, A. & Iizuka, H. Effects of bepotastine cetirizine fexofenadine and olopatadine on histamine induced wheal and flare response sedation and psychomotor performance. (2004).

42. Inceler, N., Yilmaz, A. & Baytas, S. N. Synthesis of ester and amide derivatives of 1-phenyl-3-(thiophen3-yl)-1H-pyrazole-4-carboxylic acid and study of their anticancer activity. (2013).

43. Al-Ghorbani, M., Gouda, M. A. & Ranganatha, L. V. Piperazine hetereocycles as potential anticancer agents: A review. (2022).

44. El-Nakeeb, M. A., Abou-Shleib, H. M., Khalil, A. M., Omar, H. G. & El-Halfwy, O. M. In vitro antibacterial activity of some antihistaminics belonging to different groups against multi-drug resistant clinical isolates. *Brazilian J. Microbiol.* **42**, 980–991 (2011).

45. Nehme, H. Antibacterial activity of antipsychotic agents , their association with lipid nanocapsules and its impact on the properties of the nanocarriers and on antibacterial activity. *PLoS One* **13**, 1–18 (2018).

46. Perlmutter, J. I. Repurposing the antihistamine terfenadine for antimicrobial activity against staphylococcus aureus. *J. Med. Chem.* **57**, 8540–8562 (2014).

47. Areej, S., Sattar, A., Javeed, A. & Raza, S. Diphenhydramine and levofloxacin combination therapy against antimicrobial resistance in respiratory tract infections. *Future Microbiol.* **16**, 409–420 (2021).

48. Mandi, Y., Molnar, J., Holland, I. B. & Beladi, I. Efficient curing of an Escherichia coli F-prime plasmid by phenothiazines.pdf. 109–111 (1975).

49. Shi, J., Votruba, A. R., Farokhzad, O. C. & Langer, R. Nanotechnology in drug delivery and tissue engineering: From discovery to applications. *Nano Lett.* **10**, 3223–3230 (2010).

50. Zhang, L. *et al.* Nanoparticles in medicine: Therapeutic applications and developments. *Clin. Pharmacol. Ther.* **83**, 761–769 (2008).

51. Lammers, T., Hennink, W. E. & Storm, G. Tumour-targeted nanomedicines: Principles and practice. *Br. J. Cancer* **99**, 392–397 (2008).

52. Lammers, T., Kiessling, F., Hennink, W. E. & Storm, G. Drug targeting to tumors: Principles, pitfalls and (pre-) clinical progress. *J. Control. Release* **161**, 175–187 (2012).

53. Sahoo, A. K. & Pant, P. Nanoformulations for Cancer Therapy. 157–181 (2017).

54. Choi, Y. H. & Han, H. K. Nanomedicines: current status and future perspectives in aspect of drug delivery and pharmacokinetics. *J. Pharm. Investig.* **48**, 43–60 (2018).

55. Suk, J. S., Xu, Q., Kim, N., Hanes, J. & Ensign, L. M. PEGylation as a strategy for improving nanoparticle-based drug and gene delivery. *Advanced Drug Delivery Reviews* vol. 99 28–51 (2016).

56. Amoozgar, Z. & Yeo, Y. Recent advances in stealth coating of nanoparticle drug delivery systems. *Wiley Interdisciplinary Reviews: Nanomedicine and Nanobiotechnology* vol. 4 219–233 (2012).

57. Cui, L., Lin, Q., Jin, C. S. & Jiang, W. A PEGylation-Free Biomimetic Porphyrin Nanoplatform for Personalized Cancer Theranostics. 4484–4495 (2015).

58. Luk, B. T. & Zhang, L. Cell membrane-camouflaged nanoparticles for drug delivery. 600–607 (2015).

59. Ealias, A. M. & Saravanakumar, M. P. A review on the classification, characterisation, synthesis of nanoparticles and their application. *IOP Conf. Ser. Mater. Sci. Eng.* **263**, 1–15 (2017).

60. Kashyap, B. K. *et al.* Smart Nanomaterials in Cancer Theranostics: Challenges and Opportunities. *ACS Omega* vol. 8 14290–14320 (2023).

61. Albanese, A., Tang, P. S. & Chan, W. C. W. The effect of nanoparticle size, shape, and surface chemistry on biological systems. *Annu. Rev. Biomed. Eng.* **14**, 1–16 (2012).

62. Preiss, M. R. & Bothun, G. D. Stimuli-responsive liposome-nanoparticle assemblies. *Expert Opin. Drug Deliv.* **8**, 1025–1040 (2011).

63. Kumbhar, P. *et al.* Nanoparticulate drugs and vaccines: Breakthroughs and bottlenecks of repurposing in breast cancer. *Journal of Controlled Release* vol. 349 812–830 (2022).

64. Sen, K. & Mandal, M. Second generation liposomal cancer therapeutics: Transition from laboratory to clinic. *Int. J. Pharm.* **448**, 28–43 (2013).

65. Shukla, S. K. *et al.* Metformin-encapsulated liposome delivery system: An effective treatment approach against breast cancer. *Pharmaceutics* **11**, (2019).

66. Meng, J. *et al.* Combination Therapy using Co-encapsulated Resveratrol and Paclitaxel in Liposomes for Drug Resistance Reversal in Breast Cancer Cells in vivo. *Sci. Rep.* **6**, 1–11 (2016).

67. Matbou Riahi, M., Sahebkar, A., Sadri, K., Nikoofal-Sahlabadi, S. & Jaafari, M. R. Stable and sustained release liposomal formulations of celecoxib: In vitro and in vivo anti-tumor evaluation. *International Journal of Pharmaceutics* vol. 540 89–97 (2018).

68. Jin, M. *et al.* In vivo study of effects of artesunate nanoliposomes on human hepatocellular carcinoma xenografts in nude mice. *Drug Delivery* vol. 20 127–133 (2013).

69. Jain, R. K. & Stylianopoulos, T. Delivering nanomedicine to solid tumors. *Nat. Rev. Clin. Oncol.* **7**, 653–664 (2010).

70. Narang, A., Chang, R.-K. & Hussain, M. A. Pharmaceutical Development and Regulatory Considerations for Nanoparticles and Nanoparticulate Drug Delivery Systems. *J. Pharm. Sci.* **102**, 3867–3882 (2013).

71. Duncan, R. Polymer conjugates as anticancer nanomedicines. *Nat. Rev. Cancer* **6**, 688–701 (2006).

72. Pridgen, E. M., Langer, R. & Farokhzad, O. C. Biodegradable, polymeric nanoparticle delivery systems for cancer therapy. *Nanomedicine* **2**, 669–680 (2007).

73. Moghimi, S. M. Recent developments in polymeric nanoparticle engineering and their applications in experimental and clinical oncology. *Anticancer. Agents Med. Chem.* **6**, 553–561 (2006).

74. Banerjee, S. S., Aher, N., Patil, R. & Khandare, J. Poly(ethylene glycol)-Prodrug Conjugates: Concept, Design, and Applications. *J. Drug Deliv.* **2012**, 1–17 (2012).

75. Sah, H., Thoma, L. A., Desu, H. R., Sah, E. & Wood, G. C. Concepts and practices used to develop functional PLGA-based nanoparticulate systems. *Int. J. Nanomedicine* **8**, 747–765 (2013).

76. Cleveland, M. V, Flavin, D. P., Ruben, R. A., Epstein, R. M. & Clark, G. E. New polyethylene glycol laxative for treatment of constipation in adults: a randomized, double-blind, placebo-controlled study. *South. Med. J.* **94**, 478–481 (2001).

77. Knop, K., Hoogenboom, R., Fischer, D. & Schubert, U. S. Poly(ethylene glycol) in drug delivery: Pros and cons as well as potential alternatives. *Angew. Chemie - Int. Ed.* **49**, 6288–6308 (2010).

78. Kommareddy, S., Tiwari, S. B. & Amiji, M. M. Long-circulating polymeric nanovectors for tumor-selective gene delivery. *Technol. Cancer Res. Treat.* **4**, 615–625 (2005).

79. Gundersen, E. T. & Forde, J.-L. Repurposing chlorpromazine for anti-leukaemic therapy by nanoparticle encapsulation. (2021).

80. Astete, C. E. & Sabliov, C. M. Synthesis and characterization of PLGA nanoparticles. *J. Biomater. Sci. Polym. Ed.* **17**, 247–289 (2006).

81. Li, S. & McCarthy, S. Influence of crystallinity and stereochemistry on the enzymatic degradation of poly(lactide)s. *Macromolecules* **32**, 4454–4456 (1999).

82. Muthu, M. S. Nanoparticles based on PLGA and its co-polymer: An overview. *Asian J. Pharm.* **3**, 266–273 (2009).

83. Gilding, D. K. & Reed, A. M. Biodegradable polymers for use in surgery-polyglycolic/poly(actic acid) homo- and copolymers: 1. *Polymer (Guildf).* **20**, 1459–

1464 (1979).

84. Acharya, S. & Sahoo, S. K. PLGA nanoparticles containing various anticancer agents and tumour delivery by EPR effect. *Adv. Drug Deliv. Rev.* **63**, 170–183 (2011).

85. Peng, J. *et al.* Dual-targeting of artesunate and chloroquine to tumor cells and tumor-associated macrophages by a biomimetic PLGA nanoparticle for colorectal cancer treatment. *International Journal of Biological Macromolecules* vol. 244 (2023).

86. Chang, C.-S., Ryu, J.-Y. & Choi, J.-K. Anti-cancer effect of fenbendazole incorporated PLGA nanoparticles in ovarian cancer. (2023).

87. Katiyar, S. S. & Muntimadugu, E. Co-delivery of rapamycin and piperine loaded polymeric nanoparticles for breast cancer treatment. (2015).

88. Fasehee, H., Ghavamzadeh, A., Alimoghaddam, K., Ghaffari, S. H. & Faghihi, S. A comparative cytotoxic evaluation of disulfiram encapsulated PLGA nanoparticles on MCF-7 cells. *International Journal of Hematology-Oncology and Stem Cell Research* vol. 11 102–107 (2017).

89. Wang, J. J. *et al.* Recent advances of chitosan nanoparticles as drug carriers. *International journal of nanomedicine* vol. 6 765–774 (2011).

90. Guadarrama-Escobar, O. R. *et al.* Chitosan Nanoparticles as Oral Drug Carriers. *Int. J. Mol. Sci.* **24**, 1–17 (2023).

91. Sachdeva, B. *et al.* Chitosan Nanoparticles-Based Cancer Drug Delivery: Application and Challenges. *Mar. Drugs* **21**, 1–23 (2023).

92. Khayati, M. *et al.* Microfluidic synthesis of zoledronic acid loaded chitosan nanoparticles used for osteogenic differentiation of mesenchymal cells. *International Journal of Biological Macromolecules* vol. 234 (2023).

93. Kefayat, A. & Hosseini, M. Biodegradable and biocompatible subcutaneous implants consisted of paH sensitive mebendazole- loaded.folic acid targeted chitosan nanoparticles for murine TNBC treatment. (2022).

94. Baksi, R. *et al.* In vitro and in vivo anticancer efficacy potential of Quercetin loaded polymeric nanoparticles. *Biomedicine and Pharmacotherapy* vol. 106 1513–1526

(2018).

95. Letchford, K. & Burt, H. A review of the formation and classification of amphiphilic block copolymer nanoparticulate structures: micelles, nanospheres, nanocapsules and polymersomes. *Eur. J. Pharm. Biopharm.* **65**, 259–269 (2007).

96. Xiao, Y., Wang, S., Zong, Q. & Yin, Z. Co-delivery of Metformin and Paclitaxel Via Folate-Modified pH-Sensitive Micelles for Enhanced Anti-tumor Efficacy. *AAPS PharmSciTech* **19**, 2395–2406 (2018).

97. Paulmurugan, R. & Bhethanabotla, R. Folate Receptor Targeted Polymeric Micellar nanocarriers for delivery of orlistat as a repurposed drug against triple negative breast cancer. (2016).

98. Xu, P. *et al.* Hydrogen-bonded and reduction-responsive micelles loading atorvastatin for therapy of breast cancer metastasis. *Biomaterials* vol. 35 7574–7587 (2014).

99. Joao G., A. & Gaspar, V. M. Synthesis and characterization of micelles as carriers of NSAID for application in breast cancer therapy. (2014).

100. James, J. R. *et al.* Hydrogel-Based Pre-Clinical Evaluation of Repurposed FDA-Approved Drugs for AML. *Int. J. Mol. Sci.* **24**, (2023).

101. He, C., Lu, J. & Lin, W. Hybrid nanoparticles for combination therapy of cancer. *Journal of Controlled Release* vol. 219 224–236 (2015).

102. Suh, J. *et al.* PEGylation of nanoparticles improves their cytoplasmic transport. *International Journal of Nanomedicine* vol. 2 735–741 (2007).

103. Yousaf, R. & Khan, M. I. Development and in vitro evaluation of chitosan and glyceryl monostearate based matrix lipid polymer hybrid nanoparticles for oral delivery of itraconazole. (2023).

104. Shi, J., Xiao, Z. & Votruba, A. R. Differentially Charged Hollow Core Shell Lipid Polymer Lipid hybrid nanoparticles for small interferign RNA delivery. (2011).

105. Rico, S. R. A. & Abbasi, A. Z. Diruthenium metallodrugs of ibuprofen and naproxen encapsulated in intravenously injectable polymer-lipid nanoparticles exhxibit enha ced activity against breast and prostate cancer cells.

106. Jiao, M. *et al.* Recent advancements in biocompatible inorganic nanoparticles towards biomedical applications. *Biomaterials Science* vol. 6 726–745 (2018).

107. Gibier, P. Dr. Koch's Discovery. (1890).

108. Forestier, J. The Treatment of Rheumatoid Arthritis with Gold Salt Injections. *Archives of Internal Medicine* vol. 109 134–135 (1932).

109. Bae, Y. & Kataoka, K. Intelligent polymeric micelles from functional poly(ethylene glycol)-poly(amino acid) block copolymers. *Adv. Drug Deliv. Rev.* **61**, 768–784 (2009).

110. Deng, C., Jiang, Y., Cheng, R., Meng, F. & Zhong, Z. Biodegradable polymeric micelles for targeted and controlled anticancer drug delivery: Promises, progress and prospects. *Nano Today* **7**, 467–480 (2012).

111. Balfourier, A. *et al.* Gold-based therapy: From past to present. *Proc. Natl. Acad. Sci. U. S. A.* **117**, 22639–22648 (2020).

112. Choudhury, K., Chattopadhyay, A. & Ghosh, S. S. Mannosylated Gold Nanoclusters Incorporated with a Repurposed Antihistamine Drug Promethazine for Antibacterial and Antibiofilm Applications. 257–272 (2022) doi:https://doi.org/10.1021/acsabm.2c00867.

113. Zhao, Y. Salinomycin Loaded Gold Nanoparticles for Treating Cancer Stem cells by ferroptosis induced cell death. (2019).

114. Mohammadkarimi, V. & Azarpira, N. Synthesis of Silver Doxycycline Complex Nanoparticles and Their biological evaluation on MCF7 cell line of reast cancer. (2021).

115. Mahalunkar, S. Functional design of pH responsive folate targeted polymer coated gold nanoparticles for drug delivery and in vivo therapy in breast cancer.

116. Yoo, J. W., Doshi, N. & Mitragotri, S. Adaptive micro and nanoparticles: Temporal control over carrier properties to facilitate drug delivery. *Advanced Drug Delivery Reviews* vol. 63 1247–1256 (2011).

117. Hwang, J. H., Kim, S. J. & Kim, Y.-H. Susceptibility to gold nanoparticle induced hepatotoxicity is enhanced in a mouse model of nonalcoholic steatohepatitis. 27–35 (2012).

118. Simpson, C. A., Salleng, K. J. & Cliffel, D. E. In vivo toxicity, biodistribution, and clearance of glutathione-coated gold nnoparticles. 257–263 (2013).

119. Levy, M. *et al.* Long term in vivo biotransformation of iron oxide nanoparticles. *Biomaterials* **32**, 3988–3999 (2011).

120. Anselmo, A. C. & Mitragotri, S. A Review of Clinical Translation of Inorganic Nanoparticles. *AAPS J.* **17**, 1041–1054 (2015).

121. Hauksdóttir, H. L. & Webster, T. J. Selenium and Iron Oxide Nanocomposites for Magnetically-Targeted Anti-Cancer Applications. *J. Biomed. Nanotechnol.* **14**, 510–525 (2018).

122. Shevtsov, M. A. *et al.* 70-kDa heat shock protein coated magnetic nanocarriers as a nanovaccine for induction of anti-tumor immune response in experimental glioma. *J. Control. Release* **220**, 329–340 (2015).

123. Bocanegra Gondan, A. I. *et al.* Effective cancer immunotherapy in mice by polyIC-imiquimod complexes and engineered magnetic nanoparticles. *Biomaterials* **170**, 95–115 (2018).

124. Ruiz-De-Angulo, A., Zabaleta, A., Gómez-Vallejo, V., Llop, J. & Mareque-Rivas, J. C. Microdosed lipid-coated 67Ga-magnetite enhances antigen-specific immunity by image tracked delivery of antigen and cpg to lymph nodes. *ACS Nano* **10**, 1602–1618 (2016).

125. Jin, H. *et al.* Magnetic enrichment of dendritic cell vaccine in lymph node with fluorescent-magnetic nanoparticles enhanced cancer immunotherapy. *Theranostics* **6**, 2000–2014 (2016).

126. Yadav, N., Kannan, D., Patil, S., Singh, S. & Lochab, B. Amplified Activity of Artesunate Mediated by Iron Oxide Nanoparticles Loaded on a Graphene Oxide Carrier for Cancer Therapeutics. *ACS Applied Bio Materials* vol. 3 6722–6736 (2020).

127. Ding, Y. & Wan, J. Localized Fe II Induced Cytotoxic Reactive Oxygen Species Generating Nanosystem For Enhanced Anticancer Therapy. (2018).

128. Wang, D., Zhou, J. & Chen, R. Magnetically guided delivery of DHA and Fe ions for enhanced cancer therapy based on pH-responsive degradation of DHA-loaded

Fe3O4@C@MIL-100(Fe) nanoparticles. (2016).

129. Ankamwar, B., Lai, T. C., Juang, J. H. & Liu, R. S. Biocompatibility of Fe3O4 nanoparticles evaluated by in vitro cytotoxicity assays using normal glia and breast cancer cells. (2009).

130. Laurent, S., Saei, A. A., Behzadi, S., Panahifar, A. & Mahmoudi, M. Superparamagnetic iron oxide nanoparticles for delivery of therapeutic agents: Opportunities and challenges. *Expert Opinion on Drug Delivery* vol. 11 1449–1470 (2014).

131. Yang, W. J. *et al.* Difference between toxicities of iron oxide magnetic nanoparticles with various surface-functional groups against human normal fibroblasts and fibrosarcoma cells. *Materials (Basel).* **6**, 4689–4706 (2013).

132. Abdelhamid, A. S. Lactoferrin-tagged quantum dots-based theranostic nanocapsules for combined COX-2 inhibitor/herbal therapy of breast cancer.

133. Lovrić, J. *et al.* Differences in subcellular distribution and toxicity of green and red emitting CdTe quantum dots. *J. Mol. Med.* **83**, 377–385 (2005).

134. Derfus, A. M., Chan, W. C. W. & Bhatia, S. N. Probing the Cytotoxicity of Semiconductor Quantum Dots. *Nano Letters* vol. 4 11–18 (2004).

135. Rosenthal, S. J., Chang, J. C., Kovtun, O., McBride, J. R. & Tomlinson, I. D. Biocompatible quantum dots for biological applications. *Chemistry and Biology* vol. 18 10–24 (2011).

136. Iranshahy, M. & Hanafi-Bojd, M. Y. Curcumin-loaded mesoporous silica nanoparticles for drug delivery: synthesis, biological assays and therapeutic potential – a review. (2023).

137. Liu, T. *et al.* Single and repeated dose toxicity of mesoporous hollow silica nanoparticles in intravenously exposed mice. *Biomaterials* vol. 32 1657–1668 (2011).

138. Kanwal, F., Ma, M. & Rehman, M. F. ur. Aspirin Repurposing in Folate-Decorated Nanoparticles: Another Way to Target Breast Cancer. (2022).

139. Fu, C. *et al.* The absorption, distribution, excretion and toxicity of mesoporous silica nanoparticles in mice following different exposure routes. *Biomaterials* vol. 34 2565–

2575 (2013).

140. Recent development of silica nanoparticles as delivery vectors for cancer imaging and therapy. (2014).

141. Zhang, J. *et al.* Multifunctional envelope-type mesoporous silica nanoparticles for tumor-triggered targeting drug delivery. *J. Am. Chem. Soc.* **135**, 5068–5073 (2013).

142. Chen, J. & Guo, Z. Multifunctional mesoporous nanoparticles as pH-responsive Fe2+ reservoirs and artemisinin vehicles for synergistic inhibition of tumor growth. 8–9 (2014).

143. Gisbert-Garzaran, M. *et al.* Designing Mesoporous Silica Nanoparticles to Overcome Biological Barriers by Incorporating Targeting and Endosomal Escape. *ACS Applied Materials and Interfaces* vol. 13 9656–9666 (2021).

144. Ahmadi, F., Sodagar-Taleghani, A. & Ebrahimnejad, P. A review on the latest developments of mesoporous silica nanoparticles as a promising platform for diagnosis and treatment of cancer. (2022).

145. Ahmed, N., Fessi, H. & Elaissari, A. Theranostic applications of nanoparticles in cancer. *Drug Discovery Today* vol. 17 928–934 (2012).

146. Liu, Z. *et al.* Drug delivery with carbon nanotubes for in vivo cancer treatment. *Cancer Research* vol. 68 6652–6660 (2008).

147. Huang, Y., Hsu, J. C., Koo, H. & Cormode, D. P. Repurposing ferumoxytol: Diagnostic and therapeutic applications of an FDA-approved nanoparticle. *Theranostics* vol. 12 796–816 (2022).

148. Zanganeh, S. *et al.* Iron oxide nanoparticles inhibit tumour growth by inducing pro-inflammatory macrophage polarization in tumour tissues. *Nature Nanotechnology* vol. 11 986–994 (2016).

149. Cho, K., Wang, X., Nie, S., Chen, Z. & Shin, D. M. Therapeutic nanoparticles for drug delivery in cancer. *Clinical Cancer Research* vol. 14 1310–1316 (2008).

150. Gmeiner, W. H. & Ghosh, S. Nanotechnology for cancer treatment. *Nanotechnol. Rev.* **3**, 111–122 (2014).

151. Gavas, S., Quazi, S. & Karpinski, T. M. Nanoparticles for Cancer Therapy: Current Progress and Challenges. (2021).

152. Maeda, H. Tumor-Selective Delivery of Macromolecular Drugs via the EPR Effect : Background and future prospects. *Bioconjugate Chemistry* vol. 21 797–802 (2010).

153. Kandula, S., Singh, P. K., Kaur, G. A. & Tiwari, A. Trends in smart drug delivery systems for targeting cancer cells. *Materials Science and Engineering: B* vol. 297 (2023).

154. Tran, P. H. L. Aspirin-loaded nanoexosomes as cancer therapeutics. (2019).

155. Singh, R. *et al.* Development and characterization of folate anchored Saquinavir entrapped PLGA nanoparticles for anti-tumor activity. *Drug Development and Industrial Pharmacy* vol. 41 1888–1901 (2015).

156. Yang, L. *et al.* Single chain epidermal growth factor receptor antibody conjugated nanoparticles for in vivo tumor targeting and imaging. *Small* vol. 5 235–243 (2009).

157. Wang, J.-L. & Wang, L. In vitro cancer cell imaging and therapy using transferrin conjugated gold nanoparticles. (2009).

158. Fay, F. & Mclaughlin, K. M. Conatumumab (AMG 655) coated nanoparticles for targeted pro-apoptotic drug delivery. (2011).

159. Greish, K. *Enhanced permeability and retention (EPR) effect for anticancer nanomedicine drug targeting. Methods in molecular biology (Clifton, N.J.)* vol. 624 (2010).

160. Yu, C., Hu, Y. & Duan, J. Novel Aptamer Nanoparticle Bioconjugates Enhances Delivery of Anticancer Drug to MUC1 Positive Cancer Cells In Vitro. (2011).

161. Choudhury, K., Chattopadhyay, A. & Ghosh, S. S. Therapeutic Targeting of Lung Adenocarcinoma with Mannose-Coated Chitosan/Copper Nanocluster–Levocetirizine Nanocomposite. 21371–21384 (2023).

162. Paunovska, K., Loughrey, D. & Dahlman, J. E. Drug delivery systems for RNA therapeutics. (2022).

163. Attia, M. F., Anton, N., Wallyn, J., Omran, Z. & Vandamme, T. F. An overview of active and passive targeting strategies to improve the nanocarriers efficiency to tumour sites. *Journal of Pharmacy and Pharmacology* vol. 71 1185–1198 (2019).

164. Singh R, E. H. *Antibody–Cytotoxic Agent Conjugates: Preparation and Characterization*. *Angewandte Chemie International Edition, 6(11), 951–952.* (2009).

165. Martinez-Negro, M. & Gonzalez-Rubio, G. Insights into colloidal nanoparticle-protein corona interactions for nanomedicine application. (2021).

166. Kaushik, N. *et al.* Nanocarrier cancer therapeutics with functional stimuli-responsive mechanisms. *J. Nanobiotechnology* **20**, 1–23 (2022).

167. Webb, B. A., Chimenti, M., Jacobson, M. P. & Barber, D. L. Dysregulated pH: A perfect storm for cancer progression. *Nature Reviews Cancer* vol. 11 671–677 (2011).

168. Brown, J. M. & Wilson, W. R. EXPLOITING TUMOUR HYPOXIA IN CANCER TREATMENT. (2004).

169. Rica, R. de la, Aili, D. & Stevens, M. M. Enzyme responsive nanoparticles for drug release and diagnostics. (2012).

170. Wu, D., Si, M., Xue, H. Y. & Wong, H. L. Nanomedicine applications in the treatment of breast cancer: Current state of the art. *Int. J. Nanomedicine* **12**, 5879–5892 (2017).

171. Farcas, C. G. *et al.* Thermosensitive betulinic acid-loaded magnetoliposomes: A promising antitumor potential for highly aggressive human breast adenocarcinoma cells under hyperthermic conditions. *Int. J. Nanomedicine* **15**, 8175–8200 (2020).

172. Zhang, T. *et al.* A pH-sensitive nanotherapeutic system based on a marine sulfated polysaccharide for the treatment of metastatic breast cancer through combining chemotherapy and COX-2 inhibition. *Acta Biomaterialia* vol. 99 412–425 (2019).

173. Polireddy, K. *et al.* High dose parenteral ascorbate inhibited pancreatic cancer growth and metastasis: Mechanisms and a phase I/IIa study. *Scientific Reports* vol. 7 (2017).

174. Li, Y., Wang, L.-H. & Zhang, H.-T. Disulfiram combined with copper inhibits metastasis and epithelial–mesenchymal transition in hepatocellular carcinoma through the NF-jB and TGF-b pathways. (2017).

175. Shaashua, L. *et al.* Perioperative COX-2 and β-adrenergic blockade improves metastatic biomarkers in breast cancer patients in a phase-II randomized trial. *Clinical Cancer Research* vol. 23 4651–4661 (2017).

176. Granados-Principal, S. *et al.* Inhibition of iNOS as a novel effective targeted therapy against triple-negative breast cancer. *Breast Cancer Research* vol. 17 (2015).

177. Davila-Gonzalez, D., Choi, D. S., Rosato, R. R. & Granados-Principal, S. M. Pharmacological Inhibition of NOS Activates ASK1/JNK Pathway Augmenting Docetaxel-Mediated Apoptosis in Triple-Negative Breast Cancer. (2018).

178. Schacke, M. *et al.* PARP-1/2 inhibitor olaparib prevents or partially reverts EMT induced by TGF-β in NMuMG cells. *Int. J. Mol. Sci.* **20**, 9–11 (2019).

179. Kolosionek, E., Savai, R. & Ghofrani, H. A. Expression and Activity of Phosphodiesterase Isoforms during Epithelial Mesenchymal Transition: The Role of Phosphodiesterase 4. (2009).

180. Kato, S. *et al.* Simvastatin interferes with cancer 'stem-cell' plasticity reducing metastasis in ovarian cancer. *Endocr. Relat. Cancer* **25**, 821–836 (2018).

181. Wang, G. *et al.* Simvastatin induces cell cycle arrest and inhibits proliferation of bladder cancer cells via PPARγ signalling pathway. *Scientific Reports* vol. 6 (2016).

182. Shah, S. *et al.* The close relationship between heparanase and epithelial mesenchymal transition in gastric signet-ring cell adenocarcinoma. *Oncotarget* **9**, 33778–33787 (2018).

183. Zhao, H. *et al.* Up-regulation of glycolysis promotes the stemness and EMT phenotypes in gemcitabine-resistant pancreatic cancer cells. *Journal of Cellular and Molecular Medicine* vol. 21 2055–2067 (2017).

184. Fischer, K. R. *et al.* Epithelial-to-mesenchymal transition is not required for lung metastasis but contributes to chemoresistance. *Nature* **527**, 472–476 (2015).

185. Zheng, X. *et al.* Epithelial-to-mesenchymal transition is dispensable for metastasis but induces chemoresistance in pancreatic cancer. *Nature* **527**, 525–530 (2015).

186. Horn, L. A., Fousek, K. & Palena, C. Tumor Plasticity and Resistance to

Immunotherapy. *Trends in Cancer* vol. 6 432–441 (2020).

187. Papadaki, M. A. Circulating Tumor Cells with Stemness and Epithelial-to-Mesenchymal Transition Features Are Chemoresistant and Predictive of Poor Outcome in Metastatic Breast Cancer. (2019).

188. Campbell, S. L. & Wellen, K. E. Metabolic Signaling to the Nucleus in Cancer. *Molecular Cell* vol. 71 398–408 (2018).

189. Halldorsson, S. *et al.* Metabolic re-wiring of isogenic breast epithelial cell lines following epithelial to mesenchymal transition. *Cancer Letters* vol. 396 117–129 (2017).

190. Mathow, D. *et al.* Zeb1 affects epithelial cell adhesion by diverting glycosphingolipid metabolism. *EMBO Rep.* **16**, 321–331 (2015).

191. Dong, C., Yuan, T. & Wu, Y. Loss of FBP1 by Snail-Mediated Repression Provides Metabolic Advantages in Basal-like Breast Cancer. (2013).

192. Viswanathan, V. S. *et al.* Dependency of a therapy-resistant state of cancer cells on a lipid peroxidase pathway. *Nature* **547**, 453–457 (2017).

193. Pandey, H., Rani, R. & Agarwal, V. Liposome and their applications in cancer therapy. *Brazilian Archives of Biology and Technology* vol. 59 1–10 (2016).

194. Rommasi, F. & Esfandiari, N. Liposomal Nanomedicine: Applications for Drug Delivery in Cancer Therapy. *Nanoscale Research Letters* vol. 16 (2021).

195. Zhang, C., Xu, C., Gao, X. & Yao, Q. Platinum-based drugs for cancer therapy and anti-tumor strategies. (2022).

196. Mundekkad, D. & Cho, W. C. Nanoparticles in Clinical Translation for Cancer Therapy. **23**, 1–29 (2022).

197. Persano, F., Gigli, G. & Leporatti, S. Lipid-polymer hybrid nanoparticles in cancer therapy: current overview and future directions. (2021).

198. Jana, D. *et al.* Clearable Black Phosphorus Nanoconjugate for Targeted Cancer phototheranostics. 18342–18351 (2020).

199. An, C. *et al.* Nanomaterials and nanotechnology for the delivery of agrochemicals: strategies towards sustainable agriculture. *J. Nanobiotechnology* **20**, 1–19 (2022).

200. Sharma, R., Singh, D., Gaur, P. & Joshi, D. Intelligent automated drug administration and therapy: future of healthcare. *Drug Delivery and Translational Research* vol. 11 1878–1902 (2021).

201. Gupta, R. *et al.* Artificial intelligence to deep learning: machine intelligence approach for drug discovery. 1315–1360 (2021).

202. Soltani, M., Kashkooli, F. M., Souri, M. & Harofte, S. Z. Enhancing Clinical Translation of Cancer Using Nanoinformatics. **13**, (2021).

203. Xie, J., Zheng, Y. & Ying, J. Y. Protein-directed synthesis of highly fluorescent gold nanoclusters. *J. Am. Chem. Soc.* **131**, 888–889 (2009).

204. Jian, W., He, J., Sun, Y. & Pang, J. Comparative studies on physicochemical properties of bovine serum albumin-glucose and bovine serum albumin-mannose conjugates formed via Maillard reaction. *LWT - Food Science and Technology* vol. 69 358–364 (2016).

205. Martins, S. I. F. S., Jongen, W. M. F. & Van Boekel, M. A. J. S. A review of Maillard reaction in food and implications to kinetic modelling. *Trends in Food Science and Technology* vol. 11 364–373 (2000).

206. Jian, W., He, J., Sun, Y. & Pang, J. Comparative studies on physicochemical properties of bovine serum albumin-glucose and bovine serum albumin-mannose conjugates formed via Maillard reaction. *LWT - Food Sci. Technol.* **69**, 358–364 (2016).

207. Das, M., Goswami, U. & Bhattacharyya, S. Integration of a Nonsteroidal Anti-Inflammatory Drug with Luminescent Copper for in Vivo Cancer Therapy in a Mouse Model. *ACS Applied Bio Materials* vol. 3 227–238 (2020).

208. Blanco, E., Shen, H. & Ferrari, M. Principles of nanoparticle design for overcoming biological barriers to drug delivery. *Physiol. Behav.* **33**, 941–951 (2015).

209. Alexis, F., Pridgen, E., Molnar, L. K. & Farokhzad, O. C. Factors affecting the clearance and biodistribution of polymeric nanoparticles. *Mol. Pharm.* **5**, 505–515 (2008).

210. Häkkinen, H. The gold-sulfur interface at the nanoscale. *Nature Chemistry* vol. 4 443–455 (2012).

211. Simon, A. T., Dutta, D., Chattopadhyay, A. & Ghosh, S. S. Copper Nanocluster-Doped Luminescent Hydroxyapatite Nanoparticles for Antibacterial and Antibiofilm Applications. *ACS Omega* vol. 4 4697–4706 (2019).

212. Ebrahimi, S., Farhadian, N., Karimi, M. & Ebrahimi, M. Enhanced bactericidal effect of ceftriaxone drug encapsulated in nanostructured lipid carrier against gram-negative Escherichia coli bacteria: Drug formulation, optimization, and cell culture study. *Antimicrob. Resist. Infect. Control* **9**, 1–12 (2020).

213. Cegelski, L., Marshall, G. R., Eldridge, G. R. & Hultgren, S. J. The biology and future prospects of antivirulence therapies. *Nature Reviews Microbiology* vol. 6 17–27 (2008).

214. Wright, K. J., Seed, P. C. & Hultgren, S. J. Development of intracellular bacterial communities of uropathogenic Escherichia coli depends on type 1 pili. *Cell. Microbiol.* **9**, 2230–2241 (2007).

215. Soto, G. E. & Hultgren, S. J. Bacterial adhesins: Common themes and variations in architecture and assembly. *J. Bacteriol.* **181**, 1059–1071 (1999).

216. Krogfelt, K. A. Bacterial adhesion: Genetics, biogenesis, and role in pathogenesis of fimbrial adhesins of Escherichia coli. *Rev. Infect. Dis.* **13**, 721–735 (1991).

217. Martins, M., Dstidar, S. G. & Fanning, S. Potential role of non-antibiotics (helper compounds) in the treatment of multidrug-resistant Gram-negative infections: mechanisms for their direct and indirect activities. 198–208 (2008).

218. SALTON, M. R. The relationship between the nature of the cell wall and the Gram stain. *J. Gen. Microbiol.* **30**, 223–235 (1963).

219. Kaatz, G. W., Moudgal, V. V., Seo, S. M. & Kristiansen, J. E. Phenothiazines and thioxanthenes inhibit multidrug efflux pump activity in Staphylococcus aureus. *Antimicrob. Agents Chemother.* **47**, 719–726 (2003).

220. Wassmann, C. S., Lund, L. C. & Mette, T. Molecular mechanisms of thioridazine resistance in staphylococcus aureus. *PLoS One* **13**, 1–17 (2018).

221. Grimsey, E. M. & Piddock, L. J. V. Do phenothiazines possess antimicrobial and efflux inhibitory properties? *FEMS Microbiol. Rev.* **43**, 577–590 (2019).

222. Xie, Y., Liu, Y. & Yang, J. Gold Nanoclusters for Targeting Methicillin-Resistant Staphylococcus aureus In Vivo. *Angew. Chemie - Int. Ed.* **57**, 3958–3962 (2018).

223. Yougbare, S., Chnag, T.-K. & Tan, S.-H. Antimicrobial Gold Nanoclusters Recent Developments and Future Perspectives. 1–17 (2019).

224. Farber, J. L. Mechanisms of cell injury by activated oxygen species. *Environ. Health Perspect.* **102**, 17–24 (1994).

225. Kuo, J. C., Tan, S. H. & Hsiao, Y. C. Unveiling the Antibacterial Mechanism of Gold Nanoclusters via In Situ Transmission Electron Microscopy. *ACS Sustainable Chemistry and Engineering* vol. 10 464–471 (2022).

226. Vilela, S. F. G., Junqueira, J. C. & Barbosa, J. O. Photodynamic inactivation of Staphylococcus aureus and Escherichia coli biofilms by malachite green and phenothiazine dyes: An in vitro study. *Archives of Oral Biology* vol. 57 704–710 (2012).

227. Costerton, J. W., Stewart, P. S. & Greenberg, E. P. Bacterial biofilms: A common cause of persistent infections. *Science (80-.).* **284**, 1318–1322 (1999).

228. Skariyachan, S., Sridhar, V. S., Packirisamy, S., Kumargowda, S. T. & Challapilli, S. B. Recent perspectives on the molecular basis of biofilm formation by Pseudomonas aeruginosa and approaches for treatment and biofilm dispersal. *Folia Microbiol. (Praha).* **63**, 413–432 (2018).

229. Martin, I., Waters, V. & Grasemann, H. Approaches to targeting bacterial biofilms in cystic fibrosis airways. *International Journal of Molecular Sciences* vol. 22 1–15 (2021).

230. Thi, M. T. T., Wibowo, D. & Rehm, B. H. A. Pseudomonas aeruginosa Biofilms. 1–25 (2020).

231. Bhattacharya, M., Wozniak, D. J., Stoodley, P. & Hall-Stoodley, L. Prevention and treatment of Staphylococcus aureus biofilms. 1499–1516 (2015).

232. Liang, Y., Xu, H. & Guo, B. pH/Glucose Dual Responsive Metformin release hydrogel

dressings with adhesion and self-healing via dual-dynamic bonding for athletic diabetic foot wound healing. 3194–3207 (2022).

233. Chen, J., Qiao, L., Zhang, J. & Guo, B. Antibacterial adhesive self-healing hydrogels to promote diabetic wound healing. *Acta Biomaterialia* vol. 146 119–130 (2022).

234. Ramchandani, M. & Robinson, D. In vitro and in vivo release of ciprofloxacin from PLGA 50:50 implants. *Journal of Controlled Release* vol. 54 167–175 (1998).

235. Amann, L. C., Gandal, M. J., Lin, R., Liang, Y. & Siegel, S. J. In Vitro–In VivoCorrelations of Scalable PLGA-RisperidoneImplants for the Treatment of Schizophrenia.pdf. 1730–1737 (2010).

236. Herdiana, Y., Wathoni, N., Shamsuddin, S. & Muchtaridi, M. Drug release study of the chitosan-based nanoparticles. *Heliyon* vol. 8 (2022).

237. Patel, B. K., Parikh, R. H. & Aboti, P. S. Development of Oral Sustained Release Rifampicin Loaded Chitosan Nanoparticles by Design of Experiment. *Journal of Drug Delivery* vol. 2013 1–10 (2013).

238. Feng, H. & Yang, X. Mannose Modified Chitosan Poly(lactic-co-glycolic acid) Microspheres Act as a Mannose Receptor-Mediated Delivery System Enhancing the Immune Response. (2021) doi:10.3390/polym13132208.

239. Yin, L., Chen, Y. & Zhang, Z. Biodegradable micelles capable of mannose-mediated targeted drug delivery to cancer cells. 483–489 (2015).

240. Soni, N., Soni, N. & Pandey, H. Augmented delivery of gemcitabine in lung cancer cells exploring mannose anchored solid lipid nanoparticles. 107–116 (2016).

241. Wang, Y. & Xu, F.-J. Mannose-functionalized star polycation mediated CRISPR/Cas9 delivery for lung cancer therapy. (2022).

242. Vedove, E. D. & Merkel, O. M. Mannose and Mannose-6-Phosphate Receptor-targeted Drug Delivery Systems and their application in Cancer Therapy. (2018).

243. Gupte, A. & Mumper, R. J. Elevated copper and oxidative stress in cancer cells as a target for cancer treatment. *Cancer Treatment Reviews* vol. 35 32–46 (2009).

244. Zong, D., Haag, P. & Viktorsson, K. Chemosensitization by phenothiazines in human lung cancer cells: impaired resolution of cH2AX and increased oxidative stress elicit apoptosis associated with lysosomal expansion and intense vacuolation. 1–12 (2011).

245. Wu, C.-H., Bai, L.-Y. & Tsai, M.-H. Pharmacological exploitation of the phenothiazine antipsychotics to develop antitumour agents - A drug repurposing strategy. 1–11 (2016).

246. Xue, Q., Kang, R. & Klionsky, D. J. Copper metabolism in cell death and autophagy. *Autophagy* (2023) doi:10.1080/15548627.2023.2200554.

247. Dubmann, H., Rehm, M. & Kogel, D. Outer Mitochondrial Membrane. *Definitions* 525–536 (2003) doi:10.1242/jcs.00236.

248. Jin, C. & Yuan, P. Implications of lipid droplets in lung cancer : Associations with drug resistance (Review). *Oncol. Lett.* **20**, 2091–2104 (2020).

249. Olzmann, J. A. & Carvalho, P. Dynamics and functions of lipid droplets. *Nat. Rev. Mol. Cell Biol.* **20**, 137–155 (2019).

250. Pavlova, N. N. & Thompson, C. B. The Emerging Hallmarks of Cancer Metabolism. *Cell Metabolism* vol. 23 27–47 (2016).

251. Zagani, R., El-Assaad, W., Gamache, I. & Teodoro, J. G. Inhibition of adipose triglyceride lipase (ATGL) by the putative tumor suppressor G0S2 or a small molecule inhibitor attenuates the growth of cancer cells. *Oncotarget* **6**, 28282–28295 (2015).

252. Patterson, A. D., Maurhofer, O. & Beyoglu, D. Aberrant Lipid Metabolism in Hepatocellular Carcinoma revealed by plasma metabolomics and lipid profiling. 6590–6600 (2011) doi:10.1158/0008-5472.

253. Zhang, X. De, Li, W. & Zhang, N. Identification of adipophilin as a potential diagnostic tumor marker for lung adenocarcinoma. *International Journal of Clinical and Experimental Medicine* vol. 7 1190–1196 (2014).

254. Jonkman, J. E. N. & Cathcart, J. A. An introduction to the wound healing assay using live-cell microscopy. (2014).

255. Chen, Y. Scratch Wound Healing Assay —BIO-PROTOCOL. (2012).

256. Turksen, K. *Epidermal Cells*. *Epidermal Cells* (2004). doi:10.1385/1592598307.

257. Gilazieva, Z., Ponomarev, A., Rutland, C., Rizvanov, A. & Solovyeva, V. Promising applications of tumor spheroids and organoids for personalized medicine. *Cancers (Basel).* **12**, 1–19 (2020).

258. Kamatar, A., Gunay, G. & Acar, H. Natural and synthetic biomaterials for engineering multicellular tumor spheroids. *Polymers (Basel).* **12**, 1–23 (2020).

259. Murakami, H., Kobayashi, M., Takeuchi, H. & Kawashima, Y. Preparation of poly(DL-lactide-co-glycolide) nanoparticles by modified spontaneous emulsification solvent diffusion method. 143–152 (1999).

260. Cheng, J. & Al., B. A. T. et. Formulation of functionalized PLGA–PEG nanoparticles for in vivotargeted drug delivery.pdf.

261. Kantaria, T. *et al.* Biodegradable nanoparticles made of amino-acid-based ester polymers: Preparation, characterization, and in vitro biocompatibility study. *Appl. Sci.* **6**, (2016).

262. Huang, W. & Zhang, C. Tuning the Size of Poly(lactic-co-glycolic Acid) (PLGA) Nanoparticles Fabricated by Nanoprecipitation. *Biotechnol. J.* **13**, 1–8 (2018).

263. Jiang, X. Y., Zhou, C. S. & Tang, K. W. Preparation of PLA and PLGA nanoparticles by binary organic solvent diffusion method. *J. Cent. South Univ. Technol. (English Ed.* **10**, 202–206 (2003).

264. Hernández-Giottonini, K. Y. *et al.* PLGA nanoparticle preparations by emulsification and nanoprecipitation techniques: Effects of formulation parameters. *RSC Advances* vol. 10 4218–4231 (2020).

265. Ramchandani, M. a, Pankaskie, M. & Robinson, D. The influence of manufacturing procedure on the degradation of poly(lactide-co-glycolide) 85:15 and 50:50 implants. 161–173 (1997).

266. Carew, J. S., Giles, F. J. & Nawrocki, S. T. Histone deacetylase inhibitors: Mechanisms of cell death and promise in combination cancer therapy. 7–17 (2008).

267. Pteruccelli, L. A. *et al.* Vorinostat Induces Reactive Oxygen Species and DNADamage

in Acute Myeloid Leukemia Cells.pdf.

268. Zong, D., Hååg, P., Yakymovych, I., Lewensohn, R. & Viktorsson, K. Chemosensitization by phenothiazines in human lung cancer cells: Impaired resolution of γh2AX and increased oxidative stress elicit apoptosis associated with lysosomal expansion and intense vacuolation. *Cell Death Dis.* **2**, (2011).

269. Wu, C. H. *et al.* Pharmacological exploitation of the phenothiazine antipsychotics to develop novel antitumor agents-A drug repurposing strategy. *Scientific Reports* vol. 6 (2016).

270. Perillo, B. *et al.* ROS in cancer therapy: the bright side of the moon. 192–203 (2020).

271. Rameshthangam, P. & Chitra, J. P. Synergistic anticancer effect of green synthesized nickel nanoparticles and quercetin extracted from Ocimum sanctum leaf extract. *J. Mater. Sci. Technol.* **34**, 508–522 (2018).

272. Wu, S., Luo, Z., Yu, P.-J., Xie, H. & He, Y.-W. Suberoylanilide hydroxamic acid (SAHA) promotes the epithelial mesenchymal transition of triple negative breast cancer cells via HDAC8/FOXA1 signals. 75–83 (2016).

273. Rossi, M. & Blasi, P. Multicellular Tumor Spheroids in Nanomedicine Research: A Perspective. *Front. Med. Technol.* **4**, 1–7 (2022).

List of Publications

From Thesis Work:

1. **Choudhury, K.**, Chattopadhyay, A., Ghosh, S. S. Mannosylated Gold Nanoclusters Incorporated with Repurposed Antihistamine Drug Promethazine for Antibacterial and Antibiofilm Applications. *ACS Applied Bio Materials. 2022,* 5 (12), 5911–5923

   DOI: 10.1021/acsabm.2c00867
2. **Choudhury, K.**, Chattopadhyay, A., Ghosh, S. S. Therapeutic Targeting of Lung Adenocarcinoma with Mannose-Coated Chitosan/Copper Nanocluster - Levocetirizine Nanocomposite. *ACS Applied Nano Materials. 2023*, 6 (22), 21371-21384

   DOI: 10.1021/acsanm.3c04868
3. **Choudhury, K.**, Ghosh, S. S. Ameliorating Old Drugs with New Tricks in the Nano Realms. *ACS Applied Nano Materials. 2024*, 7 (4), 3564-3579

   DOI: 10.1021/acsanm.3c06195
4. **Choudhury, K.**, Sen, P., and Ghosh, S. S. Pre-treatment with SAHA potentiates the activity of repurposed drug promethazine loaded PLGA nanoparticles towards altering EMT dynamics of Triple-negative breast cancer cells. **(Communicated)**

From Collaborative Work:

1. Nandi, N., **Choudhury, K.**, Sarkar, P., Barnwal Neha and Sahu, K. Ratiometric Multimode Detection of pH and Fe^{3+} by Dual-Emissive Heteroatom-Doped Carbon Dots for Living Cell Applications. *ACS Applied Nano Materials. 2022,* 5 (11), 17315–17324

   DOI: 10.1021/acsanm.2c0453
2. Bhuyan, T., **Choudhury, K**. Anticancer Therapeutic Efficacy of Biogenic Silica Nanoparticles on 3D Tumor Spheroids. (**Manuscript under preparation**)
3. Nandi, N., **Choudhury, K.**, Sahu K. Studying the Antibacterial Application of Cobalt-cp and Nickel-cp. (**Manuscript under preparation**)

Conferences

1. **Participated** in 6th International Conference on Advanced Nanomaterials and Nanotechnology (ICANN2019) during 18th-21st December, 2019; organised by Centre for Nanotechnology, IIT Guwahati.
2. **Participated** in 6th Workshop on Nanoelectronics and Theranostics in Post COVID-19 Pandemic Centre for Nanotechnology NWNTD-2020 during 1-3rd December 2020; organised by the Centre for Nanotechnology, IIT Guwahati.
3. **Participated** in Online workshop on Flow Cytometry Techniques and Applications, December 21 & 22, 2020; organized by North East Centre for Biological Sciences and Healthcare Engineering (NECBH) and IIT Guwahati.
4. **Participated** in Online workshop on Scanning Electron Microscopy: Technique and its Applications on 29th – 30th July 2021; organized by North East Centre for Biological Sciences and Healthcare Engineering (NECBH) and Indian Institute of Technology Guwahati, Assam.
5. **Participated** in 7th International conference on Advanced Nanomaterials and Nanotechnology (ICANN2021) on 14th-17th December, 2021; organized by Centre for Nanotechnology, IIT Guwahati.
6. **Participated** in poster presentation on *"Drug repurposing for cancer and antimicrobial therapy"* at 1st offline INUP-i2i 2022 workshop on Nanoelectronics- Fabrication and Characterization on 4th-6th April, 2022; organized by Centre for Nanotechnology, IIT Guwahati. **[Best poster award]**
7. Poster presentation at the **42nd annual conference of the Indian Association of Cancer Research "Bringing basic and translational research to the clinic: Challenges and Opportunities"** held on 12-16 January, 2023; organized by ACTREC, Tata Memorial Centre, Khargar, Navi Mumbai-India.
8. **Resource person** at the offline workshop titled **"Hands-on workshop on basic flow cytometry"** conducted by BioNEST, IIT Guwahati Technology Innovation and Development foundation on January 18th, 2023.
9. **Participated** in Offline familiarization workshop on Nanoelectronics: Fabrication and Characterization under Indian Nanoelectronics Users' Program-Idea to Innovation (INUP-

i2i) during 25th-27th April, 2023; organized by Centre for Nanotechnology, IIT Guwahati. **[Best poster award]**

10. **Participated** in 3-minute Thesis presentation on *"Nanotechnology-based drug repurposing to bypass therapeutic bottlenecks"* in Research and Industrial Conclave 2023 during 14th-16th May, 2023; organised by IIT Guwahati.
11. **Participated** in oral presentation at the Indo-Japan Symposium on Nanotheranostics (InJaNa 2024) [23-25 April 2024] – "Teaching New Tricks to Old Drugs with Nanomaterials"; organized by Department of Biosciences and Bioengineering and the Centre for Nanotechnology, IIT Roorkee. **[Best oral presentation award]**

Appendix

4 X protein loading dye (for 10 ml)	2 ml 1M Tris-HCl (pH 6.8), 0.8 g SDS, 4.0 ml 100 % glycerol, 0.4 ml 14.7 M β- mercaptoethanol, 8 mg bromophenol blue in water
30% Acrylamide solution	29.2 % (w/w) Acrylamide, 0.8 % (w/w) N, N' -methylenebisacrylamide.
Blocking buffer for Western blot	4 % (w/v) BSA in PBST/ TBST
Gel running buffer(10x)	250 mM Tris base, 1.92 M glycine, and 1 % SDS
Phosphate buffer saline	137 mM NaCl, 2.68 mM KCl, 7.98 mM Na2HPO4, 1.4 mM KH2PO4, pH 7.4
Tris buffered saline	Tris-HCl (50Mm), NaCl (150 mM), pH 7.5
Tris buffered saline Tween - 20 (TBST)	Tris-HCl (50Mm), NaCl (150 mM), Tween 20 (0.1% v/v) pH 7.5
Tris acetate EDTA(TAE) 50 X, (100 ml)	24.2 g Tris base, 5.71 ml of glacial acetic acid, 10 ml of 0.5 EDTA (pH 8)
Towbin Buffer (5X)	25 mM Tris base, 192 mM glycine, and 20 % methanol

Permissions

ACS Publication Licensing Terms and Conditions

Chapter 1

1.1. Ameliorating Old Drugs with New Tricks in the Nano Realms

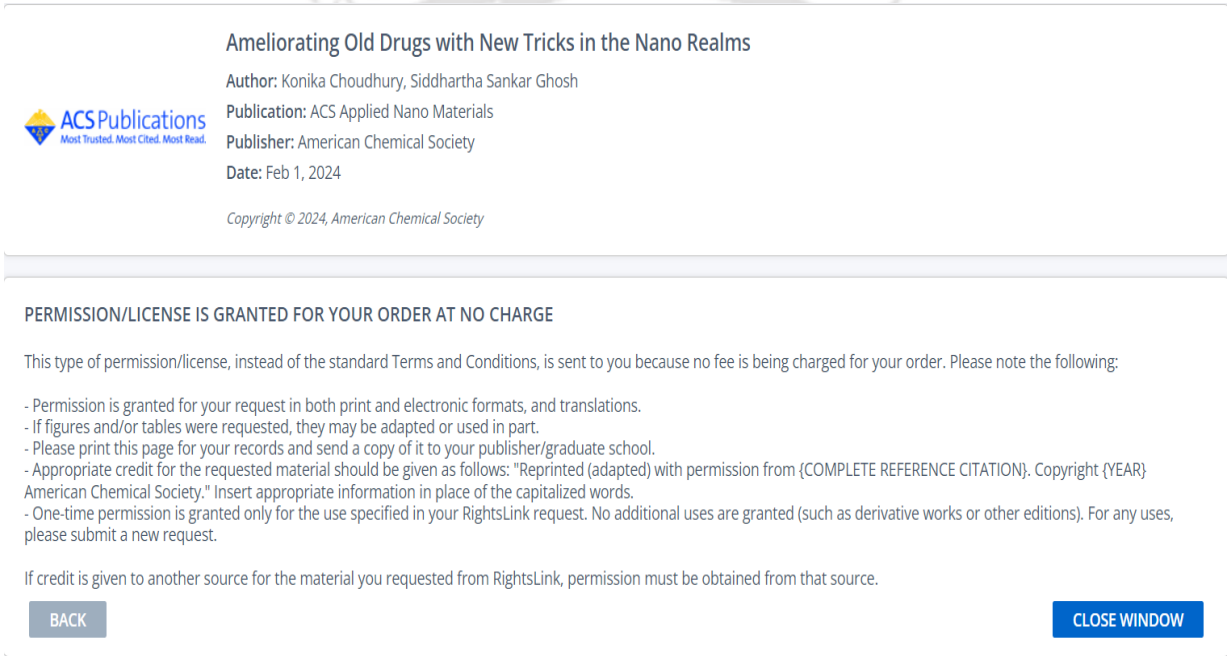

Ameliorating Old Drugs with New Tricks in the Nano Realms

Author: Konika Choudhury, Siddhartha Sankar Ghosh

Publication: ACS Applied Nano Materials

Publisher: American Chemical Society

Date: Feb 1, 2024

Copyright © 2024, American Chemical Society

PERMISSION/LICENSE IS GRANTED FOR YOUR ORDER AT NO CHARGE

This type of permission/license, instead of the standard Terms and Conditions, is sent to you because no fee is being charged for your order. Please note the following:

- Permission is granted for your request in both print and electronic formats, and translations.
- If figures and/or tables were requested, they may be adapted or used in part.
- Please print this page for your records and send a copy of it to your publisher/graduate school.
- Appropriate credit for the requested material should be given as follows: "Reprinted (adapted) with permission from {COMPLETE REFERENCE CITATION}. Copyright {YEAR} American Chemical Society." Insert appropriate information in place of the capitalized words.
- One-time permission is granted only for the use specified in your RightsLink request. No additional uses are granted (such as derivative works or other editions). For any uses, please submit a new request.

If credit is given to another source for the material you requested from RightsLink, permission must be obtained from that source.

BACK CLOSE WINDOW

Permissions

ACS Publication Licensing Terms and Conditions

Chapter 3

3.1. Mannosylated Gold Nanoclusters Incorporated with Repurposed Antihistamine Drug Promethazine for Antibacterial and Antibiofilm Applications.

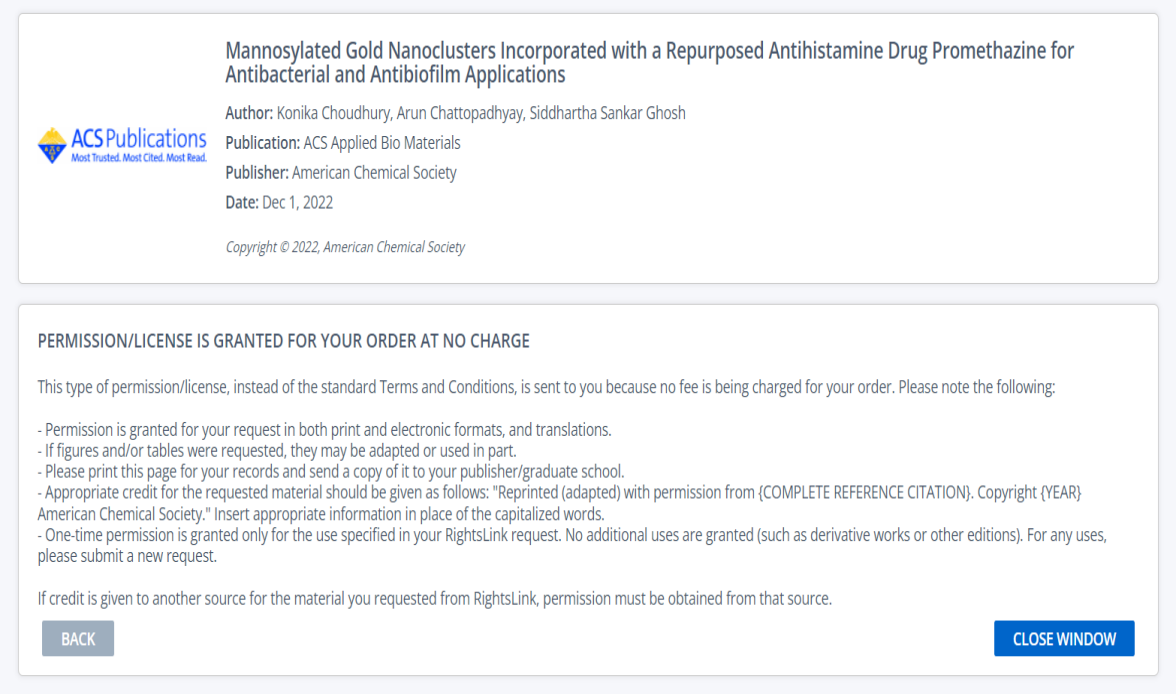

Mannosylated Gold Nanoclusters Incorporated with a Repurposed Antihistamine Drug Promethazine for Antibacterial and Antibiofilm Applications

Author: Konika Choudhury, Arun Chattopadhyay, Siddhartha Sankar Ghosh

Publication: ACS Applied Bio Materials

Publisher: American Chemical Society

Date: Dec 1, 2022

Copyright © 2022, American Chemical Society

PERMISSION/LICENSE IS GRANTED FOR YOUR ORDER AT NO CHARGE

This type of permission/license, instead of the standard Terms and Conditions, is sent to you because no fee is being charged for your order. Please note the following:

- Permission is granted for your request in both print and electronic formats, and translations.
- If figures and/or tables were requested, they may be adapted or used in part.
- Please print this page for your records and send a copy of it to your publisher/graduate school.
- Appropriate credit for the requested material should be given as follows: "Reprinted (adapted) with permission from {COMPLETE REFERENCE CITATION}. Copyright {YEAR} American Chemical Society." Insert appropriate information in place of the capitalized words.
- One-time permission is granted only for the use specified in your RightsLink request. No additional uses are granted (such as derivative works or other editions). For any uses, please submit a new request.

If credit is given to another source for the material you requested from RightsLink, permission must be obtained from that source.

BACK CLOSE WINDOW

Permissions

ACS Publication Licensing Terms and Conditions

Chapter 3

3.2. Therapeutic targeting of lung adenocarcinoma with mannose-coated chitosan/Cu nanocluster-levocetirizine nanocomposite.

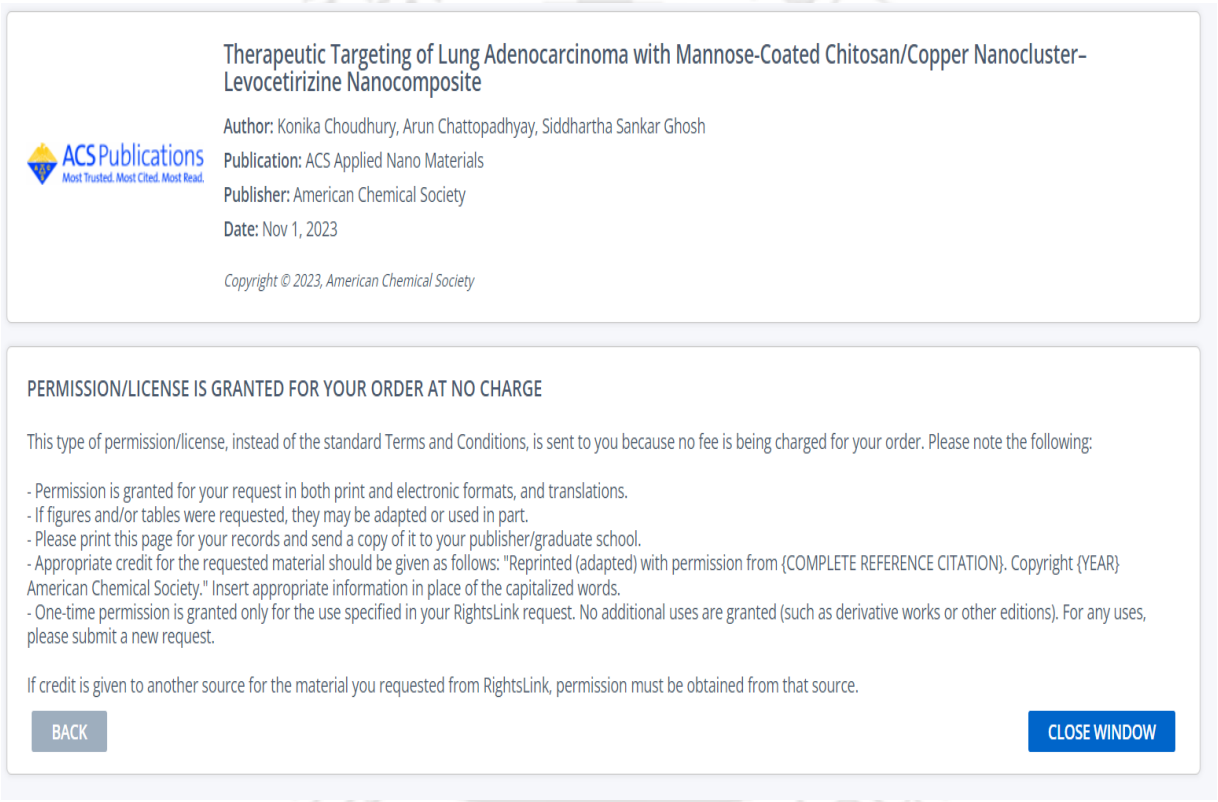

Therapeutic Targeting of Lung Adenocarcinoma with Mannose-Coated Chitosan/Copper Nanocluster-Levocetirizine Nanocomposite

Author: Konika Choudhury, Arun Chattopadhyay, Siddhartha Sankar Ghosh

Publication: ACS Applied Nano Materials

Publisher: American Chemical Society

Date: Nov 1, 2023

Copyright © 2023, American Chemical Society

PERMISSION/LICENSE IS GRANTED FOR YOUR ORDER AT NO CHARGE

This type of permission/license, instead of the standard Terms and Conditions, is sent to you because no fee is being charged for your order. Please note the following:

- Permission is granted for your request in both print and electronic formats, and translations.
- If figures and/or tables were requested, they may be adapted or used in part.
- Please print this page for your records and send a copy of it to your publisher/graduate school.
- Appropriate credit for the requested material should be given as follows: "Reprinted (adapted) with permission from {COMPLETE REFERENCE CITATION}. Copyright {YEAR} American Chemical Society." Insert appropriate information in place of the capitalized words.
- One-time permission is granted only for the use specified in your RightsLink request. No additional uses are granted (such as derivative works or other editions). For any uses, please submit a new request.

If credit is given to another source for the material you requested from RightsLink, permission must be obtained from that source.

BACK CLOSE WINDOW